What is Light-Induced Damage?

PRE-ABLATION REGIME OPTICAL
AND MORPHOLOGICAL CHANGES
IN NANOMETER THICK FILMS
AND GRATING STRUCTURES

Printed by: Gildeprint

Front & Back: Adinda de Lange

What is Light-Induced Damage?

Pre-ablation regime optical and morphological changes in nanometer thick films and grating structures

ACADEMISCH PROEFSCHRIFT

ter verkrijging van de graad van doctor

aan de Universiteit van Amsterdam

op gezag van de Rector Magnificus

prof. dr. ir. P.P.C.C. Verbeek

ten overstaan van een door het College voor Promoties ingestelde commissie,

in het openbaar te verdedigen in de Aula der Universiteit

op vrijdag 20 juni 2025, te 14.00 uur

door Ester Abram

geboren te Amsterdam

Wrijving

Verlangen naar het oppervlak
overschaduwt de kracht
van vernieling en gaten.

Experimenten geven wrijving.
De laser richt zijn stralen:
een gekartelde rand,
een brandgat,
een blaar,
een wond.

Verwondering schijnt
door een spectrum —
onderschat destructie niet,
noch het voortdurende bevragen
van de diepte
van die (licht)lagen.

Binkie Bloemheuvel

CONTENTS

PREFACE

From an early age, I learned that a true understanding of a subject means being able to explain it to anyone. During my PhD research, while focusing on a niche area within physics, I have come to believe that, regardless of educational background, patience, or individual interests, there are aspects of it that are interesting to anyone.

Therefore, I added yellow pages to provide background context or fun insights for a general audience alongside the academic/scientific content-focused white pages. While the committee will assess my academic abilities based solely on the white pages, I encourage everyone to have a look around. I have structured this book with the aim that any reader will find at least one part to enjoy.

Ester Abram
Amsterdam, March 2025

SCIENTIFIC SUMMARY

What is Light-Induced Damage?

Pre-ablation regime optical and morphological changes in nanometer thick films and grating structures

In this thesis we present a study of light-induced material changes by exposing materials to single-shot femtosecond laser pulses while probing the resulting optical changes. For high-fluence laser pulses, material will be catastrophically removed. However, for fluences below the onset of this so-called ablation, subtle optical changes are induced. Therefore, new questions arise:

> **If a permanent change in the material is measured, can that be considered damage? When does this change occur, and what exactly is causing the material to change?**

To address these questions, we conduct a series of experiments on nanometer-thick films of gold, aluminum, and ruthenium, as well as on gratings etched in silicon. After exposing these materials to single-shot femtosecond laser pulses of varying fluences, we observed a consistent light-induced phenomenon: a permanent increase in reflectivity. This optical change is accompanied by morphological alterations, often seen as small changes in the surface topography, which varies depending on the material and layer thickness. Although the onset of these detected morphological changes coincides with the measured pre-ablation optical changes, they are not directly causative of each other.

To gain deeper insight, we employ additional characterization techniques such as optical microscopy, scanning electron microscopy including electron backscatter diffraction, and atomic force microscopy. These analyses reveal that the primary cause of both the optical and morphological changes is melting of the material, followed by resolidification, induced by single-shot illumination.

We utilize various computational models to support our experimental findings. Transfer-matrix method calculations are used to determine the absorption profiles and reflectivity of multilayer stacks. Subsequent two-temperature model and 3D heat diffusion simulations allow us to predict the temperature distribution within the material upon illumination with a femtosecond pulse. These simulations confirm that the melting point was reached already within the pre-ablation fluence regime.

Our study focuses on the behavior of thin metallic films, specifically gold, aluminum, and ruthenium layers. In addition to these metallic films, we investigate the impact of surface topography on damage thresholds and light-induced deformations by exposing

silicon etched gratings to single-shot ultrafast pulses. Given the cost and time-intensive nature of determining damage thresholds for grating structures experimentally, we compare our results with absorbed power density profiles, and diffraction efficiencies obtained through rigorous coupled-wave analysis (RCWA) calculations. This approach aims to develop a predictive model for determining the damage threshold of a grating structure relative to that of a flat surface.

FLAT NANOMETER THICK LAYERS

For gold, the observed increase in reflection is likely due to delamination, where a void forms between the gold layer and the substrate. This void induces an etalon effect, as confirmed by atomic force microscopy and transfer-matrix method calculations, where voids as thin as $\approx 10\,\mathrm{nm}$ account for the 0.1-2% relative reflection increase in gold layers ranging from 8 to 80 nm in thickness.

In contrast, no delamination is observed in aluminum. Instead, the regions exceeding the pre-ablation fluence threshold are covered with small sub-wavelength (50-200 nm) of missing, or vertically displaced, groups of grains, a process called *spallation*. Two-temperature model calculations show that the temperatures reached in the pre-ablation regime exceed the melting temperature of aluminum, with the spallation fluence being approximately 1.5 times the melting fluence. Electron backscatter diffraction measurements indicate recrystallization, with grain sizes increasing from approximately 150 to 400 nm, as the fluence approaches the ablation threshold. This grain growth, which increases the electron mean free path and therefore reduces resistivity, likely contributes to the increase in reflectivity.

Ruthenium has appeared as a possible alternative to copper and tungsten because of its good nanoscale conductivity. However, in semiconductor device manufacturing, deposited materials must also be able to withstand high optical fluences used by optical metrology tools. We studied optical changes in 8 to 40 nm thick ruthenium films on various substrates. In line with our results on gold and aluminum, for fluences below the full-ablation damage thresholds, the reflectivity initially increases with a few percent. When the fluence increases further, the reflectivity shows fairly abrupt changes for samples with nominal layer thicknesses of 15 nm and higher. Additionally, at fluences below full-level ablation, different morphological changes such as nanovolcano formation and top-level ablation are observed, which differs from the spallation observed in the aluminum layers. The nanovolcanoes appear to have been formed by molten ruthenium that has locally been pushed outward and has overflowed the surrounding area. Furthermore, nanovolcanoes appear to be positioned on crack lines in the ruthenium. In top-level ablation, only the top part of the ruthenium layer is ablated, while the lower part still remains on the substrate, which occurs in ruthenium layers of 20 nm thick and more. Here, a concentration of nanovolcanoes is located around the top-level ablation edge. Neither top-level ablation, nor nanovolcano formation can explain the small increase in reflectivity at low fluences directly. Instead, using electron backscatter diffraction as before, we find that the ruthenium grains have melted and resolidified into bigger ones, most likely giving rise to the small increase in reflectivity caused by the accompanying increase in the mean free path of the electrons, which is in line with our findings on aluminum.

PATTERNED STRUCTURES

Semiconductor devices are composed of hundreds of different layers containing complex patterns deposited on a silicon wafer. To ensure accuracy, the wafer must be precisely aligned before each layer is fabricated. Alignment markers, often small gratings etched into the silicon wafer, are used for this purpose. The wafer's position is determined by measuring light diffracted from these markers. However, since these alignment markers have to become smaller and smaller to save wafer real estate, the light intensity must be increased to achieve a sufficient diffracted signal. Unfortunately, this also increases the risk of light-induced damage. Therefore, building on our findings from flat layers, we extended our study to patterned structures, specifically focusing on silicon gratings.

Several gratings with pitches between 430 and 980 nm and varying duty cycles as well as a flat silicon surface are exposed to single ultrafast laser pulses with varying fluences. Here, the pump pulse polarization is either parallel or perpendicular to the grating lines. In contrast to flat surfaces, the gratings show more pronounced pre-ablation optical changes, with reflection increases of up to 30%. Additionally, we identify fluence thresholds corresponding to structural changes such as grating line deformation, ablation and crater formation.

The fluence thresholds for damage of the gratings are 10 to 50% lower than those for flat silicon surfaces. This highlights the critical role of localized field enhancements caused by the grating's topography, which significantly influences energy absorption and thus has an effect on the damage resistance. Hence, the damage in gratings is governed not solely by total energy absorption but by localized effects, explaining the differences in damage thresholds between flat and patterned structures.

Given the complexity of studying damage thresholds in grating structures experimentally, we applied near-field rigorous coupled-wave analysis (RCWA) to calculate absorbed power density profiles for the gratings and flat layers. While this approach provides a time-efficient method for estimating damage thresholds, the results show only moderate correlation with experimental data, indicating that incorporating other effects such as heat diffusion and nonlinear absorption in future models could improve accuracy.

Our experiments on gratings confirm that the onset of optical change coincides with that of grating line deformation, implying that the melting temperature is reached. Depending on fluence, grating parameters and pump-polarization, different forms of deformation occur. For an increasing fluence, the grating lines first become higher, then more curved, broaden, and eventually flatten. At even higher fluences, peak-valley inversion occurs, with the valleys exceeding the original grating amplitudes. We find that the enhanced optical change for gratings, compared to the optical change in flat silicon, is solely due to grating line deformation.

CONCLUSION

In both flat and patterned structures, single-shot ultrafast pulses below the ablation threshold induced optical and morphological changes driven by processes such as ultrafast melting and resolidification. The in situ probing of the optical change is a quick and easy way to detect very subtle changes, making this technique suitable to use as an early warning signal for catastrophic damage. This is particularly relevant in the semicon-

ductor manufacturing industry, where thin films and grating structures are exposed to increasingly high optical powers used in metrology, which heightens the risk of optical damage.

For patterned topographies, characteristic deformation patterns of grating lines as a function of fluence were observed in the pre-ablation fluence regime. This further improves our understanding of the progression of morphological changes for increasing fluences in periodic structures. We found that localized field enhancements, caused by the grating topography, correlate better with the measured damage thresholds than the total absorbed power. This indicates that localized effects, rather than total power absorption, dictate damage resistance. The local absorbed power density profiles vary with grating parameters, such as pitch and duty cycle, resulting in damage thresholds that are 10 to 50% lower than those for flat silicon. For such gratings, smaller pitches show a greater threshold reduction than larger pitches.

In nanolithography processes, even small material changes, occurring well below the threshold for catastrophic damage, can affect the functionality of semiconductor devices. Such changes, often resulting from exceeding the melting threshold, enable material mobility and lead to structural alterations, such as spallation in nanometer-thick films of aluminum, or nanovolcano formation in ruthenium films. When the melting threshold is exceeded in structured layers, the shapes of these structures can change. Therefore, for optical metrology in semiconductor device manufacturing, small light-induced changes in the reflectivity, due to changes in conductivity and morphology, may serve as early warning signals to prevent this catastrophic damage.

WETENSCHAPPELIJKE SAMENVATTING

Wat is licht-geïnduceerde schade?

Pre-ablatieregime optische en morfologische veranderingen in nanometer-dikke lagen en traliestructuren

In dit proefschrift presenteren we onze studie naar licht-geïnduceerde materiaalveranderingen. Deze veranderingen worden veroorzaakt door de materialen te belichten met enkele felle ultrakorte 'femtoseconde' pulsen, waarbij tegelijkertijd de optische veranderingen worden geïnspecteerd. Bij pulsen met een hoge lichtsterkte of *fluentie*, zal het materiaal weggeslagen worden. Maar wanneer de fluentie wordt verlaagd tot onder de drempelwaarde voor deze zogeheten *ablatie*, blijken de lichtpulsen subtiele optische veranderingen in het materiaal te induceren. Vandaar dat de volgende vragen zich aandienen:

> **Als een permanente verandering in het materiaal te meten is, wordt dit dan beschouwd als *schade*? En als deze veranderingen plaatsvinden, wat heeft er dan precies voor gezorgd dat het materiaal is veranderd?**

Om deze vragen te beantwoorden, hebben we een serie experimenten uitgevoerd op nanometer-dikke lagen van verschillende materialen, en in silicium geëtste tralies. Na de belichting van deze materialen met een enkele femtosecondelaserpuls en dat vervolgens te herhalen voor verschillende pulsfluenties, namen we altijd een consistent licht-geïnduceerd fenomeen waar: een permanente reflectiviteitstoename. Wanneer deze optische verandering plaatsvindt, doet zich ook vaak een morfologische verandering van het materiaal voor. Vaak zijn dit kleine veranderingen in de topografie van het oppervlak, maar dit varieert voor de verschillende materialen en laagdiktes. Hoewel de veranderingen in morfologie exact vanaf dezelfde fluentie zijn waargenomen als de gemeten pre-ablatie optische veranderingen, is er geen direct causaal verband tussen die twee, maar ligt een andere onderliggende, licht-geïnduceerde verandering ten grondslag aan beide.

Voor een beter begrip, hebben we daarom verdere karakterisatiemethoden gebruikt, zoals optische microscopie, rasterelektronenmicroscopie waaronder elektronenterugverstrooiingsdiffractie, en atoomkrachtmicroscopie. Deze analysetechnieken toonden aan dat de primaire oorzaak van zowel de optische als de morfologische veranderingen het ultrasnel smelten en stollen is, geïnduceerd door de *single-shot* belichting.

Om deze experimentele bevindingen verder te ondersteunen, hebben we gebruik-gemaakt van verschillende rekenmodellen. Met de transfer-matrixmethode berekenen we de absorptieprofielen, reflectie en transmissie in een meerlaagse stapel van dunne lagen. Door deze resultaten verder te gebruiken in het twee-temperaturenmodel en de 3D-warmteoverdrachtsimulaties, hebben we de temperatuurprofielen kunnen bepalen van een meerlaagse sample dat wordt belicht met een femtoseconde lichtpuls. Deze berekeningen bevestigen inderdaad dat de smelttemperatuur al wordt overschreden als we in het pre-ablatie fluentieregime zitten.

Ons onderzoek spitst zich vooral toe op het gedrag van dunne metaallagen, voorna-melijk goud, aluminium en ruthenium. Aanvullend op deze vlakke metaallagen, is ook de invloed van oppervlaktetopografie op optische schadedrempels onderzocht. Dit is gedaan door verschillende, in silicium geëtste, tralies ook te belichten met single-shot lichtpulsen. Vanwege de tijds- en kostenintensieve aard van het bepalen van de schadedrempels voor elk tralie, of voor andere oppervlaktetopografieën, hebben we onze resultaten vergele-ken met berekende vermogensdichtheden en diffractieefficiënties, bepaald door middel van rigorous coupled-wave analysisberekeningen (RCWA). Deze strategie van het linken van experimentele resultaten met RCWA-berekeningen leidt tot een model om optische schadedrempelwaardes van gestructureerde lagen van een materiaal te berekenen in vergelijking met dat van een vlakke laag van hetzelfde materiaal, iets dat experimenteel makkelijker en sneller te bepalen is.

VLAKKE NANOMETER-DIKKE LAGER

Voor goud komt de gemeten verhoogde reflectie zeer waarschijnlijk door delaminatie. Hierbij laat het goud los van het substraat en zo ontstaat er een holte tussen de twee. Deze holte creëert een etaloneffect, wat is bevestigd door atoomkrachtmicroscopiemetingen en transfer-matrixmethodeberekeningen. Een holte van slechts $\approx 10\,\mathrm{nm}$ zorgt hierbij al voor een reflectie verhoging van 0.1-2% in 8 tot en met 80 nm dikke goudlagen.

In tegenstelling tot de goudlagen, is er geen delaminatie gemeten in de belichte alumi-niumlagen. In plaats daarvan zijn de gebieden die belicht zijn met een fluentie boven de pre-ablatie fluentiedrempel bedekt met kleine (50-200 nm) missende of omhooggeduwde korrelgroepen, dat noemen we *spallatie*. Twee-temperaturenmodelberekeningen laten zien dat de behaalde temperaturen in deze gespalleerde gebieden boven de smelttempe-ratuur van aluminium liggen. De gemeten spallatiedrempelfluentie is hier ongeveer 1.5 keer hoger dan deze berekende smeltfluentie. Aanvullende elektronenterugverstrooiings-diffractiemetingen laten vervolgens ook zien dat de gemiddelde korrelgrootte inderdaad is vergroot van ongeveer 150 tot wel 400 nm bij het benaderen van de ablatie-fluentie. Smelten en herkristallisatie is hiermee aangetoond. Het is daardoor zeer aannemelijk dat deze korrelgroei, die de vrije weglengte van de elektronen vergroot en daarmee de weerstand verlaagt, direct de oorzaak is van de verhoging van de reflectiviteit.

Een alternatief voor de goed geleidende metalen koper en wolfraam, is ruthenium. In tegenstelling tot koper en wolfraam, behoudt ruthenium namelijk deze goed geleidende eigenschap wanneer elektrisch geleidende draden zeer dun worden. In de halfgeleiderin-dustrie worden de materialen op de wafer, waaronder ruthenium, blootgesteld aan zeer hoge optische fluenties. Deze optische fluenties zijn afkomstig uit de lichtbronnen in de

metrologiesensoren. Daarom onderzochten we 8 tot 40 nm dikke lagen ruthenium op verscheidene substraten. Zoals bij onze experimenten met goud- en aluminiumlagen is gebleken, is hier ook een toename van de reflectiviteit waargenomen van een paar procent bij fluenties ver onder de ablatiedrempelwaarde. Voor iets hogere fluenties, toont de reflectiviteit versus fluentie behoorlijk abrupte veranderingen voor de rutheniumlagen van 15 nm dik. Bovendien, voor fluenties (net) onder de (totale-)ablatie drempelwaarde, zijn er verschillende morfologische veranderingen waargenomen, zoals nanovulkaan-vorming en bovenlaagablatie, die verschillen met de spallatie die zich voortdoet in de aluminiumlagen. In het midden van elke nanovulkaan is het gesmolten ruthenium naar boven gedrukt en naar de buitenkant gestroomd. Bovendien liggen de nanovulkanen allemaal op scheuren in de ruthenium laag. Bij bovenlaagablatie is alleen het bovenste gedeelte (ongeveer de helft) van de laag weggeslagen, waarbij de onderste laag nog in zijn geheel op het substraat zit. Bovenlaagablatie komt voor bij de rutheniumlagen van 20 nm en dikker. Aan de buitenkant bij de bovenlaagablatierand is er een grotere concentratie van nanovulkanen. Het directe gevolg van zowel bovenlaagablatie, als nanovulkaanforma-tie is een verlaging van de reflectiviteit. De gemeten reflectiviteit is echter juist hoger bij deze lage fluenties. Met hulp van elektronenterugverstrooiingsdiffractie, zoals ook bij de aluminiumlagen, kan dit wel verklaard worden. We vonden hier ook dat het ruthenium smelt en stolt tot grotere korrels dan aanwezig waren in het oorspronkelijke materiaal. Deze korrelvergroting vergroot de vrije weglengte van de elektronen, wat zeer waarschijn-lijk de directe oorzaak voor de verhoging van de reflectiviteit is. Dit komt overeen met onze bevindingen bij de aluminiumlagen.

STRUCTUREN

Halfgeleiderchips bestaan vaak uit honderden verschillende lagen met complexe patro-nen, aangebracht op een siliciumwafer (schijf). Om er zeker van te zijn dat deze lagen nauwkeurig gepositioneerd worden, moet de wafer tijdens en na het aanbrengen van elke laag ook zeer precies gepositioneerd worden. Speciale 'uitlijnmarkeringen', doorgaans kleine tralies geëtst in het silicium, worden hiervoor gebruikt. Aan de hand van licht dat diffracteert aan deze markeringen wordt de positie van de wafer bepaald. Vanwege de nodige ruimtebesparing op de wafer moeten deze uitlijnmarkeringen kleiner worden. Deze ruimtebesparing resulteert in een kostenbesparing. Dit zorgt ervoor dat een hogere lichtintensiteit nodig is om een voldoende sterk diffractiesignaal te krijgen. Helaas ver-groot dit ook de kans op licht-geïnduceerde schade. Voortbordurend op onze bevindingen voor de vlakke lagen, verleggen wij daarom onze aandacht ook naar structuren, waar we ons focussen op tralies geëtst in silicium.

Verschillende tralies, met periodes tussen de 430 en 980 nm en verschillende vul-lingsgraden, en ook vlak silicium zijn belicht met single-shot ultrakorte laserpulsen van verschillende fluenties. Dit is uitgevoerd zowel met een polarisatie parallel, als loodrecht op de tralielijnen. In tegenstelling tot het vlakke silicium, tonen de traliestructuren ster-kere pre-ablatie optische veranderingen, waarbij de reflectie tot wel 30% hoger wordt. Verder hebben we verschillende fluentiedrempelwaardes bepaald, behorend bij verschil-lende structuurveranderingen zoals tralielijndeformatie, ablatie en kraterformatie.

De gevonden fluentiedrempelwaardes voor schade van de tralies zijn 10 tot 50% lager dan de drempelwaardes voor het vlak silicium. Dit benadrukt de cruciale rol van lokale

veldversterkingen geïnduceerd door de tralietopografieën. Deze veldversterkingen beïnvloeden de lokale energieabsorptie significant en daarmee de schadebestendigheid. Vandaar dat de schadedrempel in traliestructuren niet alleen afhangt van de totaal geabsorbeerde energie, maar van lokale effecten. Dit verklaart het grote verschil in de schadedrempelfluenties tussen vlak silicium en tralies geëtst in silicium.

Door de complexiteit van het experimenteel bepalen van de schadedrempels in traliestructuren in het algemeen, voerden we nabije-veld rigorous coupled-wave analysisberekeningen (RCWA) uit om de geabsorbeerde vermogensdichtheidsprofielen in de tralies en de vlakke laag te bepalen. Ook al verschaft deze methode een tijdsefficiënte en kostenbesparende methode om de schadedrempels te bepalen aan de hand van de schadedrempel van de vlakke laag, toch laten de resultaten slechts een lichte overeenstemming zien met de experimenteel verkregen waardes. Dit laat zien dat wanneer andere effecten, zoals warmteoverdracht en niet-lineaire absorptie in toekomstige modellen worden geïmplementeerd, dit voor significante verbeteringen zou kunnen zorgen.

Onze experimenten met tralies bevestigen dat de eerste tekenen van optische veranderingen samenvallen met die van tralielijnvervormingen, wat impliceert dat de smelttemperatuur hier wordt overschreden. Voor toenemende fluenties, en afhankelijk van de tralieparameters en pomplichtpolarisatie, worden de tralielijnen achtereenvolgens hoger, meer gekromd, breder, platter, en vindt lijn-ruimteinversie plaats. Bij lijn-ruimteinversie zijn de ruimtes hoger geworden dan de originele (onbelichte) lijnen. Bovendien hebben we ontdekt dat het grote versterkte effect in licht-geïnduceerde optische veranderingen van de tralies vergeleken met die van het vlak silicium, uitsluitend komt door de vervorming van de tralielijnen.

CONCLUSIE

In zowel vlakke lagen als (periodieke) structuren, induceert een enkel ultrakorte lichtpuls, met een fluentie lager dan de ablatieschadedrempel, permanente optische en morfologische veranderingen die gedreven zijn door processen zoals ultrasnel smelten en stollen. Het ter plaatse meten van deze optische veranderingen is een snelle en makkelijke manier om deze subtiele veranderingen te detecteren, wat maakt dat deze meting uitermate geschikt is als een vroeg waarschuwingssignaal voor verdere catastrofale schade. Dit is vooral relevant bij de fabricage van halfgeleidercomponenten, waar dunne lagen en gestructureerde patronen worden blootgesteld aan steeds hogere lichtintensiteiten voor metrologiedoeleinden. Deze verhoogde lichtintensiteit verhoogt daarmee ook het risico op optische schade.

In de structuren zijn karakteristieke vervormingspatronen van de tralielijnen als functie van de fluentie waargenomen in het pre-ablatiefluentieregime. Dit draagt verder bij aan het begrip van de progressie in morfologische veranderingen bij een toenemende fluentie in periodieke structuren. We toonden verder aan dat lokale veldversterkingen, veroorzaakt door de topografie van de tralies, beter correleren met de gemeten schadedrempels, dan het totale geabsorbeerde vermogen dat doet. Hiermee is aangetoond dat deze lokale veldversterkingen bepalend zijn voor de optische schadebestendigheid. Deze lokale geabsorbeerde vermogensdichtheidsprofielen variëren voor de verschillende tralieparameters, zoals periode en vullingsgraad, wat resulteert in een 10 tot wel 50% lagere schadedrempelfluentie dan de schadedrempelfluentie van vlak silicium. Hierbij

geldt dat kleinere tralieperiodes een hogere schadedrempelreductie laten zien dan grotere.

Bij nanolithografie kunnen zelfs kleine materiaalveranderingen, die ontstaan bij belichting ver onder de catastrofale schadedrempel, een grote invloed op de functionaliteit van de geïntegreerde schakelingen (chips) hebben. Zulke veranderingen ontstaan vaak doordat de temperatuur de smelttemperatuur overschrijdt, waardoor een verhoogde mobiliteit in het materiaal wordt geïnduceerd. Dit leidt tot structurele veranderingen, zoals spallatie in nanometer-dikke lagen aluminium, of nanovulkaanformatie in rutheniumlagen. Wanneer in gestructureerde lagen de smelttemperatuur is bereikt, zullen de structuren ook kunnen vervormen.

Bij optische metrologie voor de fabricage van halfgeleidercomponenten kunnen daarom kleine veranderingen in de reflectie van de wafer materialen, geïnduceerd door veranderingen in de geleidbaarheid en morfologie, dienen als waarschuwingssignaal in een vroeg schade-stadium. Hiermee kan catastrofale schade voorkomen worden.

PLAIN LANGUAGE SUMMARY

What is Light-Induced Damage?

Pre-ablation regime optical and morphological changes in nanometer thick films and grating structures

LET'S START AT THE BEGINNING

An **integrated circuit**, better known as a **chip**, is a device that you probably own several of. A high-tech chip can, for example, perform calculations or save information. Nowadays, the majority of electronic devices contains such a chip. Your phone and computer have at least one, but you can find also one in most of the modern thermostats. This thesis presents research performed concerning the fabrication of such chips. So what do chips look like exactly?

Computer chips consist of several layers, which you can compare to an apartment building. We first start with a foundation, which is a big thin piece, or **wafer**, made out of the material silicon, which gave *Silicon Valley* its name.

It consists of several floors, or **layers**, and within these layers, several structures are manufactured. You can compare this to hallways, doors and stairs. Apartment buildings are constructed floor by floor on its foundation, which is the same for chips. Each time, a layer of a certain material will be deposited on the silicon wafer, forming a new floor. After each new layer, structures will be carved out of the layer. Let's look at this as carving out room for stairs. We have to be certain that the stairs are placed at the same position in each layer, to allow movement between floors. The machines that fabricate these chips, therefore, need to contain certain sensors. These sensors use light to shine onto the silicon wafer. Some of that light will be directed back to the sensor, and after measuring this light and some processing, the position of the wafer is acquired. By determining the position, the machine knows where the structures of the next deposited layer have to come.

In apartment buildings, the stairs at the second floor can be positioned with some **margin** relative to those of the first floor. However, in chips, the structures are way smaller and therefore the margin or, **overlay**, is really small as well. To reach these small margins, the sensors need to determine the wafer position really accurately. Therefore, they will shine a more intense light onto the wafer to achieve this. However, at one point, this light will be too bright, and the layers deposited on the wafer, or even the wafer itself, will get damaged.

WHAT THIS THESIS IS ABOUT

In this thesis we want to know what those first signs of damage are, what happens to the materials, and if there are any **warning signs** before any catastrophic damage will take place.

We therefore conducted a series of experiments on thin metallic films, including gold, aluminum and ruthenium. They were illuminated by single bright light pulses, while optical properties were measured, and subsequently were examined by different types of microscopes. We found that when the laser intensity was high enough to melt the layers, the layers can rapidly resolidify, however in a different fashion. This subtle difference can be measured and used as an early warning signal for catastrophic damage.

Further on, we moved from these flat layers into silicon **gratings**, which is silicon with a ridged surface. We found that damage occurs faster in these gratings, so for a less bright laser pulse than for a flat surface. Throughout this study, we combined these experimental measurements with several calculations, to get a better understanding of the processes that induce permanent changes into the materials, induced by bright laser pulses. This helps us understand the underlying processes, and is a first step toward building a comprehensive framework that can predict damage thresholds of structured layers with respect to the known damage threshold of the flat configuration.

INTRODUCTION FOR A GENERAL AUDIENCE

Everything can be explained to everyone. Accordingly, I intended to explain the subject of this thesis in a way for **everybody to understand and for 'learned' people not to be bored by** [1, p.6].

Following this idea, I introduce the research subject by posing four questions as asked from the reader's perspective towards me, the author:

"What is light?",   **"What to do with it?",**
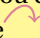
"What did you do?",   **"What can I expect?"**

These rather simple questions follow a gradual buildup. It starts with the common phenomenon of **light**, and ends with the research presented throughout the rest of this thesis. This way of introducing the performed light-induced damage research will hopefully stimulate curiosity and engagement among every reader.

What is light?

Light is a term commonly known to almost every human and most animals. However, what is it? It gives warmth, makes sight possible, and is often related to positive things: It sparkles, moves, reflects, colors and gives energy. One often seeks light, to survive, or just to be entertained by. But what is it? Can you catch it? Change it?

Why is this **word** black and this space⌒ yellow?

The light is *generated* in, for instance, the Sun, or the lamp on your desk. It then *travels* through the air, and *shines* onto this page. The words and spaces have a different *interaction* with the light, as is *observed* by your eyes. So this common term has a lot of properties: Generation, propagation, interaction and observation.

So while being a familiar concept in day-to-day life, it is a versatile and therefore complex phenomenon. In the search for the physical definition, it took until the mid

Figure 1: Graphic depiction of the development in communicating using electromagnetic waves [7–14]

19th century when Michael Faraday first concluded that light was related to electromagnetism [2, 3]. A couple of decades later, this work led to the discovery by James Clerk Maxwell that light is an electromagnetic wave that travels through empty space at constant speed [4, 5]. Heinrich Hertz then experimentally proved this, showing that radio waves, although invisible for the human eye, are electromagnetic waves as well [6]. This resulted in the vast development of radio, television, imaging and communication as depicted in figure 1.

What to do with it?

Interestingly, technological development using light (optics) never really slowed down. Over the last decades, optics are used to measure time and to facilitate communication. All of these developed technologies paved the way for the use of optics in construction: using it for optical lithography, and nowadays even for *nanolithography*.

The next chapter is the General introduction, which starts with discussing nanolithography in more detail. Hereafter, the sections Damage and Thesis outline will provide answers to the two remaining questions — **"What did you do?"** and **"What can I expect?"** — in more detail.

GENERAL INTRODUCTION

NANOLITHOGRAPHY

Lithography is a printing process that involves creating images or text on a flat surface. Here, an *image* is carved/etched into a stone or metal plate that acts as a *mask*. Inking the mask and pressing it onto a piece of paper will *transfer* the image onto the paper. This printing technique is used to communicate ideas and to tell stories, but its applications extend far beyond this single area.

When carving narrower lines into the mask, smaller images can be printed. However, there is a limit in the size of the details and the resolution one can achieve here. To overcome this, one can switch from ink to light as the printing source, which is called **photolithography**. Here, a light pattern is created by selectively blocking and allowing light to pass through slits in a mask. Using lenses and mirrors, this light is then projected as a smaller copy of the mask's pattern onto a surface. Additional processing steps will 'cut out' this pattern from the surface, achieving a vastly smaller resolution. This resolution depends on the "inherent length scale" of the used light which is expressed in the color or *wavelength* of the light. In state of the art **nanolithography**, the used light has a wavelength as small as 13.5 nm. With this wavelength, the smallest achievable feature size, known as the critical dimension CD, is currently smaller than 5 nm — about $10,000$ times thinner than a human hair. To put this in perspective, if you were to blow up the width of that hair to the length of the Eiffel tower, that 5 nm would have the size of a couple of centimeters, so comparable to the size a typical little finger.

COMPUTER CHIPS

The small features described above are needed in the fabrication of computer chips. These chips, or integrated circuits (IC's), are essential components in modern electronics. They are used to perform a wide range of functions, from simple logic operations to complex processing tasks, and are the building blocks of nearly all electronic devices today. An IC consists of a set of electronic components, like transistors, on a small, flat piece (or "chip") of semiconductor material, typically silicon. As computer chips continue to grow in complexity, and storage density increases [15, 16], the semiconductor industry is always developing new methods to print smaller structures. A schematic illustration of the steps required to pattern a thin layer by photolithography is shown in figure 2. A thin film is first deposited onto a silicon wafer, which is subsequently coated with a layer of photoresist. The wafer is then exposed to 13.5 nm EUV light, with a mask containing the desired pattern positioned between the light source and the wafer. This mask selectively blocks portions of the light, preventing it from reaching certain areas of the photoresist. During the development stage, the exposed regions of a positive resist are removed, while for a negative resist, the unexposed areas are removed. Consequently, the pattern from the mask is transferred onto the resist. Following this, an etching process removes the
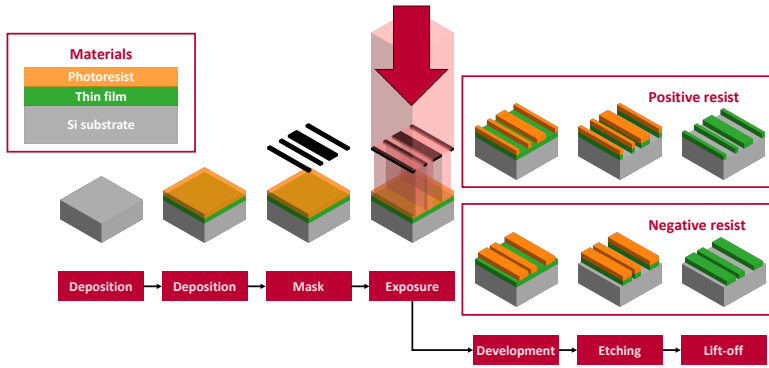
Figure 2: Schematic illustration of the steps required in an optical nanolithographic process

unprotected areas of the film by the photoresist. Finally, after the etching and the lift-off of the remaining photoresist, the thin film is precisely patterned according to the original mask design.

Repeating this collection of steps with different masks and/or different layer thicknesses/materials will result in a stack of multiple structured layers on top of each other, resulting in three-dimensional computer chips [17].

Often, a feature is fabricated in each layer with a width that can be as small as ≈ 7 nm [18–20] in each layer[21]. This is done at the same position in each layer, to connect all these features, and forming a vertical interconnect to ensure inter-layer communication (see figure 3).
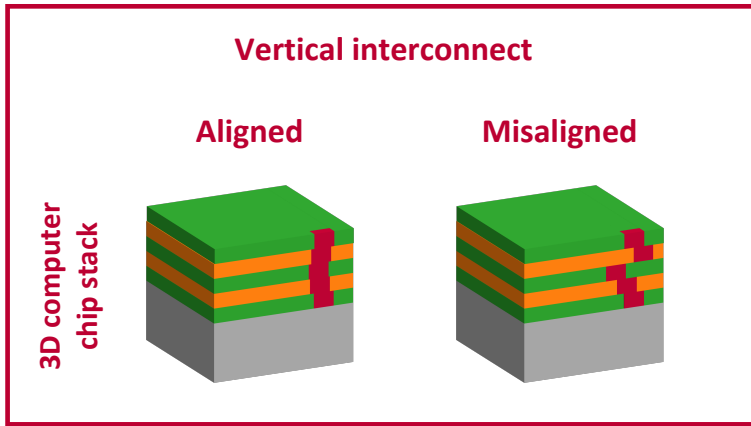
Figure 3: Two 3D computer chip stacks with an vertical interconnect for interlayer communication shown in red through all layers (green and orange). Although the position of the interconnect varies, it is still within acceptable margins in the left stack. However in the right one, the misalignment is bigger, resulting in a broken connection.

After a layer is fabricated, the wafer exits the lithography machine for further pro-

cessing, but re-enters the machine later again to define the next new layer. However, to ensure that all parts of each interconnect are properly aligned, the wafer should have the same orientation and position with respect to the exposure beam and mask as it had before. Therefore, each layer has to be inspected, and repositioned to compensate for any misalignment.

This is done by first etching **alignment markers** into the silicon wafer, containing several gratings that are used as positional references. The wafer is illuminated by light from a **metrology** sensor, a tool that accurately measures the position of the wafer. The light from the sensor diffracts upon hitting the gratings, and the first-order (+1 and −1) diffracted beams are directed back into the metrology sensor, by which the wafer position is obtained. During exposure, the wafer moves laterally (along the x-axis) relative to both the metrology tool and a reference grating within the tool, as schematically shown in figure 4. This movement induces a phase shift, $\Delta\phi$, between the first-order (+1 and −1) diffracted beams of the alignment grating. The intensity of the light transmitted by the reference grating depends on the phase shift between the two diffracted beams. The measured phase shift can then be translated into the lateral offset Δx. However, to accurately determine $\Delta\phi$ and the positional offset, the output signal from the metrology detector must be sufficiently strong. Alignment markers are often buried beneath opaque layers deposited during lithography, which can significantly reduce the intensity of the diffracted beams. Moreover, due to the small widths of, for instance, interconnects, lateral offset must be determined with sub-nanometer precision [18, 19]. Consequently, a brighter light source is required. However, this gives rise to new technological challenges. By exposing the layer to such bright light sources, one can permanently change the layer and even potentially cause catastrophic damage. This automatically leads to the question: At what light intensities does this happen?

Light-induced damage (LID) has been studied extensively in the past, particularly since the invention of the Q-switched laser in the late 1950s and early 1960s [23, 24], which enabled laser pulse durations of tens of nanoseconds. Although high-quality optical components were available, even small surface defects that passed quality control could trigger LID when exposed to these powerful lasers. With these high powers, the field of nonlinear optics took off, introducing new mechanisms for LID, such as self-focusing [25]. Nowadays, tightly focused pulses from lasers with a relatively modest output power, can generate electric fields strong enough to induce dielectric breakdown in materials used for laser components [26, pp.3-4]. To minimize the risk of LID, light intensity can be reduced by lowering the pulse energy, increasing the spot size, or extending the pulse duration. While these measures may be feasible for optical components in laser systems, the semiconductor manufacturing industry often requires higher intensities for metrology purposes. Furthermore, semiconductor devices consist of structured layers made of metals, semiconductors, and dielectrics which are not designed to withstand high optical fluences. Consequently, this increases the risk of light-induced damage. While the main focus of most LID research is on optical components [26], often a more phenomenological approach is taken to examining how various factors, such as material [27], wavelength [28–30], pulse duration [31, 32] and thickness [33, 34], influence LID. In contrast, our research aims to gain insight into the occurring damage mechanisms, while focusing on materials used in the semiconductor manufacturing industry [35, 36]
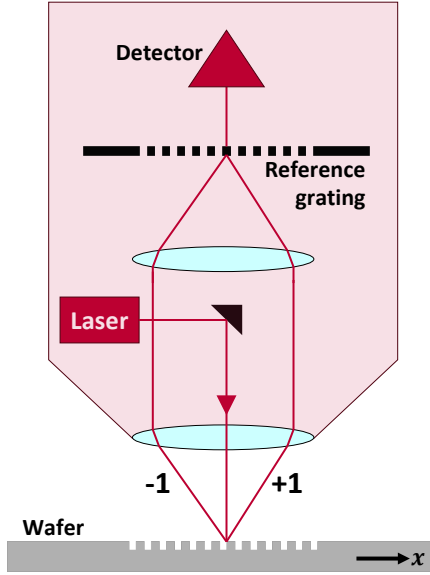
Figure 4: Schematic drawing of the phase-grating alignment sensor. The alignment grating in the wafer is exposed by the sensor while moving over x. The first-order (+1 and −1) diffracted beams are projected on a reference grating. The intensity of the transmitted light by the reference grating is measured by the detector from which the lateral offset Δx can be obtained. This figure is based on figure 5 in [22].

The onset of optical damage is not solely determined by some critical value of the total energy or the peak intensity of the light. Peak-intensity, pulse duration and wavelength-/bandwidth can also play significant roles. In addition to these *light parameters*, the characteristics of the layer itself also influence the damage onset. The *layer parameters* such as thickness, material, refractive index, surface topography, stack composition, and adhesion to surrounding layers all contribute to where the light is absorbed and how and where the material is affected.

The total parameter space that determines the light-induced **damage threshold** is huge. Therefore, throughout our research, we selected a parameter subspace to further investigate. We exposed the different layers to the same pulsed laser, maintaining consistent wavelength and bandwidth. Our primary focus was on metals, where the pulse duration has a relatively negligible impact on the damage threshold within the pulse lengths under consideration (typically $\approx 50\,\mathrm{fs}$). Additionally, we studied single thin layers of varying thicknesses (8-100 nm) and materials deposited on transparent substrates. This approach allowed us to ignore the effects of absorption in the substrate or any other layer except the metal. To introduce a second level of complexity, we also examined patterned structures alongside flat layers to investigate the influence of surface topography on the damage threshold. A schematic representation of the parameter subspace investigated is shown in figure 5.
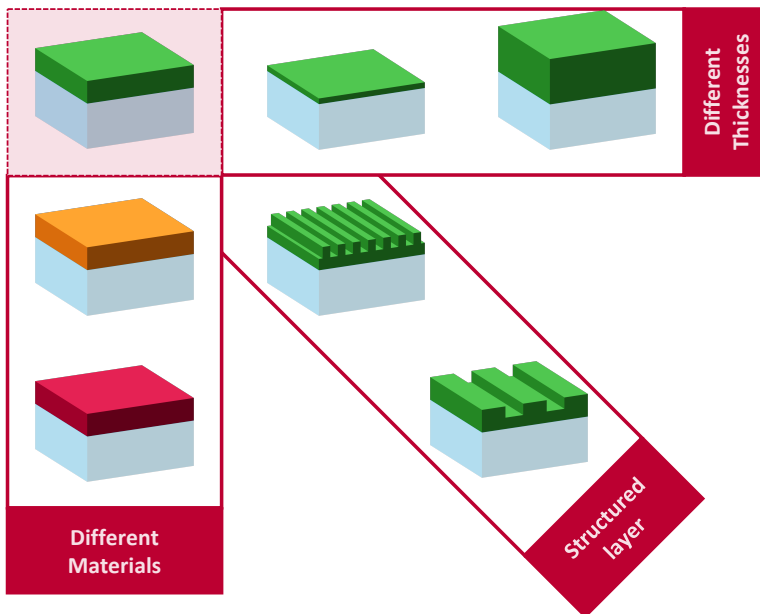
Figure 5: A schematic depiction of the investigated parameter subspace. We varied the material and layer thickness and obtained the damage threshold for each such sample. Additionally we looked into the influence of surface topography on the damage thresholds compared to the flat layer.

DAMAGE

Each of these samples is illuminated by a single laser pulse with a pulse duration in the **femtosecond** range (typically 50 fs, i.e. 5.0×10^{-14} s). This is repeated for varying pulse energies, with a translation between each pulse, so that each single laser pulse hits a different site on the sample.

When a material is strongly excited by a laser pulse, light-matter interaction processes induce various physical mechanisms on different timescales. In the case of femtosecond laser excitation, three fundamental processes typically unfold, roughly separated in time: energy deposition, melting, and ablation [31].

In the femtosecond regime, the absorbed laser energy primarily excites the electrons within the conduction bands of metals, while it generates free charge carriers in semiconductors and dielectrics. In metals, our main focus here, the electron gas heats up on a femtosecond timescale and then transfer the thermal energy to the lattice, causing it to heat up as well. Depending on the laser intensity, melting can begin within a few picoseconds [31, 37]. On a nanosecond timescale, resolidification occurs, which can result in a different crystal structure than the original material if the intensity is high enough. At even higher intensities **ablation** occurs, in which material is rapidly removed. This can cause **catastrophic damage**, in the form of morphological changes, removal of the top part of the layer, or potentially removal of the entire layer.

The complex nature of light-induced damage involves various mechanisms that occur over a wide range of timescales. Sophisticated models attempt to describe these processes, such as combining fast heating with hydrodynamic models [38], or integrating molecular dynamics with Monte Carlo methods [35]. However, these models are often only valid within specific fluence ranges, wavelengths, or material types. Given the diversity of damage mechanisms that can appear within the same sample, a more phenomenological approach is often needed. A question that then arises and that has so far not been addressed here is: What is light-induced damage?

At energies below the threshold for catastrophic damage, light-induced material changes can still occur. However, when these changes are difficult to measure or go unnoticed, these may seem irrelevant and thus negligible. Nonetheless, if these material changes introduce unwanted effects, such as local alterations in conductivity, they can be considered damage. In essence, damage is only significant if it results in some form of 'inconvenience'. However, the onset of any measurable permanent change is a sign that something did happen. This can then be used as an early warning signal for catastrophic damage. This can be very useful, especially when the light-induced damage threshold depends on so many parameters of the light and the material.

Therefore, the **onset of any measurable optical or material change** is the main focus of the light-induced damage research presented in this thesis. This is done by investigating what caused these small optical or material changes, and to find out what is actually happening to the material.

THESIS OUTLINE

CHAPTER 1 describes mathematical and physical modules that are used throughout this thesis. This **theory** chapter includes calculations of light absorption by a multilayer stack using the transfer-matrix method, fast electron gas heating using the two-temperature model, heat diffusion, scattering on slightly rough surfaces, and electromagnetic waves interacting with a periodic surface structure. The chapter concludes with a description of an experimental method to accurately determine light-induced damage fluence thresholds.

In CHAPTER 2, the **experimental details** used in the work are described. First, sample fabrication and characterization techniques are presented. The used ultrafast laser system and light-induced damage setup are presented, along with the measurement procedure. Next, the inspection of the damaged samples by various techniques such as optical microscopy, scanning electron microscopy and atomic force microscopy is described.

The following chapters contain the results of the scientific research. PART I, containing CHAPTER 3 and CHAPTER 4, presents our experiments on light-induced damage in flat layers.

In CHAPTER 3, we explore light-induced damage in thin metal films exposed to single-shot femtosecond laser pulses. We first examined 8 to 80 nm thick gold films on borosilicate glass substrates. Similar experiments were conducted on 10 to 30 nm thick aluminum layers. For both the gold and aluminum layers pre-ablation optical and morphological changes were found. We present results on the inspection of the layers, which explain what caused these changes.

In CHAPTER 4, further studies on 8 to 40 nm thick ruthenium layers are shown. This revealed increased reflectivity and various nanostructural changes, including the formation of nanovolcanoes, for fluences below the catastrophic damage thresholds.

After examining different materials and layer thicknesses, we transition to PART II, where we explore light-induced optical and structural changes in patterned structures. In CHAPTER 5, we investigate how single ultrafast laser-pulses affect gratings etched in silicon and compare this with results for flat silicon surfaces. This is done by measuring the thresholds and by using a computational model to predict threshold scaling with respect to that of flat silicon. Furthermore, grating lines deform under high fluences, with deformation progressing from height increases to broadening, flattening, and eventually peak-valley inversion, for increasing fluences.

CHAPTER 6 presents the **valorization** aspect of our work, featuring an automated framework for determining damage thresholds directly from microscopy images, along with an overview of the experimentally obtained thresholds. Here, light-induced damage of other materials (besides gold, aluminum and ruthenium) such as amorphous carbon, EUV resists, Si_3N_4 and SiO_2 is presented.

1

THEORY

Light impinging on matter can lead to material damage. To understand, predict and quantify the underlying light-matter interaction, some mathematical and theoretical framework is essential. This chapter presents methods for calculating the intensity of light reflected off and transmitted by a material, as well as the spatial profile of the locally absorbed power inside the material. This analysis applies to flat multilayer stacks composed of different materials. Subsequently, the absorbed power results in heating of the material. To describe this process, two models are employed: one for heat transfer of the electrons to the lattice of the absorbing material, and another for the subsequent lattice heat diffusion throughout the layer stack.

When considering rough surfaces, scattering theories can be employed to examine the influence of slight surface roughness on the overall light reflectivity and transmissivity, as compared to a perfectly flat layer. For heavily patterned layers where the topography varies considerably, like grating structures, a different approach is required. In these cases, Maxwell's equations are numerically solved for the electric and magnetic field by forward diffraction modelling. This approach yields a comprehensive set of optical properties, including reflectivity, transmissivity, diffraction efficiencies, and a spatial distribution map of the absorbed power.

The processes of light absorption, lattice heating and heat diffusion, lead to a thermal buildup that can cause damage to the material. Therefore, this chapter concludes with a precise method for determining damage thresholds, which is a critical aspect of this research.

1.1. FROM LIGHT TO HEAT

The foremost thing that this research entails is the illumination of materials by light. This light interacts with the material. The material will partially *transmit*, *reflect* and *absorb*

the light. The absorbed power will *heat up* the electron gas, and subsequently the lattice, where this heat will *diffuse*. Therefore, the following three theoretical models have been used to describe these three mechanisms:

- **Light absorption:** Transfer-matrix method (TMM) calculations are used to calculate the absorption profile of light in a stack of materials (see section 1.1.1)

- **Fast heating:** Two-temperature model (TTM) calculations are performed to calculate the temperature increase of the electron gas and the subsequent heating of the lattice, shortly after excitation by a laser pulse (see section 1.1.2 and Python package *Multilayers*)

- **Heat diffusion:** The 1D heat diffusion equation is analytically solved in cylindrical coordinates (*r* only), and the 2D heat equation is numerically solved to shed some light on the spatiotemporal diffusion of the heat (see section 1.1.3)

1.1.1. Transfer-matrix method

To calculate the reflection, transmission and absorption (profile) of a multilayer stack of different materials, the *transfer-matrix method* (TMM) is used. This method describes the electromagnetic plane wave that propagates between each medium of the multilayer stack, by describing both a forward $\widetilde{E}_\rightarrow$ and backward $\widetilde{E}_\leftarrow$ propagation wave everywhere in the stack (see figure 1.1). The TMM is essentially a combination and slight generalization of several methods and expressions that can be found separately in the standard textbooks [39–41]. In this subsection however, a concise description of the most relevant parts is presented. A more complete treatment, starting from the macroscopic Maxwell equations, can be found in the provided document in [42] and additional expressions in appendix A.

At each interface between two layers (medium *i* and *j*), there is an *interface matrix* M_{ij}. Matrix multiplication of M_{ij} with the forward and backward propagating waves in medium *j* ($\widetilde{E}_{j\rightarrow}$ and $\widetilde{E}_{j\leftarrow}$) results/transfers into the ones in neighboring medium *i* ($\widetilde{E}_{i\rightarrow}$ and $\widetilde{E}_{i\leftarrow}$). Next to this interface matrix, a propagation matrix M_j is introduced that describes the waves traveling through the (absorbing) layer *j*.

The reflected, transmitted and absorbed powers, as well as the spatially dependent local absorbed power can be obtained by performing matrix multiplications for every transition into, and propagation through a layer in the multilayer stack. This works for both *s* and *p* polarized (oblique) incident waves. Next to the polarization and the angle of incidence, only the complex refractive indices and thicknesses of all layers in the stack are needed as input parameters.

Notation

This method considers a continuous wave propagating through space, illuminating a stack under an oblique angle with its normal. The wave may be *s* or *p* polarized. Between every transition from one medium to the next, part of the light will be reflected and transmitted. Absorption will take place when the light propagates through an absorbent medium.

The *transfer-matrix method* (TMM) describes the incoming and outgoing waves at each interface between medium *i* and *j* as is schematically shown in figure 1.1. Here,
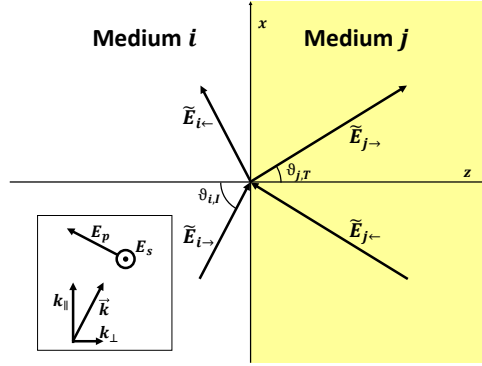
Figure 1.1: The interface between medium i and j with the incoming and outgoing waves $\widetilde{E}_{i\rightarrow}$, $\widetilde{E}_{i\leftarrow}$, $\widetilde{E}_{j\rightarrow}$ and $\widetilde{E}_{j\leftarrow}$. Here, the plane of incidence is in the xz-plane, and the normal of the interface is along the z-axis. $\widetilde{E}_{i\rightarrow}$ propagates in the direction of $\vec{k}$ with $k_{\parallel}$ and $k_{\perp}$ its component parallel and perpendicular to the transition layer (xy-plane) respectively. $\widetilde{E}_{i\rightarrow}$ and $\widetilde{E}_{j\rightarrow}$ make an angle $\theta_{i,I}$ and $\theta_{j,T}$ with the normal. The polarization can either be s or p as indicated by the figure. The polarization direction and the direction of the magnetic field are defined as $\hat{x}'$ and $\hat{y}'$ respectively (not shown in the figure) as indicated in equation (1.1). For p polarization, the direction of $\hat{x}'$ and $\hat{y}'$ are along E_p and E_s respectively, and for s polarization, the direction of $\hat{x}'$ and $\hat{y}'$ are along E_s and E_p respectively.

the electromagnetic plane wave, with angular frequency ω_0, propagating along the $\vec{k}$ direction in a linear, isotropic medium j is described in complex form as:

$$
\begin{aligned}
\widetilde{\vec{E}}_j(\vec{r}, t) &= \hat{x}' \widetilde{E}_j e^{i(\widetilde{\vec{k}} \cdot \vec{r} - \omega_0 t)}, \\
\widetilde{\vec{B}}_j(\vec{r}, t) &= \hat{y}' \frac{\widetilde{k}}{\omega_0} \widetilde{E}_j e^{i(\widetilde{\vec{k}} \cdot \vec{r} - \omega_0 t)},
\end{aligned}
\tag{1.1}
$$

where $\hat{x}'$, $\hat{y}'$ and $\vec{k}$ form an orthogonal set, $\vec{k} = \langle x, y, z \rangle$, and $\widetilde{\vec{k}}$ the complex wave vector. The actual fields are the real parts:

$$
\begin{aligned}
\vec{E}_j(\vec{r}, t) &= \Re\left(\widetilde{\vec{E}}_j(\vec{r}, t)\right) = \frac{1}{2}\left(\widetilde{\vec{E}}_j(\vec{r}, t) + cc\right), \\
\vec{B}_j(\vec{r}, t) &= \Re\left(\widetilde{\vec{B}}_j(\vec{r}, t)\right) = \frac{1}{2}\left(\widetilde{\vec{B}}_j(\vec{r}, t) + cc\right).
\end{aligned}
\tag{1.2}
$$

$\widetilde{\vec{k}}$ can be expressed in the complex refractive index $\widetilde{n}$:

$$
\widetilde{\vec{k}} = k_0 \widetilde{\vec{n}},
\tag{1.3}
$$

$$
\widetilde{\vec{n}} = \vec{n} + i\vec{\kappa},
\tag{1.4}
$$

$$
k_0 = \frac{2\pi}{\lambda_0} = \frac{\omega_0}{c},
\tag{1.5}
$$

where k_0 is the vacuum wave vector, λ_0 the wavelength, ω_0 the angular frequency and c the speed of light (in vacuum). Note that both $\vec{n}$ and $\vec{\kappa}$ have a component parallel ($\parallel$) and perpendicular ($\perp$) with respect to the interface.

1

INTERFACE MATRIX BETWEEN MEDIA

We consider linear, isotropic and homogeneous media and $\mu_i = \mu_j$. Therefore, the standard Fresnel equations can be used. Let us consider *normal incidence* first ($\vec{r}$ points along the positive z-axis):

$$\beta_{ij} \equiv \frac{\widetilde{k}_j}{\widetilde{k}_i} = \frac{\widetilde{n}_j}{\widetilde{n}_i}, \tag{1.6}$$

$$t_{ij} = \frac{2}{1 + \beta_{ij}} = \frac{2\widetilde{n}_i}{\widetilde{n}_i + \widetilde{n}_j}, \tag{1.7}$$

$$r_{ij} = \frac{1 - \beta_{ij}}{1 + \beta_{ij}} = \frac{\widetilde{n}_i - \widetilde{n}_j}{\widetilde{n}_i + \widetilde{n}_j}, \tag{1.8}$$

where r_{ij} and t_{ij} are the reflection and transmission coefficients. These equations can be used to express $\widetilde{E}_{j\rightarrow}$ and $\widetilde{E}_{j\leftarrow}$ into $\widetilde{E}_{i\rightarrow}$ and $\widetilde{E}_{i\leftarrow}$ at the **boundary** as shown in figure 1.1:

$$\begin{pmatrix} \widetilde{E}_{j\rightarrow} \\ \widetilde{E}_{i\leftarrow} \end{pmatrix} = \begin{pmatrix} t_{ij} & -r_{ij} \\ r_{ij} & \beta_{ij} t_{ij} \end{pmatrix} \begin{pmatrix} \widetilde{E}_{i\rightarrow} \\ \widetilde{E}_{j\leftarrow} \end{pmatrix}. \tag{1.9}$$

This can be rewritten such that the electric fields in medium j can be transformed into the field in medium i (at their boundary):

$$\begin{pmatrix} \widetilde{E}_{i\rightarrow} \\ \widetilde{E}_{i\leftarrow} \end{pmatrix} = \underbrace{\begin{pmatrix} \frac{1}{t_{ij}} & \frac{r_{ij}}{t_{ij}} \\ \frac{r_{ij}}{t_{ij}} & \frac{r_{ij}^2}{t_{ij}} + \beta_{ij} t_{ij} \end{pmatrix}}_{\text{interface matrix } M_{ij}} \begin{pmatrix} \widetilde{E}_{j\rightarrow} \\ \widetilde{E}_{j\leftarrow} \end{pmatrix}, \tag{1.10}$$

where M_{ij} is called the interface matrix between medium i and j.

The derivation of M_{ij} for oblique angles, and s or p polarized incident electric field, becomes more complicated (see figure 1.1). Here, the macroscopic Maxwell equations are used, along with the applicable boundary conditions (see equations (A.23) to (A.27)). As is derived in appendix A.2, the general expression for the interface matrix M_{ij}, accounting for oblique incidence, can be obtained.

$$M_{ij} = \frac{1}{2} \begin{pmatrix} \alpha + \beta & \alpha - \beta \\ \alpha - \beta & \alpha + \beta \end{pmatrix}, \tag{1.11}$$

with

$$\alpha_s = 1, \tag{1.12}$$

$$\beta_s = \frac{\widetilde{n}_{\perp j}}{\widetilde{n}_{\perp i}}, \tag{1.13}$$

$$\alpha_p = \frac{N_i}{N_j}, \tag{1.14}$$

$$\beta_p = \frac{\widetilde{n}_j^2}{\widetilde{n}_i^2} \frac{\widetilde{n}_{\perp i}}{\widetilde{n}_{\perp j}} \frac{N_i}{N_j}, \tag{1.15}$$

$$N_i = \sqrt{1 + \frac{n_{\parallel i}^2}{n_{\perp i}^2 + \kappa_{\perp i}^2}}, \tag{1.16}$$

where the subscripts s and p denote the parallel and perpendicular polarizations respectively. Note that for normal incidence, equation (1.11) equals that of M_{ij} as expressed in equation (1.10).

PROPAGATION MATRIX FOR HOMOGENEOUS MEDIA

When the light propagates through a medium with thickness d, the propagation matrix equals:

$$M_d = \begin{pmatrix} e^{-ik_0 \tilde{n}_\perp d} & 0 \\ 0 & e^{+ik_0 \tilde{n}_\perp d} \end{pmatrix}. \tag{1.17}$$

REFLECTION AND TRANSMISSION

For a stack of layers labeled from 0 to m, the total transfer-matrix M_{tot} is then:

$$M_{\text{tot}} = M_{01} M_1 M_{12} M_2 ... M_{m-1\ m}, \tag{1.18}$$

where

$$\begin{pmatrix} \tilde{E}_{0\rightarrow} \\ \tilde{E}_{0\leftarrow} \end{pmatrix} = M_{\text{tot}} \begin{pmatrix} \tilde{E}_{m\rightarrow} \\ \tilde{E}_{m\leftarrow} \end{pmatrix}. \tag{1.19}$$

In the last (infinite) layer m, there is no wave traveling back to the stack so $\tilde{E}_{m\leftarrow} = 0$ (no incident light from layer m). By writing the local amplitudes as $\tilde{E}_{i\rightarrow} = \alpha_{i\rightarrow} E_0$ and $\tilde{E}_{i\leftarrow} = \alpha_{i\leftarrow} E_0$, equation (1.19) can be rewritten as

$$\begin{pmatrix} \alpha_{0\rightarrow} \\ \alpha_{0\leftarrow} \end{pmatrix} = M_{\text{tot}} \begin{pmatrix} 1 \\ 0 \end{pmatrix}. \tag{1.20}$$

Then the total amplitude transmission and reflection coefficient r and t equal $1/\alpha_{0\rightarrow}$ and $\alpha_{0\leftarrow}/\alpha_{0\rightarrow}$ respectively.

To go to the *intensity* reflection and transmission coefficients R and T from here, the angles between the interface and the wavefronts have to be considered. This is because the intensity is defined as energy per unit area of the *interface*:

$$I = \frac{1}{2}\epsilon_0 n c E^2 \cos\theta. \tag{1.21}$$

So, for the incoming and transmitted angle θ_I and θ_T and real part of the refractive indices n_I and n_T, the intensity transmission coefficient becomes:

$$T = \frac{I_T}{I_I} = |t|^2 \frac{n_T \cos\theta_T}{n_I \cos\theta_I}, \tag{1.22}$$

where $\cos\theta_T$ can be computed by Snell's law:

$$\frac{\sin\theta_T}{\sin\theta_I} = \frac{n_I}{n_T}. \tag{1.23}$$

Since the incident and reflected beams are in the same medium (*medium* 0), $\theta_R = \theta_I$ and $n_R = n_I$ applies. Therefore, the intensity reflection coefficient equals:

$$R = \frac{I_R}{I_I} = |r|^2. \tag{1.24}$$

Note that layer 0 and m always have to be nonabsorbing layers with an infinite thickness. Now, the total absorbed intensity fraction is:

$$Abs = 1 - T - R. \tag{1.25}$$

1

LOCALLY ABSORBED POWER

Using the transfer-matrix method, the locally absorbed (cycle-averaged) power density can also be derived. This is done by using Poynting's theorem [39]. The case of normal incidence is presented here and is used as an example. For the oblique case, the reader is referred to appendix A.3.7.

The energy density u can be derived from electric and magnetic fields. For isotropic, linear, homogeneous, nonmagnetic media, u is

$$u = \frac{1}{2}\left(\epsilon E^2 + \frac{1}{\mu_0}B^2\right),$$ (1.26)

and the Poynting vector is defined as

$$\vec{S} = \frac{1}{\mu_0}\vec{E} \times \vec{B}.$$ (1.27)

The cycle-averaged locally absorbed power density is then:

$$p = -\langle\vec{\nabla}\cdot\vec{S}\rangle.$$ (1.28)

We consider now an arbitrary position z in the multilayer stack with $\widetilde{E}_{j\rightarrow} = \alpha_\rightarrow(z)E_0$ and $\widetilde{E}_{j\leftarrow} = \alpha_\leftarrow(z)E_0$. Using equation (1.1) for the fields results in the relative absorbed power density p_{rel} (scaled to the incident intensity I_0),

$$p_{\text{rel}}(z) = 2k_0 n_j \kappa_j f(z)\frac{1}{n_I|\alpha_{0\rightarrow}|^2},$$ (1.29)

with

$$f(z) = \alpha_\rightarrow(z)\alpha_\rightarrow^*(z) + \alpha_\leftarrow(z)\alpha_\leftarrow^*(z) + \alpha_\rightarrow(z)\alpha_\leftarrow^*(z) + \alpha_\leftarrow(z)\alpha_\rightarrow^*(z),$$ (1.30)

and

$$p = p_{\text{rel}}I_0 = p_{\text{rel}}\cdot\frac{1}{2}\epsilon_0 n_0 cE_0^2,$$ (1.31)

which is derived in detail in appendix A.3.7.

Here, the medium at position z is j and the local amplitudes are obtained by selecting the proper matrix:

$$\begin{pmatrix}\alpha_\rightarrow(z)\\\alpha_\leftarrow(z)\end{pmatrix} = M(z)\begin{pmatrix}1\\0\end{pmatrix},$$ (1.32)

with

$$M(z) = \underbrace{M_j(\sum_{i=0}^{j}d_i - z)}_{\substack{\text{propagation matrix}\\\text{in (part of) medium } j}}\cdot\left(M_{jk}M_kM_{kl}M_l...M_{m-1m}\right),$$ (1.33)

where d_i is the layer thickness of medium i.

For oblique incident angles, a more detailed derivation can be found in appendix A, and all required theory is described in [40]. In appendix A, the expression for the locally absorbed power $p_{\text{rel}}(z)$ for oblique incidence is derived (equations (A.72) to (A.77)). A Python-script is provided [42] where the material/refractive indices, layer thicknesses,
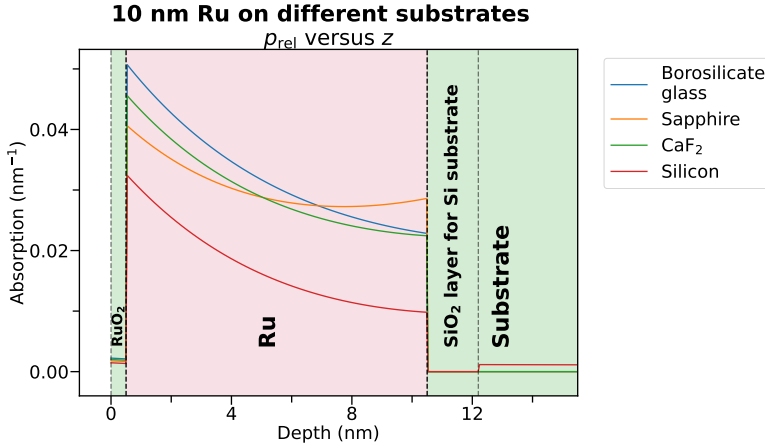
Figure 1.2: The calculated relative locally absorbed power density $p_{\text{rel}}(z)$ induced by a 400 nm wave at normal incidence in multilayer stack. Here, four multilayer stacks are considered: 10 nm ruthenium with an 0.5 nm native oxide on borosilicate glass, sapphire, CaF_2 or a silicon (including a 1.7 nm SiO_2 oxide) substrate.

polarization, and incident angle are used as an input, to calculate the total reflection, transmission and absorption, as well as the locally absorbed power density. Figure 1.2 shows an example of the relative absorbed power density $p_{\text{rel}}(z)$ through a multilayer stack containing a RuO_2, Ru and substrate layer, for various substrates. As can be seen from figure 1.2, the RuO_2 and Ru layer are thin enough for light to reach the substrate underneath. This leads to interference in the layers, and thus affects the absorption profile in the RuO_2 and Ru as well. This results in a higher (total) absorbed power when using a sapphire substrate with respect to silicon. Additionally, the absorbed power density profiles are different using various transparent substrates as well (borosilicate glass, sapphire, CaF_2). Note that $p_{\text{rel}}(z)$ is expressed as the fraction per unit of length of the total incident power. Integrating $p_{\text{rel}}(z)$ over z will result in the total absorbed fraction *Abs* (see equation (1.25)).

1.1.2. TWO-TEMPERATURE MODEL

SOURCE TERM
From transfer-matrix method (TMM) calculations, the locally absorbed power density $(p(z, \lambda))$ is obtained in a multilayer stack for a plane wave with wavelength λ. However, in this research, ultrashort Gaussian pulses with a FWHM pulse duration τ and FWHM spectrum $\Delta\lambda$ are used. Therefore, the assumption is made that the total locally absorbed power density $p(z)$ is equal to $p(z, \lambda)$ integrated and multiplied by its normalized Gaussian distribution of λ[1]:

---

[1]When using equation (1.34), no interference effects between light of different wavelengths are considered. It is only effectively averaged over different wavelengths to include wavelength dependent refractive index values. One can also choose to calculate $p(z)$ by only considering the (central) wavelength λ_0 ($p(z) = p(z, \lambda_0)$).

1

$$p(z) = \int p(z,\lambda) \cdot \underbrace{\frac{1}{\Delta\lambda} \sqrt{\frac{4\ln(2)}{\pi}} \cdot e^{-4\ln(2)\frac{\lambda^2}{\Delta\lambda^2}}}_{\substack{\text{Normalized Gaussian} \\ \text{distribution } g(\lambda)}} d\lambda. \tag{1.34}$$

From this, the source term for the *two-temperature model* equals:

$$S(r,z,t) = p(z)\, e^{-4\ln(2)\frac{r^2}{d^2}}\, e^{-4\ln(2)\frac{t^2}{\tau^2}}, \tag{1.35}$$

where d is the full width at half maximum (FWHM) of the beam profile and r the distance from the illumination center.

COUPLED EQUATIONS

When a femtosecond laser pulse is absorbed by a metal, the energy is initially deposited in the electron gas. In metals, electrons transition to higher-energy unoccupied states in the conduction band. Electron-electron scattering then causes the initially excited non-thermal electron gas to form a thermal Fermi distribution. It is assumed that the electrons reach this quasi-equilibrium state quickly, leading to a well defined electron temperature T_e. Similarly, the lattice subsystem is assumed to quickly reach a quasi-equilibrium state due to phonon-phonon interactions, resulting in a well-defined lattice temperature T_l. Initially, the electron temperature significantly exceeds that of the lattice, but electron-phonon coupling will lead to cooling of the electron gas and subsequent heating of the lattice. The evolution of this coupled electron-lattice system, with both the electron gas and lattice assumed to be internally thermalized, is effectively described by the *two-temperature model* (TTM) [43–45]. For times scales longer than the electron thermalization time, the TTM provides a proper description of the spatial and temporal evolution of the electron gas temperature T_e and lattice temperature T_l.

The TTM consists of two coupled equations containing several terms, where each term on the right represents the power gained or lost in the electron gas or lattice by a specific interaction:

$$
\begin{aligned}
C_e(T_e)\frac{\partial T_e}{\partial t} &= \overbrace{\nabla\cdot\kappa_e(T_e,T_l)\nabla T_e}^{\text{Thermal conduction}} + \overbrace{G(T_e,T_l)\cdot(T_l-T_e)}^{\text{Electron-phonon coupling}} + \overbrace{S(r,z,t)}^{\text{Source}}, \\
(C_l + H_m\delta\,(T_l-T_m))\frac{\partial T_l}{\partial t} &= \underbrace{\nabla\cdot\kappa_l(T_e,T_l)\nabla T_l}_{\text{Thermal conduction}} + \underbrace{G(T_e,T_l)\cdot(T_e-T_l)}_{\text{Electron-phonon coupling}},
\end{aligned}
\tag{1.36}
$$

with the

- **Source** term $[S(r,z,t)] = \mathrm{W\,m^{-3}}$, is the energy absorbed per unit of time and volume of the light pulse by the electron gas (equation (1.35))

- **Electron-phonon coupling** describes the energy exchange between the electron gas and lattice, with $[G(T_e,T_l)] = \mathrm{W\,m^{-3}\,K^{-1}}$ the electron-phonon coupling 'constant'

- **Thermal conduction** describes the heat diffusion of the electron gas energy and lattice energy, with $[\kappa_e] = \mathrm{W\,m^{-1}\,K^{-1}}$ and κ_l the thermal conductivities of the electron gas and lattice respectively

The total net gain or loss of energy per unit of time changes the temperatures through their heat capacities $[C_e] = \mathrm{J\,m^{-3}\,K^{-1}}$ and C_l, as indicated at the left sides of equation (1.36). When the lattice melting temperature T_m is reached, the melting enthalpy H_m has to be overcome before the lattice heats any further. This is included by adding a delta function to C_l [46]. However, C_e, κ_e and G depend on T_e and/or T_l as well. Therefore, the following relations are assumed:

$$C_e(T_e) = A_e T_e, \tag{1.37}$$

$$\kappa_e(T_e, T_l) = \kappa_0 \frac{T_e}{T_l}, \tag{1.38}$$

where $[A_e] = \mathrm{J\,m^{-3}\,K^{-2}}$ is the electron specific heat constant and κ_0 the electron thermal conductivity at 273 K [47]. The linear relationship of equation (1.37) stems from the fact that, in a metal, only electrons near the Fermi level contribute to the heat capacity. As the temperature increases, more electrons within an energy range proportional to $k_B T_e$ around the Fermi level become thermally active. The expression of κ_e (equation (1.38)) originates from using the Wiedemann-Franz law [48] and the assumption that $T_e \gg T_l$. For metals, κ_l can be neglected because lattice heat diffusion in a metal typically takes place through electron energy diffusion. Figure 1.3 shows the calculated electron (top) and lattice (bottom) surface temperature at the center of an illuminated spot versus time for 20 nm gold on glass for a $0.8\,\mathrm{mJ/cm^2}$ incident fluence. The absorbed power density is calculated using TMM calculations (section 1.1.1) at a 400 nm wavelength, and an infinite heat resistance at the interface between the gold layer and glass substrate is assumed (no heat transfer).

Ultrafast and high excitation

The TTM quantitatively describes the temperature evolution of a coupled electron-lattice system under out-of-equilibrium successfully, provided the material parameters are known [49]. However, there is often some uncertainty, especially of the reported electron-phonon coupling constant $G(T_e, T_l)$ [50]. Experiments can only estimate $G(T_e, T_l)$ indirectly because transient optical reflectance measurements [47, 51, 52] and ultrafast diffraction techniques [53, 54] only probe *integral* electron gas or lattice responses. Theoretically, several models have been developed to determine $G(T_e, T_l)$ [50, 55–58]. However, the approximated values can still vary by one order of magnitude.

Despite these significant theoretical efforts to calculate $G(T_e, T_l)$ in the regime of strong laser excitation [50, 55, 57] and recent experiments addressing the topic of electron-phonon coupling measurements [59], there remains a certain ambiguity in the choice of $G(T_e, T_l)$ [55]. Care must be taken in choosing the value of the electron-phonon coupling constant. It is therefore necessary to numerically solve equation (1.36) and obtain T_e and T_l for a range of $G(T_e, T_l)$ values, to gain insight into the electron gas and lattice temperature dependence on the chosen electron-phonon coupling constant, as is done in this thesis. Although not taken into account here, for strong laser excitation, the source

20 nm Au on glass
Surface temperature at center (r = 0, z = 0)
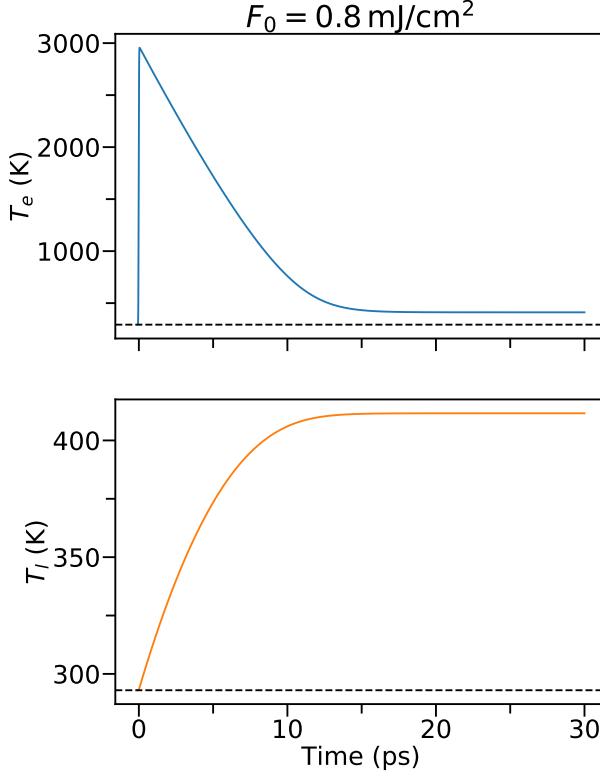
Figure 1.3: Surface temperature at the center of illumination ($r = 0$, $z = 0$) versus time for 20 nm gold on glass obtained by 1D two-temperature model calculations for a $0.8\,\mathrm{mJ/cm^2}$ incident fluence. Shown at the top and bottom are the electron, and the lattice surface temperature T_e and T_l respectively. Here, the black lines indicate the initial temperature (293 K). The absorbed power density is calculated using transfer-matrix method calculations (section 1.1.1) at a 400 nm wavelength, and an infinite heat barrier between the gold layer and glass substrate is assumed (no heat transfer). The used parameters are: $C_{l,\mathrm{Au}} = 2.42 \times 10^6\,\mathrm{J\,m^{-3}\,K^{-1}}$, $A_{e,\mathrm{Au}} = 67.96\,\mathrm{J\,m^{-3}\,K^{-2}}$, $\kappa_{e0,\mathrm{Au}} = 318\,\mathrm{W\,m^{-1}\,K^{-1}}$, $\kappa_{l,\mathrm{Au}} = 0\,\mathrm{W\,m^{-1}\,K^{-1}}$ (neglect lattice heat conduction), $h_{\mathrm{glass-Ru}} = \infty\,\mathrm{W\,m^{-2}\,K^{-1}}$, $H_{m,\mathrm{Au}} = 6.33 \times 10^9\,\mathrm{J/m^3}$, and $T_{m,\mathrm{Au}} = 1337\,\mathrm{K}$.

term should be modified as well, e.g. by nonlinear effects, shadowing effects, and self-enhanced absorption. The description and modelling of strong laser excitation of metals has for example been carried out by the XUV Group at the University of Twente [35, 36, 50].

1.1.3. HEAT DIFFUSION

HEAT DIFFUSION EQUATION

After approximately a few picoseconds (depending on the material and stack geometry), the electron and lattice temperatures in the absorbing metal are in equilibrium, as calculated by the two-temperature model (TTM). From this point onward, the system's overall (lattice) temperature T can be determined by solving the heat diffusion equation (equation (1.39)). In the case where the incident beam exhibits a Gaussian profile and assuming radial symmetry (no angular dependence), the heat diffusion equation in cylindrical coordinates is expressed as:

$$\kappa \left(u_{rr} + \frac{1}{r} u_r \right) + (\kappa u_z)_z = C_l u_t, \tag{1.39}$$

with the coordinates z and r the height and r the radial distance from the z-axis respectively, $u(r, z, t)$ the temperature profile, and the subscripts denoting the (partial) derivatives, κ the heat conductivity, and C_l the (lattice) heat capacity. We can make κ z-dependent to account for different materials in a multilayer stack.

INITIAL AND BOUNDARY CONDITIONS

The initial spatial temperature distribution is set equal to the lattice temperature obtained by two-temperature model calculations, taken at a time t_{eq} where the electron gas and lattice temperature are approximately in equilibrium $u(r, z, t = t_{eq}) \approx T_l(r, z, t = t_{eq})$. The temperature at the outer boundary of the cylindrical system r_{end}, is assumed to be at a constant temperature $u(r_{end}) = T_0$ (Neumann boundary condition [60]), where r_{end} needs to be taken much larger than the FWHM spot size of the beam.

At each material interface, the following boundary conditions are applied:

- **Air-layer boundary:** No heat transfer at air-layer boundary (0-1 at $z = L_{01}$):

$$\kappa_1 \left. \frac{\partial T_1}{\partial z} \right|_{z=L_{01}} = 0. \tag{1.40a}$$

- **Layer-layer boundary:** Continuity of heat flux across the layer-layer interface (1-2 at $z = L_{12}$):

$$\kappa_1 \left. \frac{\partial T_1}{\partial z} \right|_{z=L_{12}} = \kappa_2 \left. \frac{\partial T_2}{\partial z} \right|_{z=L_{12}}, \tag{1.40b}$$

or, when there is a thermal interface resistance [61, 62]:

$$\kappa_1 \left. \frac{\partial T_1}{\partial z} \right|_{z=L_{12}} = h_{bd,12} \left(T_1(z = L_{12}, t) - T_2(z = L_{12}, t) \right), \tag{1.40c}$$

with the thermal boundary conductivity $[h_{bd,12}] = Wm^{-2}K^{-1}$.

- **Radial symmetry:** This applies since both the multilayer stack is assumed to be infinitely large, and the incident beam profile is circularly symmetric. This results in a boundary condition at $r = 0$:

$$\left.\frac{\partial u}{\partial r}\right|_{r=0} = 0. \tag{1.40d}$$

Using these conditions, $u(r, z, t)$ can be solved numerically [63], or, for some cases, analytically [60].

Figure 1.4 shows the calculated surface temperature at the center of illumination ($r = 0$, $z = 0$) versus time for 20 nm ruthenium on glass, for four different beam profiles with spot diameters of 1, 2, 20 and 70 µm FWHM and a incident peak fluence of $F_0 = 31.2\,\text{mJ/cm}^2$. In our case, the material boundaries are at constant z, and the pump pulse is at normal incidence. The initial temperature profile $u(r, z, t = 2.5\,\text{ps})$ is obtained by two-temperature model calculations, for a circular Gaussian beam profile. From this, the temperature profile $u(r, z, t)$ is obtained by solving the heat equation (equation (1.39)) numerically. The $u(r = 0, z = 0, t)$ curve decays faster for the 1 µm spot than the 2 µm one. This is because lateral diffusion (u_r) is greater for smaller spot sizes because of the bigger lateral gradient of the beam profile and thus for $u(r, z, t)$ as well. However, for the 20 and 70 µm spots, the lateral diffusion is much slower than u_z, and $u(r = 0, z = 0, t)$ is approximately equal for both spot sizes. This is not only at $r = 0$, $z = 0$, but inside the entire layer.

In the experiments presented in this thesis, the beam spot size is approximately 70 µm, allowing lateral heat diffusion to be neglected. Although the beam is slightly elliptical, with its width up to 20% larger or smaller than its height, the effect on lateral diffusion still remains minimal, and can therefore be neglected.

1.2. NON-FLAT SURFACES

When considering rough surfaces, scattering theories such as the Rayleigh-Rice theory (see section 1.2.1) can be employed. This approach allows for the examination of the influence of slight surface roughness on the overall reflection and transmission, as compared to a perfectly flat layer.

For heavily-patterned periodic structures, like gratings (see chapter 5), a different approach is required. In these cases, Maxwell's equations are numerically solved for the electric and magnetic far-field by forward diffraction modelling using rigorous coupled-wave analysis [64]. The electric near-field is calculated in the material from which the locally absorbed power can be obtained. From the far-field calculations, the (total) intensity of reflected and diffracted light is calculated (see section 1.2.2).

1.2.1. SURFACE SCATTERING

For a perfectly flat layer, there is no scattering, and the intensity of the specular reflection P_r is maximized. However, for the slightly rough surfaces considered in this thesis, some of the incident laser power P_i will be scattered, which lowers P_r. For slightly rough surfaces, the total amount of scattering P_s can be estimated by using an appropriate theory. First the height profile of the surface is needed.

The height profile $h(x, y)$, as obtained by AFM (see section 2.3.2), can be described as a collection of gratings with different spatial frequencies, as is done by making a 2D
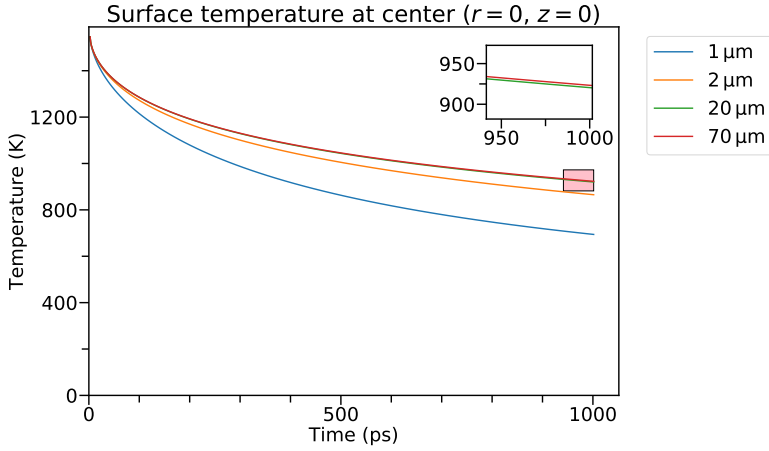
Figure 1.4: Calculated surface temperature at the center of illumination ($r = 0$, $z = 0$) versus time for 20 nm ruthenium on glass, for spot sizes of 1, 2, 20 and 70 μm FWHM. For all spot sizes, the incident light pulse has a peak fluence of 31.2 mJ/cm^2, pulse duration of 50 fs and wavelength of 400 nm. Using two-temperature model calculations (see section 1.1.2), the lattice temperature is calculated at 2.5 ps and taken as the initial temperature. The red rectangle marks the zoomed-in section as shown in the inset. The used parameters are: $C_{l,\text{glass}} = 820\,\text{J kg}^{-1}\,\text{K}^{-1} \cdot \rho_{\text{glass}}$, $C_{l,\text{Ru}} = 238\,\text{J kg}^{-1}\,\text{K}^{-1} \cdot \rho_{\text{Ru}}$, $\kappa_{\text{glass}} = 1.14\,\text{W m}^{-1}\,\text{K}^{-1}$, $\kappa_{\text{Ru}} = 1.20\,\text{W m}^{-1}\,\text{K}^{-1}$, $h_{\text{glass}-\text{Ru}} = 5.0 \times 10^8\,\text{W m}^{-2}\,\text{K}^{-1}$.

spatial Fourier transform of the profile. For each grating/spatial frequency, the power ΔP_s that scatters into a small solid angle $\Delta \Omega_s$ can be calculated. Figure 1.5 shows a schematic drawing of this geometry. Effectively summing over all gratings and over all solid angles that form the backward hemisphere of the surface, will result in the total scattered power P_s. To achieve this, the angle resolved scattering function must be determined first.

ANGLE RESOLVED SCATTERING

Angle Resolved Scattering (ARS) is defined as the power ΔP_s that scatters into a small solid angle $\Delta \Omega_s$, normalized by the incident power P_i [65]:

$$ARS(\theta_s) = \frac{\Delta P_s(\theta_s)}{\Delta \Omega_s P_i}. \tag{1.41}$$

The total backscattering (TS_b) fraction is defined as the power P_s *scattered* from a surface into the backward hemisphere, normalized to the incident power P_i. TS_b is obtained by integrating *ARS* over the scattering angle θ_s:

$$TS_b = \frac{P_s}{P_i} = 2\pi \left(\int_{\theta_i + \delta\alpha}^{\beta} ARS(\theta_s) \sin\theta_s d\theta_s + \int_{0°}^{\theta_i - \delta\alpha} ARS(\theta_s) \sin\theta_s d\theta_s \right). \tag{1.42}$$

Here, the light scattered within $\pm \delta\alpha$ from the incident angle θ_i is considered to be specular reflected. Following the ISO standard [66], the values for $\delta\alpha$ and β are set to 2° and 85° respectively.
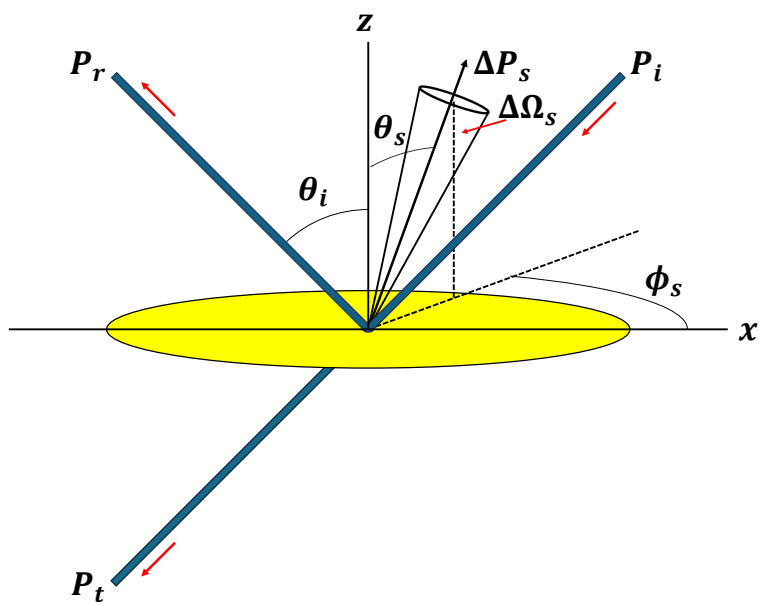
1

Figure 1.5: The considered geometry of a incident laser beam with power P_i, incidence angle θ_i and reflected and transmitted power P_r and P_t. The power ΔP_s that scatters into a small solid angle $\Delta\Omega_s$ makes an angle θ_s with the surface normal.

RAYLEIGH-RICE SCATTERING THEORY

Different surface scattering models estimate $ARS(\theta_s)$ from which the total backscattering can be obtained (equation (1.42)). The Rayleigh-Rice approach [67] is commonly used in cases where the Root Mean Square (RMS) height of a surface (σ) is significant smaller than the wavelength λ [68], and here we use the rather strict criterion $\sigma < 0.01\lambda$ [69]. For the 'flat' layers fabricated during this research (see section 2.1), σ is lower than $< 0.01\lambda$. Therefore the Rayleigh-Rice theory can be applied.

The surface topography of our samples is used to estimate the amount of scattered light. Experimentally, a height scan obtained by atomic force microscopy $h(x, y)$ (see section 2.3.2) can be used as input [70, 71]. From $h(x, y)$, the radial 1D power spectral density function $PSD(f)$ can be obtained.

To obtain the $PDS(f)$ from the 2D height profile $h(x, y)$, the 2D power spectral density $PSD_2(f_x, f_y)$ needs to be calculated first,

$$PSD_2(f_x, f_y) = \lim_{L\to\infty} \frac{1}{L^2} \left| \underbrace{\int_0^L \int_0^L h(x, y) e^{-2\pi i(f_x x + f_y y)} dx dy}_{\text{2D Fourier transform}} \right|^2, \tag{1.43}$$

where the $PSD_2(f_x, f_y)$ is obtained by using the Discrete Fourier Transform of $h(x, y)$. To go from the 2D to the *radial* 1D power spectral density, $PSD_2(f_x, f_y)$ is reparametrized by using $f = \sqrt{f_x^2 + f_y^2}$ as the radial spatial frequency and $\psi = \arctan(f_y/f_x)$ as the angle. $PSD(f)$ can be obtained by integrating $PSD_2(f, \psi)$ over the angle ψ:

$$PSD(f) = \frac{1}{2} \int_0^{2\pi} PSD_2(f, \psi) d\psi. \tag{1.44}$$

According to the Rayleigh-Rice theory, the relationship between $ARS(\theta_s)$ and $PSD(F)$ is [65]:

$$ARS(\theta_s) = \frac{16\pi^2}{\lambda^4} \cos(\theta_i) \cos^2(\theta_s) \theta_s Q \cdot PSD(f), \tag{1.45a}$$

where

$$f = \frac{|\sin\theta_s - \sin\theta_i|}{\lambda}. \tag{1.45b}$$

Here, Q is the angle dependent polarization reflectance factor [65] that contains information about the dielectric function as well as the conditions of illumination and detection, i.e. angles of incidence and scattering, and polarization. The derivation and full expression for Q can be found in [72, pp. 99-103]. However for smooth surfaces, Q approaches the specular reflectance fraction. The relation between f and θ_s is given by the grating equation 1.45b. Note that only the first diffraction order is considered here, since the 0th order describes the specular reflection. Higher orders can be neglected for the relatively smooth surface regime the Rayleigh-Rice theory is valid for.

Combining equations (1.45a) and (1.45b) into equation (1.42) will result in the estimation of the total backscattered fraction for relatively smooth surfaces ($\sigma < 0.01\lambda$).

1.2.2. PERIODIC SURFACE STRUCTURES

For periodic surface structures, e.g. gratings, Maxwell's equations are solved by using the discretization technique known as the rigorous coupled-wave analysis (RCWA) and is also based on a mode expansion method [39, 73]. This method is described by M.G.M.M. van Kraaij in [64, pp.53-68] in great detail. His corresponding RCWA MATLAB code has been made available to us, and is used to perform RCWA near- and far-field calculations.

NEAR-FIELD CALCULATIONS

The locally absorbed power in a grating is obtained by performing near-field calculations. Here, the local electric $\mathbf{E}$ and magnetic field $\mathbf{H}$ near and inside a grating, exposed by a plane wave, are derived.

First, an infinite periodic structure along the x-direction and flat topography along the y-direction is assumed. Then the rigorous coupled-wave analysis (RCWA) discretization strategy is used to solve the Maxwell equations by forward diffraction modelling [64, pp.53-68].

To connect the calculations with the actual experiments, 2D AFM scans (see section 2.3.2) of the considered gratings are used, thereby providing the grating profiles as input for the RCWA calculations. The cross sections are obtained by taking the median of the 2D heightmap in the direction of the grating lines to get a 1D profile. From this, one single grating line is isolated. For relatively symmetric grating lines (pristine), the single grating line is mirrored and placed next to the original during calculations, forming the unit cell. Because of this, artifacts due to the height jumps at the boundaries of the cross section are avoided. However, for asymmetric/deformed grating lines, the unit cell is taken over one grating period. From this, the local $\mathbf{E}(x,z)$ and $\mathbf{H}(x,z)$ fields are obtained for wavelength λ of the incident waves. This results in the cycle-averaged Poynting vector, $\langle\mathbf{S}\rangle$:

$$\langle\mathbf{S}\rangle(x,z) = \frac{1}{2}\operatorname{Re}\left(\mathbf{E}(x,z)\times\mathbf{H}^*(x,z)\right), \tag{1.46a}$$

from which the local absorbed power density $\widehat{\frac{du}{dt}}$ can be calculated,

$$\widehat{\frac{du}{dt}}(x,z) = -\nabla\cdot\langle\mathbf{S}\rangle(x,z). \tag{1.46b}$$

The incident electric and magnetic field amplitudes scale with the fluence F, which has not yet been taken into account. The total local absorbed power density $\frac{du}{dt}$ is therefore proportional to:

$$\frac{du}{dt}(x,z) \propto F\cdot\widehat{\frac{du}{dt}}(x,z), \tag{1.47}$$

with F the fluence, which is taken constant over the considered unit cell. The derived $|\mathbf{E}|$, $|\mathbf{H}|$, $|\mathbf{S}|$ and $\frac{du}{dt}$ profiles for a 980 nm pitch, 50% duty-cycle silicon grating, exposed to 400 nm incident pump light, as well as for a flat silicon layer to compare the profiles with, are shown in figure 1.6.

FAR-FIELD CALCULATIONS

The total reflected, transmitted and absorbed light are obtained by RCWA far-field calculations. Here, the RCWA MATLAB code [64] calculates the power fraction of light
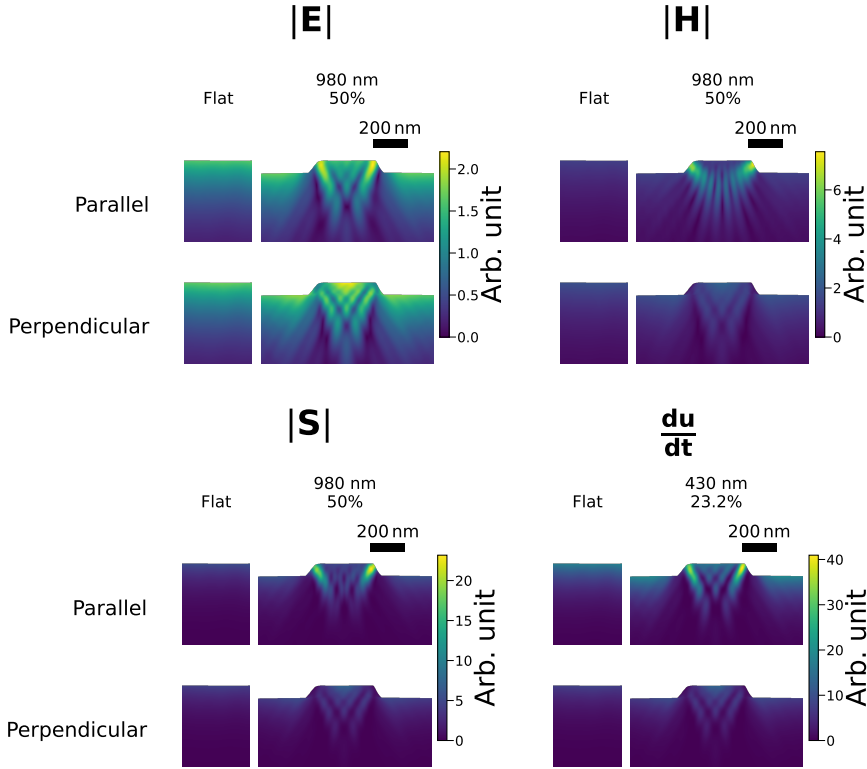
Figure 1.6: $|\mathbf{E}|$, $|\mathbf{H}|$, $|\mathbf{S}|$ and $\frac{du}{dt}$ profiles in silicon, obtained by near-field RCWA calculations. These calculations are performed on flat silicon (left) and a silicon grating with 980 nm pitch and 50% duty cycle (right), illuminated by a 400 nm pump pulse at normal incidence at parallel or perpendicular polarization with respect to the direction of the grating lines. A SiO$_2$ native oxide thickness of 2.1 nm is included.

that is specularly reflected, transmitted, and diffracted (for each order separately). The remaining fraction is then equal to the total absorbed power fraction.

1.3. Threshold and spot size determination

Let's consider a single-shot damage experiment. Each pump shot n hits a new pristine site on the sample with a slightly different pump fluence $F(n)$, defined as the pulse energy divided by a constant area, given by the beam profile. Damage occurs at a threshold fluence F_{th}, so damage will only occur at sites where $F(n) > F_{th}$.

To extract F_{th} from the experiment, we can use:

$$F_{no\ damage} = \max\{F(n) \mid F(n) < F_{th}\},$$

and

$$F_{damage} = \min\{F(n) \mid F(n) \geq F_{th}\}.$$

The true value F_{th} lies between these values. With this method, the uncertainty depends on the difference between $F_{no\ damage}$ and F_{damage}, which depends on the fluence sampling resolution, and can be quite substantial. However, with additional information about the beam profile, F_{th} can be obtained more accurately. The shape of the beam profile defines how the fluence varies locally. When the peak fluence F_0 exceeds F_{th}, the damaged area will be bound where the local fluence F_{local} equals F_{th}. This is schematically shown in figure 1.7. Using the damaged area A and knowing the beam profile, will lead to an accurate determination of the threshold fluence F_{th}. This method is described in section 1.3.1. Applying this to Gaussian beam-profiles results in the Liu-analysis [74], which is presented in sections 1.3.2 and 1.3.3.

1.3.1. Threshold and beam profile

Each pump shot has a varying peak fluence F_0 and a fluence distribution F_{local} defined by the beam profile $g(x, y)$:

$$F_{local}(F_0, x, y) = F_0 \cdot g(x, y), \tag{1.48}$$

where $g(x, y) = 1$ at its maximum. Since a damage mechanism starts to occur from F_{th} onwards, at the border of a damaged site $F_{local} = F_{th}$. The area A bounded by the curve $F_{local} = F_{th}$, can easily and accurately be obtained from (optical) microscopy images (see section 2.3.2). When, for instance, the damage mechanism is ablation, A is simply the area covered by the crater. While knowing $g(x, y)$, F_{th} can be determined by the obtained areas A at different F_0:

$$F_{th} = f(F_0, A(F_0)) = f(F_0), \tag{1.49}$$

where f is a function which depends on the beam profile $g(x, y)$. To make equation (1.49) deterministic, $g(x, y)$ should be continuous and not flat, e.g. a top hat profile will give the same values for A if $F_0 > F_{th}$. In the case of Gaussian beam-profiles, this F_{th} derivation is called the *Liu analysis* [74]. Since $g(x, y)$ can be estimated by a Gaussian elliptical beam in our experiments as well, the function $f(F_0)$ will be analytically obtained for a Gaussian beam here. We first start with a circular Gaussian beam-profile, which is later on used to get to the general expression of f for an elliptical Gaussian profile.

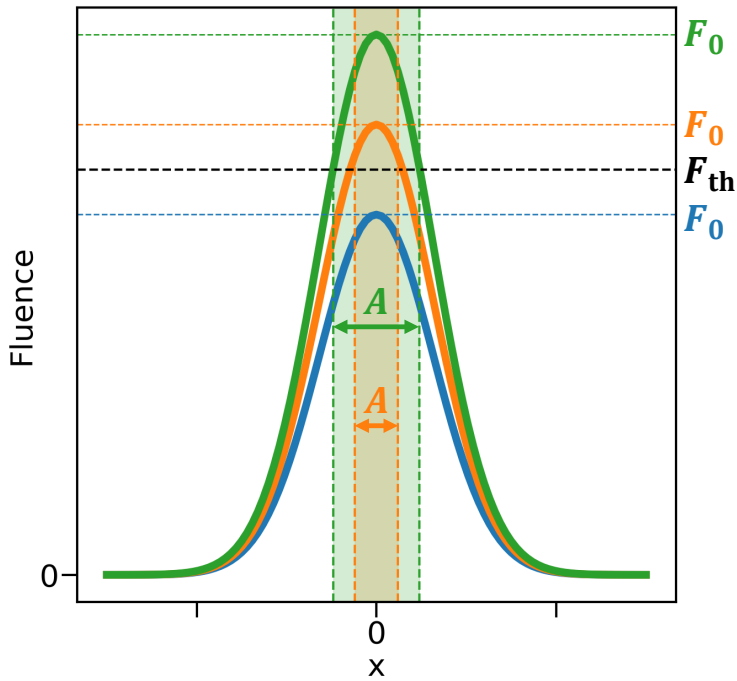Figure 1.7: A schematic drawing of the same three 1D beam-profiles, scaled with different peak fluences F_0. The areas where the green and orange profiles exceed the threshold fluence F_{th} are marked and indicated by A. For the blue beam-profile, $F_0 < F_{th}$, and therefore $A = 0$. This image shows that A is determined by the given shape of the beam profile and the peak fluence F_0.

1

1.3.2. GAUSSIAN BEAM-PROFILE

A spatial and temporal Gaussian beam has a pulse length of τ and spot size d both defined at the FWHM intensity. For a peak intensity I_0, radial distance r and time t, the intensity profile is:

$$I(r, t) = I_0 e^{-4\ln 2 \frac{r^2}{d^2}} e^{-4\ln 2 \frac{t^2}{\tau^2}}. \tag{1.50}$$

When integrating over time, the spatial distribution of the energy is then:

$$F(r) = \int_{-\infty}^{\infty} I(r, t)\, dt = \sqrt{\frac{\pi}{4\ln 2}} \tau I_0 e^{-4\ln 2 \frac{r^2}{d^2}} = F_0 e^{-\frac{r^2}{\rho^2}}, \tag{1.51}$$

with F_0 the peak fluence and $\rho = \frac{d}{\sqrt{4\ln 2}}$. When F_0 exceeds F_{th}, a damaged area will form. The edge of this area is positioned at r_{th}, so $F(r_{th}) = F_{th}$. A relation between the damaged area A and peak fluence F_0 can be derived. From

$$F_{th} = F_0 \exp(-\frac{r_{th}^2}{\rho^2}). \tag{1.52}$$

Taking the natural logarithm on both sides of the equal sign gives

$$\ln F_0 - \ln F_{th} = \frac{r_{th}^2}{\rho^2} = \frac{A}{\pi \rho^2}, \tag{1.53}$$

and thus

$$A = \pi \rho^2 (\ln F_0 - \ln F_{th}). \tag{1.54}$$

This shows that crater area A depends linearly on $\ln F_0$. Equation (1.54) is of the form $A = a \ln(F_0) + b$, with $a = \pi \rho^2$ and $b = \pi \rho^2 \ln(F_{th})$. F_{th} and d can directly be obtained by plotting A versus $\ln(F_0)$ in a so-called Liu-plot. By determining the offset b and slope a of the linear regression line $A = a \ln F_0 + b$ it follows that:

$$F_{th} = \exp(-\frac{b}{a}), \tag{1.55}$$

$$d = \sqrt{\frac{4\ln(2)a}{\pi}}. \tag{1.56}$$

This analysis is valid for circularly symmetric Gaussian beam-profiles. For elliptical Gaussian profiles, there are two spot size parameters: the FWHM along the long axis (d_x) and along the short axis (d_y) of the ellipse. The damage area has corresponding long and short axes of x_{th} and y_{th} respectively. This gives an area A equal to $\pi \cdot x_{th} \cdot y_{th}$. Following the same method as used for circular beam-profiles as expressed in equations (1.50) to (1.54), the elliptical spot size parameters d_x and d_y are derived by the linear regression line ($A = a \ln F_0 + b$) in a Liu-plot as follows:

$$F_{th} = \exp(-\frac{b}{a}), \tag{1.57}$$

$$d_x = \sqrt{\frac{4\ln(2)a}{\pi c}}, \tag{1.58}$$

$$d_y = d_x c. \tag{1.59}$$

where c is the ratio $\frac{d_y}{d_x}$.

1.3.3. Spot size

Integrating the fluence profile $F(x, y)$ (see equation (1.51)) over the area results in the total pulse energy:

$$F(x, y) = F_0 e^{-4\ln(2)\frac{x^2}{d_x^2}} e^{-4\ln(2)\frac{y^2}{d_y^2}}, \tag{1.60}$$

$$E = \int_{-\infty}^{\infty} \int_{-\infty}^{\infty} F(x, y)\, dx\, dy, \tag{1.61}$$

$$\Rightarrow E = \frac{\pi d_x d_y}{4\ln(2)} \cdot F_0 = \frac{\pi d^2}{4\ln(2)} \cdot F_0. \tag{1.62}$$

Experimentally, the pulse energy E, d_x and d_y (or d) are directly measured, from which the fluence F_0 is determined:

$$F_0 = \frac{4\ln(2)E}{\pi d_{\text{meas}}^2}. \tag{1.63}$$

Here, the FWHM spot size d is always obtained by measuring the beam profile directly (d_{meas}). However, equations (1.55) to (1.56) show that d can also be calculated from a and b as derived by the Liu-analysis (d_{Liu}). These two values for d should be equal. However, when a proper Liu-analysis can be performed, i.e. if there are enough data points to fit, d_{Liu} is preferred. The fluence F_0 as defined in equation (1.63) should then be adjusted as follows:

$$F_{0,\text{adjusted}} = F_0 \cdot \left(\frac{d_{\text{meas}}}{d_{\text{Liu}}}\right)^2. \tag{1.64}$$

2

EXPERIMENTAL METHODS

Three ingredients are needed for the light-induced damage measurements that are performed and discussed in this thesis. First, sample fabrication and characterization: the desired materials and nominal thicknesses are deposited, whereafter the optical parameters and inferred thicknesses are determined. Second, light exposure: the samples are exposed to high intensity pump laser pulses. At the same time, in situ light-induced optical and/or morphological changes are measured using probe pulses. Finally, the exposed sites on the samples are examined ex situ with the use of various microscopic techniques, such as optical microscopy, scanning electron microscopy, and atomic force microscopy.

2.1. SAMPLE FABRICATION

2.1.1. DEPOSITION

In the experiments presented in this thesis, we used three different metals, namely gold, aluminum and ruthenium. All metals are deposited on either silicon [75], borosilicate glass (BS) [76], sapphire [77] or calcium fluoride (CaF_2) [78] substrates. Before deposition, the substrates were cleaned using an ultrasonic bath, and ammonia and isopropanol solutions for silicon, and a base Piranha solution for the other substrates. The gold and aluminum layers were deposited by electron-beam physical vapor deposition (EBPVD) (Polyteknik Flextura M508 E). Because of its high melting temperature, ruthenium is deposited by Magnetron Sputter Physical Vapor Deposition (MSPVD) (Polyteknik Flextura M506 S). An overview of the samples used in the experiments is given in appendix B. Additionally, relevant gold (Au), aluminum (Al), aluminum oxide (Al_2O_3), ruthenium (Ru), ruthenium oxide (RuO_2), silicon (Si) and silicon oxide (SiO_2) properties are given in appendix C.

2.1.2. Characterization

Material properties, such as density, can vary for different deposition rates and techniques, which also has an effect on the optical properties. The actual inferred thickness can deviate from the intended thickness as well. In addition, for the aluminum and ruthenium samples, a native oxide layer is formed after exposure to the ambient atmosphere. During layer deposition, an extra silicon test-sample was always loaded into the deposition chamber. Unlike the target samples, these test-samples have an opaque substrate so that no internal substrate reflection can occur. For that reason, these test-samples are used to obtain the refractive index and the inferred thicknesses of all samples by ellipsometry. Using a J.A. Woollam VB-400 variable angle spectroscopic ellipsometer (VASE) with a Woollam HS 190 monochromator, spectroscopic scans for wavelengths within a maximum wavelength range between 300 and 1700 nm, and under various angles of incidence, around $\approx \pm 10°$ from their Brewster angle (at ≈ 500 nm are obtained. For several layer thicknesses, the deposition took place under the same vacuum conditions, evaporation pressures and deposition rates. For each such batch of samples, the spectroscopic data is combined to perform *Multi-Sample Analysis* in the CompleteEASE [79] software to obtain their common refractive index $n + ik$ and (possible) native oxide thickness d_{ox} as well as their individual inferred thicknesses d_{inf}. d_{inf} depends on the deposition time t_{dep} and rate v_{dep} as follows:

$$d_{inf}(t_{dep}) = d_{dep} - \underbrace{d_{ox} \cdot \frac{u_M}{u_{M_xO_y}} \cdot \frac{\rho_{M_xO_y}}{\rho_M}}_{\substack{\text{thickness of } M \text{ that ended} \\ \text{up in the oxide } M_xO_y}} ,$$

$$d_{dep} = v_{dep} \cdot t_{dep},$$

(2.1)

where d_{dep} is the deposited thickness of material M, so before oxidation, and u and ρ are the molecular/atomic weight and density respectively. Different thicknesses are fabricated by varying the deposition time t_{dep} while keeping the deposition rate constant. When not enough test-samples were available, the refractive index was obtained for a few thickness only. When these refractive indices did not vary much for the different thicknesses, a common refractive index was assumed. This common refractive index is obtained by combining the ellipsometry data for the different layers, and using the known t_{dep} and v_{dep} together with equation (2.1) as an extra condition, which gives us the layer thickness for all layers and the common refractive index. For gold, aluminum, aluminum oxide, ruthenium, and ruthenium oxide, the extracted inferred thicknesses, and refractive indices, can be found in appendices B and C respectively.

2.2. Light-induced damage setup

After the sample fabrication and characterization, the samples are mounted inside the laser pump-probe setup where the light-induced damage experiments are performed.

2.2.1. Laser system

All laser experiments where performed with a multi-pass Ti:Sapphire amplifier system (FEMTOPOWER™HE [80], Spectra-Physics, formerly Femtolasers). The functional block diagram of the laser system is shown in figure 2.1. Here, a mirror-dispersion controlled
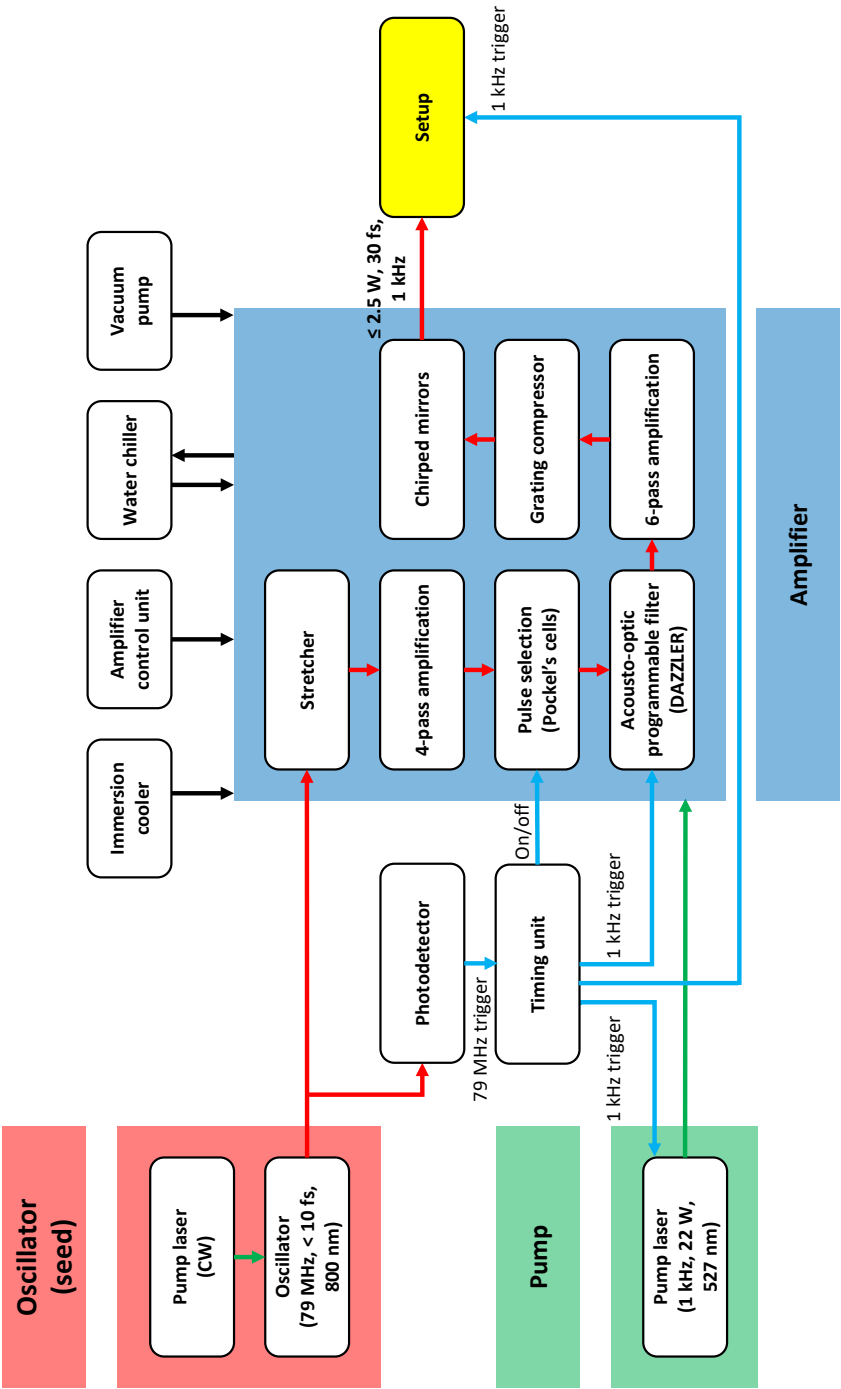
Figure 2.1: Functional block diagram of the laser system

titanium-sapphire oscillator (INTEGRAL[TM] element[TM] PRO) generates ≤10 fs pulses at a 79 MHz repetition rate and is used as the seed. In the amplifier, the seed pulses are stretched to a safe value for amplification by transmitting the pulses through thick optical glass. The pulses are then amplified by multiple passes through a kHz-pumped Ti:Sapphire crystal. Here, the 22 W, 1 kHz pump pulses are generated by a frequency-doubled, Q-switched, diode-pumped Nd:YLF system (Ascent 60). After the first four passes, single pulses are selected from the 79 MHz-pulse train with two Pockels cells, which lowers the repetition rate to 1 kHz. Hereafter, the pulse is sent through an acousto-optic programmable filter (Fastlite's DAZZLER) that is optimized to pre-compensate third- and fourth-order dispersion of the pulse after compression, and also spectrally shapes the optical pulse in order to reduce the effect of gain narrowing inside the amplifier. After six more passes, the pulse is picked off and re-compressed by a grating compressor and sent to a set of chirped mirrors. The final output power can reach ≈2.5 W at a 1 kHz repetition rate but can be lowered by adjusting the DAZZLER settings. Moreover, the retroreflector and one of the two gratings inside the grating compressor are both mounted on a translation stage that allows to change the grating separation. This stage is adjusted to optimize the dispersion and output pulse width, as measured by a near-IR GRENOUILLE (GRENOUILLE 8-9-USB, Swamp Optics) or cross-correlation measurement. GRENOUILLE measures the spectral phase as done by a Frequency-resolved optical gating (FROG) system. However, simplified by replacing its beamsplitter, variable-delay stage, and beam-recombining optics by a Fresnel biprism [81]. The cross-correlate is measured by replacing the sample from the setup by a Beta Barium Borate (BBO) crystal. The 267 nm sum-frequency signal that is generated by the 400 nm pump and 800 nm probe pulses in the BBO crystal, is measured by a UV-photodiode. Changing the time separation between the two pulses using a mechanical delay line, the cross-correlate is obtained from which the pulse length of both the pump and probe is extracted. This is done by solving equation (E.4) as presented in appendix E.

2.2.2. Pump-probe setup
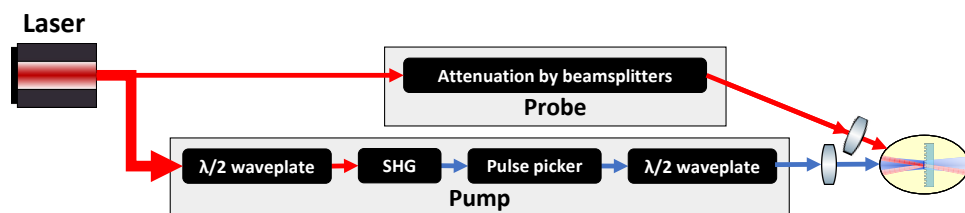
Figure 2.2: Block diagram of the total experimental setup. The output of the laser system (see figure 2.1) is used as a input for the pump-probe setup which is schematically drawn in figure 2.3, and the schematic of the pump and probe beams at the sample site is shown in figure 2.4.

The high power femtosecond laser pulses generated by the laser system are sent to the pump-probe setup used for the experiments. A block diagram of the laser system is shown in figure 2.2, and the pump-probe setup is schematically depicted in figure 2.3. The output of the laser system is split by a 99/1 beamsplitter into a strong pump and a
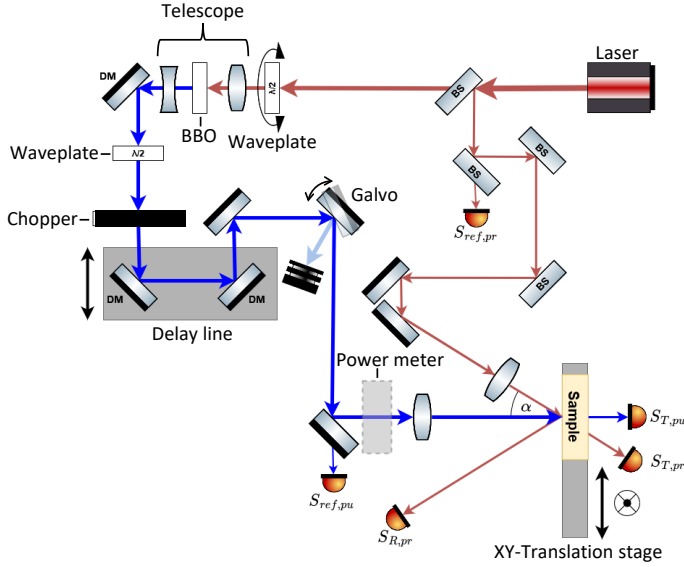
Figure 2.3: Schematic drawing of the pump-probe setup. The 45 fs, 800 nm laser output is split into a strong pump and a weak probe beam. The pump beam passes through a telescope and a Beta Barium Borate (BBO) crystal to frequency-double it to a 400 nm wavelength. The pump beam is reflected by three consecutive dichroic mirrors (DM) to filter out the fundamental beam. Next, it passes through a $\lambda/2$-plate after which the beam is p-polarized, a chopper to lower the repetition rate to 100 Hz, and a galvo mirror to pulse-pick a single pulse. The pump beam is focused using a $f = 20$ cm lens and the sample is placed a short distance before the focal point. The pump is at normal incidence on the sample and the probe beam is at an angle α of $\approx 10°$ with respect to the normal. The power of the probe beam is attenuated by reflecting the beam off three beamsplitters (BS) before it is focused onto the sample. The pump pulse energy can be varied by rotating the first $\lambda/2$-plate. The location of the power meter used during calibration is indicated. R and T indicate the reflected and transmitted beam of the probe and/or pump respectively.

Figure 2.4: The schematic drawing of the beam configuration on the sample

weak probe beam. The pump is frequency-doubled in a BBO crystal to a wavelength of 400 nm. It then passes through a 10% duty-cycle chopper which lowers the repetition rate to 100 Hz. This repetition rate is low enough for a galvo mirror to pulse-pick single pulses. The pump is reflected off three consecutive dichroic mirrors (DM) to r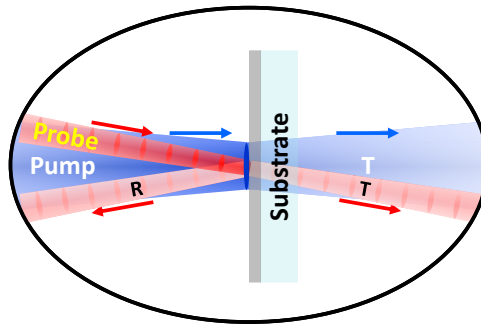emove the 800 nm fundamental beam. Both the pump and probe beam illuminate the sample as is schematically shown in figure 2.4. Here, the 400 nm pump and the 800 nm probe beam are focused onto a sample to a spot size of ≈70 μm and ≈15 μm FWHM respectively so that the pump spot is probed in the central region, where the pump fluence is fairly homogeneous. The angle α, the angle that the probe beam makes with the normal of the sample, is approximately 10°. The pump illuminates the sample at near-normal incidence (see figure 2.4). In our pump-fluence-dependent single-shot measurements, the sample is moved automatically by the XY-translation stage. In this way, every new pump shot hits a pristine site. Between subsequent shots, a piezoelectric rotation stage rotates a $\lambda/2$ plate, placed before the BBO crystal, which changes the second harmonic generation (SHG) efficiency and thus changes the pump pulse fluence. For the experiments described in chapter 5, an additional $\lambda/2$-plate is used to rotate the pump polarization from p to s-polarization before illuminating the sample. To perform pulse-length-dependent measurements, a set of interchangeable UVFS glass windows of varying thicknesses can be placed in the pump beam path before the focusing lens, which allows us to stretch the pump pulse duration from ≈45 fs up to ≈1.5 ps (see appendix E).

In total, six switchable-gain silicon (Si) detectors are used (Thorlabs PDA100A2) in the experiment, all of which are shown in figure 2.3. Two of these measure the pump and probe reference signals ($S_{\mathrm{ref,pu}}$ and $S_{\mathrm{ref,pr}}$), two measure the pump and probe reflection signal ($S_{R,\mathrm{pu}}$ and $S_{R,\mathrm{pr}}$) coming from the sample, and the final two measure the pump and probe transmission signals ($S_{T,\mathrm{pu}}$ and $S_{T\mathrm{pr}}$). The pump reference and reflection signal are taken from pump light leaking through the mirror placed in front of the focusing lens. The probe reference signal is formed by residual light transmitted by the 2/3 beamsplitter. All detector signals are digitized by an analogue-to-digital converter (ADC) and collected by a computer. The signals $S_{R,\mathrm{pr}}$ and $S_{\mathrm{ref,pr}}$ are first sent to a boxcar averager (SRS SR250 2 ns Gated Integrator) before being digitized. This is done for each individual shot produced by the laser. In addition, the chopper and galvo states (blocked or open) and the sample position are recorded. The ADC, chopper and galvo mirror are all triggered by the 1 kHz signal from the timing unit (see figure 2.1).

The translation stage and the first $\lambda/2$-plate are controlled by Oberon+ software, developed in-house. This software is also used to read out all signals coming from the ADC, which includes all photodetectors, the galvo and chopper states, and the signal from the power meter.

2.3. Measurement procedure
The measurement procedure involves two steps:

- The sample is placed into the pump-probe setup where it is continuously probed **in situ** by the weak probe beam and illuminated with one single pump-pulse. This is further explained in section 2.3.1

- Several microscopy techniques are performed **ex situ** for further inspection of the

potentially damaged sites. This will be described in section 2.3.2

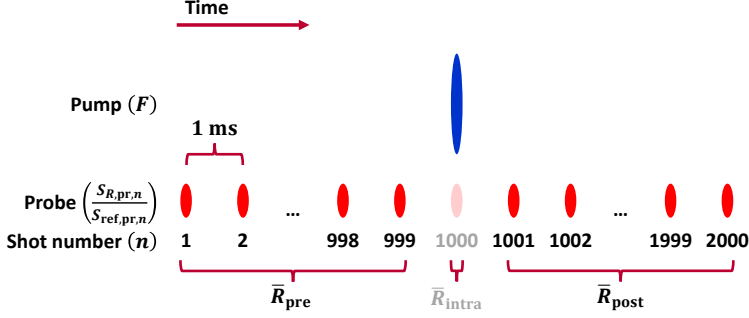### 2.3.1. MEASURING LIGHT-INDUCED DAMAGE IN SITU

Figure 2.5: Schematic overview of the pulse train that is incident on each individual site on a sample. The first 999 probe shots form the pre-pump reflection $\bar{R}_{\text{pre}}$, and shot 1001 to 2000 the post-pump reflection $\bar{R}_{\text{post}}$ (see equation (2.3)). The first probe pulse that samples the post-pump reflection arrives 1 ms after the pump pulse, when all pump-induced transient effects have disappeared. Note that probe pulse 1000 ($\bar{R}_{\text{intra}}$), which more or less coincides with the pump pulse, is omitted in the analysis.

Figure 2.5 is a schematic depiction of the experiment. Before each pump shot, 999 probe pulses illuminate a pristine spot on the sample. This is followed by one pump and one additional probe shot after which a thousand more probe shots hit the spot, which is potentially damaged by the pump. After this, the sample is translated and the measurement is repeated on a different spot for a different pump energy. The reflection of, and the transmission through the sample of each probe shot are measured by the photodetectors and used to calculate the pump-induced changes in the reflection. The reflection of the sample *before* the pump pulse hits the sample $\bar{R}_{\text{pre}}$ is obtained by averaging over 999 shots

$$\bar{R}_{\text{pre}} = \frac{\sum_{n=1}^{999} \frac{S_{R,\text{pr},n}}{S_{\text{ref},\text{pr},n}}}{999}, \tag{2.2a}$$

and the reflection *after* the pump pulse has hit the sample $\bar{R}_{\text{post}}$ is obtained by averaging over 1000 shots and given by

$$\bar{R}_{\text{post}} = \frac{\sum_{n=1001}^{2000} \frac{S_{R,\text{pr},n}}{S_{\text{ref},\text{pr},n}}}{1000}. \tag{2.2b}$$

From this, we define the pump-induced relative reflection change as

$$\Delta R = \frac{\bar{R}_{\text{post}} - \bar{R}_{\text{pre}}}{\bar{R}_{\text{pre}}}, \tag{2.3}$$

where n is the probe pulse index and $S_{R,\text{pr},n}$ and $S_{\text{ref},\text{pr},n}$ are the measured reflection and reference signals of the probe (see figure 2.3). Therefore, $\bar{R}_{\text{pre}}$ is the average relative reflection before, and $\bar{R}_{\text{post}}$ after pump illumination. ΔR is defined as the pump-induced

relative reflection change of the probe. The pump-induced *relative transmission change* of the probe (ΔT) is obtained in a similar fashion.

In a typical experimental cycle, the pump-pulses hit the sample in a six-by-six grid, with each subsequent pump-shot having a slightly higher fluence. To check reproducibility, each such cycle is repeated several times, leading to the formation of multiple grids.

Fluence calibration

Before each measurement series, a Gentec-EO Beamage-4M beam-profiler is placed at the sample position to obtain the pump and probe beam-profiles. Furthermore, a Coherent thermopile power sensor is placed in the pump beam path after the last mirror before the focusing lens. This is to calibrate the reference photodetector in order to convert the detector signal $S_{\mathrm{ref,pu}}$ into a pump (peak) fluence. By rotating the $\lambda/2$-plate, positioned before the BBO crystal, the pump (peak) fluence is varied. Therefore, the $\lambda/2$-plate rotated in steps of 1° to sample over the entire fluence range. For each position of the $\lambda/2$-plate, the power meter P_{pump} and the pump reference photodetector $S_{\mathrm{ref,pu}}$ measure the unpicked 1 kHz pump pulse train for a duration of 10 seconds as is shown in the example on the left side in figure 2.6. Only the last second of this period, containing a thousand pulses, is considered for each $\lambda/2$-plate position. This is to make sure that the thermopile power sensor signal P_{pump} has settled and therefore is stable. For each $\lambda/2$-plate position, both an average value for the photodetector $\bar{S}_{\mathrm{ref,pu}}$ and the power meter signal $\bar{P}_{\mathrm{pump}}$ is obtained by averaging over these last thousand pulses. On the right side of figure 2.6, a calibration run is shown where these values for $\bar{P}_{\mathrm{pump}}$ are plotted versus $\bar{S}_{\mathrm{ref,pu}}$. Hereafter, the linear, or slightly quadratic, regression function $\bar{P}_{\mathrm{pump}} = f(\bar{S}_{\mathrm{ref,pu}})$ is obtained:

$$\bar{P}_{\mathrm{pump}}(F) = f(\bar{S}_{\mathrm{ref,pu}}) = a \cdot \bar{S}_{\mathrm{ref,pu}}{}^2 + b \cdot \bar{S}_{\mathrm{ref,pu}} + c. \tag{2.4}$$

This regression function is indicated by the orange line in figure 2.6. Multiplying this *power* calibration function $f(S_{\mathrm{ref,pu}})$ by a factor containing the spot size (d_x and d_y) and repetition rate (ν_{rep}), leads to the *fluence* calibration function $F_0(S_{\mathrm{ref,pu}})$ of the photodetector signal:

$$F_0(S_{\mathrm{ref,pu}}) = \frac{E_{\mathrm{pump}} \ln(2)}{A_{\mathrm{FWHM}}} = \frac{1}{\nu_{\mathrm{rep}}} \cdot \pi \frac{d_x \, d_y}{4} \cdot f(S_{\mathrm{ref,pu}})), \tag{2.5}$$

where F_0 is the peak fluence, $S_{\mathrm{ref,pu}}$ the pump reference signal, ν_{rep} the repetition rate (=1 kHz), and a, b and c are the fitted second-order polynomial parameters. Note that $f(\bar{S}_{\mathrm{ref,pu}}) = f(S_{\mathrm{ref,pu}})$ because the pump reference photodetector measures single pulses. E_{pump} is the energy of a single pump pulse, and A_{FWHM} is defined by the area bounded by the FWHM of the long axis d_x and short axis d_y of the slightly elliptical Gaussian beam-profile of the pump. The values for d_x and d_y can either be obtained by recording the beam profile or from Liu-analysis (see section 1.3). The ln(2) factor is included for Gaussian beam profiles.

2.3.2. Post-processing

After each measurement series, the sample is taken out of the laser setup for inspection of the illuminated sites.
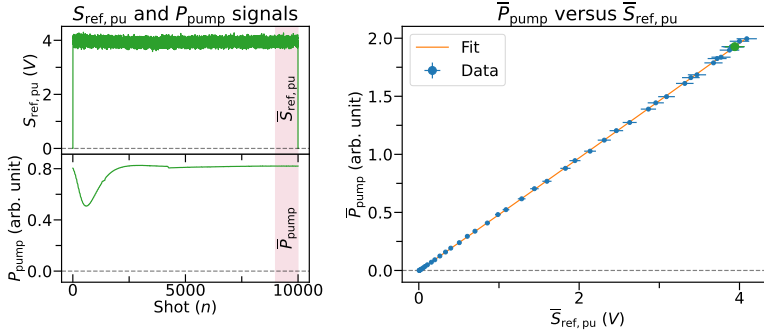
Calibration measurement and fit example

Figure 2.6: On the left are the pump reference signal $S_{\mathrm{ref,pu}}$ measured by the reference photodetector and the power signal P_{pump} measured by the thermopile power sensor. These signals are measured for 10000 shots at a 1 kHz repetition rate (10 s) for a single position of the $\lambda/2$-plate, which is positioned before the BBO (see figure 2.3). During the first and last couple of pulses, a shutter is closed and no pulses will reach the power meter and photodetector. Since the power meter has a slow response, the signals are averaged over the last 1000 pulses before the shutter closes, as is indicated in light red. This 10 s measurement is repeated for multiple positions of the $\lambda/2$-plate. From all measurements, the average values $\bar{S}_{\mathrm{ref,pu}}$ and $\bar{P}_{\mathrm{pump}}$ form the data points shown in the right figure. Here, the green data point shows the values corresponding to the measurement shown in the left figure. The orange line is the quadratic regression between $\bar{S}_{\mathrm{ref,pu}}$ and $\bar{P}_{\mathrm{pump}}$ which forms the calibration function of the power sensor according to equation (2.5).

OPTICAL MICROSCOPY

First, each grid containing 36 illuminated sites, is inspected by an optical microscope (Zeiss Axio images, Axiocam 305) in bright-field (BF), differential interference contrast (DIC/Nomarski) and/or dark-field (DF) mode. With dark-field microscopy, the pristine flat surface will be dark and any irregularities in the surface will light up. This technique is therefore sensitive to any light-induced ablation edges or any other nanoscale irregularities of the flat layer. Because of this, *all* microscopy images of *all* illuminated sites are processed to obtain the area coverage of any damage mechanism. This will be discussed in more detail in section 6.1. An example of a DIC/Nomarski and DF image of an illuminated grid are shown in figures 2.7a to 2.7b.

SCANNING ELECTRON MICROSCOPY

A FEI Helios 600 DualBeam scanning electon microscope (SEM) is used to study possible changes in morphology. Here secondary electrons (SE) or back-scattered electrons (BSE) are measured using an ETD (Everhardt Thornley Detector) or TLD (Through the Lens Detector) in Field Free or Immersion configurations of the magnetic lens. Of each grid, a low-resolution image is obtained (Field Free, SE) as is shown in figures 2.7c and 2.7d. For a selection of individual pump-illuminated sites, higher-resolution images are obtained (Field free or Immersion, figures 2.7e and 2.7f). Some (sub-micrometer) details are then further inspected and compared with the optical images, or stitched together to obtain line scans. In figure 2.7, some examples can be found. A focused ion beam (FIB, Sidewinder Gallium Liquid Metal Ion Source, Ga LMIS), inside the SEM can be used to locally "drill" a pattern in the sample. These shapes are used as location markers for

2

further inspection by atomic force microscopy.

For some sites, energy-dispersive X-ray spectroscopy (EDX), is used to obtain the spatial distribution/concentration of the elements present in the layer, and/or electron backscatter diffraction (EBSD) is used to map the crystal orientation and structure and to obtain grain sizes. Both EDX and EBSD were performed in a Thermo Fisher Scientific Verios. The EBSD patterns were collected using EDAX APEX software, and post-processed using EDAX OIM software.

ATOMIC FORCE MICROSCOPY

A Bruker Dimension Icon atomic force microscope (AFM) is used to obtain height profiles of selected sites (see figure 2.7g). Here, the AFM operates in tapping mode, in which the tip continuously makes a sinusoidal tapping height movement, while scanning along a line. As is shown in figure 2.7g, the collection of neighboring scanned lines forms the total scanned plane. When the tip moves to an area with slightly different mechanical properties, the phase of the sinusoidal tapping signal changes (see figure 2.7h). Although this phase is also influenced by sudden height changes, the obtained phase profile can indicate local material changes. AFM scans are mostly performed on small areas, from which height and phase profiles can be extracted.
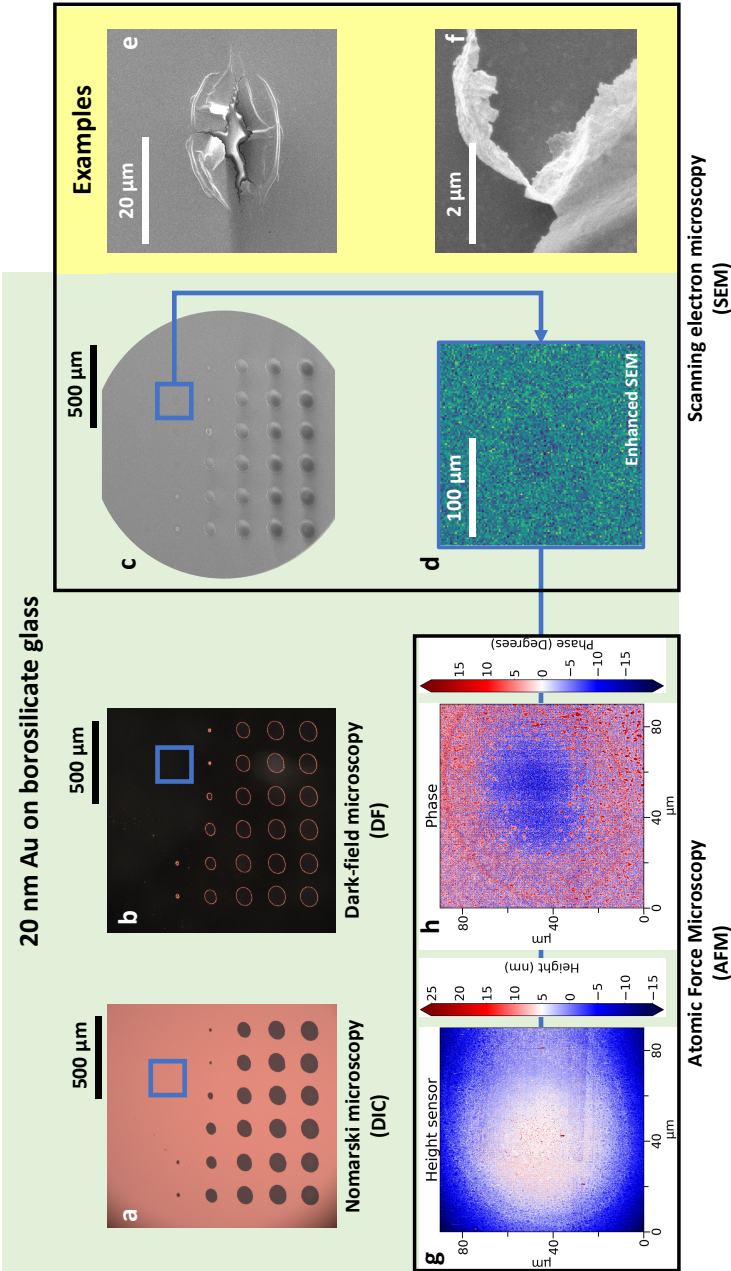
Figure 2.7: DIC/Nomarski (a), dark-field (DF) (b), and SEM (c) images of the same illuminated six-by-six grid on a 20 nm Au layer on borosilicate glass. The atomic force microscopy (AFM) scan (g and h) and numerically enhanced SEM (d) are taken of the same pre-ablation site (regime II, $\Delta R > 0$, see chapter 3) marked with the blue square in a-c. Since tapping-mode is selected both the height (g) as well as the phase (h) profile is obtained. (e) and (f) are taken at two different illuminated sites on the same sample where delamination of the gold layer from the glass substrate occurred, as can be seen by the folds, and ruptures. They are both used as an example of the inspection by SEM of an entire illuminated site (e) and zoom in on a detail (f).

PART I

PRE-ABLATION REGIME LIGHT-INDUCED OPTICAL CHANGES IN NANOMETER THICK METAL FILMS

In chapter 3, we explore light-induced damage in thin metal films exposed to single-shot femtosecond laser pulses. We first examined 8 to 80 nm thick gold films on borosilicate glass substrates and observed small increases in optical reflection in the pre-ablation fluence regime. Similar experiments were conducted on 10 to 30 nm thick aluminum layers, where we also detected small optical reflection increases. In both cases, these optical changes were accompanied by distinct morphological changes, though the underlying causes differed for gold and aluminum.

In chapter 4, further studies on 8 to 40 nm ruthenium layers revealed increased reflectivity and various nanostructural changes, including the formation of nanovolcanoes, for fluences below the onset of catastrophic damage. The increased optical response in both aluminum and ruthenium was found to have the same underlying cause, highlighting a shared mechanism behind the observed optical response changes.

Background for the General Reader

"A farmer has some chickens who don't lay any eggs. The farmer calls a physicist to help. The physicist does some calculations and says 'I have a solution but it only works for spherical chickens in a vacuum!'"

When starting with a complicated problem, we first try to understand the most simple case for it. Knowing when materials get damaged due to exposure to high intense light, is such a complicated problem. This is because a lot of factors are involved. These factors, or **parameters**, can, for instance, depend on the type of light used, or the illuminated material.

Light can shine onto the material continuously, but we choose to have it pulsed. The pulse duration, number of pulses and color of the light are the parameters concerning the light. Is the material thick and rough or thin and smooth? And is there a difference between metal layers and non-metal ones? These are parameters concerning the material.

These are a lot of variables, making the problem quite complex. Therefore we consider the same type of light: one shot, one color, and one pulse duration. For the material, the easiest shape is a smooth, thin flat layer. Furthermore, the interaction between light and a metal is also less complex than in other types of materials.

This results in **single-shot measurements of thin metallic films**. We exposed gold layers since they do not react with air around it, and a lot about light-gold interaction is already studied. Single-shot measurements on thin gold films are therefore our *spherical chickens*. Hereafter, we looked carefully to determine how they damage, by looking at the damaged sites. We also calculated how bright you have to illuminate the gold layers before it gets damaged, to obtain **damage threshold** values. Hereafter, we added one level of complexity: repeat these experiments with aluminum layers. Opposed to gold, aluminum does react with oxide in the air.

How will this influence the damage threshold in comparison with the gold layers? And does light-induced damage look different for aluminum films than for the gold ones?

3

GOLD AND ALUMINUM

In this chapter, we report on small optical reflection increases after illumination of nanometer thick gold and aluminum thin films on different substrates with single, femtosecond 400 nm wavelength pump laser pulses, in a pre-ablation fluence regime. In this fluence regime, small, irreversible and subtle morphological changes of the sample are observed. Dark-field, scanning electron, and atomic force microscopy images reveal subwavelength spallation features in the aluminum, and delamination in the gold layers in this pre-ablation regime. All of these morphological changes coincide with minute optical increases in the reflectivity, at the 0.1 – 2% level, as observed in situ with a weak probe beam. From Liu-analysis, transfer-matrix, and two-temperature model calculations, we infer that in this pre-ablation regime, the aluminum layers already reach the melting temperature. Electron backscatter diffraction measurements show that the aluminum grains melt and resolidify into bigger grains. This suggests that for aluminum, resolidification into bigger grains is responsible for both the increased reflectivity, and the spallation in the pre-ablation regime. For gold, the optical change is most likely due to the etalon effect, caused by delamination.

3.1. INTRODUCTION

In the semiconductor manufacturing industry, increasingly high optical powers, used in metrology, heighten the risk of optical damage.

While much light-induced damage research has been done on bulk gold [82, 83] and/or aluminum [84–87], or on layers that are micrometers thick and thus qualify as bulk materials for fluences close to the damage threshold, semiconductor devices typically consist of thin films with thicknesses ranging from several, to hundreds of nanometers. For metrology applications it is clear that ablation [35, 36, 82, 88–92], the rapid removal of material upon optical excitation, or other large film deformations [93, 94], should be avoided at all times. In this high fluence regime, one has looked extensively into transient effects upon laser excitation [86, 95–98].

Interestingly, subtle changes can already be induced by light fluences below the ablation threshold. From an applications perspective, it is essential to investigate this pre-ablation fluence regime on thin films to understand the underlying mechanisms and to study whether in situ optical probe techniques can be used to detect these changes before catastrophic damage occurs.

In this study, we look at the aftermath of pump-induced reflection and transmission changes in tens of nanometers thick gold and aluminum layers in a fluence regime below that of where catastrophic damage occurs. When probing the exposed regions more than one millisecond after exposure, when all transient effects have disappeared, we observe optical reflection and transmission changes as small as 0.1% in a fluence regime before the onset of crater formation (ablation). For thin gold layers, scanning electron microscopy (SEM) and atomic force microscopy (AFM) strongly suggest that this increase is caused by delamination. This creates a void between the metal and substrate that leads to constructive interference in the reflecting direction. This observation is supported by transfer-matrix calculations [40, 99]. For aluminum, we do not observe delamination. Instead, electron backscatter diffraction (EBSD) measurements suggest that we can attribute the positive reflection change to melting and resolidification into larger grains of the aluminum. In addition, optical dark-field microscopy shows an area with bright spots that grows in size for increasing fluences. SEM and AFM images reveal that each spot in the area corresponds to groups of grains that are either slightly elevated with respect to the surrounding surface, or missing entirely. Liu-analysis [74], as well as two-temperature model (TTM) calculations [43–45], suggest that this spallation is a thermally driven process.

Our results provide new insights into the pre-ablation fluence regime: the fluence regime where light begins to affect materials before catastrophic damage occurs. As these morphological changes coincide with subtle changes in the optical reflectivity, the optical change can act as an early warning signal to prevent further damage.

3.2. EXPERIMENTAL DETAILS

3.2.1. SAMPLE FABRICATION

8 to 80 nm thick gold and 10 to 30 nm aluminum layers are deposited by electron-beam physical vapor deposition (Polyteknik Flextura M508 E) on 0.5 mm borosilicate glass substrates, which have been cleaned in a base Piranha solution. Borosilicate glass [76] is

chosen because of the negligible absorption of the 400 and 800 nm light. For comparison, in order to characterize substrate dependence, also sapphire, CaF$_2$ and silicon substrates were used. An overview of the samples used in the experiments is listed in table B.1. Additionally, relevant gold and aluminum properties are given in table 3.1.

Table 3.1: Optical and thermal mechanical properties of gold and aluminum.

	Gold (Au)	Aluminum (Al)
$n + ik$ @ 400 nm	$1.4684 + 1.9530i$[a]	$0.31448 + 3.8005i$[b]
$n + ik$ @ 400 nm ellipsometry	$1.57 + 1.89i$	$0.68 + 4.34i$
$n + ik$ @ 800 nm	$0.15352 + 4.9077i$[a]	$1.8385 + 6.9757i$[b]
$n + ik$ @ 800 nm ellipsometry	$0.23 + 4.74i$	$2.25 + 7.30i$
T_m (K)	1337.33[b]	933.47[b]
Native oxide thickness (nm)	None	4
κ_l (Wm^{-1}K^{-1})	318[d]	246[e]
C_l (10^6 Jm^{-3}K^{-1})	2.4[f]	2.42[e]

[a]Ref. [100], [b]Ref. [101], [c]Ref. [102, p.6-146 and p.6-148], [d]Ref. [47], [e]Ref. [103], [f]Ref. [104]

3.2.2. SETUP

The pump-probe setup used for the experiments is shown schematically in figure 3.1. A multi-pass Ti:Sapphire amplifier generates 45 fs laser pulses with a central wavelength of 800 nm at a repetition rate of 1 kHz. The output of the laser is split by a 99/1 beamsplitter into a strong pump and a weak probe beam. The pump is frequency-doubled in a Beta Barium Borate (BBO) crystal to a wavelength of 400 nm. It then passes through a 10% duty-cycle chopper which lowers the repetition rate to 100 Hz. This repetition rate is low enough for a galvo mirror to pulse-pick single pulses. The pump is reflected on three consecutive dichroic mirrors to filter out the fundamental beam. Both the pump and probe beam are focused onto a sample to a spot size of 70 μm and 15 μm FWHM respectively so that the pump spot is probed where the fluence varies only a little bit. The angle α, the angle of the probe beam with the normal of the sample, is approximately 10°. The pump illuminates the sample at near-normal incidence. In our pump-fluence-dependent single-shot measurements, the sample is moved automatically by the XY-translation stage. In this way, every new pump shot hits a pristine site. Between subsequent shots, a piezoelectric rotation mount rotates a $\lambda/2$ plate, placed before the BBO crystal, to change the pump pulse fluence.

In total, five switchable-gain Si detectors are used (Thorlabs PDA100A2) in the experiment, all of which are shown in figure 3.1. Two of these measure the pump and probe reference signals ($S_{\mathrm{ref,pu}}$ and $S_{\mathrm{ref,pr}}$), one the probe reflection signal ($S_{R,\mathrm{pr}}$) coming from the sample, and two the pump and probe transmission signals ($S_{T,\mathrm{pu}}$ and $S_{T\mathrm{pr}}$). The pump reference signal is the pump light leaking through the mirror placed in front of the focusing lens. The probe reference signal is formed by light transmitted by the 2/3 beamsplitter. All detector signals are digitized by an analogue-to-digital converter (ADC)

and collected by a computer. The signals $S_{R,\mathrm{pr}}$ and $S_{\mathrm{ref,pr}}$ are first send to a boxcar averager (SRS SR250 2ns Gated Integrator) before being digitized. This is done for each individual shot produced by the laser. In addition, the chopper and galvo state (blocked or open) and the sample position are recorded. Before each measurement series, a Gentec-EO Beamage-4M beam-profiler is placed at the sample position to obtain the pump and probe beam profiles. Furthermore, a Coherent thermopile power sensor is placed in the pump beam path after the last mirror before the focusing lens. This is to calibrate the reference photodetector in order to convert the detector signal into a pump fluence (see section 2.3.1).
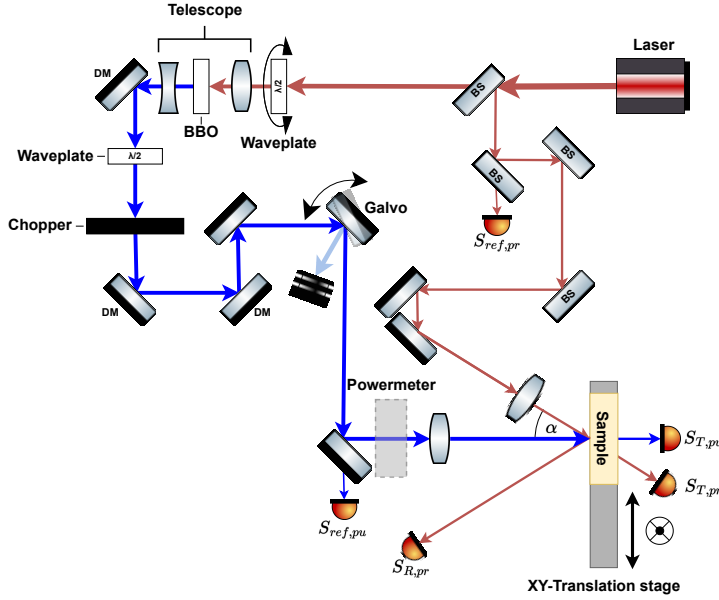

Figure 3.1: Schematic of the experimental setup. The 45 fs, 800 nm laser output is split into a strong pump and a weak probe beam. The pump beam passes through a telescope and a Beta Barium Borate (BBO) crystal to frequency-double it to a 400 nm wavelength. The pump beam is reflected by three consecutive dichroic mirrors (DM) to filter out the fundamental beam. Next, it passes through a $\lambda/2$-plate after which the beam is p-polarized, a chopper to lower the repetition rate to 100 Hz, and a galvo mirror to pulse-pick a single pulse. The pump beam is focused using a $f = 20$ cm lens and the sample is placed a short distance before the focal point. The pump is at normal incidence on the sample and the probe beam is at an angle α of $\approx 10°$ with respect to the normal. The power of the probe beam is attenuated by reflecting the beam off three beamsplitters (BS) before it is focused onto the sample. The pump pulse energy can be varied by rotating the first $\lambda/2$-plate. The location of the power meter used during calibration is indicated.

3.2.3. MEASUREMENTS/EXPERIMENTAL PROCEDURE

Figure 3.2 is a schematic depiction of the experiment. Before each pump shot, 999 probe pulses illuminate a pristine spot on the sample. This is followed by one pump and one additional probe shot after which a thousand more probe shots hit the spot, potentially damaged by the pump. After this, the sample is translated and the measurement is
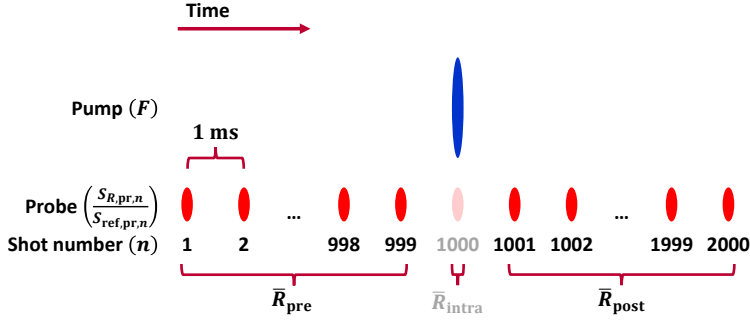
Figure 3.2: Schematic overview of the pulse train that is incident on each individual site on a sample. The first 999 probe shots form the pre-pump reflection $\bar{R}_{\text{pre}}$ and shot 1001 to 2000 the post-pump reflection $\bar{R}_{\text{post}}$ (see equation (3.1)). The first probe pulse that samples the post-pump reflection arrives 1 ms after the pump pulse, when all pump-induced transient effects have disappeared. Note that probe pulse 1000 ($\bar{R}_{\text{intra}}$), which coincides with the pump pulse, is omitted in the analysis.

repeated for a different pump (peak) fluence (F_0). The reflection of, and the transmission through the sample of each probe shot are measured by the photodetectors and used to calculate the pump-induced changes in the reflection as follows:

$$\bar{R}_{\text{pre}} = \frac{\sum_{n=1}^{999} \frac{S_{R,\text{pr},n}}{S_{\text{ref},\text{pr},n}}}{999}, \tag{2.2a/3.1a}$$

$$\bar{R}_{\text{post}} = \frac{\sum_{n=1001}^{2000} \frac{S_{R,\text{pr},n}}{S_{\text{ref},\text{pr},n}}}{1000}, \tag{2.2b/3.1b}$$

$$\Delta R = \frac{\bar{R}_{\text{post}} - \bar{R}_{\text{pre}}}{\bar{R}_{\text{pre}}}, \tag{2.3/3.1c}$$

where n is the probe pulse index and $S_{R,\text{pr},n}$ and $S_{\text{ref},\text{pr},n}$ are the measured reflection and reference signals of the probe (see figure 3.1). Therefore, $\bar{R}_{\text{pre}}$ is the average relative reflection before, and $\bar{R}_{\text{post}}$ after pump illumination. ΔR is defined as the pump-induced *relative reflection change* of the probe. The pump-induced *relative transmission change* of the probe (ΔT) is obtained in a similar fashion.

In a typical experimental cycle, the pump pulses hit the sample in a six-by-six grid where each subsequent pump shot has a slightly higher fluence. To check reproducibility, each such cycle is repeated several times, leading to the formation of multiple grids.

3.2.4. POST-PROCESSING
After each measurement series, the sample is taken out of the laser setup for inspection of the illuminated sites. First, each grid containing 36 illuminated sites, is inspected by differential interference contrast (DIC/Nomarski) and dark-field (DF) microscopy. Subsequently, a Helios Nanolab 600 scanning electron microscopy (SEM) is used to study possible changes in morphology. Selected sites are inspected further with a Bruker Dimension Icon atomic force microscope (AFM). For some sites, electron backscatter

diffraction (EBSD) is used to map the crystal orientation and structure and to obtain grain sizes. EBSD was performed using an EDAX Clarity direct detector. The patterns were collected using EDAX APEX software, 100 pA beam current, 8 kV accelerating voltage and 200 ms pixel integration. The patterns were post-processed using EDAX OIM software. All obtained patterns were indexed using Spherical Indexing with the Al phase (Fm-3m space group) and did not fit to the γ-Al$_2$O$_3$ phase (Fd-3m space group). This is in full agreement with literature data [105, 106], which reports that the Al$_2$O$_3$ film grows in amorphous form. Therefore, the aluminum oxide does not generate any EBSD signal.

If the assumption that the fluence at the observed crater edge is equal to the threshold fluence F_{abl} is correct, a simple analysis can be used to extract that fluence from the data using a so-called Liu-analysis [74]. This analysis is valid for (elliptical) Gaussian beams with a peak fluence F_0. The crater area A and the natural logarithm of the fluence, $\ln(F_0)$, then follow a linear relation. When plotting A versus $\ln(F_0)$ in a so-called Liu-plot, the values a and b of the linear regression line $A = a\ln(F_0) + b$ are obtained. This is used to obtain the desired ablation threshold fluence F_{abl} and the FWHM of the Gaussian beam waist d_x (long axis) and d_y (short axis),

$$F_{abl} = \exp(-\frac{b}{a}), \tag{3.2a}$$

$$d_x = \sqrt{\frac{4\ln(2)a}{\pi c}}, \tag{3.2b}$$

$$d_y = d_x c. \tag{3.2c}$$

The ratio $c = \frac{d_y}{d_x}$ can either be directly obtained from the crater dimensions or taken from the measured beam profile. A more detailed derivation of equations (3.2a) to (3.2c) can be found in section 1.3.2.

3.3. RESULTS AND DISCUSSION

Single layers of gold with thicknesses between 8 to 80 nm and aluminum with thicknesses from 10 to 30 nm on 0.5 mm borosilicate glass were illuminated with a strong pump pulse while being probed by a weak probe beam as described in section 3.2.3. A permanent change in the material occurs for illuminated sites for which the pump-induced relative reflection (ΔR, see equation (3.1)) and transmission changes (ΔT) are nonzero. By comparing these values with Nomarski, dark-field, scanning electron (SEM) and atomic force microscopy (AFM) images of these sites, an in depth, thickness-dependent analysis of the damage mechanisms for thin gold and aluminum layers is obtained. As an example, figure 3.3 shows the differential interference contrast (DIC/Nomarski) (a), dark-field (DF) (b), scanning electron microscopy (SEM) (c, f) and the height (d) and phase (e) atomic force microscopy (AFM) profile images of the same six-by-six grid. This grid is formed by 36 single pump pulses of increasing fluence on a 20 nm thick Au layer. For fluences higher than the ablation threshold (F_{abl}), the crater edge is clearly visible as the dark ellipses in the DIC microscopy images. Because of the steepness of the ablation edges, these edges appear with a very high contrast in the dark-field images. Therefore, the dark-field images are well suited to obtain crater sizes. These sizes are obtained by using Canny edge

detection [107] and the Halir and Flusser ellipse fitting algorithm [108] on the dark-field images. Subsequently, the crater sizes are used to obtain the thresholds (F_{abl}) and spot sizes by Liu-analysis [74].

For aluminum, a few sites are inspected by electron backscatter diffraction (EBSD). This is used to map the crystal orientation and to study grain sizes, the results of which are presented in section 3.3.4.
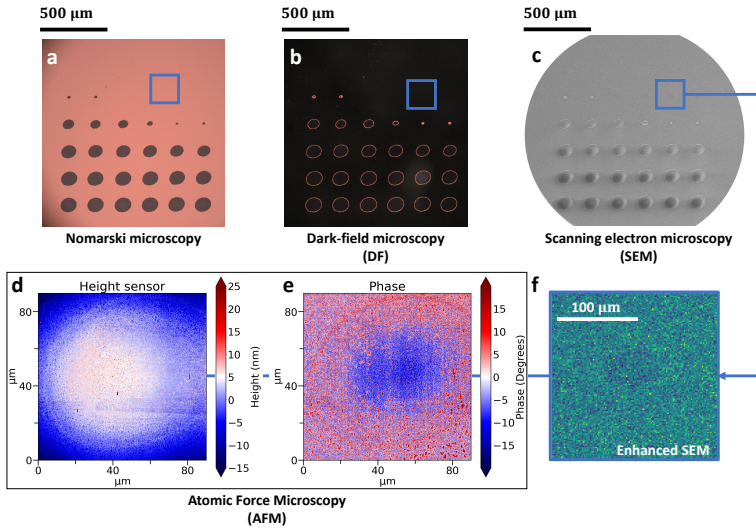

Figure 3.3: differential interference contrast (DIC/Nomarski) (a), dark-field (DF) (b), and scanning electron microscopy (SEM) (c) images of the same illuminated six-by-six grid on a 20 nm Au layer on borosilicate glass. The atomic force microscopy (AFM) scan (d and e) and numerically enhanced SEM (f) are taken of the same pre-ablation site (regime II, $\Delta R > 0$) marked with the blue square in a-c. Since tapping-mode is selected, both the height (d) as well as the phase (e) profile is obtained.

3.3.1. GOLD

Although gold (Au) is not commonly used in the semiconductor manufacturing industry, its optical and thermal mechanical properties are well-studied and known [83, 109–112]. In addition, it does not react with the ambient atmosphere, making it a logical choice as a material for the first experiments. Figure 3.4 shows the change in the probe reflection (equation (3.1)) as a function of pump fluence for 20 nm of Au on a 0.5 nm thick borosilicate glass substrate.

Figure 3.4 shows that $\Delta R(F_0)$ can be divided into three fluence regimes:

I **Low fluence regime**: Here the reflection is not affected by the pump ($\Delta R \approx 0$)

II **Medium fluence regime**: There is a slight (positive) ΔR of a few percent only, induced by the pump ($\Delta R > 0$)

III **High fluence regime**: ΔR becomes negative due to a steep ΔR decrease ($\Delta R < 0$ and $\partial \Delta R / \partial F << 0$)
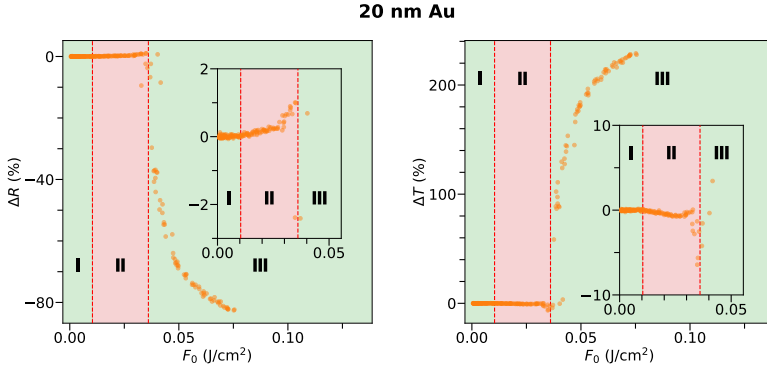
20 nm Au

Figure 3.4: Relative probe reflection ΔR (left) and transmission ΔT (right) change versus peak pump-fluence F_0 for 20 nm gold on a 0.5 mm borosilicate glass substrate. I, II and III mark the low ($\Delta R = 0$), medium ($\Delta R > 0$) and high fluence ($\Delta R < 0$) regimes respectively. The red lines mark corresponding thresholds between those regions.

Note that the same holds for ΔT but with opposite sign and therefore, in what follows, we will focus on ΔR only.

In regime I, the pump fluence is too low to permanently affect the illuminated site. Inspection of those sites with AFM and SEM showed no morphological or any other light-induced changes, as schematically indicated in figure 3.5a. For high fluences (regime III), ablation is seen in the form of removal of material from the substrate, leaving a crater. Because of this, the reflection of the probe will drop and the transmission will increase with respect to the initial state. The bigger the crater, the lower the reflection, as schematically shown in figure 3.5c and d. However, the way the pump influences the illuminated sites in regime II is less straightforward. SEM images show an elliptical region with a slightly darker shade at the regime II-illuminated sites. However, this shading is only visible when numerically enhancing the contrast of a grid image as is shown in figure 3.3f.

(a) $\Delta R = 0$ (b) $\Delta R > 0$ (c) $\Delta R < 0$ (d) $\Delta R < 0$
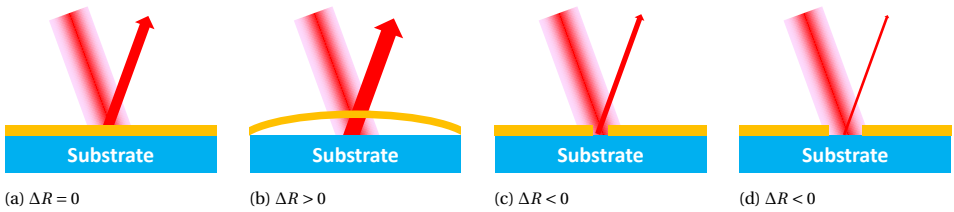
Figure 3.5: Four examples of possible pump-induced changes in the thin Au film. The thickness of the arrow indicates the strength of the probe reflection. $\Delta R = 0$ for low pump fluences (a), while for intermediate fluences, $\Delta R > 0$ (regime II), which can be caused by void formation due to delamination (b). For high fluences, the ablation regime is reached (regime III). For increasing crater sizes, the reflection will decrease until the entire probe spot fits inside the crater (c-d).

To study the effect of the thickness of the gold layer, six samples with different thicknesses were fabricated in one run. Each time when (a multiple of) 8 nm was deposited, a shutter repositioned by which a new part of the substrate array was exposed. Therefore,

all six samples were made under comparable vacuum conditions, evaporation pressures and deposition rates. Figure 3.6a shows the relative probe reflection change ΔR versus the pump fluence for these six samples with thicknesses ranging from 8 to 80 nm. The insets show the individual data with a zoomed-in vertical axis. The vertical dashed lines are the inferred ablation thresholds F_{abl} and the gray areas mark the corresponding uncertainty obtained from the Liu-analysis. The layers with thicknesses from 16 to 40 nm display a positive ΔR increase for fluences lower than the ablation threshold. For the 8 nm thickness there is a negative ΔR. However, this thickness is close to the percolation threshold and the layer is therefore not continuous. The 80 nm thick film does not display a ΔR change in the pre-ablation regime. Figure 3.6b is the corresponding Liu-plot in which the lines are the obtained Liu-fits (see section 3.2.4). From these linear regression lines, the ablation threshold fluence F_{abl} and the FWHM of the beam profile d are obtained and are given in table 3.2.
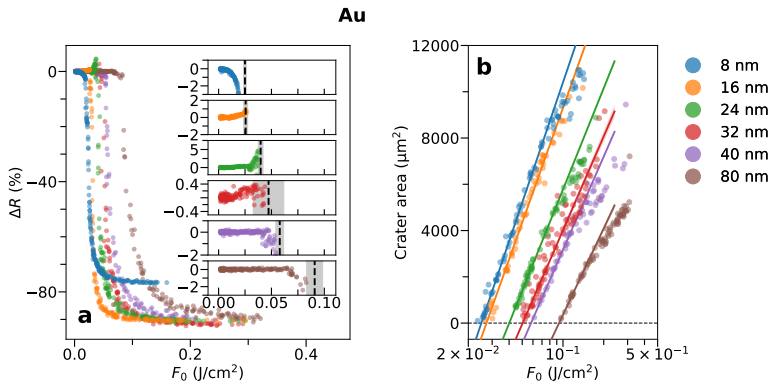

Figure 3.6: (a) ΔR versus peak fluence F_0 for gold layers on borosilicate glass with thicknesses of 8, 16, 24, 36, 40 and 80 nm respectively. The insets show the individual data zoomed in on the vertical axis. The vertical dashed lines are the ablation thresholds and the gray area the corresponding error obtained by Liu-analysis. (b) is the Liu-plot of these gold films. In the Liu-plot, the crater area is plotted versus the natural logarithm of the pump peak-fluence. The lines are the corresponding linear fits for each sample. The intersection of those lines with the horizontal axis is the ablation fluence F_{abl} and the slope gives the pump spot size (see section 3.2.3). The slope is slightly different for the different layers which indicates that the spot size on the sample is different. This is mainly due to repositioning of new samples into the setup giving rise to small variations in sample distance with respect to the focal point.

In fluence regime II, before the ablation thresholds, all Au sample thicknesses, except for 8 and 80 nm, display a (small) positive ΔR, and at the ablation threshold, there is a steep ΔR decrease. As already mentioned, SEM images of regime II-illuminated sites appear to be slightly darker than unilluminated sites, but the contrast is low, see figure 3.3c. Comparing the grain structure with that of a pristine site shows no discernible difference. However, a large-area AFM scan, such as shown in figure 3.3d, indicates that the gold layer is slightly elevated in the center. The adhesion of gold to glass is known to be weak and SEM images of ablated sites (example shown in figure 3.7) clearly illustrate that delamination has occurred at high fluences. One hypothesis for the small positive ΔR in fluence regime II is that before the film ruptures, which occurs at high fluences in regime III, a void is formed between the Au layer and the glass as schematically depicted

Table 3.2: Ablation threshold fluences and inferred laser illumination diameters, including fitting uncertainties for gold, obtained by Liu-analysis.

Thickness (nm)	F_{abl} (mJ/cm^2)	d (μm)
8	25.0 ± 0.20	81.3 ± 0.3
16	27.2 ± 0.7	79.4 ± 0.6
24	40.1 ± 0.7	74.7 ± 0.4
32	50 ± 3	72 ± 1.3
40	58 ± 1.7	71.7 ± 0.6
80	94 ± 5.4	69 ± 1.1

in figure 3.5b. The phase profile of the AFM scan in figure 3.3e shows a faint elliptical outline (reddish curve in figure 3.3e). The phase signal is not only sensitive to the height changes and adhesion strength between the tip and the layer, it is also sensitive to the viscoelasticity of the layer. Therefore, the faint elliptical outline might indicate a local change in (bending) stiffness of the layer, and thus can be an indication of the edge of the buried void. However, it is challenging to draw direct conclusions from discrepancies in AFM phase images, as subtle as shown here. Nevertheless, the local fluence at the outline of the ellipse is calculated using the dimensions from the AFM scan and known spot size. This local fluence is ≈ 12 mJ/cm^2 which equals the threshold value between the $\Delta R = 0$, and $\Delta R > 0$ regime as shown in (the inset of) figure 3.4. Therefore, the area within the ellipse corresponds both to an increase in height, and it marks the $\Delta R > 0$ area.

The combination of the gold layer, void and the substrate forms an etalon for the probe beam, which changes the reflectivity of the stack. Because the penetration dept of gold is ≈ 16 nm at a wavelength of 800 nm [100], this etalon effect will not be seen by the probe in thicker layers. This would also explain why there is no significant ΔR increase for the 80 nm thick layer. If the ΔR increase is not due to the etalon effect but to a (morphological) change throughout the entire layer or at the void-gold interface, this effect would also be apparent at the 80 nm thick layer. The 8 nm thick layer has a thickness around the percolation threshold of gold [113], making this layer structurally and optically significantly different from the others.

3.3.2. ALUMINUM

Unlike gold, aluminum (Al) is commonly used in the semiconductor manufacturing industry [114]. Because of its strong adhesion to glass and the presence of an oxide layer that forms rapidly, aluminum layers are expected to behave differently from gold layers. Figure 3.8a shows the measured pump-induced relative reflection change ΔR versus the pump peak-fluence F_0 for a 20 nm thick aluminum layer on 0.5 mm borosilicate glass. The data points marked in green, red and purple correspond to the optical dark-field images in figures 3.8b to 3.8d. At a pump fluence where ΔR begins to increase slightly (green data point, regime II), figure 3.8b shows that bright spots, locations of increased scattering, start to appear in a location that corresponds to the center of the pump pulse.
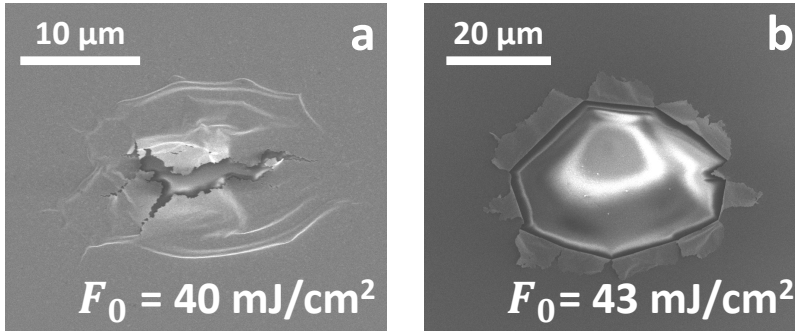
Figure 3.7: SEM images of two ablation sites of a 20 nm gold layer on 0.5 mm borosilicate glass for two different fluences. For a fluence just above the ablation threshold (a), folds start to appear around the ripped center. At a higher fluence (b) flaps have formed at the crater sides while there is no indication of melting.

For increasing fluences, the area covered with these spots increases and a ring with a somewhat higher density of spots develops as shown by figure 3.8c. Figure 3.8d shows that the spots are also visible in the ablation regime, outside of the ablated area, were the ablation area is defined by the small, brighter ring in the center. In appendix F.2, a dark-field image containing a single six-by-six grid is presented containing 36 illuminated areas at different pump fluences, as well as a dark-field image of a pristine site. This image can be used to gain a better insight into the spallation-onset fluence and the pristine material conditions.

In figures 3.9a to 3.9c, we show a dark-field, SEM and an AFM image of the same area presented in figure 3.8b where bright spots are formed. As can be seen, the bright spots appear as dark spots in the SEM images. The corresponding AFM image shows a height difference at those spots. By further zooming in on these groups of grains, as shown by the SEM image in figure 3.9d, it appears that these spots have an irregular shape and appear to follow grain boundaries. Since the oxide is expected to be amorphous [106], these grain boundary lines might originate from the pristine aluminum layer the oxide grew on. The shape of the spots marked by A and B in figure 3.9d correspond to a slight depression and elevation respectively in the AFM heightmap shown in figure 3.9e. This AFM image shows that spot A corresponds to an area that is ≈ 4 nm lower than the area surrounding the spot. This suggests that a group of grains has been removed from the layer. At spot B, a group of grains seems to have been partially vertically displaced, sticking out of the pristine surface. Both A and B type spots are present in the 14 to 30 nm thick aluminum layers that have been studied. However, for layers of 22 nm and more, the groups of missing grains dominate. For layers having a thickness of 20 nm and lower, the group of grains that are sticking out from the surface dominate. An example of this is shown in figure 3.10a and c where we plot the height profiles obtained by tapping mode AFM. figure 3.10a shows two grains that stick out of the surface of an 18 nm thick aluminum layer, whereas figure 3.10c shows multiple grains that are missing from a 22 nm thick aluminum layer. Figure 3.10b and d are the corresponding phase images. These phase maps display a significant negative phase jump at the spallated sites. This means that, at the spallated sites, the AFM tip bounces back with a slight delay indicating that the
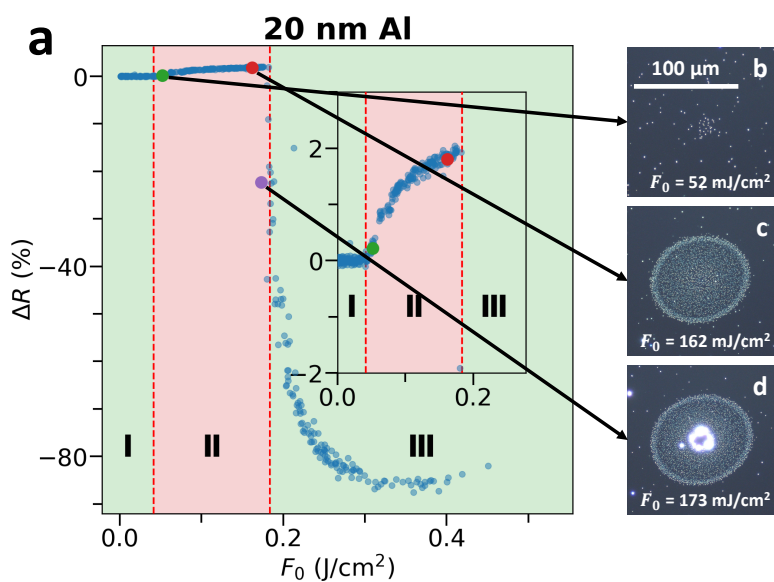
Figure 3.8: Relative reflection change ΔR versus peak fluence F_0 of 20 nm aluminum on borosilicate glass. I, II and III mark the low ($\Delta R = 0$), medium ($\Delta R > 0$) and high fluence ($\Delta R < 0$) regimes respectively. The red dashed lines mark corresponding boundaries between those regions. The inset shows a zoom-in to the regime II of the main graph. The dark-field microscopy pictures correspond to the following three data points: Just beyond the spallation threshold (green, b), just below ablation (red, c) and just beyond the ablation threshold (purple, d).

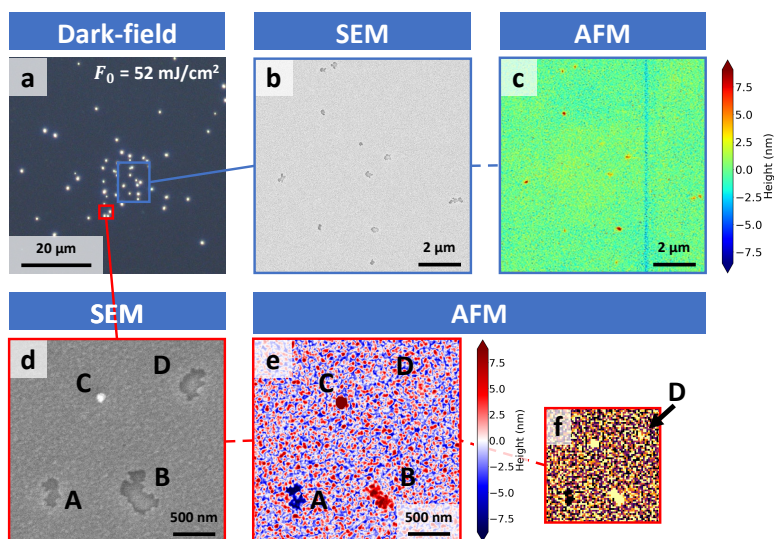Figure 3.9: Optical dark-field image (a) of a regime II ($\Delta R > 0$) illuminated spallated site of a 20 nm aluminum layer on borosilicate glass. (b) SEM and (c) AFM image of the area marked by the blue rectangle in the dark-field image. (d) and (e) SEM and AFM scans of the area marked by the red rectangle in figure (a). Lowering the resolution and enhancing the contrast of figure (e) resulted in figure (f). The group of grains marked by A and B look similar in the SEM image. However the AFM scan shows that the group of grains marked by A is missing from the surface, while the grains marked by B are sticking out of the surface. Note that the contrast of SEM image (b) is enhanced to show the group of grains more clearly. The original picture is darker, indicating decent conduction. Note that D also marks a vertically displaced group of grains. However, it is somewhat difficult to see this by eye from the AFM scan in figure (e), but it shows up more clearly in (f) where the same data is shown but with enhanced contrast and lower resolution. Because the area marked by C is not present in the dark-field picture (a), it is probably a dust particle that has settled on the surface after acquiring dark-field pictures and before performing the SEM and AFM scan.

viscoelasticity of the layer is different or interaction of the forces between the tip and the layer has changed [115]. Nevertheless, the contrast of this phase jump where groups of grains are sticking out from the surface is lower than where they are missing. This can be caused by the fact that at the missing grains site, the native oxide layer has been removed and a new slightly different oxide layer is formed on the affected aluminum. At positions where the groups of grains are elevated, the original native oxide is still present.
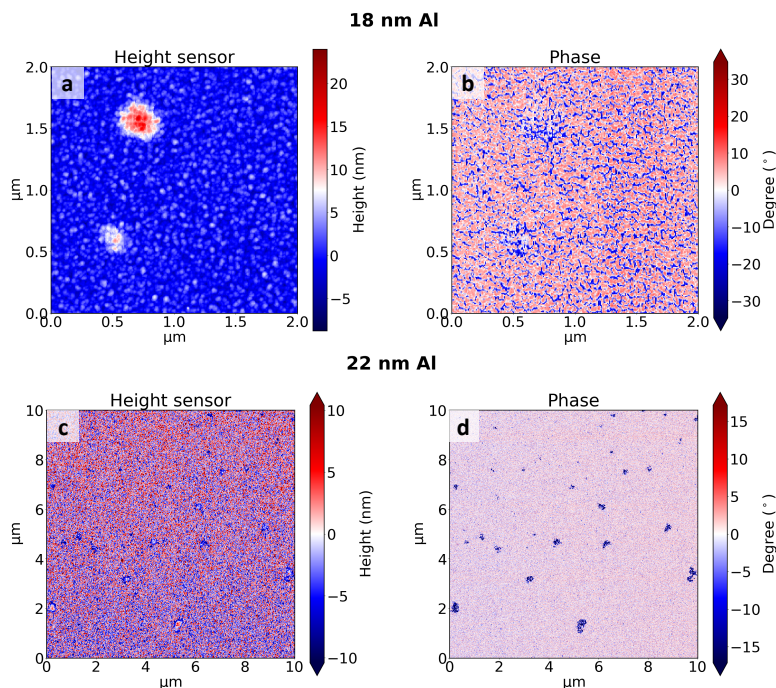

Figure 3.10: AFM tapping mode height and phase profiles after illumination with a 400 nm pump pulse in the pre-ablation fluence regime. A detail of the height (a) and phase (b) profiles of a 18 nm thick aluminum layer on glass. (c) and (d) are the height and phase profile of a detail of an AFM scan of a 22 nm thick layer of aluminum. For the 18 nm thick layer, (a) shows two groups of grains sticking out of the surface. They are both weakly visible in the phase image (b). For the 22 nm thick layer, (c) displays multiple groups of missing grains which are clearly visible in the phase image (d). The missing grains, as well as the groups of grains that are sticking out of the surface, are also visible in the phase image by a slight phase drop.

Each spot in a dark-field image resembles a group of missing grains, or a group of grains sticking out of the surface. We hypothesize that the group of grains sticking out of the surface is representative of an intermediate stage, before the complete removal of the grains. From here on, we will refer to both processes as *spallation*.

Figures 3.11a and 3.11b show a dark-field image and a zoomed-in version of a site illuminated by a high-end regime II-fluence. For these fluences, the spallation area, covered by the ellipse, has a brighter ring at the edge with a finite width of around 5 μm. Here the spots still have similar irregular shapes such as those shown in figure 3.9d. However, the corresponding SEM image of figure 3.11c shows that there are more and

slightly larger spots present at this ring than closer to the center. From additional SEM and AFM data we conclude that these spots near the edge are more likely to correspond to a group of missing grains than to a group of grains sticking out of the surface compared to the spots found closer to the center of illumination.
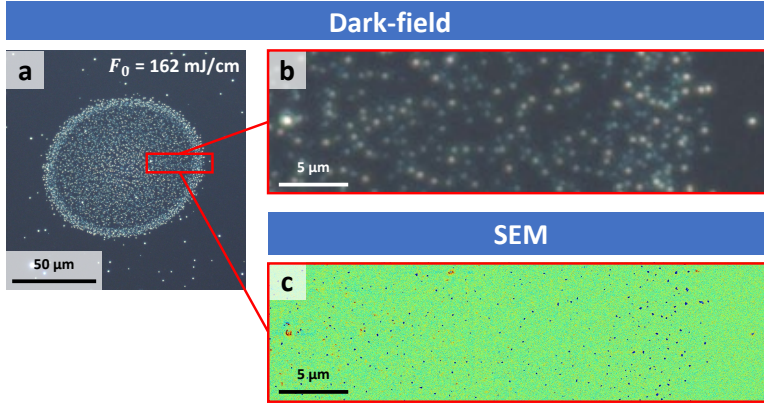

Figure 3.11: (a) optical dark-field image of a regime II illuminated ($\Delta R > 0$) spalled site of a 20 nm aluminum layer on borosilicate glass. The fluence used is in the high range of regime II. Near the edge of the elliptical dotted area, a bright rim appears. (b) shows a numerically zoomed-in view of the data in the red rectangle in figure (a), and (c) is the corresponding SEM image.

The spallation spots first start to appear exactly when fluence regime II is reached for the 20 nm layer, as shown in figure 3.8. To investigate this further, six aluminum layers with thicknesses ranging from 10 to 30 nm were fabricated. The same pump-fluence-dependent single-shot measurements are performed to investigate the thickness-dependence of the spallation behavior. Figure 3.12a shows the measured ΔR versus the pump fluence for those layers. The spallation area A versus $\ln(F_0)$ is shown in the Liu-plot in figure 3.12b, where the linear regression lines are the corresponding fits from which the spallation thresholds are determined (see section 3.2.4). From these linear regression lines, the spallation threshold, and from the crater areas the ablation threshold fluences F_{spal} and F_{abl}, and the FWHM of the beam profile d are obtained and given in table 3.3. Except for the 10 nm layer, all Al layers display a positive ΔR regime. The spallation thresholds F_{spal} extracted from the Liu-plot are shown as solid vertical lines in figure 3.12a. In this figure it is clear that the spallation thresholds strongly correlate with the onset of the $\Delta R > 0$ fluence regime. This same procedure is followed to determine the ablation thresholds F_{abl} which are shown as vertical dashed lines. The $\Delta R > 0$ fluence regime is bounded by F_{spal} and F_{abl}. However, in contrast to other thicknesses, the 10 nm layer does not display a positive ΔR regime. No spallation of groups of grains is observed for this layer, and for higher fluences there is no clear crater edge. SEM images of the illuminated sites show charging and optical microscopy images show an increase in transmission, all indicative of enhanced oxidation.
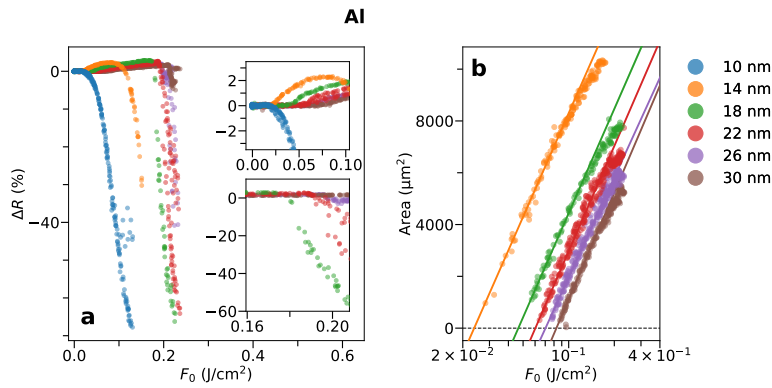
Figure 3.12: (a) ΔR versus pump peak-fluence F_0 for 10, 14, 18, 22, 26 and 30 nm aluminum on borosilicate glass. In (a), the vertical dashed lines mark the ablation fluence F_{abl} extracted from a Liu-plot of the crater area versus fluence (not shown here). The solid lines represent the spallation fluence F_{spal} obtained from (b), which shows the Liu-plot of the spallation area as a function of fluence. The values of F_{spal} are obtained from the linear regression lines shown in (b). Note that the 10 nm Al layer is omitted in (b) because this layer displayed no clear spallation and ablation edges.

Table 3.3: Spallation and ablation threshold fluences and inferred laser illumination spot diameters for aluminum layers, obtained by Liu-analysis.

Thickness (nm)	F_{spal} (mJ/cm^2)	F_{abl} (mJ/cm^2)	d (μm)
14	24 ± 1.3		71.4 ± 0.3
18	47 ± 3		71.6 ± 0.4
20	50 ± 3	177 ± 4	69.9 ± 0.4
22	60 ± 2.4	189 ± 0.2	71.9 ± 0.3
26	70 ± 1.6	194 ± 1.7	70.0 ± 0.2
30	83 ± 3	205 ± 5	72.5 ± 0.3

To examine the role of the substrate on the occurrence of spallation, 20 nm-thick aluminum layers were deposited on four different substrates simultaneously: borosilicate glass, sapphire, calcium fluoride (CaF_2) and silicon, having thicknesses of 0.5, 1.1, 0.5 and 0.5 nm respectively. Sapphire is chosen because its thermal conductivity is over 40 times higher than that of borosilicate glass. Additionally, sapphire has a melting and evaporation temperature of 2300 K and 3252 K respectively, compared to the much lower value of 950 K and ≈2500 K for borosilicate glass [77, 116, 117]. Note that the evaporation temperatures are not reached in our experiments. CaF_2 is the only substrate with no oxygen in it, thus a possible effect of an aluminum reaction with the oxygen atoms in the substrates is excluded. Silicon is used because it is the benchmark substrate in the semiconductor industry. Here we use (100) p-doped silicon with a 1.7 nm native oxide as obtained by ellipsometry. Figure 3.13 shows the relative reflection change versus the pump fluence of these four samples. The difference in F_{spal} between the borosilicate glass, sapphire and CaF_2 substrates is remarkably small, indicating that the substrate plays a fairly minor role in the spallation process. Note that these three substrates are non-absorbing, transparent materials whereas silicon is not. Due to the differences in optical parameters between the substrates, the absorption of the pump-light in the 20 nm thick aluminum layer is different. Using the transfer-matrix method [40, 99], the calculated total absorbed fraction of pump-light is much lower for the Al layer on silicon (9%) compared to the other substrates (15-17%). It is very likely that this difference in absorption causes the increased F_{spal} threshold of the aluminum on the silicon substrate. For all substrates used, a $\Delta R > 0$ pre-ablation fluence regime is observed. All except the sapphire substrate, display groups of spallated grains in this regime (not shown here).

3.3.3. CALCULATIONS

As demonstrated in previous sections 3.3.1 and 3.3.2, when thin layers of gold or aluminum are illuminated by pump fluences below the ablation threshold, irreversible optical changes occur ($\Delta R > 0$). In this fluence regime, different material and/or morphological changes such as delamination, melting, and enhanced oxidation coincide with optical changes. Morphological changes can also influence the reflectivity, and therefore ΔR directly. We performed some calculations to investigate whether these changes are directly causing this reflectivity change.

It is known that the adhesion of gold to glass is weak if no adhesion layer such as Chromium (Cr) or titanium (Ti) is used [118]. This is confirmed by the formation of wrinkles near the ablation edges for pump fluences in the ablation regime. It is therefore plausible that some delamination, which precedes ripping and wrinkling, already occurs in the pre-ablation regime. When the gold layer detaches from the substrate, a void layer is formed in between the glass substrate and the gold layer as schematically shown in figure 3.5b. We use the transfer-matrix method (TMM)[40, 99] to directly calculate the reflectivity of the gold sample. Here, the used refractive index and extinction coefficient values n and k of Au are obtained from ellipsometry measurements (Ellipsometer VB-400 J.A. Woollam) and the CompleteEase analysis software [79]. To investigate whether the void will directly cause an reflection increase ($\Delta R > 0$), as we measured, we compare the calculated reflectivity of gold on glass including a void, with gold on glass without a
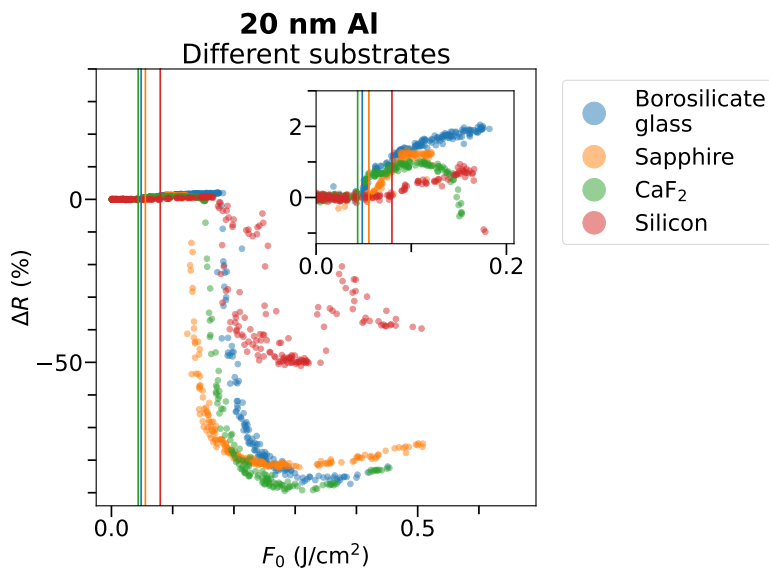
Figure 3.13: Relative reflection change ΔR versus peak fluence F_0 of 20 nm aluminum on 0.5 mm thick borosilicate glass, 1.1 mm thick sapphire, 0.5 mm thick CaF_2 and 0.5 mm thick silicon substrates. The start of the steep decrease marks the ablation thresholds. Below the ablation threshold, all samples display a $\Delta R > 0$ fluence regime. The solid vertical lines indicate the beginning of this fluence regime F_{spal}. Ablation starts to occur from where ΔR decreases rapidly.

void. Figure 3.14 shows the ΔR versus void thickness, obtained from these calculations, for 8 to 80 nm thick gold layers on borosilicate glass. For all thicknesses, ΔR increases for an increasing void thickness. The enhanced reflection is the result of increased constructive interference in the reflected direction caused by the void. The calculations clearly indicate that small void thicknesses of ≈ 10 nm are already enough to explain the increased reflectivity of a few percent, as observed in the experiments. Note that the effect is smaller for thicker layers which is in reasonable agreement with our measurements. For thicker layers, significantly less light will be transmitted by the Au and therefore the interference effect is strongly reduced.

For aluminum, the above explanation seems to be unlikely as no delamination was observed for aluminum on glass. This is consistent with the fact that the adhesion of aluminum to glass is known to be strong [119, 120]. In addition, we have looked into enhanced oxidation as a possible explanation for the pre-ablation ΔR increase. Transfer-matrix method calculations are performed to obtain ΔR when the upper part of the Al layer actually consists of Al_2O_3. When assuming a pristine layer with a native oxide thickness of 4 nm, these calculations show that the reflectivity would in fact decrease when there would be additional pump-induced oxidation. However, this is opposite to what we observe. This is not only the case for oxide growing between air and aluminum but also for oxide between the aluminum and substrate. Therefore, enhanced oxidation cannot explain the ΔR increase directly. Enhanced scattering from the spallation sites,
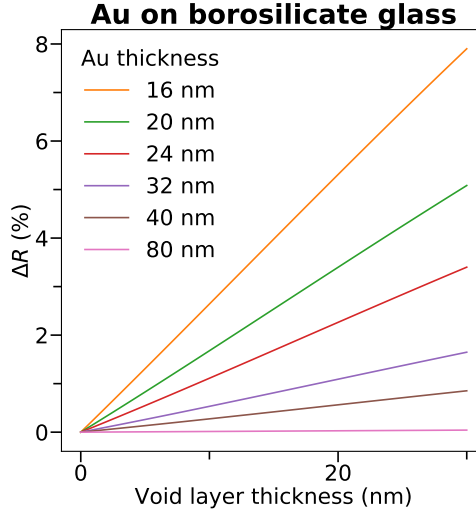
Figure 3.14: Calculated relative reflection change ΔR versus the thickness of the void formed between the borosilicate glass substrate and gold, using the transfer-matrix method (TMM). ΔR is obtained for a probe beam with a 10° angle of incidence and p-polarization. The central wavelength is 800 nm with a FWHM of 50 nm. The refractive index and extinction coefficient n and k used are obtained from ellipsometry measurements (Ellipsometer VB-400 J.A. Woollam) and the CompleteEase analysis software [79]. The 8 nm thickness calculation is omitted in this figure since this thickness is around the percolation threshold and can therefore not be considered as a fully closed layer.

which are clearly visible in the dark-field microscopy images, can also not be responsible for $\Delta R > 0$. Both the raised grains in the 14 to 20 nm thick layers as well as the group of spallated grains in the 22 to 30 nm aluminum layers will not increase the reflectivity directly. In fact, they are more likely to lower the specular reflection due to increased scattering.

Liu-analysis shows that the spallation area scales linearly with $\ln(F_0)$, which means that the spallation area is bordered by the threshold fluence F_{spal}. This strongly suggests that spallation is a thermally driven process. Because of this, we calculate the temperature reached in the aluminum film to further look for a possible explanation for the increased reflectivity upon laser radiation. Comparing this reached temperature with the melting temperature T_m will give insight into the spallation process. The peak temperature will already be reached in the first few picoseconds. Therefore we only calculate the temperature during the first 5 ps.

We use the two-temperature model (TTM, see section 1.1.2) [43–45] to calculate the melting threshold of a 20 nm aluminum film on a borosilicate glass substrate:

$$\begin{cases} C_e(T_e)\frac{\partial T_e}{\partial t} = \frac{\partial}{\partial z}(\kappa_e(T_e, T_i)\frac{\partial T_e}{\partial z}) - G(T_e)(T_e - T_l) + S, \\ C_l(T_l)\frac{\partial T_l}{\partial t} = G(T_e)(T_e - T_l). \end{cases} \tag{3.3}$$

Here $T_e = T_e(z, t)$ and $T_l = T_l(z, t)$ are the unknown temperatures of the electrons and lattice respectively, as a function of depth and time. For the electronic system

parametrization, we use the electron heat capacity $C_e(T_e)$ and electron-phonon coupling $G(T_e)$ from [57]. The electron thermal conductivity $\kappa_e(T_e, T_l)$ equals $\kappa_0 \frac{T_e}{T_l}$ with $\kappa_0 = 246\,\text{W}/(\text{m K})$ as taken from [103], and for the lattice we use $C_l = 2.42\,\text{J}/(\text{m}^3\,\text{K})$. We neglect the lattice thermal conductivity since this is much smaller than the electronic one κ_e [103].

We use the transfer-matrix method to calculate the depth-dependent absorption profile, $A(z)$, of the laser pump energy[121]. The thickness of the film is comparable to the optical skin depth, therefore the effect of light reflection and transmission at various interfaces must be considered. We calculate the absorption profile considering the full material stack, namely a thin top layer of aluminum oxide (4 nm thickness), aluminum, and a borosilicate glass substrate. We use the absorption profile in aluminum only in the heat source term $S = S(z, t)$ in the TTM equation (3.3) as follows:

$$S(z,t) = \sqrt{\frac{4\ln(2)}{\pi}} \frac{A(z) F_0}{\tau} e^{-4\ln(2)(\frac{t}{\tau})^2}. \tag{3.4}$$

Here F_0 is the incident peak fluence and τ is the pulse duration (expressed in FWHM). We solve the two-temperature model (TTM) equations only for the aluminum layer, therefore, we do not take into account the heat transfer from the aluminum film into the oxide and substrate since it plays a minor role on the considered timescale of the first 5 ps. Therefore, Neumann boundary conditions: no heat flux through both aluminum interfaces (see section 1.1.3), and room temperature initial conditions are applied, whereafter equation (3.3) is solved numerically. We consider only one spatial dimension, namely depth, since the laser spot size ($\approx 70\,\mu\text{m}$ FWHM) is much larger than the 20 nm film thickness. Therefore, we neglect lateral heat diffusion on the timescales considered (see section 1.1.3).

Figure 3.15 shows the results of the TTM calculation for $F_0 = 34\,\text{mJ}/\text{cm}^2$, where the time evolution of the electron and lattice temperatures at the aluminum surface is plotted. The lattice temperature increases as a result of heat transfer from the laser-heated electrons via electron-phonon coupling. The melting threshold is defined as the minimum peak fluence required to overcome the effective melting temperature $T_m^{\text{eff}} = T_m + H_m/C_l$. Here $T_m = 933.47\,\text{K}$ is the equilibrium melting temperature of aluminum, and $H_m = 1.0 \times 10^6\,\text{kJ}/\text{m}^3$ is the enthalpy of melting [102, p. 6-146]. In such a way, we roughly include the enthalpy of melting effect in our melting threshold calculation. As one can see, the chosen fluence corresponds to the melting threshold defined with such a method. The calculated F_{melting} of 32 mJ/cm^2 is below our measured value of the spallation threshold $F_{\text{spal}} = 50 \pm 3\,\text{mJ}/\text{cm}^2$ as shown in table 3.3. This means that according to these calculations, when F_{spal} is reached, the aluminum also reaches the melting temperature.

The calculation of the melting threshold is most sensitive to the choice of the electron-phonon coupling parameter G. Despite significant theoretical efforts to calculate this parameter in the regime of strong laser excitation [55], and recent experiments addressing the topic of electron-phonon coupling measurements [59], there remains a certain ambiguity in the choice of this coupling parameter practically for any material [55]. However, in the case of aluminum, several model predictions largely overlap and are consistent

3
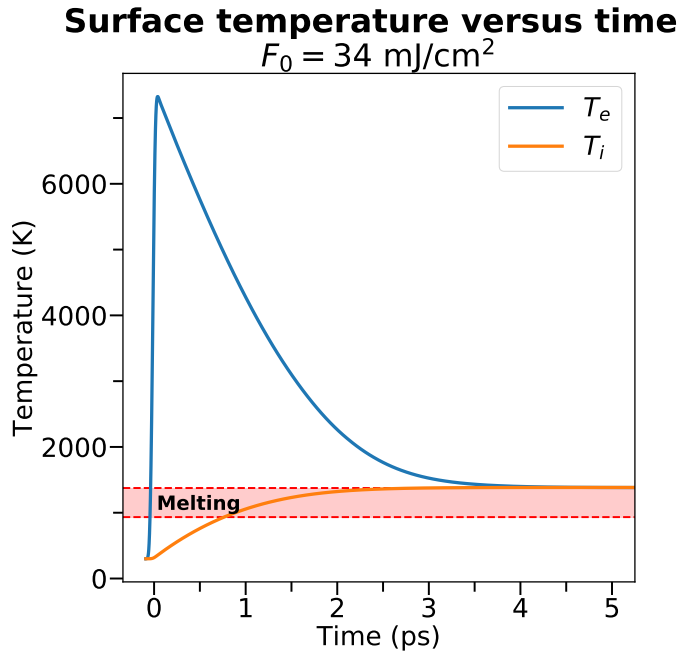
Figure 3.15: Surface temperature evolution of an aluminum film calculated with the TTM at a laser fluence of $F_0 = 34\,\mathrm{mJ/cm^2}$. The 20 nm thick layer consists of a 16 nm thick aluminum film on a borosilicate glass substrate including a 4 nm thick oxide. The lower red dashed line shows the melting temperature T_m and the upper line the effective melting temperature T_m^{eff} of aluminum used to define the melting threshold.

with the experimental results [55], therefore we believe that our choice of the coupling parameter is reliable.

We perform the same calculation to obtain the melting threshold for different aluminum thicknesses F_{melting}. As described before, the absorption profile is calculated with the oxide (4 nm) and substrate included, whereas the TTM calculations are performed for the aluminum layer only. The calculated F_{melting} values, as well as the experimentally obtained F_{spal} are shown as a function of layer thickness in figure 3.16. Note that in this figure, the thickness is that of the aluminum plus its 4 nm oxide. For thicknesses between ≈10 and 50 nm, both the calculated melting, and measured spallation fluences follow a linear increase with thickness, where $F_{\text{spal}}/F_{\text{melting}} \approx 1.5$. The calculated melting threshold saturates at large aluminum thicknesses, corresponding to the bulk behavior. For all measured thicknesses the spallation threshold is higher than the calculated melting threshold. This is in line with [35, 122] where it is reported that melting precedes ablation.
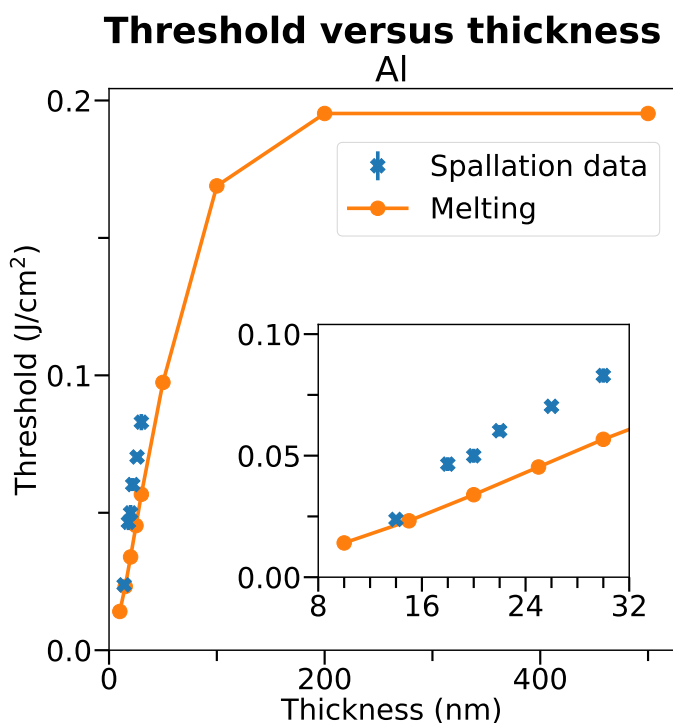
Figure 3.16: Experimentally obtained spallation F_{spal} and calculated melting thresholds F_{melting} versus layer thickness for aluminum on glass. The blue and orange lines are the experimentally obtained F_{spal} and the calculated F_{melting} respectively. The inset zooms in on the data for small layer thicknesses, to show the differences between the calculation and measured data points more clearly. Note that the total thickness is that of the aluminum plus that of the native oxide layer.

3.3.4. ELECTRON BACKSCATTER DIFFRACTION

If the reflectivity change in the $\Delta R > 0$ regime, where spallation occurs, is caused by melting and resolidification of the aluminum, there might be structural change in the aluminum present. The melting temperature of aluminum oxide is 2327 K [102, p. 6-146], which is much higher than that of aluminum (933.47 K). This implies that the aluminum oxide structure is not significantly affected at the temperatures where Al melts, as confirmed by the AFM scans. Except for the spallated groups of grains, AFM scans did not show any surface change, like modified roughness or grain size, except for the spallated groups of grains. To determine whether the Al structure underneath the Al_2O_3 has changed, we use electron backscatter diffraction (EBSD). By comparing this with the pristine material, changes in grain size and crystal orientations can be obtained. Several EBSD maps are obtained from a single ablated site on a sample of 20 nm aluminum on borosilicate glass. Figure 3.17a is a dark-field microscopy image of this site where the red rectangles indicate the positions of the corresponding EBSD maps. These scans are obtained at different distances from the center of the illuminated site. Thereby, each spot samples a different local fluence F_{local} for which $F_{local} < F_{spal}$, figure 3.17b-c, and $F_{local} > F_{spal}$, as shown in d-f. From figure d-f it is visible that the average grain size has increased.

All EBSD maps consists of hexagonal pixels with each having an area A_{pixel} equal to:

$$A_{pixel} = \frac{\sqrt{3}}{2}s^2, \tag{3.5}$$

where s is the equivalent step size in the EBSD map. Multiplying this with the number of pixels N that belong to the same grain results in the total grain area A_{grain}. The grain size is expressed as the diameter D of the circle with an area equal to A_{grain}. Therefore D equals to:

$$D = 2\sqrt{\frac{N \cdot A_{pixel}}{\pi}}. \tag{3.6}$$

For each EBSD map shown in figure 3.17b-f, the grain size distribution is obtained (see appendix F.3). From this, the average and spread in grain size D are obtained using the bootstrapping method. This is plotted versus the local fluence F_{local} as is shown in figure 3.18. Here it is shown that the average grain size starts to increase for local fluences exceeding F_{spal} and keeps increasing for increasing fluences. The growth of the grain size is a clear indication that single-shot melting and resolidification took place. As this fluence regime F_{local} coincides with the $\Delta R > 0$ regime, it seems very likely that the increase in grain size, the microstructural change, is responsible for the slightly enhanced reflection.

To directly compare a $F_{local} > F_{abl}$ and $F_{spal} < F_{local} < F_{abl}$ site, we also performed an EBSD scan over part of the ablation edge, covering both regimes. To compare the positions of the spallated grains, two images are obtained: an EBSD map and a corresponding SEM image as is shown in figure 3.19a and b respectively. EBSD-map (a) shows increased grain sizes outside the crater, due to melting and resolidification, as well as no signal in the ablation crater. The later shows the removal of aluminum since only the aluminum creates an EBSD signal. Although, it is reported that the initially amorphous oxide layer
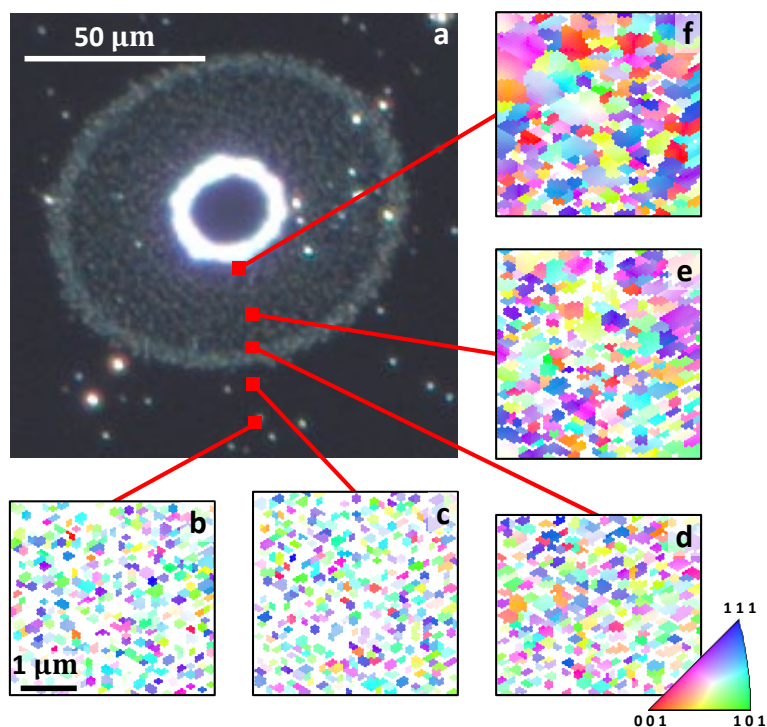
3

Figure 3.17: (a) dark-field microscopy image of an ablated site on a 20 nm aluminum on borosilicate glass sample. The red rectangles indicate the positions of the corresponding electron backscatter diffraction (EBSD) maps (b-f). The different colors show the different crystal orientations, while similar neighboring pixel colors indicate that they belong to the same aluminum grain. The scans are obtained at different distances from the center of the illuminated site. Therefore, each spot samples a different local fluence F_{local} for which $F_{\text{local}} < F_{\text{spal}}$ (b-c), and $F_{\text{local}} > F_{\text{spal}}$ (d-f). From (d-f) it is clearly visible that the average grain size has increased.
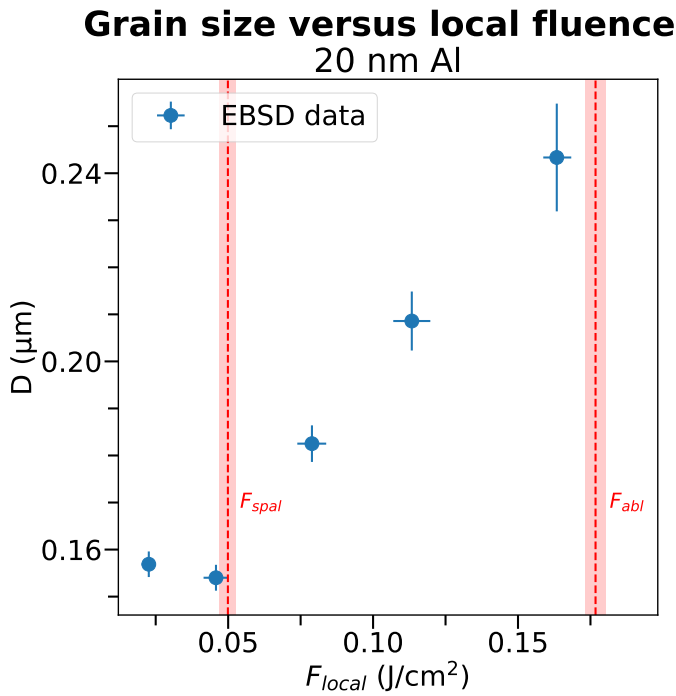
Figure 3.18: The average grain size versus local fluence F_{local} obtained for each EBSD map shown in figure 3.17b-f of a 20 nm thick aluminum illuminated site. The values of the grain sizes are defined by the equivalent circular diameter of the grain area ($D = 2\sqrt{\frac{A_{grain}}{\pi}}$). F_{spal} and F_{abl} are the spallation and ablation threshold fluence respectively.

can transform into crystalline γ-Al_2O_3 [105, 106], in our case, there is an absence of EBSD patterns that correspond to γ-Al_2O_3. This confirms that Al_2O_3 still remained amorphous and that therefore the EBSD signal only originates from the aluminum. At the SEM image (b), both the ablation edge as well as the pushed-up/missing spallated sites are visible. The original grayscale image is converted into a colored one resulting in an enhanced image to increase the visibility of the spallated sites. Figure 3.19c is the original SEM image (before enhancing) with the spallated sites, which are drawn by hand, marked in yellow. When overlaying these marks with the EBSD map (d), it shows that spallation sites often occur at the edges or between the resolidified grains. Since a stress increase is necessary to remove or push-up a spallated site, this implies that local stress increase is more likely to occur at the resolidified grain boundaries. Interestingly, the shape of these spallation sites mimic grain boundaries of a group of grains. As explained before, these grain boundary lines might originate from the pristine aluminum layer the oxide grew on.
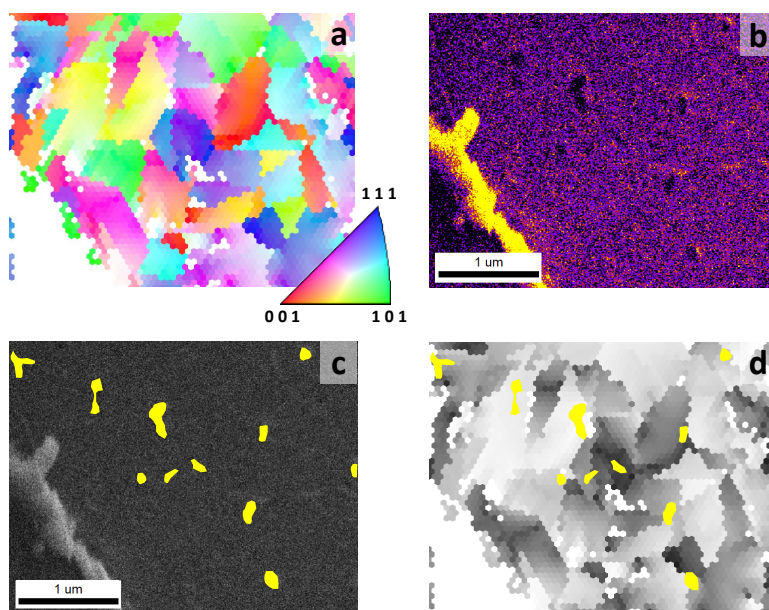

Figure 3.19: (a) EBSD map and (b) corresponding SEM image. (a) shows increased grain sizes outside of the crater, as well as no signal in the ablation crater indicating the removal of Al. In (b), both the ablation edge as well as the pushed-up/missing spallated sites are visible. Here, (b) is the original grayscale image converted into a colored one resulting in an enhanced image to increase the visibility of the spallated sites. (c) is the original SEM image with the spallated sites, which are drawn by hand, marked in yellow. (d) is the EBSD map in grayscale overlayed with the marked spallation grains. This shows that spallation sites are often formed at the edges or between the resolidified grains.

3.4. CONCLUSIONS

We studied optical and morphological changes induced by a single ultrafast laser pulse on 8 to 80 nm thick gold and aluminum films. We have shown that the reflection increases

with a few percent after illuminated with pump-pulse of fluence lower than the ablation threshold. This *pre-ablation* fluence regime coincides with morphological changes. These morphological changes are observed using dark-field microscopy, SEM and AFM.

For gold, the reflection increase is most likely caused by delamination: the gold layer detaches from the substrate whereby a void is formed in between. The optical change is directly induced by the etalon effect caused by the creation of this void. According to transfer-matrix method calculations, the reflectivity of the weak 800 nm probe beam should increase with void thickness, which is in agreement with our measurements. Void layers as thin as ≈10 nm are already enough to cause the measured 0.1-2% positive relative reflection change for 8 to 80 nm thick gold layers.

For aluminum, there are no signs of delamination. However, the area, where the pre-ablation fluence threshold is exceeded, is covered with small subwavelength (50 to 200 nm) groups of grains. These groups of grains are vertically displaced or missing entirely from the surface and their thickness matches the thickness of the native oxide (4 nm). Unlike the void with gold, these *spallation* grains do no directly explain the increase of the measured reflectivity. However, the spallation and increase in reflectivity do coincide. Liu-analysis shows that the area, covered with the spallation sites, scales linearly with $\ln(F_0)$. Since the pump beam has a Gaussian profile, this means that this area is bordered by the threshold fluence F_{spal}, and that the formation of these spallated sites is a thermally driven process. For a total thickness of the aluminum plus its oxide (4 nm) between 10 and 30 nm, the measured F_{spal} ranges between 24 ± 1.3 and 83 ± 3 mJ/cm^2. Furthermore, two-temperature model calculations show that the temperature reached in this pre-ablation fluence regime exceeds the melting temperature of aluminum. For thicknesses between ≈ 10 and 50 nm, both the calculated melting, and measured spallation fluences follow a linear increase with thickness, where $F_{spal}/F_{melting} \approx 1.5$. AFM and SEM cannot directly probe the structural changes caused my melting of the aluminum. This is because the aluminum is buried underneath its native oxide. Since the oxide did not reach its melting temperature, the surface of the oxide is, except for the spallation sites, unaffected. To study the changes in the aluminum underneath the oxide layer, electron backscatter diffraction (EBSD) is used. EBSD shows the effects of recrystallization: the melting and resolidification of the aluminum into bigger grains. The average pristine grain size of 150 nm starts to grow where the local fluence exceeds the spallation threshold F_{spal}. The grain size grows up to 400 nm just before the ablation threshold fluence is reached.

The formation of spallation sites coincides with the increase in reflectivity, $\Delta R > 0$. Still, we found no direct causality since spallation cannot increase the reflectivity directly. In fact, spallation sites are more likely to lower the specular reflection due to increased scattering while no change in surface roughness was found. The melting and resolidification of the aluminum into bigger grains, as is measured by EBSD, coincides with the $\Delta R > 0$ fluence regime as well. Interestingly, it is known that different structures can lead to different optical parameters [123]. Increasing the grain size leads to a bigger mean free path of the electrons which will decrease the resistivity of our aluminum layer. Previous research has shown that a resistivity decrease increases reflectivity [124] and in [125] it follows from classical reflection theory. It is therefore possible that this microstructural change in grain size directly causes the small reflection increase observed in the measurements. The spallation sites, which consist of the native oxide, are mostly formed at the

edges or in between resolidified aluminum grains. Since a stress increase is necessary to remove or push-up part of the native oxide (spallation), this implies that local stress increase is more likely to occur at the newly formed grain boundaries.

In summary, optical and morphological changes induced by single pump pulses already occur in the pre-ablation fluence regime. The in situ probing of the optical changes presented in this chapter is a quick and easy way to detect very subtle changes in thin films, making this technique suitable to use as an early warning signal for catastrophic damage. Monitoring this signal can be of use in the semiconductor manufacturing industry, since these thin films are exposed to increasingly high optical powers used in metrology, which heightens the risk of optical damage.

Background for the General Reader

"Je gaat het pas zien als je het door hebt."

"You'll only see it when you understand it."

Johan Cruijff

By exposing both gold and aluminum films to single laser pulses, we could determine when they fail. Here, *failure* is a bit ambiguous, because both materials have different modes of failure, or **damage mechanisms**. At the highest laser brightnesses, material is blasted away. However, for somewhat lower intensities, the material will still remain on its glass substrate, but *some change* in the properties of the material has been measured. It was somewhat hard to find what the root cause of this change actually was.

So if there is any observable change, can that be considered damage?

It may all depend on what you will be doing with the material. However, in the context of nanolithography, this slight change may be already crucial. If not, we can measure this change and use it as a warning signal for potential damage at higher light intensities.

Background for the General Reader

"Since light travels faster than sound, people may appear bright until you hear them speak."

Philomena Cunk/Diane Morgan in *Cunk on Earth*

When you shine light onto something transparent, you can see that the light can travel though it. However, when doing this to an opaque material, where does the light actually go? Is it still in the material, or has it changed into something else? The answer lies in the latter, because opacity means that the light will be **absorbed** by the material. The same happens in your skin when you are sunning on the beach, when this absorption of light results in the heating of your skin.

So when will this light actually induce damage? And when this heat will cause a thin layer to melt, is that damage? What if it melts due to the bright laser pulse and resolidifies in the same fashion? Or did something occur that **permanently changed** the material? Luckily, there are some tricks to employ that enable us to look really carefully into the material to check for any measurable change.

However, determining when something has melted is often not that simple. We illuminate the material **ultrafast**, so with a really short laser pulse. The heat that is generated in the metallic layer behaves therefore differently. It can, for instance, induce a strong sound wave, that echoes back and forth inside the layer. In some cases, it can give the top part of the layer a kick and will be separated from the bottom half; and other phenomena can cause the formation of **nanovolcanoes**.

How will some of these light-induced damage phenomena or morphological changes look like in thin ruthenium films?

4

RUTHENIUM

In semiconductor device manufacturing, wafer materials may be exposed to intense light sources by optical metrology tools. The desired light fluence often needs to be maximized to levels just below the optical damage threshold of materials deposited on the wafer, such as ruthenium. We, therefore, investigate light-induced permanent structural changes to thin Ru films after exposure to single 400 nm wavelength femtosecond pulses in the fluence regime before catastrophic damage. For fluences below that where full-ablation occurs, small optical increases in the reflection of up to 4% are observed in the aftermath with a weak probe beam. In this fluence regime, dark-field, scanning electron, and atomic force microscopy images reveal morphological changes such as *top-level ablation*, where only the top part of the ruthenium layer is ablated whereas the lower part still remains on the substrate, and *nanovolcano formation.* However, neither top-level ablation nor nanovolcano formation is responsible for the reflection increase. Instead, electron backscatter diffraction reveals that in this low fluence regime where reflectivity increases, Ru grains melt and resolidify into larger grains, which is likely responsible for the observed reflectivity increases. This result is reminiscent of our earlier work on aluminum layers and it suggests that there may be more metals that display this behavior.

4.1. INTRODUCTION

In semiconductor device manufacturing, new technological challenges arise as device structures become smaller and smaller [15, 16]. For example, the resistivity of copper and tungsten increases when the dimensions of conducting lines become smaller [126–128]. Ruthenium (Ru) has appeared as a suitable alternative to copper and tungsten because of its good nanoscale conductivity [129, 130]. However, in semiconductor device manufacturing, deposited materials must also be able to withstand high optical fluences used by optical metrology tools, for example for wafer alignment in nanolithography machines.

For wafer alignment, diffraction signals from alignment markers, often buried under various deposited, partially opaque materials, are used to determine the absolute position of the wafer [131, 132]. For this, visible/NIR light beams, having a Gaussian beam profile, are often used with wavelengths in the range from about 400 to 1100 nm. For proper wafer alignment, a sufficient amount of diffracted light from the buried alignment markers is required to accurately determine the wafer position. In recent years, however, there has been a clear trend toward making alignment markers smaller and smaller which, for the same incident fluence, would reduce the amount of diffracted light. Therefore, to keep the amount of diffracted light the same, a further increase in the incident light fluence is required, thereby reaching levels where optical damage becomes a possibility. Of particular importance, therefore, is the optical fluence regime around the optical damage threshold. Subtle, light-induced changes that may affect the conductivity of the Ru, can already occur at fluence levels below the threshold for catastrophic damage and should be avoided at all costs. It is, therefore, of critical importance to study light-induced changes to nanometer thick Ru films.

On ruthenium, extensive light-induced damage studies have been performed in the EUV/hard X-ray range [36, 133, 134]. Interestingly, it was reported [134] that the absorbed energy spatial distribution in this wavelength regime is similar to that formed by visible light, resulting in a similar thermo-mechanical response. Additionally, using near IR excitation, ablation processes, such as crater formation, a fine pattern of dense cracking (craquelure [135]), and top-level ablation [35] in the film after illumination were modeled and measured [36]. In *top-level ablation*, only the top part of the ruthenium layer is ablated whereas the lower part still remains on the substrate, whereas in *full-ablation*, the substrate is exposed due to the removal of the entire layer. These studies, however, focused mostly on fluence levels above the full-ablation threshold, whereas it is likely that subtle material changes can also occur at fluence levels *below* the full-ablation threshold.

In this study, we have looked at what happens when Ru thin films of 8 to 40 nm thick are exposed to single laser pulses with optical fluences above and below the threshold value for catastrophic damage. At high fluences, catastrophic damage in the form of crater formation, top-level ablation, and the formation of cracks in the Ru are seen, confirming earlier results [35, 36]. Within the area exposed by the pump pulse, scanning electron microscopy (SEM) images and atomic force microscopy (AFM) however, reveal the existence of round *nanovolcanoes* with diameters ranging from 50 to 500 nm. These structures appear to have been formed by molten Ru that has locally been pushed outward and has overflowed the surrounding area. AFM measurements also show that at the bottom of the volcanic crater, the glass surface is exposed and appears to be undamaged.

Measurements on samples with the Ru layer deposited on scratched substrates show that nanovolcanoes are mostly located along the scratch lines. This suggests that on nominally flat surfaces, stochastic variations in surface roughness increase the chance of nucleation and may therefore be responsible for the random positions of the nanovolcanoes on the substrate.

Interestingly, *below* the threshold fluence for catastrophic damage, small, 0.1 to 4% pump-induced increases in the optical reflectivity are observed. electron backscatter diffraction (EBSD) measurements indicate that in a fluence regime below that where catastrophic damage occurs, Ru grains have melted and resolidified into bigger grains. In this fluence regime, a small increase in reflectivity is observed, similar to what was measured for aluminum thin films [136]. This suggests that this effect may perhaps be more universal than original thought and could serve as an indication of impending catastrophic optical damage for a wider range of metals.

4.2. Experimental details

4.2.1. Sample fabrication

8 to 40 nm thick ruthenium (Ru) layers are deposited by Magnetron Sputter Physical Vapor Deposition (Polyteknik Flextura M506 S) on 0.5 mm thick borosilicate glass substrates, which have been cleaned in a base Piranha solution. Borosilicate glass [76] is chosen because of the negligible absorption at optical wavelengths of 400 and 800 nm. To study the dependence of the substrate, also sapphire, CaF_2 and silicon substrates were used. An overview of the samples used in the experiments is shown in table B.2. Additionally, relevant ruthenium and ruthenium oxide properties, and used layer thicknesses are given in table 4.1.

Table 4.1: Optical and thermal mechanical properties of ruthenium and ruthenium oxide.

	Ruthenium (Ru)	Ruthenium oxide (RuO_2)
$n + ik$ @ 400 nm	$2.40 + 4.64i$[a]	
$n + ik$ @ 400 nm by ellipsometry	$2.60 + 5.04i$	$3.30 + 0.16i$
$n + ik$ @ 800 nm	$5.04 + 3.94i$[a]	
$n + ik$ @ 800 nm by ellipsometry	$5.51 + 5.10i$	$2.64 + 0.028i$
Melting point T_m (K)	2606[b]	
Boiling point T_b (K)	4420[b]	
Thickness (nm)	8–40	0.5 (native oxide)
Thermal conductivity κ_l ($Wm^{-1}K^{-1}$)	117[b]	
Specific heat C_l ($10^6 Jm^{-3}K^{-1}$)	2.88[b]	

[a]Ref. [111, pp.256-261], [b]Ref. [102, p.12-218]

4.2.2. Setup

The pump-probe laser setup used for the experiments is shown schematically in figure 3.1 and is explained in more detail in section 2.2.2. All experiments presented here are

performed in ambient atmosphere.

A Ti:Sapphire oscillator-amplifier combination generates 45 fs laser pulses with a central wavelength of 800 nm at a repetition rate of 1 kHz. In the setup, the beam is split into a weak 800 nm probe beam, and a strong pump beam that is frequency-doubled by a Beta Barium Borate (BBO) crystal to 400 nm (type 1 second harmonic generation). Next, a pulse picker system, formed by a 10% duty-cycle chopper and a galvo mirror, selects a single pump pulse. The pump beam is focused using a $f = 20$ cm lens and the sample is placed a short distance before the focal point. The pump is at normal incidence on the sample and the probe beam is at an angle of $\approx 10°$ with respect to the surface normal. Before it is focused onto the sample, the probe beam is reflected off a set of beamsplitters to attenuate the power by a factor of $\approx 10^{-4}$ to a pulse energy $\approx 0.1 \mu$J. The pump-pulse energy can be varied by rotating the $\lambda/2$-plate which is placed before the BBO. The probe and pump are focused onto the sample to spot sizes of ≈ 15 and $\approx 75 \mu$m respectively. The geometry of the beams and the sample is schematically shown in figure 3.1. Here, R and T indicate the reflected and transmitted beams. The laser beams used in these experiments have Gaussian beam profiles (see appendix D.1). Whereas it is not uncommon to use flat-top beam profiles in laser damage experiments [137, 138], Gaussian beam profiles are typically used in metrology tools for wafer alignment. Our experiments are thus closer to the actual use cases. A detailed description of the entire setup can be found in section 2.2.2.

Before each measurement series, a Gentec-EO Beamage-4M beam-profiler is placed at the sample position where the pump and probe beam spatially overlap, to measure the pump and probe beam spatial profiles. Furthermore, a Coherent thermopile power sensor is placed in the pump beam path after the last mirror before the focusing lens. This is to calibrate the reference photodetector in order to convert the detector signal into a pump fluence (see section 2.3.1).

In a typical experimental cycle, single pump pulses hit the sample in a six-by-six grid where each subsequent pump shot has a slightly higher fluence. Here, the fluence ranges from well below any measurable morphological or optical change to above the threshold for crater formation. Each site in the six-by-six grid is hit by only one pump pulse. To check reproducibility, each such cycle is repeated several times, leading to the formation of multiple grids. Before each measurement series, the probe alignment with respect to the pump is optimized by maximizing/minimizing the measured power of the probe transmission/reflection after creating a small ablation site by the pump. The same is done after the measurement series to check if no beam drifting occurred and to confirm that the sample and sample stage were aligned properly (see appendix D.2). At each illuminated site, before pump excitation, the 800 nm reflection (R_{pre}) is obtained by measuring the probe reflection and a reference signal using photodetectors. R_{pre} is averaged over a thousand shots giving $\bar{R}_{\text{pre}}$, which enhances the detection sensitivity. The same is done for a thousand probe shots, measured well after pump excitation (> 1 ms), when all transient effects have disappeared, giving the average $\bar{R}_{\text{post}}$. The relative difference between $\bar{R}_{\text{pre}}$ and $\bar{R}_{\text{post}}$ normalized to $\bar{R}_{\text{pre}}$ is the *relative reflection change* ΔR:

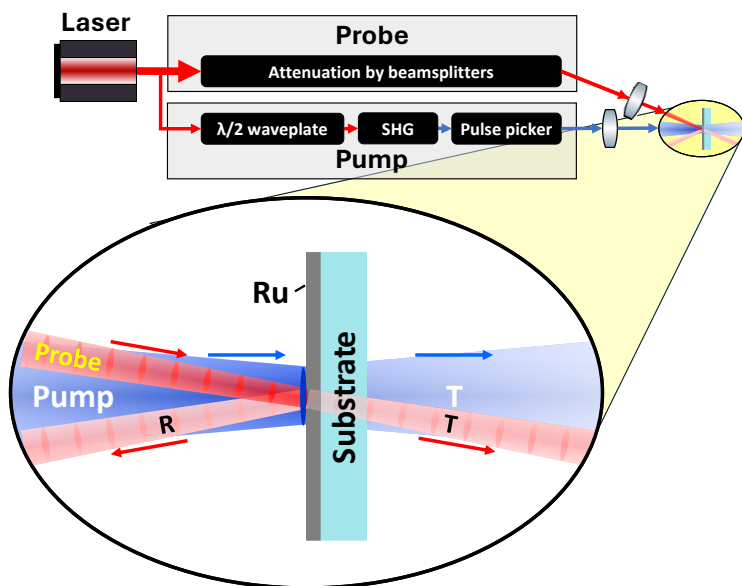$$\Delta R(F) = \frac{\bar{R}_{\text{post}} - \bar{R}_{\text{pre}}}{\bar{R}_{\text{pre}}}. \qquad (2.3/4.1)$$

Figure 4.1: Schematic of the pump-probe laser setup used for the experiments (top) and the geometry of the beams and the sample (bottom). A detailed description of the entire setup can be found in section 2.2.2.

These values for ΔR depend on the pump fluence F and are obtained for all ruthenium layers. They are presented in section 4.3.

4.2.3. POST-PROCESSING

After each measurement series, the sample is taken out of the laser setup for the inspection of the illuminated sites. Each grid containing 36 illuminated sites is inspected by DIC and DF microscopy. Hereafter, a Helios Nanolab 600 scanning electron microscopy (SEM) is used to study possible morphological changes. Selected sites are inspected further with a Bruker Dimension Icon atomic force microscope (AFM). For some sites, energy-dispersive X-ray spectroscopy (EDX), to obtain the spatial distribution/concentration of the elements (Ru and O) present in the layer and/or electron backscatter diffraction (EBSD) is used to map the crystal orientation and structure and to obtain grain sizes. EBSD was performed in a Thermo Fisher Scientific Verios 460 SEM using an EDAX Clarity direct detector. The patterns were collected using EDAX APEX software, a 100 pA beam current, 7 kV accelerating voltage, and a 15–200 ms pixel integration time. The patterns were processed in the EDAX OIM software. All obtained patterns were indexed using the Spherical Indexing (SI) approach with Neighbor Pattern Averaging and Reindexing (NPAR) with the Ru phase ($P6_3$/mmc space group).

For an (elliptical) Gaussian pump beam, where the intensity distribution is Gaussian having a different width in the two orthogonal directions of the ellipse, the local fluence profile, $F(x, y)$, varies with position. In this profile, lines of constant fluence ($F = const.$) take the shape of ellipses. These ellipses correspond to lines where the energy per unit

area has a constant value. When a damage mechanism is bounded by a certain threshold fluence F_{th}, the area A bounded by this ellipse equals the area spanned by that damage mechanism. Therefore, for Gaussian beam profiles [74] with a peak fluence of F_0 at its center, A and $\ln(F_0)$ follow the linear relation:

$$A = a \ln(F_0) + b. \tag{4.2}$$

Since the onset of damage occurs at $A = 0$, where $F_0 = F_{th}$, F_{th} as well as the FWHM of the Gaussian beam waist d_x (long axis) and d_y (short axis) can be expressed in the linear parameters a and b:

$$F_{th} = \exp(-\frac{b}{a}), \qquad d_x = \sqrt{\frac{4\ln(2)\,a}{\pi\sqrt{1-e^2}}}, \qquad d_y = d_x\sqrt{1-e^2} \qquad \text{with} \qquad d \equiv \sqrt{d_x d_y}, \tag{4.3}$$

with e being the eccentricity of the elliptical beam profile, which is directly measured ($e \approx 0.70$). Here, a and b are determined from the linear fit to the measurement data of area A versus $\ln(F_0)$ in the so-called Liu-plot [74] (see section 1.3). A more detailed derivation of equations (4.2) and (4.3) can be found in section 1.3.2. Since lateral heat diffusion can be neglected here (see section 1.1.3) and we consider metals here, damage occurs where $F_{local} > F_{th}$. By using a Gaussian, instead of a flat-top beam profile [137, 138], F_{th} can be obtained with a high accuracy because of the relation between the damaged area A and the peak fluence F_0 (see equation (4.2)).

4.3. Results and Discussion

4.3.1. Nanovolcano formation and top-level ablation

We used six samples with nominal ruthenium layer thicknesses of 8, 10, 15, 20, 25, and 40 nm on borosilicate glass substrates[a]. Each sample is illuminated by single-shot 400 nm pulses of different fluences, and probed by weak 800 nm pulses. The relative reflection change, ΔR (see equation (2.3/4.1)), is measured. These ΔR values are plotted versus peak pump fluence F_0 and are shown in figure 4.2. For low fluences, $\Delta R = 0$ because the pump fluence is too low to permanently change the ruthenium layers. For high enough fluences, ruthenium is removed. Since the transmission of the probe light is higher without the ruthenium layer present, this *full-ablation* will always cause a decrease in ΔR (see figure G.6). In between these low and high fluence regimes, for the 8 and 10 nm ruthenium layer (figure 4.2a-b), there is a small increase in the reflectivity ($\Delta R > 0$). This is slightly different for the 15 to 40 nm thick (nominal) ruthenium layers (figure 4.2c-f). Although there the reflectivity increase is present as well, additional, fairly abrupt changes in the slope of $\Delta R(F_0)$ are also observed. Each abrupt change may be located at a fluence threshold corresponding to a different damage mechanism. The same figure is shown in part of figure G.5, which includes all found damage mechanisms.

Using SEM and optical microscopy, images of all illuminated sites have been obtained. Different damage mechanisms such as cracking, nanovolcano growth and top-level ablation of the layer were observed below the threshold fluences for full-ablation. With

---

[a]The reported thicknesses throughout this chapter are the aimed nominal thicknesses. The inferred thickness from ellipsometry are $\approx$ 15% higher than the nominal ones, and are obtained from ellipsometry measurements where a native oxide of 0.5 nm is assumed. Both the nominal and inferred thicknesses can be found in table B.2. Note that the inferred thicknesses are used for the calculations.
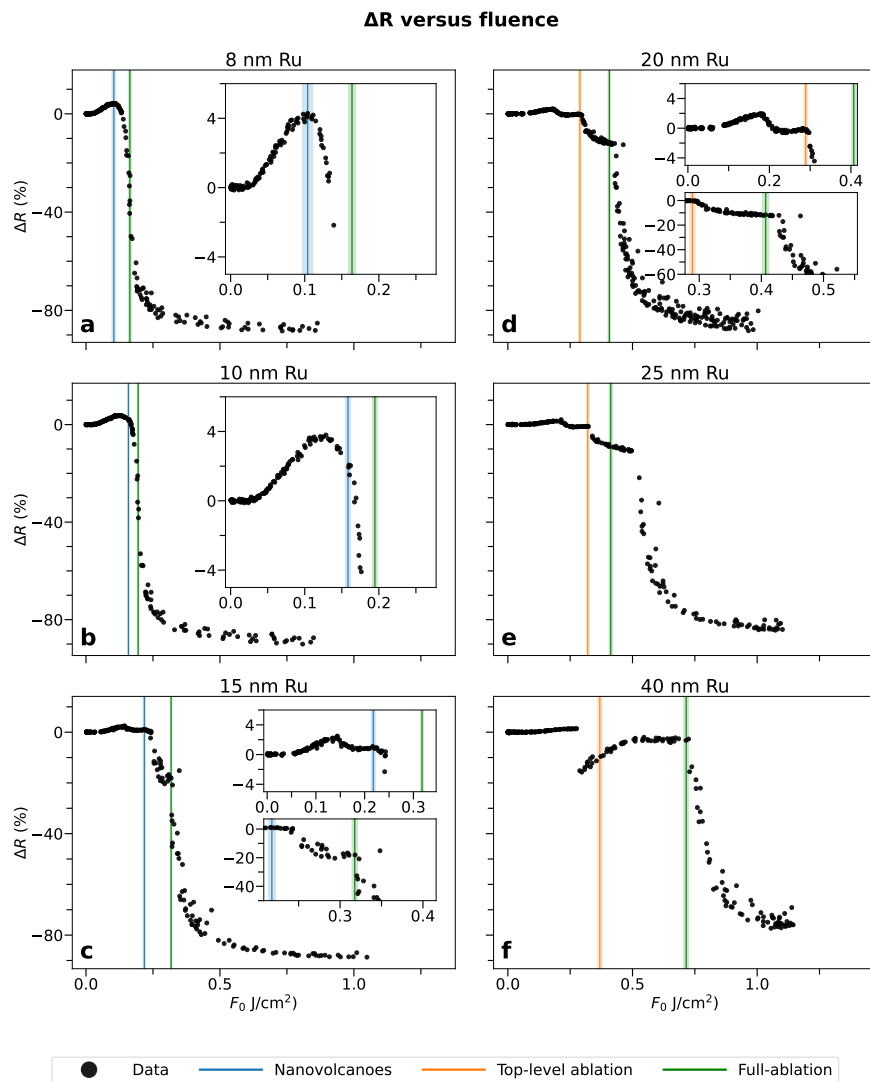
Figure 4.2: Relative reflection change ΔR versus peak fluence F_0 for (nominal) 8, 10, 15, 20, 25 and 40 nm ruthenium on borosilicate glass substrates. Only the threshold fluences for three damage mechanisms, as identified by SEM, for each layer thickness are shown by the vertical lines. The blue vertical lines indicate the fluence threshold for nanovolcano formation in (a-c), and the orange lines in (d-f) indicate the top-level ablation threshold fluence. In all figures, the green lines mark the full-ablation threshold fluence. The corresponding uncertainty in these values is indicated by the lighter band around each vertical line, which is due to their small widths, only visible in the insets.

top-level ablation, roughly the top half of the layer of ruthenium has ablated from the lower half, and the lower part is still intact and remains on the substrate. This is due to the expansion of overheated material at near and above critical conditions at the top-level layer [35]. For higher fluences, both the top and lower part ablate from the substrate. We define the complete removal of Ru as *full-ablation*.
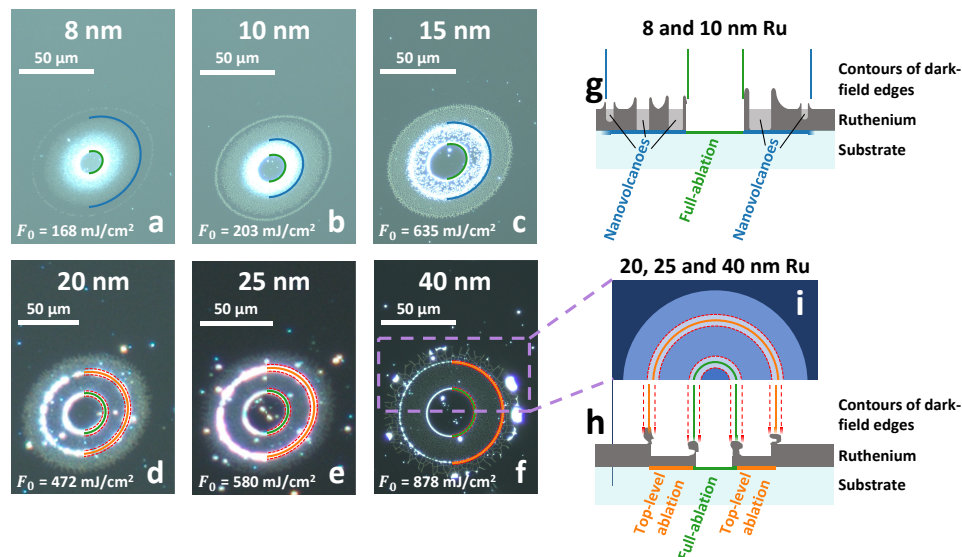

Figure 4.3: (a-f) Dark-field microscopy pictures of single pump-shot illumination of 8, 10, 15, 20, 25 and 40 nm thick (nominal) ruthenium layers on borosilicate glass. At each picture, all damage mechanisms are present since the pump fluence is above the full-ablation thresholds ($F > F_{FA}$). Therefore, for all six layer thicknesses, the most inner damage edge is at a fluence level where full-ablation starts to occur (green). At the right half of each picture, semi-ellipses are drawn, indicating the onset of nanovolcano formation (blue), top-level ablation (orange), and full-ablation (green). In (d-f), each pair of neighboring dashed red contours is obtained from our analysis, and corresponds to the inner and outer side of the white bright rim, which represents the top-level and full-ablation edges. The position of these respective ablation edges is defined to be in between each pair, as schematically shown in (i). Nanovolcanoes are found in the region between the blue and green ellipses, top-level ablation between the orange and green ellipses, and full-ablation inside the green ellipses. (g-h) Schematic drawings of the cross sections of 8 and 10 nm (g), and in 20, 25 and 40 nm (h) thick (nominal) ruthenium layers.

A selection of dark-field images of illuminated sites for each of the six Ru thicknesses is shown in figure 4.3a-f. The local fluence decreases as the distance from the illumination center increases. Since the full-ablation threshold fluence is exceeded in the middle of all spots shown in the images, all damage mechanisms are present. The right halves of the images have been overlayed with semi-ellipses that outline annular regions where nanovolcanoes (between blue and green ellipses), top-level ablation (between orange and green ellipses) and full-ablation (inside the green ellipse) are seen. The green semi-ellipses indicate the full-ablation edges. Within this region, there is no ruthenium left and the substrate is exposed, as seen by bright-field microscopy. For the 8 and 10 nm thick (nominal) layer, when moving closer to the green ellipse, the nanovolcanoes grow in

size until practically all nanovolcano vents overlap, forming the full-ablation area. This is schematically drawn in figure 4.3g.

Figures 4.4a to 4.4f show SEM images for all Ru thicknesses similar to the dark-field ones as presented in figure 4.3. In the additional zoomed-in SEM images (figures 4.4g to 4.4l), round dark shapes bordered by bright rims have emerged from the ruthenium layers. Since their sizes range from 50 to 500 nm, and because AFM images show that the rims are higher than the surrounding area, these structures resemble *nanovolcanoes*. Furthermore, the onset of top-level ablation and full-ablation are shown by their respective edges. The yellow rectangles and arrows in figures 4.4a to 4.4f indicate the locations of the zoomed-in SEM images.

For the 8 and 10 nm layers, nanovolcanoes start to form on the inside of the blue ellipses as indicated in figures 4.3a and 4.3b. From here, they increase in number and size until the vents of the nanovolcanoes cover (almost) the entire area (figure 4.4g, m and 4.4h, n). From here on, no ruthenium is left and full-ablation is reached. Figure 4.3g shows a schematic drawing of the nanovolcano formation over the ruthenium layer, and its full-ablation.

For the 20, 25 and 40 nm thick (nominal) ruthenium layers, top-level ablation occurs (figures 4.4j to 4.4l). The corresponding top-level ablation edge is indicated by the orange semi-ellipses in the dark-field images (figures 4.3d to 4.3f). Between this edge and the full-ablation edge (green ellipses), the top layer of the ruthenium is missing. Here, only a few nanovolcanoes can be seen (figures 4.4j to 4.4l), which are often positioned closer to the top-level ablation *edge* than the full-ablation edge (figures 4.4p to 4.4r).

For a ruthenium nominal thickness of 15 nm, no top-level ablation has occurred (figure 4.4i). However, a slightly elevated edge is observed and is positioned slightly outside the blue ellipses at the dark-field image in figure 4.3c. Since such an elevation is not observed in the thinner layers, and top-level ablation is observed in the thicker ones, the 15 nm thick (nominal) layer seems to represent a transition layer thickness for the appearance of top-level ablation. Additionally, a fair number of nanovolcanoes are present around the elevation edge. However, the number of nanovolcanoes and sizes decrease when moving closer to the full-ablation border, which looks similar to that for thicker layers.

4.3.2. THRESHOLD FLUENCES AND LIU-ANALYSIS

With dark-field microscopy, the outer edges of the areas A spanned by the identified damage mechanisms (see figure 4.4) were obtained. When a damage mechanism is bounded by a certain threshold fluence F_{th}, A and $\ln(F_0)$ should follow the linear relation $A = a \ln(F_0) + b$ (see also equations (4.2) to (4.3)) for Gaussian beams with a peak fluence F_0 [74]. In figure 4.5, the area A spanned by the outer edge of a damage mode versus $\ln(F_0)$, the so-called *Liu-plots*, are plotted for all six samples. The blue, orange, and green data points and their linear fits indicate nanovolcano formation, or top-level ablation and the full-ablation respectively. The linear fits intersect the horizontal axis at $\ln(F_{th})$, where F_{th} is the corresponding fluence threshold of the corresponding damage mechanism (see equation (4.3)). The fits are obtained by a recursive RANSAC approach [139]. Note that only the linear fits corresponding to nanovolcano formation (blue), top-level ablation
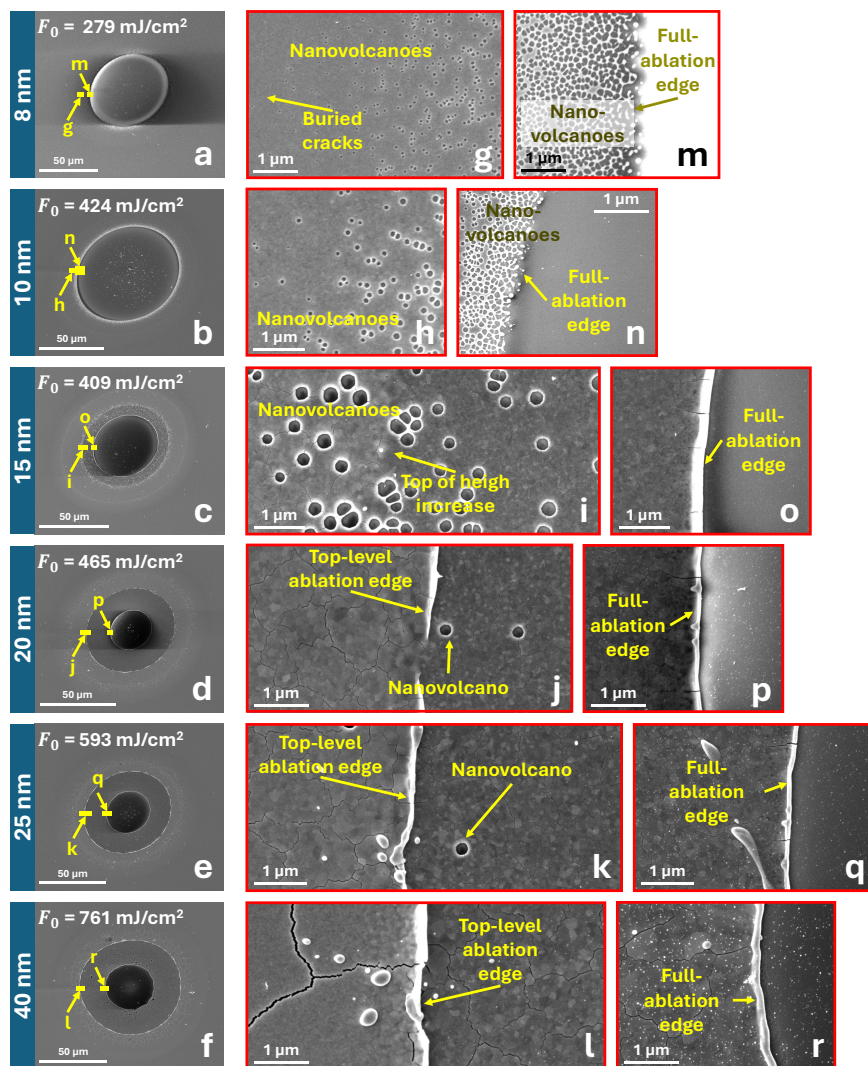
4

Figure 4.4: SEM images of 8, 10, 15, 20, 25 and 40 nm thick (nominal) ruthenium layers on borosilicate glass illuminated above the full-ablation damage threshold. The arrows that point at the small yellow rectangles in (a-f) indicate the location of the zoomed-in images shown on the right (g-r). Nanovolcanoes and/or top-level ablation edges are shown in (g-n), whereas (m-r) are taken at the full-ablation edges.

(orange), full-ablation (green), and their corresponding data points are shown, and are marked according to their color. In figure G.5, this figure is shown including other damage mechanisms as well. At figure 4.5a, the blue dashed line indicates that F_{NV}, the nanovolcano formation threshold fluence, is obtained by inspecting SEM images. SEM was used because of the low contrast of the nanovolcano formation onset in the dark-field images. Therefore, no nanovolcano formation edges were extracted from the dark-field images, and therefore no blue data points are visible in figure 4.5a. The top-level and full-ablation edges curl up as is visible in the SEM images (figures 4.4j to 4.4l and figures 4.4o to 4.4r). In the dark-field microscopy images, the entire curled up zone results in a bright annulus. Increasing the exposure time and brightness of the microscope light source can appear to widen this annulus even further. Each annulus has an inner and outer contour in the dark-field images as shown in figures 4.3h and 4.3i. Therefore, pairs of the orange and/or green linear fits are shown in figures 4.5d to 4.5f, where each fitting pair represents the inner and outer contour of an annulus. We define the corresponding top-level or full-ablation threshold fluence (F_{th}) to lie exactly in the middle between the inner and outer contour. Therefore, F_{th} is obtained by averaging the fit parameters of the two corresponding fits. Here, $F_{th} \approx \exp(-(b_i + b_o)/(a_i + a_o))$, where a_i and a_o are the slopes, and b_i and b_o the offsets of the Liu-fits corresponding to the inner and outer contour. The FWHM of the beam profile, d, is retrieved by using equation (4.3) with $a_{th} = \frac{1}{2}(a_i + a_o)$. Since these values for d are close to the measured ones, this suggests that the above assumption is valid.

All damage thresholds F_{th} for nanovolcano formation, top-level ablation and full-ablation are indicated by the blue, orange and green vertical lines in the ΔR versus F_0 plots of figure 4.2 as well. At every fairly abrupt change in the slope of ΔR in figure 4.2, a fluence threshold F_{th} was found (see figure G.5). This is a further indication that such abrupt changes mark different damage mechanisms. The increased reflectivity, nanovolcano formation, top-level ablation and full-ablation will be discussed in further detail in sections 4.3.3 and 4.3.4, whereas all other damage mechanisms are briefly described in figures G.1 and G.3. Note that not all fluence thresholds have been obtained by Liu-analysis since not all damage mechanisms create a big enough contrast in the dark-field images. These additional thresholds are obtained by estimating the position of the damage edge from SEM images, and subsequently calculating the local fluence at those borders, based on the known beam profile. In table G.1, an overview of all obtained thresholds and damage mechanisms can be found, as well as their corresponding SEM images.

4.3.3. MORPHOLOGY

Figures 4.6a and 4.6b show optical dark-field microscopy and SEM images of a site on a 10 nm thick (nominal) ruthenium layer, illuminated just above the nanovolcano threshold fluence (F_{NV}). Figures 4.6a to 4.6b are the dark-field and SEM overview images of the entire damaged site. Both show a bright center, which is the area where the nanovolcanoes are present. The red rectangle marks the position where the zoomed-in SEM and AFM images (figures 4.6c to 4.6d) were taken. Here, each nanovolcano can be identified by its round center (vent) and by the rim. These are indicated by the dark and bright color respectively in SEM, and by their height in the AFM height profile. The vent diameter varies between $\approx$ 60 and 160 nm here. Figures 4.6e to 4.6g are the height and phase profiles
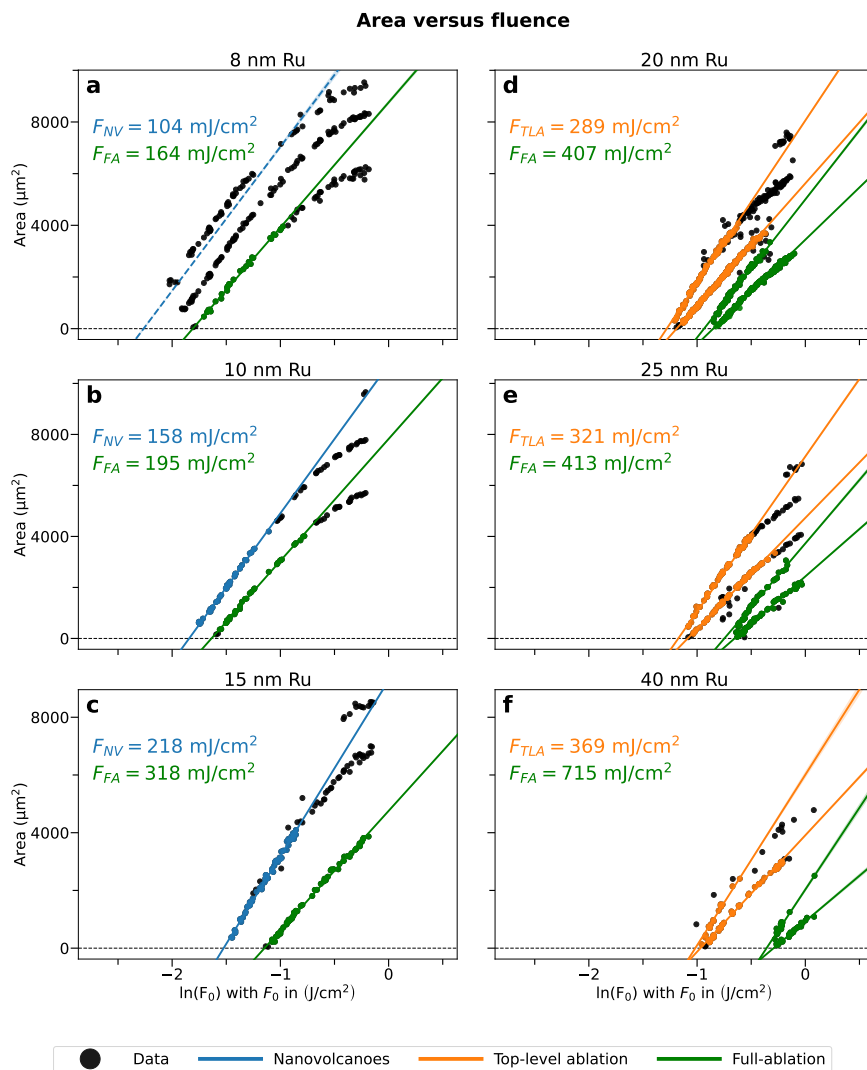
Area versus fluence

Figure 4.5: Liu-plots of single pulse laser damage experiments on 8, 10, 15, 20, 25 and 40 nm thick (nominal) ruthenium layers on borosilicate glass, obtained by inspecting dark-field images. Blue, orange, and green linear fits are shown corresponding to the onset of nanovolcano (NV), top-level ablation (TLA) and full-ablation (FA) respectively.
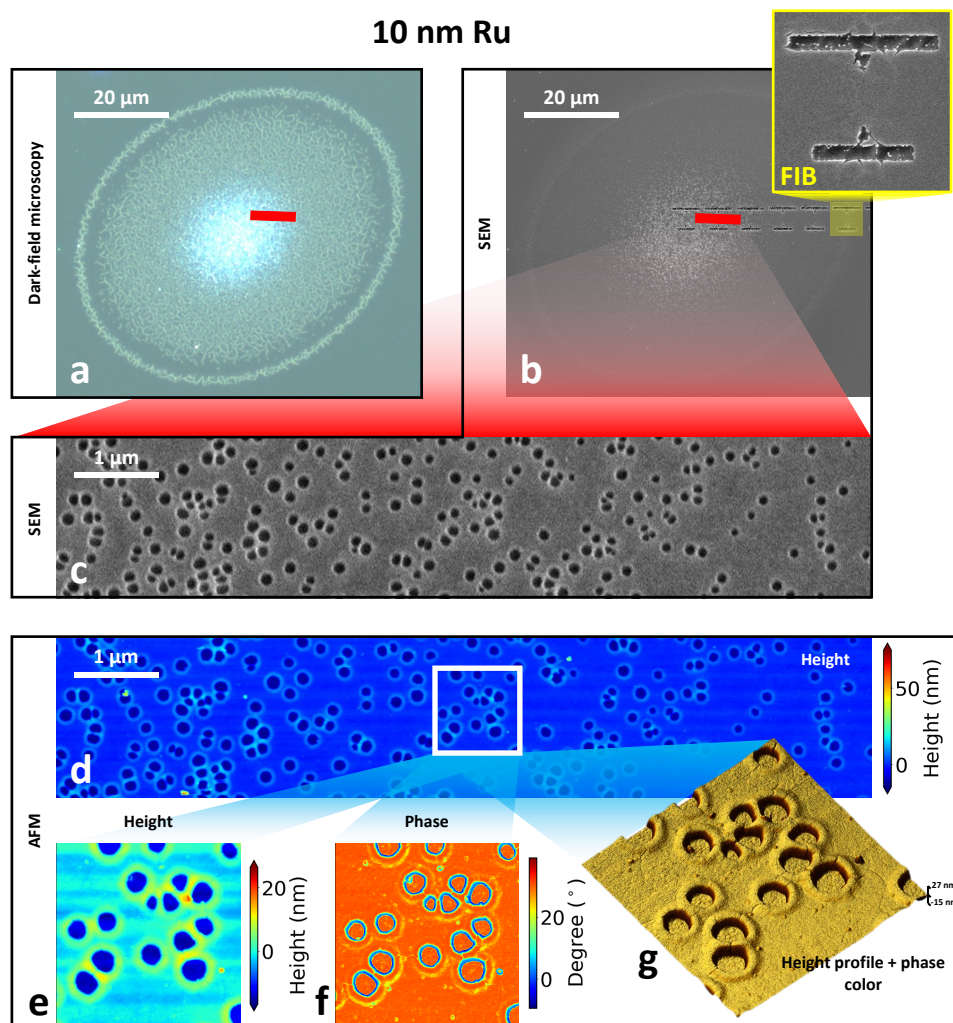
Figure 4.6: (a) Dark-field microscopy images of a single damaged site on a 10 nm Ru film on borosilicate glass. The site was illuminated with a single pulse with a fluence above the nanovolcano formation threshold (F_{NV}). (b) SEM image of the whole damaged site. After laser exposure, markers have been made in the ruthenium layer by a focused ion beam (FIB) to help find locations on the damaged spot to be imaged using an AFM. The inset of (b) shows one set of FIB markers composed of two lines and two (very small) triangles. In total, six of those FIB marker sets, that are positioned next to each other, are shown in (b). Both (a) and (b) show a bright center, the area where the nanovolcanoes have formed. The red rectangle marks the position of the zoomed-in SEM and AFM images (c) and (d). (e) and (f) are the height and phase profiles of the area marked by the white rectangle, and (g) shows the 3D height profile overlayed with the phase.

of the area marked by the white rectangle in figure 4.6d. In the SEM image, the volcanoes are evident as dark circular features in the ruthenium layer. In the nanovolcano *vents*, the AFM image shows a negative height indicating that material is indeed missing. These vents are bordered by a few nanometers higher rim, and in most cases, the substrate in the vents is exposed.

In figures 4.7a and 4.7b, the height and phase profile of a single nanovolcano obtained by AFM are shown. Here, a dashed line indicates where the height and phase cross sections are taken, that are plotted in figures 4.7c and 4.7d. Around each nanovolcano vent, a higher *rim* is formed. For fluences between F_{NV} and a bit below F_{FA}, the missing volume of the vent corresponds to the volume of the rim, indicating that no material is missing. However, for nanovolcanoes with a local fluence relatively close to the full-ablation threshold, up to $\approx 35\%$ less material is present. This means that already some material is ablated before reaching the full-ablation threshold fluence F_{FA} (see appendix G.3). Note that figure 4.7c is a cross section of a nanovolcano, at which the rim and vent area are visible. These areas are not equal, but their volumes are approximately equal. This is because the rim is positioned further away from the center of the nanovolcano, and therefore has a larger circumference than the vent.
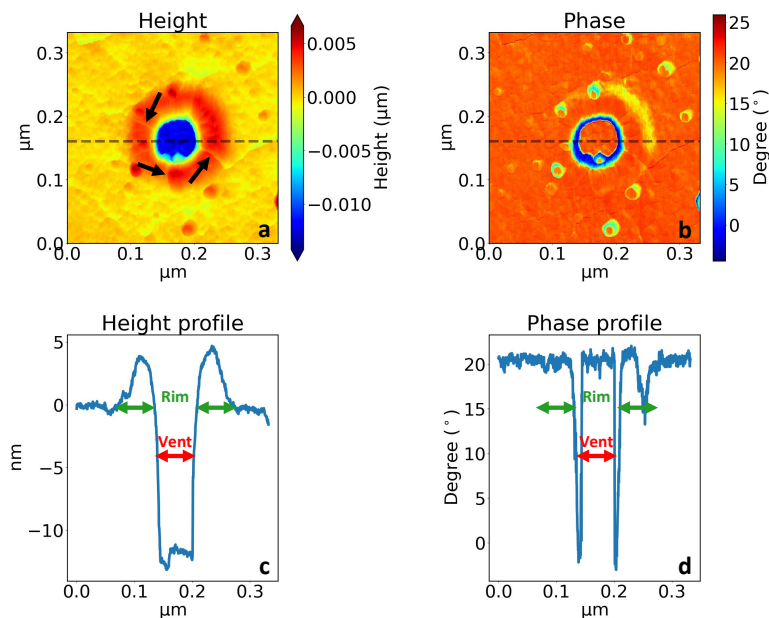

Figure 4.7: High-resolution AFM height (a) and phase profile (b) scan of a single nanovolcano. (c) and (d) correspond to cross sections along the horizontal dashed lines visible in (a) and (b). Around each nanovolcano vent, a higher rim is formed. A crack also runs through the volcano but this is difficult to see due to the limited AFM spatial resolution. The black arrows in (a) point at the parts of the crack that run through the volcano rim (see also the SEM images in figure G.2). The nanovolcano is at the same illuminated site as presented in figure 4.6, but positioned approximately 7 μm to the right of figures 4.6e to 4.6g, at a position where the fluence is lower.

In the vents, the bottom is relatively flat (see figure 4.7c) and is of the same depth as

the other nanovolcanoes in the same Ru layer. Additionally, when the AFM tip reaches the bottom, there is a big negative jump in the phase signal as can be seen in figure 4.7b and d. The flatness and alignment of the vent bottoms, combined with the observed big phase jumps suggest that the glass substrate is exposed. An energy-dispersive X-ray spectroscopy (EDX) scan covering multiple nanovolcanoes, shown in figure 4.8, further demonstrates that there is no significant amount of ruthenium present in the nanovolcano vents. We note that SEM images (see figure G.2) show that crack lines seem to run through all nanovolcanoes. Additionally, as is visible in the SEM image of figure 4.6c, the nanovolcanoes are not evenly distributed, but seem to be grouped along lines. However, this is only clearly visible in SEM images with a higher spatial resolution in which it can be seen that these ragged lines correspond to cracks that run along the ruthenium surface. These cracks already form at lower local fluences, whereas nanovolcanoes start to form at higher fluences. This suggests that, for increasing fluence, cracks form first, followed by nanovolcanoes which form along those crack lines. We note that in figure 4.7a, a crack also runs through the volcano but this is difficult to see due to the limited AFM spatial resolution.
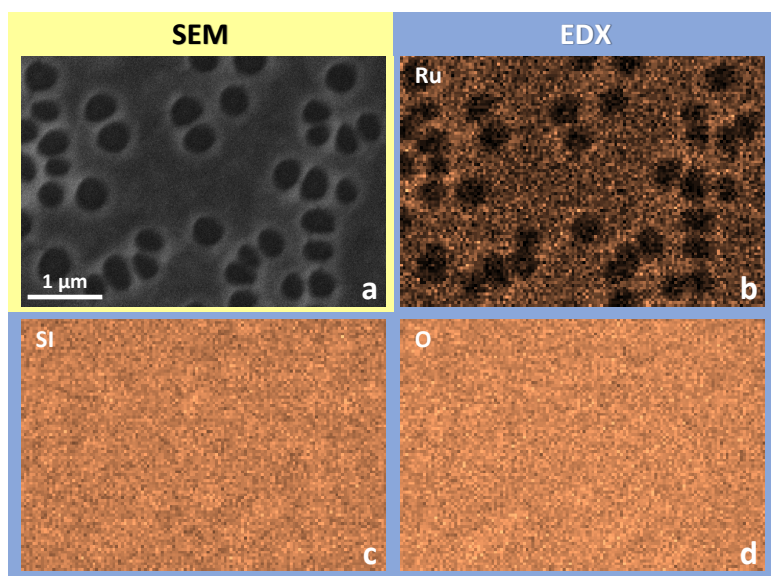

Figure 4.8: (a) SEM image of part of an illuminated site on a nominally 10 nm thick ruthenium layer on borosilicate glass. (b-d) are the corresponding EDX maps of Ru, Si and O respectively where the scaling of the colormap is optimized per element. Note the near absence of Ru in the volcano vents. Although difficult to see, in the vents, the Si and O signals are slightly higher, which is due to the direct probing of the substrate. Elsewhere, the signal is partly blocked by the Ru layer.

4.3.4. Optical changes and formation mechanism

As demonstrated by the in situ probe measurements (figure 4.2) of the sites illuminated with a single laser-shot, the first change in the reflected signal is a small increase in reflectivity at relatively low fluences. The onset of this reflectivity increase lies at a fluence

4

level where neither nanovolcano formation nor top-level ablation have yet occurred. Both these damage mechanisms are first observed at significantly higher fluences than the fluence where the reflectivity increase occurs. Neither mechanism can therefore be directly responsible for the observed reflectivity increase. However, there are additional arguments why nanovolcano formation and top-level ablation cannot explain the subtle reflectivity changes observed at low fluences. Nanovolcanoes, as seen by the dark-field images in figure 4.3, clearly scatter light in all directions. This would lower the amount of specularly reflected light rather than increase it. For top-level ablation, a significant top part of the ruthenium layer has been removed. Optical multilayer calculations, using the transfer matrix method (see section 1.1.1 and [99]), of Ru on glass show that this thinning of the layer would lead to a *decrease* of the optical reflection (see figure G.6).

To learn more about the possible causes of the small reflectivity increase, we have also performed electron backscatter diffraction (EBSD) to measure the crystallinity of the Ru layers after exposure to a single laser pulse. Since our Ru layers are polycrystalline, EBSD allows us to obtain grain size and orientation at various locations within an illuminated spot. Figure 4.9a shows a dark-field image of a single-shot illuminated site on a 8 nm thick (nominal) layer of ruthenium. Here, the red rectangles mark the locations of the obtained EBSD-scans as shown in figure 4.9c-g, and figure 4.9b is a scan of a pristine site used as a reference. The local fluences of each EBSD-map are in the $\Delta R > 0$ regime but below the nanovolcano formation threshold. From maps 4.9d-g, it is clear that for $F_{\text{local}} > 77\,\text{mJ/cm}^2$, the grain size increases with respect to the pristine material (figure 4.9b). Note that a light ring is visible in the dark-field image. Here, a band with relatively big grains with a (0001) Ru-structure can be found, which may contribute to a positive ΔR. However, its formation mechanism is currently unknown. Since the grain size of the pristine ruthenium is smaller than our spatial resolution, individual grains on maps 4.9b-c and the right side of 4.9g cannot be resolved. At the fluence level that corresponds to scan 4.9c however, $\Delta R > 0$, so it is very likely that the grain size increased here too, however not exceeding our spatial resolution ($\approx 30\,\text{nm}$). For recrystallization to take place, the ruthenium has had to reach the melting temperature ($T_m = 2606\,\text{K}$ at atmospheric pressure) first. Additional two-temperature model (TTM, see section 1.1.2) calculations are performed to obtain F_m, the fluences for which T_m is reached (see figure G.4). Here, F_m is lower than fluences for which nanovolcano formation and top-level ablation occurs, which indicates that recrystallization takes place after reaching the melting threshold. Increasing the grain size leads to a bigger mean free path of the electrons oscillating in response to the electric field of the probe, which will decrease the resistivity of our ruthenium layer, and increase reflectivity [124, 125, 136]. Therefore, it is highly probable that the nano-structural change in grain size is directly responsible for the small reflection increase we observe in the measurements. Interestingly, this is similar to what we observed for aluminum (see chapter 3), although for Ru, the pristine grain size is considerably smaller. In some places nanovolcanoes form, indicating that Ru has flowed creating a rim. These volcanoes are surrounded by topographically flat molten and subsequently recrystallized ruthenium.

The question remains what physical mechanism causes the formation of nanovol-canoes and top-level ablation. In [35], it was reported that, at high fluences, fast energy deposition in a subsurface layer leads to *two-level ablation*. Here, the top-layer is ablated as a gas-liquid mixture, whereas the bottom-layer is ablated via a cavitation process.
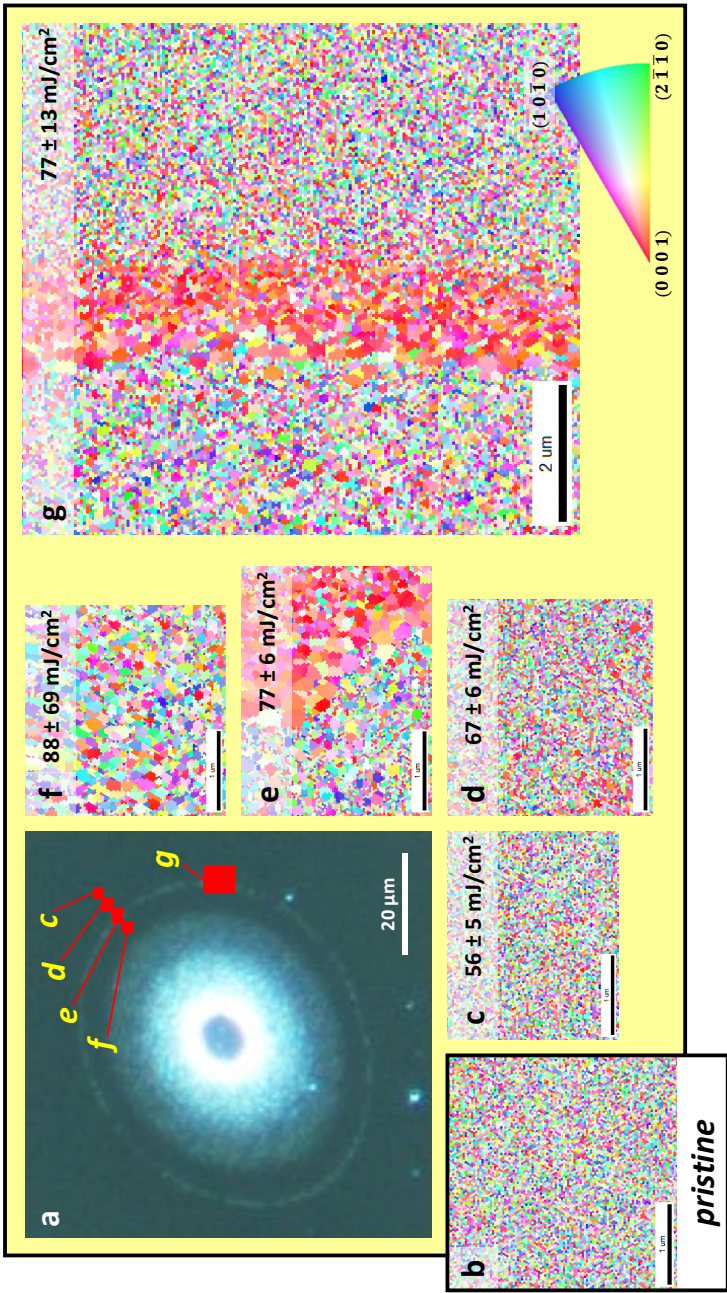
Figure 4.9: (a) Dark-field microscopy image of a single-shot-illuminated site of an 8 nm thick layer of ruthenium on borosilicate glass. The red rectangles indicate the locations of the EBSD-maps (c-f). Here, the local fluences are below the threshold fluence for nanovolcano formation ($F_{local} < 104 \, mJ/cm^2$), in the fluence regime where $\Delta R > 0$. The average values for F_{local} of each map are indicated at the corresponding EBSD image. These inverse polar figure maps show the crystal direction, which is the direction normal to the sample. Each color corresponds to the direction in the range between (0001), (10$\bar{1}$0) and (2$\bar{1}\bar{1}$0) according to the triangle legend in the bottom right of the figure.

However, for somewhat lower fluences, only the top-layer is ablated (top-level ablation), whereas the bottom-layer is still present on the surface. Therefore, the structure of this bottom-layer may have been changed perhaps giving rise to the formation of frozen cavities as reported in [35]. Our measurements show that top-level ablation occurs in ruthenium layers of ≈20 nm and thicker, which is accompanied with a fairly low number of isolated nanovolcanoes. However, for thinner layers, there is no top-level ablation and instead, nanovolcano formation is prevalent. For the 8 and 10 nm layers, the nano-volcano number density and size increase for higher local fluence. Here, the nanoscale morphology of the substrate may play a role. Some evidence for this is obtained by il-luminating a 8 nm ruthenium layer deposited on a borosilicate glass substrate that was lightly scratched with sanding paper, before cleaning the substrate in a sonic bath and base piranha solution. After deposition of the Ru, the scratch lines are visible by SEM as is shown in figure 4.10. Here, the SEM images clearly show that the nanovolcanoes tend to grow along those lines. This suggests that the roughness facilitates their formation, perhaps by increasing the local optical near-field, enhancing the probability of their formation at these locations.
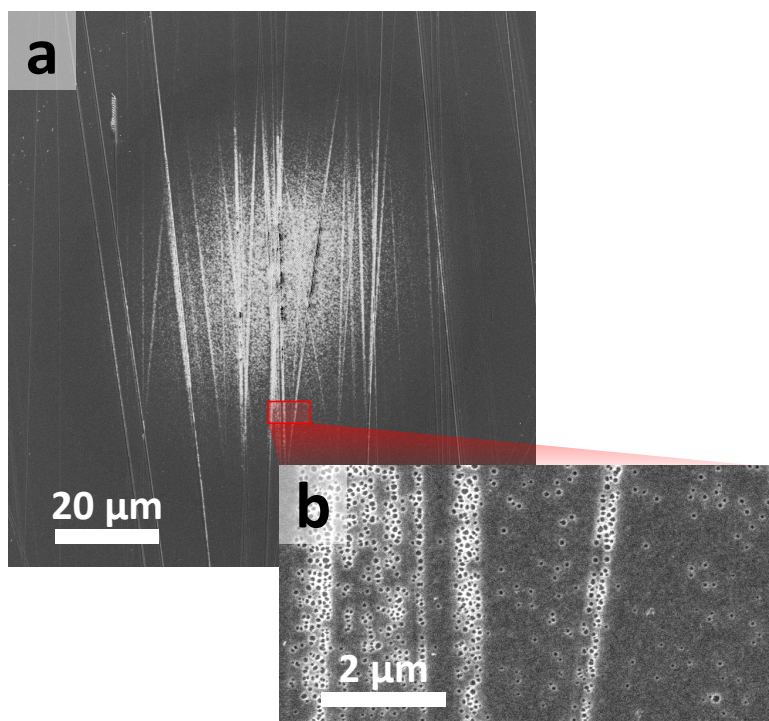

Figure 4.10: SEM images of a site on an 8 nm (nominal) thick Ru layer deposited on a 0.5 mm thick scratched borosilicate glass substrate, and illuminated with a single pump-pulse. The substrate is scratched by sanding paper and cleaned in a sonic bath and a base piranha solution before ruthenium deposition. Nanovolcanoes form predominantly along the scratch lines as is shown by the bright lines in the SEM image in (a) and from the zoomed-in section shown in (b).

In view of the use case scenarios for metrology applications related to wafer alignment, any form of light-induced material change has to be avoided. We found that this happens to be the fluence for which the smallest measurable increase in reflection occurs in response to a pump laser pulse. Theses fluences are summarized in table 4.2 for the different Ru layer thicknesses.

Table 4.2: Overview of the threshold fluences at the smallest measurable increase in reflection

Nominal thickness (nm)	Measured thickness (nm)	F_{th} (mJ/cm^2)
8	9.2	23 ± 10
10	11.6	62 ± 30
15	17.2	28 ± 15
20	23.0	66 ± 30
25	28.8	54 ± 40
40	45.9	93 ± 30

4.4. CONCLUSIONS

We studied optical changes in 8 to 40 nm thick ruthenium films on various substrates induced by a single ultrafast laser-pulse. For fluences below the full-ablation damage thresholds, for all Ru nominal thicknesses we studied, the reflection initially increases by a few percent. We have determined the damage threshold fluence at which the smallest measurable material change occurs (see table 4.2). When the fluence increases further, the reflectivity shows fairly abrupt changes for samples with nominal layer thicknesses of 15 nm and higher. Additionally, at fluences below full-level ablation, different morphological changes such as nanovolcano formation and top-level ablation are observed. The nanovolcanoes appear to have been formed by molten Ru that has locally been pushed outward and has flowed over the surrounding area. Furthermore, nanovolcanoes appear to be positioned on crack lines in the Ru. In top-level ablation, only the top part of the ruthenium layer is ablated whereas the lower part still remains on the substrate, which occurs in ruthenium layers of 20 nm thickness (nominal) and more. Here, a concentration of nanovolcanoes is located around the top-level ablation edge.

Neither top-level ablation nor nanovolcano formation can explain the small increase in reflection at low fluences directly. Instead, using electron backscatter diffraction, we find that Ru grains have melted and resolidified into bigger ones, most likely giving rise to the small increase in reflectivity by the accompanying increase in the mean free path of the electrons. This is similar to what was observed for thin Al films (see chapter 3 and [136]) and suggests that there may be more metals for which this occurs. For optical metrology in semiconductor device manufacturing, subtle light-induced changes in the reflectivity, due to changes in conductivity and morphology, may serve as early warning signals to prevent catastrophic damage. Particularly in ruthenium, the good nanoscale electrical conductivity may be influenced by the light-induced grain size change. Therefore, at low

fluence regimes, where small optical changes occur well below any catastrophic damage, the functionality of semiconductor devices may already be affected.

Background for the General Reader

"Je moet in feite gewoon niet te diep nadenken en dan klopt alles."

"You basically just shouldn't overthink things, and then everything makes sense."

Herman Finkers from *Geen Spatader Veranderd* (1995)

So far, we studied three materials: gold, aluminum, and now ruthenium as well. All of these showed subtle material changes, induced by light with an intensity well below the intensity where material will be blasted off. Therefore, at first, this result seems quite powerful. If this happens consistently, we can *use* this phenomenon to our advantage. However, when inspecting the illuminated sites more closely, it looks like every material behaves differently. The gold displays delamination from its glass substrate, the aluminum pushes out small parts of its oxidation layer, and nanovolcanoes are formed in some of the ruthenium layers.

Nonetheless, when looking more closely, the aluminum and ruthenium layers do have a common root cause for this: melting and fast resolidification. Here, the structure has changed permanently by exposure to the light pulse. It is still a flat layer, but its **grain structure**, the patchwork of crystals, changed. A quite advanced technique was necessary to spot this. Moreover, we found that these grain-size changes *are* the root cause for the optical changes. Consequently, the altered grain structure increases the reflectivity of the exposed area, a side effect that can be measured easily and directly after exposure by the light pulse.

We now know that when we measure more reflected light, it might come from a different grain structure, indicating that the material has melted and resolidified. Luckily, the films remain on its substrate as a flat layer. However, when fabricating computer chips, often non-flat surfaces will be exposed by bright light sources. Therefore, the next thing to do, is repeating the same experiment, but this time on structured samples.

How will structured samples look like after melting and resolidification?

PART II

LIGHT-INDUCED OPTICAL CHANGES AND DEFORMATIONS IN PATTERNED STRUCTURES

After examining different materials and layer thicknesses in the previous part, we transition to patterned structures, where we explore light-induced optical and structural changes in patterned structures.

In chapter 5, we investigate how single ultrafast laser-pulses affect gratings etched in silicon and compare this with results for flat silicon surfaces. This is done by measuring the thresholds and by using a computational model to predict threshold scaling with respect to that of flat silicon. Furthermore, grating lines deform under high fluences, with deformation progressing from height increases to broadening, flattening, and eventually peak-valley inversion, for increasing fluences.

Background for the General Reader

"My question to the ladies that use the anti-wrinkle cream:
If it really works, how come you've still got your fingerprints?"

Jimmy Carr from *Telling Jokes* (2009)

We now know, that a single laser pulse with a relatively low brightness can change materials by inducing melting after which it resolidifies. This is because after resolidification, the layer will have slightly different optical properties. However, the flat layer largely retains its overall shape after resolidification.

Intuitively this makes sense. The environment and material properties determine how a material looks after melting. This might sound a bit complicated, but nobody is surprised when their scoop of ice cream has melted into a flat puddle. Now, imagine starting with a frozen puddle; if we melt this, its basic shape will be unchanged, so a flat layer stays a flat layer. If we start with an ice sculpture at first, it will also melt into a flat layer.

Therefore, we will expose both a flat piece of silicon and silicon with varying ridge structures to bright laser pulses. This brings us closer to real-world conditions, as the materials in computer chips often consist of structured layers and are therefore not flat.

How will the ridges look after exposure? And do they become damaged more easily, less easily or at the same light intensities as a flat sample?

5

GRATINGS

In nanolithography, optical diffraction from gratings etched into the scribe lanes of semiconductor devices is used for wafer alignment. As these gratings become increasingly smaller, achieving sufficiently strong diffraction signals requires higher light fluences, increasing the risk of optical damage. This study explores light-induced optical and structural changes in flat silicon and gratings etched in silicon when exposed to single femtosecond laser pulses. We find that the fluence thresholds for all observed damage mechanisms are 10–50% lower in gratings compared to flat silicon. We attribute this to local field enhancements caused by the grating topography. Using near-field rigorous coupled-wave analysis (RCWA), we calculated absorbed power density profiles to establish a correlation between damage fluence thresholds and the local absorbed power density. While the method provides damage threshold estimates in a rather time-efficient manner, we found only a moderate correlation between the calculated and experimental threshold fluences.

Careful analysis of our measurements show that the observed deviations in relative pump-induced reflection changes in gratings, compared to flat silicon, are primarily due to grating line deformation, the onset of which can serve as an early warning for catastrophic damage. At high fluences, deformations become larger, even giving rise to grating line inversion, where lines become valleys and valleys become lines. Our findings offer insights into predicting and mitigating light-induced damage in silicon gratings, relevant to semiconductor device manufacturing.

5.1. INTRODUCTION

In semiconductor device manufacturing, integrated circuits (ICs) are being made which consist of hundreds of different layers containing complex patterns [141]. For each lithography step, the wafer needs to be positioned with a very high accuracy. For this, alignment markers, often small gratings, are etched into the scribe lanes between the dies on the wafer. Light diffracted by these markers is used to measure the wafer position. To save wafer real estate, these alignment gratings are becoming smaller and smaller [15, 16]. This forces the illuminated area to decrease in size too. To keep the amount of diffracted light and, thus, the signal-to-noise-ratio the same, an increase in incident optical fluence is required. Unfortunately, this also increases the risk of light-induced damage. Whereas the effect of material [27, 136, 142], wavelength [28–30], pulse duration [31, 32], thickness [33, 34] and surface topography [143] on light-induced damage has been studied extensively in the past, this has mostly been done on relatively flat surfaces. Therefore, little is known about the effects of high optical fluences on the alignment gratings used in semiconductor device manufacturing.

Here we present experimental results from exposing six silicon gratings with varying pitches and duty cycles, as well as a flat silicon sample, to single laser pulses at optical fluences above and below the threshold for catastrophic damage. Our findings show similarities with previous research on flat aluminum and ruthenium layers [136, 144], in that optical changes occur below the ablation threshold fluence. These changes are attributed to single-shot melting and resolidification processes. Once the material surpasses its melting temperature, the grating lines start to deform and, at higher fluence, show line-valley inversion, where lines become valleys and vice versa. Our results confirm that the onset of optical changes coincides with the onset of structural deformation. They demonstrate that the fluence thresholds for all observed damage mechanisms are ≈ 10-50% lower in gratings compared to that of a flat silicon surface. These findings suggest that localized field enhancements, induced by the topography of the gratings, play a significant role in determining damage thresholds. This is reasonably well supported by forward diffraction modelling using rigorous coupled-wave analysis (RCWA) [64], used to numerically solve Maxwell's equations, from which the damage threshold scaling with respect to the flat silicon surface is estimated. While this method is useful as a first step to estimate damage thresholds, we observed only a moderate correlation between the calculated and experimentally obtained threshold fluence values. This suggests that more advanced calculations that include heat diffusion, and possibly hydrodynamical models, nonlinear absorption effects in silicon, and other time-dependent effects, are needed for improved accuracy.

5.2. EXPERIMENTAL DETAILS

5.2.1. SAMPLE OVERVIEW

In this research, seven different samples have been studied: flat bulk Si and six gratings etched in Si, each having different dimensions. An overview of the dimensions of all structures is given in table 5.1. Table 5.2 lists relevant properties of Si and SiO_2. Since little is known about light-induced damage on grating structures, the samples are exposed by single-shot high intensity pulses only. This simplifies the analysis and is an important first

step in increasing our general understanding of the optical and morphological changes that are induced by the light.

5.2.2. Setup

The pump-probe setup used for the experiments is shown schematically in figure 5.1 and is explained in more detail in section 2.2.2. Here, 45 fs laser pulses with a central wavelength of 800 nm are generated by a multi-pass Ti:Sapphire amplifier system at a 1 kHz repetition rate. Hereafter, the laser beam is split into a weak 800 nm probe beam and a strong 400 nm pump beam created by second harmonic generation in a Beta Barium Borate (BBO) crystal. The probe illuminates the sample under an angle of $\approx 10°$ with respect to the normal of the sample surface with the original repetition rate of 1 kHz. The fluence of the pump beam can be varied by rotating a $\lambda/2$-plate, placed before the BBO crystal. Next, a pulse picker system, formed by a 10% duty-cycle chopper and a galvo mirror, selects a single pump-pulse. The pump-pulse illuminates the sample at near-normal incidence. The probe and pump are focused onto the sample to spot sizes of ≈ 15 and $\approx 75\,\mu m$ respectively. The geometry of the beams and the sample are schematically shown in figure 5.1. In some cases, an additional $\lambda/2$-plate before the focusing lens of the pump is used to rotate its original polarization by 90°. A detailed description of the entire setup can be found in section 2.2.2.

Before each measurement series, a Gentec-EO Beamage-4M beam profiler is placed at the sample position where the pump and probe beam spatially overlap, to measure the pump and probe beam spatial profiles. Furthermore, a Coherent thermopile power sensor is placed in the pump beam path after the last mirror before the focusing lens. This is to calibrate the reference (switchable-gain Si) photodetector in order to convert the detector signal into a pump fluence (see section 2.3.1).

A variety of different gratings is etched into each die of a silicon wafer. The grating lines have an amplitude of $\approx 70\,nm$, and each individual grating has dimensions of $2 \times 2\,mm$. Therefore, as each pump shot has to illuminate a pristine, undamaged site, only a limited number of pump shots can illuminate each grating. As the pump has a FWHM of $75\,\mu m$ on the sample, the spacing between pump shots is chosen to be $200\,\mu m$. Therefore, single pump pulses hit each grating in a 8×9 grid. Each subsequent pump shot has a slightly higher fluence until half of the grid is covered. This illumination sequence is then repeated to check reproducibility, until the entire grid is filled. Here, the fluence ranges from well below any measurable morphological or optical change, to above the ablation threshold, where material is rapidly removed.

The experiments are repeated for different polarizations of the pump and probe beam relative to the grating lines. In total four different polarization combinations are used, where each set was performed on a new die. The polarization sets are schematically shown in figure 5.2.

At each illuminated site, before pump excitation, the 800 nm reflection R_{pre}, is obtained by measuring the probe reflection and a reference signal using photodetectors. R_{pre} is averaged over a thousand shots, giving $\bar{R}_{\text{pre}}$, which improves the signal-to-noise-ratio (SNR). The same is done for the thousand probe shots measured well after pump excitation ($\geq 1\,ms$), when all transient effects have disappeared, giving the average $\bar{R}_{\text{post}}$. The relative difference between $\bar{R}_{\text{pre}}$ and $\bar{R}_{\text{post}}$ is the *relative reflection change* ΔR:

Table 5.1: Overview of the used Si samples. The pitch and duty-cycle design values, and the cross section of a single unit cell of each grating, as obtained using atomic force microscopy, are shown. The black scale bars have a length of 100 nm and all gratings have a height of ≈70 nm.

Pitch (nm)	Duty cycle (%)[a]	Cross section[b]
Flat	N/A	
430	23.2	
430	34.8	
460	50	
600[c]	50	
950	50	
980	50	

[a]The duty cycle is defined as the ratio of valley width and grating pitch. [b]The left slope appears to be less steep than the right. This is not an AFM artefact but is inherent to all gratings due to the etching process. [c]There is a slight misprint in the 600 nm pitch grating: a small dent is observed at the left side of the facet following the left slope, which is apparent throughout the entire grating. However, this has a negligible effect on its optical response.

Table 5.2: Optical and thermal mechanical properties of silicon and silicon oxide

	Silicon (Si)	Silicon oxide (SiO$_2$)
$n + ik$ @ 400 nm	$5.631716 + 0.285821i$[a]	1.744466[b]
$n + ik$ @ 800 nm	$3.679123 + 0.004060i$[a]	1.730794[b]
T_m (K)	1687[c]	
Thickness (nm)	Bulk	2.1[d] (native oxide)
κ_l @ 300 K (W m^{-1} K^{-1})	124.0[c]	
C_l @ 300 K (10^6 J m^{-3} K^{-1})	1.63[c]	

[a]Ref. [111, pp.555-569], [b]Ref. [145], [c]Ref. [102, p.12-80], [d]Obtained by ellipsometry
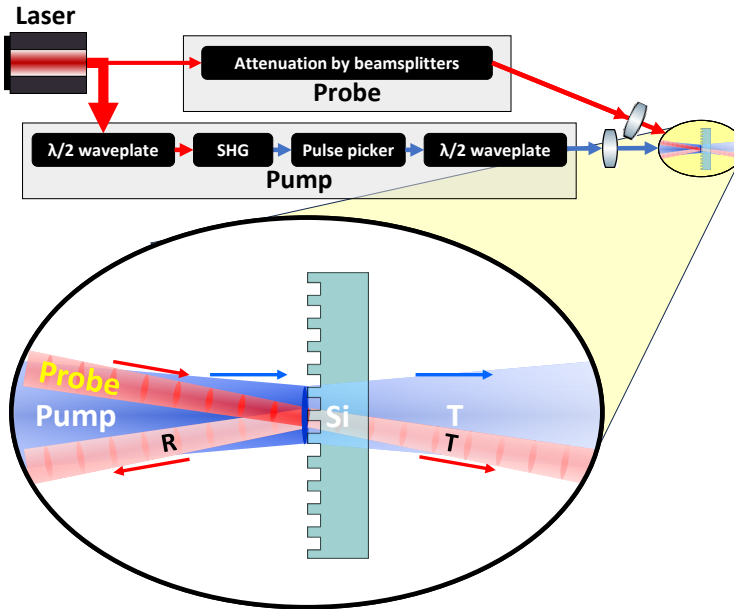

Figure 5.1: Schematic of the experimental setup. The 45 fs, 800 nm laser output is split into a strong pump and a weak probe beam. The pump beam passes a BBO crystal to frequency-double it to a 400 nm wavelength (SHG). The pulse-picking system selects up to single pulses. The pump beam is focused onto the sample using a $f = 20$ cm lens and the sample is placed a short distance before the focal point. The pump is at normal incidence on the sample and the probe beam is at an angle of $\approx 10°$ with respect to the surface normal. The power of the probe beam is attenuated by reflecting the beam off three beamsplitters before it is focused onto the sample. The pump pulse energy can be varied by rotating the $\lambda/2$-plate which is placed before the BBO. If a different polarization of the pump-beam is desired, an additional $\lambda/2$-plate is placed before the pump focusing lens that rotates the pump beam by $90°$. R and T indicate the reflected and transmitted pump and probe beams. A detailed description of the entire setup can be found in section 2.2.2.

$$\Delta R(F) = \frac{\bar{R}_{\text{post}} - \bar{R}_{\text{pre}}}{\bar{R}_{\text{pre}}}. \qquad (2.3/5.1)$$
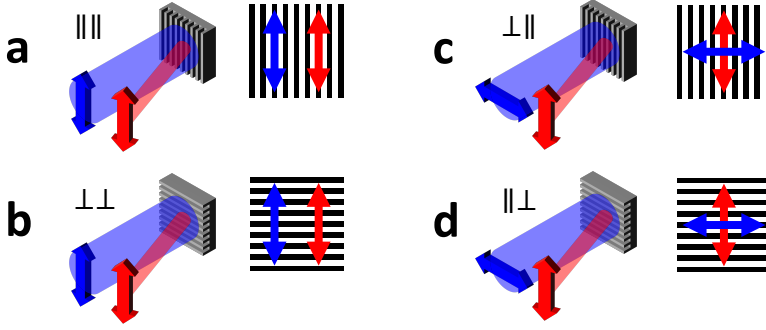
Figure 5.2: Schematic drawing of the four polarization sets. For all samples, full pump-fluence-dependent scans have been obtained for all shown polarization sets. This resulted in 28 measurement series. We only used $\parallel$ (parallel) and $\perp$ (perpendicular) polarization of the pump and probe light with respect to the grating lines. Here we inspected $\parallel\parallel$, $\perp\perp$, $\perp\parallel$ and $\parallel\perp$ polarization where the first character denotes the polarization of the pump and the second that of the probe beam with respect to the grating lines. Since $\parallel\parallel$ is the default polarization of the setup, the $\perp\parallel$ and $\parallel\perp$ polarizations have been made by transmitting the pump beam through a $\lambda/2$ waveplate. Additionally, the samples have been rotated by 90° around the normal of the sample surface to obtain the $\perp\perp$ and $\parallel\perp$ configurations.

These values for ΔR depend on the pump fluence F and are obtained for all samples, and are presented in section 5.3.1.

5.2.3. POST-PROCESSING

After each measurement series, the sample is taken out of the laser setup for inspection of the illuminated sites. Each sample containing 72 illuminated sites is inspected by bright-field (BF) and dark-field (DF) microscopy. Hereafter, a Helios Nanolab 600 scanning electron microscope (SEM) is used to study possible morphological changes. Selected sites are inspected further with a Bruker Dimension Icon atomic force microscope (AFM).

Various damage mechanisms were observed across all samples, each bounded by a contour that defines where the local fluence equals the threshold for that damage mechanism. Given the elliptical Gaussian beam profile, the boundaries of each damage mechanism manifest themselves as concentric ellipses. To quantitatively analyze these ellipses, optical microscopy images were processed using OpenCV [146] and a RANSAC algorithm [139], enabling the precise fitting of ellipses corresponding to different damage mechanisms. For a Gaussian beam profile, the area A of each fitted ellipse scales linearly with $\ln(F_0)$. By performing a linear regression of A against $\ln(F_0)$ for each damage mechanism, we obtain regression lines that intersect $A = 0$ at the fluence threshold F_{th}. This approach, known as the Liu-analysis (see sections 1.3 and 6.1), provides an accurate determination of the damage thresholds for all observed mechanisms.

5.3. Results and Discussion

5.3.1. Optical response

In situ

In figure 5.3a we show the relative reflection change induced by a single 400 nm pump pulse on a flat silicon surface, as a function of peak fluence F_0. This measurement will be used as a reference to compare the gratings with. For low fluences, F_0 is too weak to induce an optical change ($\Delta R \approx 0$). However, above a certain fluence $F_\uparrow$, there is a steep ΔR increase. For further increasing fluences, ΔR starts to decrease (around $\Delta R \approx 30\%$) near the ablation threshold, and will eventually become negative. A somewhat similar behavior is observed for all gratings in this study (figure 5.3b-g). However, next to similarities, there are also some differences. Although all gratings display a positive ΔR increase in the low fluence regime, the fluences where this occurs ($F_\uparrow$) are slightly (10-30%) lower than that for the flat silicon sample. Additionally, for $\perp$-polarized pump light, *two* local $\Delta R(F_0)$ maxima are present in some gratings. In the relatively high fluence regime, the fluence threshold values for ablation and crater formation (F_{abl} and F_{crater}), depend heavily on pump polarization and grating parameters.

As was previously shown for aluminum and ruthenium (chapters 3 and 4), the probe reflectivity can change due to single-shot melting and resolidification. There the grain structure (size and crystal orientation) changes, changing the electron mean free path, and therefore the effective refractive index of the metal. However, this is different for the silicon, which in the pristine state is monocrystalline. Nevertheless, melting and resolidification can change the single crystal into a polycrystalline [147, 148] or amorphous structure [149, 150], increasing the reflectivity up to 30-40% around 800 nm [147]. Additionally, local melting of the silicon will also result in the deformation of the grating lines, which alters the specular reflection of the probe beam. Furthermore, light-induced heating of the material can also cause enhanced oxidation [151]. Crystal structure change, grating line deformation and enhanced oxidation will all influence the probe reflection and therefore ΔR. Unfortunately, their contributions to the total reflection changes cannot easily be separated in the measurements.

Ex situ

The probe reflection (figure 5.3) versus fluence can be divided into different fluence regimes. For fluences below the onset of ablation, so before the rapid removal of material, $\Delta R(F_0)$ displays various 'jumps'. These sudden changes in $\Delta R(F_0)$, are also visible in the optical microscopy images. Here, brighter areas are visible which are bounded by a local fluence F_{th}, that can give rise to sudden jumps of ΔR or $\frac{\partial \Delta R}{\partial F}$.

Figure 5.4 shows optical bright-field (BF), dark-field (DF), and scanning electron microscopy (SEM) images of three damaged sites. Figure 5.4a-c depict a flat silicon site exposed to a pump pulse with a fluence exceeding the crater formation threshold at its center. Figure 5.4d-f and figure 5.4g-i display the same types of images for a 950 nm pitch, 50% duty-cycle grating, illuminated with $\perp$-polarized and $\parallel$-polarized pump light respectively. In all cases, the local pump fluence at the center of the illuminated sites exceeded the crater formation threshold, resulting in multiple damage mechanisms manifesting themselves at varying distances from the illumination center as the local fluence decreases.

5

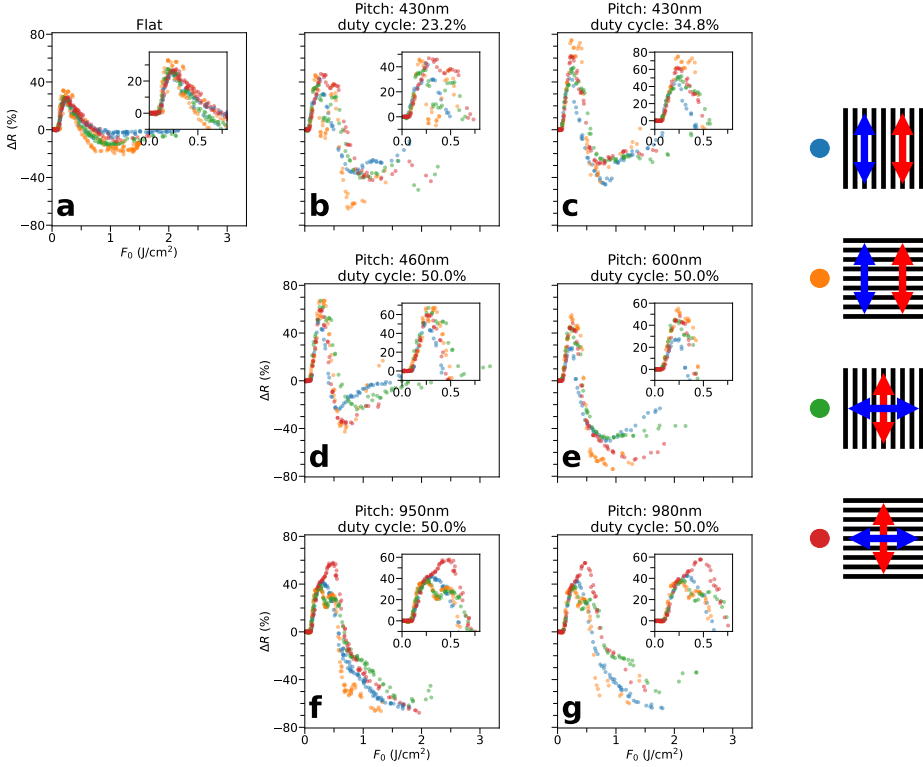Figure 5.3: Measured relative reflection change ΔR versus the peak pump-pulse fluence F_0 for the flat silicon surface (a) and six silicon etched gratings (b-g). The colors indicate the pump and probe polarizations with respect to the grating lines, which is explained in more detail in figure 5.2. For low fluences, F_0 is too weak to induce an optical change ($\Delta R \approx 0$). However, for slightly higher fluences, there is a steep ΔR increase. For further increasing fluences, ΔR starts to decrease, reaching the ablation threshold, and will eventually drop below 0%. This characteristic behavior is somewhat present in all gratings. However, $\Delta R(F_0)$ depends on grating parameters as well as pump and/or probe polarization. Multiple $\Delta R(F_0)$ peaks are present in some gratings for a $\perp$-polarization of the pump beam.
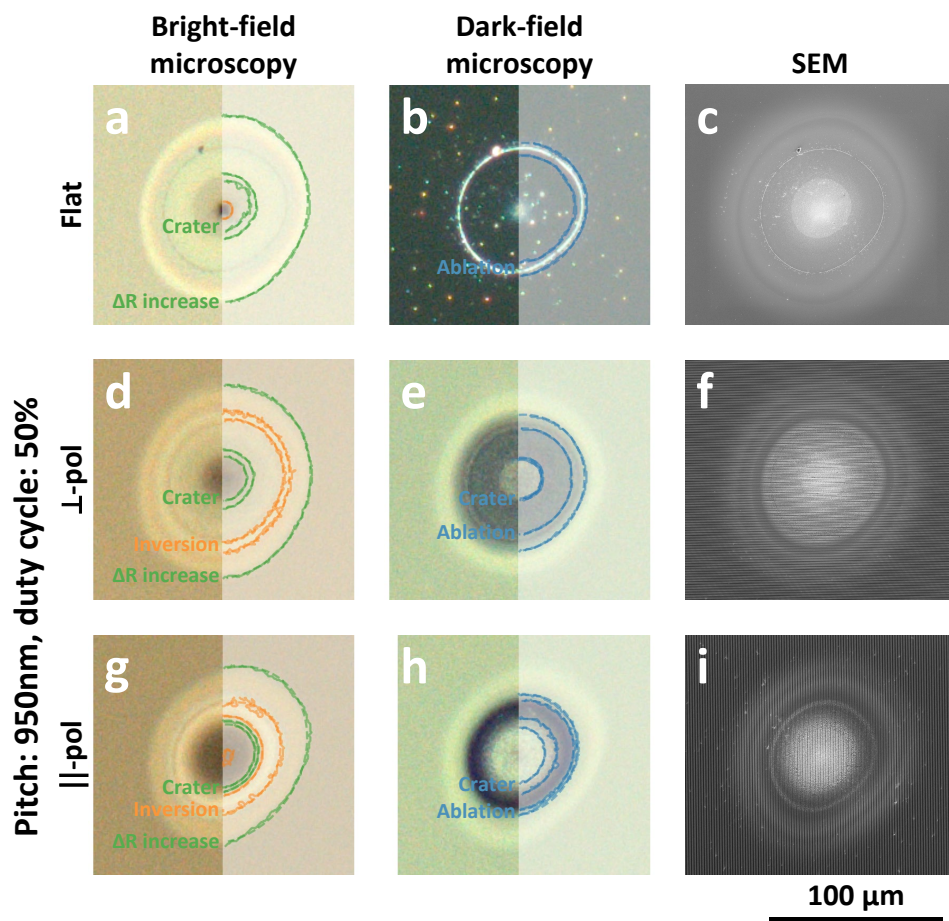
Figure 5.4: Optical bright-field, dark-field and SEM images for three damaged sites: a flat silicon surface (a-c), and a 950 nm pitch, 50% duty-cycle grating illuminated with ⊥-polarization (d-f), and ∥-polarization (g-i). Because the local pump fluence exceeded the crater formation threshold in the center of all illuminated sites, all (lower fluence) damage mechanisms are observed when moving away from the illumination center, to lower local fluences. An ellipse fitting procedure (see section 6.1) applied to the damaged contours is compiled using an algorithm three times: Once using dark-field images, and twice using the bright-field images with two different contrast settings indicated by the blue, orange and green ellipses respectively. The corresponding damage mechanism is obtained by inspection of additional SEM images. The corresponding Liu-plots are shown in figure H.2.

In figure 5.4b, the dark-field image of the flat surface displays a single bright ring which represents the ablation edge. Outside this edge, but surprisingly, also inside the ablation edge, the surface is still relatively flat, and therefore appears dark in the image. Unlike the flat surface, the gratings scatter more strongly, making the dark-field image bright (figures 5.4e and 5.4h). Extracting the ablation edge is therefore less straightforward. Because of this, a set of edges is acquired by obtaining contours and fitting ellipses to the bright and dimmer rings visible in both the bright- and dark-field images (see section 6.1). From the areas spanned by these ellipses, Liu-analysis is performed to obtain the corresponding fluence thresholds. For each fluence threshold, the corresponding damage mechanism is obtained by inspection of additional SEM images. Liu-analysis has been performed for all samples and a list of fluence thresholds and corresponding damage mechanisms can be found in appendix H.2.

5.3.2. Fluence thresholds

First, the fluence threshold $F_\uparrow$ at which ΔR increases is determined. Since this is the lowest fluence where pump-induced (optical) changes form, it is very likely that only one process contributes to the optical change. Second, the grating lines deform, as is discussed in more detail in section 5.3.3. This deformation indicates that the melting threshold has been reached. This is still at relatively low fluences, but will affect the grating topography significantly. At F_{dark}, a dark shade is seen in the SEM images (figure 5.4). This is used to select the proper F_{dark} for the flat surface, since this dark shade is also visible on the flat surface where no grating line deformation can occur. Finally, the high-fluence damage thresholds F_{abl} and F_{crater} are determined. Here, material is ablated, where at F_{abl} material is removed superficially, and at F_{crater} a crater starts to form. F_{abl} and F_{crater} are distinguished by comparing the optical microscopy images with SEM images (see figure 5.4). In this high-fluence regime, some intriguing morphological changes are found in the gratings, such as line-valley inversion (see section 5.3.3).

Figure 5.5a shows the threshold fluences $F_\uparrow$, F_{dark}, F_{abl} and F_{crater} found by Liu-analysis for the flat silicon surface and gratings. To compare the thresholds with that of the flat surface, the thresholds for each damage mechanism are shown separately in figures 5.5b to 5.5e and expressed as the fraction of their corresponding threshold value of the flat silicon surface. Additional SEM images are shown in figure H.4. Since all samples only differ in surface topography, the difference in damage thresholds can only be attributed to the difference in grating parameters.

Total absorption

To learn more about the influence of the grating period and duty cycle on the light-induced damage threshold, we determined how much light is absorbed in the gratings first. This is done by solving Maxwell's equations by performing forward diffraction modelling using rigorous coupled-wave analysis (RCWA) [64]. First, the total absorbed fraction of the pump-pulse, $Abs = 1 - \sum_{n=0}^{N} R_n$ is computed where R_n is the nth order fraction of reflected/diffracted light[a]. In figure 5.5b-e, its inverse ($\frac{1}{Abs}$) is plotted for parallel (solid black line) and perpendicular (dashed black line) pump polarization for all gratings. To compare this with the obtained fluence thresholds, $\frac{1}{Abs}$ is multiplied

---

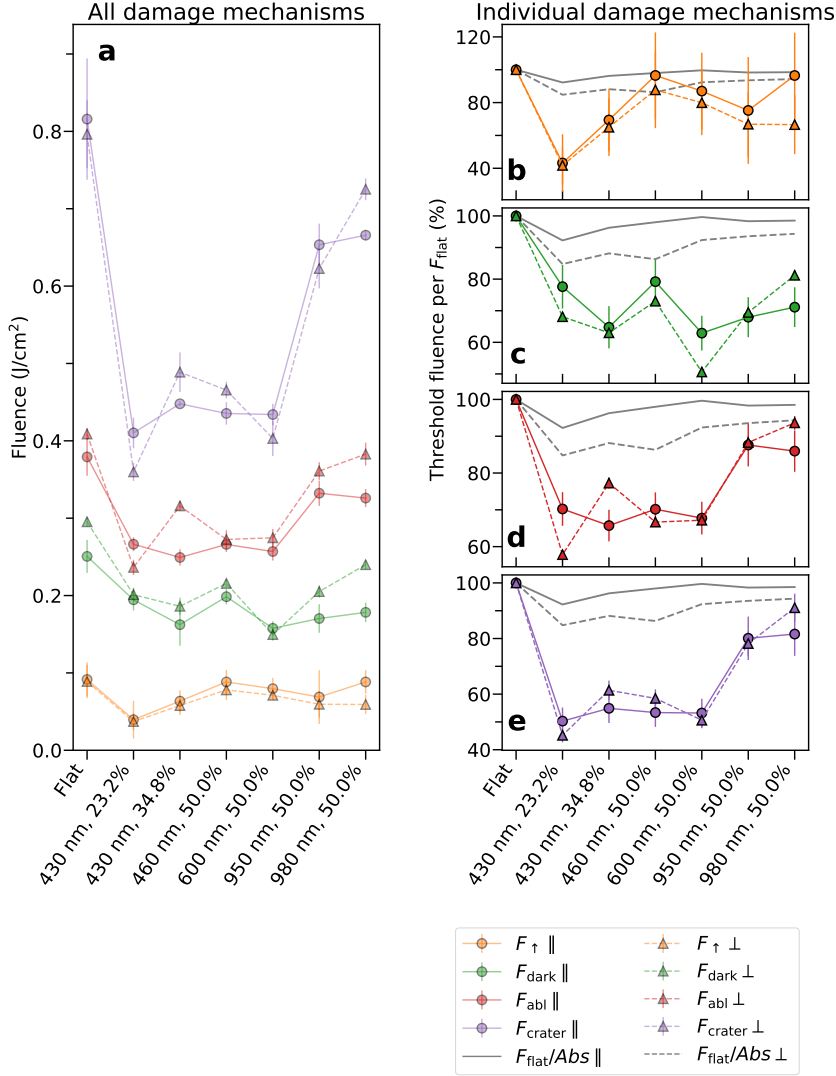[a]Here we considered the first 50 diffracted orders ($N = 50$).

Thresholds

Figure 5.5: Experimentally obtained fluence thresholds $F_\uparrow$ (orange), F_{dark} (green), F_{abl} (red) and F_{crater} (purple), shown together (a), and individually (b-e), for the flat surface and gratings. The solid lines with round markers, and the dashed lines with triangular markers indicate parallel ($\parallel$) and perpendicular ($\perp$) pump polarization respectively. The lines connect the data points, and are included as a guide to the eye only. The black lines indicate $\frac{Abs_{flat}}{Abs}$, which is a line to show the inverse of the calculated absorbed fraction (Abs) scaled to the absorbed fraction of the flat surface. If the amount of total absorbed light defines the values of the damage threshold, the black lines should follow the $F_\uparrow$, F_{dark}, F_{abl} and F_{crater} data points (orange, green, red and purple), which they do not.

by the calculated absorption for flat Si (Abs_{flat}). This is done so $\frac{1}{Abs} \cdot Abs_{\text{flat}}$ to coalesce with the scaled measured fluence thresholds $\frac{F_x}{F_{x,\text{flat}}}$ for the flat Si in figure 5.5b-e (left most data point). Here x denotes the damage mechanism ('↑', 'dark', 'abl' or 'crater'). If the damage thresholds would depend only on the total absorption, the calculated values for $\frac{Abs_{\text{flat}}}{Abs}$ would follow the same trend as the measured $\frac{F_x}{F_{x,\text{flat}}}$ thresholds for the gratings. According to the calculated $\frac{1}{Abs}$ values, damage should occur at lower fluences in gratings in comparison with the flat surface, and parallel pump illumination should correspond to a lower threshold fluence. This is qualitatively in accordance with the measured fluence threshold behavior. However, the *measured* threshold fluence *variation* with grating parameters, compared to the *calculated* $\frac{1}{Abs}$, is significantly different. The difference between the measured threshold values is on average much greater than the total calculated absorption difference would suggest. This means that the total absorption is not the determining factor for the light-induced damage. For this reason, it is also useful to study how the light is locally absorbed in the grating, as it seems plausible that the grating parameters influence the *local* absorbed power density due to local field effects. Therefore, near-field RCWA calculations are performed from which the local power density is calculated.

NEAR-FIELD CALCULATIONS

From the calculated $\mathbf{E}(x,z)$ and $\mathbf{H}(x,z)$ fields (see appendix H.3), the time-averaged Poynting vector, $\langle\mathbf{S}\rangle$, is derived,

$$\langle\mathbf{S}\rangle(x,z) = \frac{1}{2}\operatorname{Re}(\mathbf{E}(x,z) \times \mathbf{H}^*(x,z)), \qquad (1.46a/5.2a)$$

from which the local absorbed power density $\frac{du}{dt}$ equals:

$$\frac{du}{dt}(x,z) = -\nabla \cdot \langle\mathbf{S}\rangle. \qquad (1.46b/5.2b)$$

In the case of linear absorption, the local absorbed power density $\frac{du}{dt}$ is proportional to the incident fluence F. Furthermore, the fluence is taken constant over the unit cell. In figure 5.6, $\frac{du}{dt}(x,z)$ is shown for all gratings illuminated with the same fluence F for both parallel and perpendicular polarization with respect to the grating lines. While for the flat surface, $\frac{du}{dt}$ falls of approximately exponentially when moving deeper into the material (Beer-Lambert law), concentrated 'hot-spots' emerge in the grating structures. The local absorbed power in those hot-spots can exceed the maximum value of $\frac{du}{dt}$ found in the flat samples by approximately a factor of 3, and strongly depends on grating parameters. Moreover, the grating parameters, as well as pump-polarization, determine the locations of the hot-spots. For parallel pump-polarization, the hot-spots are more localized at the grating line slopes, and for perpendicular pump polarization more towards the center of the lines.

We can use the derived $\frac{du}{dt}(x,z)$ spatial profiles to calculate what the highest optical absorbed power density in the grating is and where this is reached. This can then be compared with that of a flat Si sample and with the measured damage thresholds to determine whether there is a correlation between the calculations and the experimentally
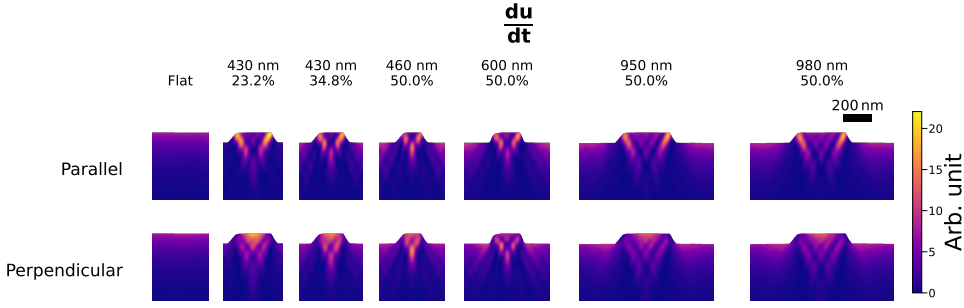
Figure 5.6: The calculated absorbed local power density $\frac{du}{dt}(x,z)$ for all samples illuminated by the same incident fluence with a polarization parallel (top) and perpendicular (bottom) to the grating lines. The $\frac{du}{dt}(x,z)$ profiles are derived using forward diffraction modelling using rigorous coupled-wave analysis (RCWA) [64] and linear absorption is assumed.

obtained thresholds. This is done by calculating the mean value of $\frac{du}{dt}$ over an area A. While keeping the area size fixed, the exact shape of A is defined by maximizing the mean value of $\frac{du}{dt}$ bounded by A. More information can be found in appendix H.4. By using these local power density maxima, and the experimentally obtained threshold fluences for the flat surface, we get the calculated fluence thresholds of the gratings (see appendix H.4). The correlation between the experimentally obtained F_{dark}, F_{abl} and F_{crater}, and the calculated values is stronger using the highest local absorbed power densities, compared to only considering the total integrated absorption. However, we still observe only a moderate correlation between the calculated and experimentally obtained values. In figure H.6 we show that this also strongly depends on the chosen value for A. It seems likely, though, that localized field enhancements induced by the topography of the gratings play a significant role. From the $\frac{du}{dt}$ profiles in figure 5.6, it is clearly visible that these enhancements are experimentally lower in gratings with a larger pitch of 950 and 980 nm, which is in line with the experimentally observed higher damage thresholds. In principle, incorporating heat diffusion and, possibly, hydrodynamical models and nonlinear absorption effects in silicon, could significantly improve the model to estimate the fluence threshold of a patterned surface with respect to the threshold of the flat topography more quantitatively. This is, however, beyond the scope of this work.

5.3.3. DEFORMATIONS
HEIGHT INCREASE, FLATTENING AND INVERSION
In the fluence range between the optical change threshold ($F_\uparrow$) and crater formation (F_{crater}), the grating lines undergo various deformations. Figure 5.7 illustrates these deformations with detailed SEM and AFM images using a 600 nm pitch, 50% duty-cycle grating illuminated by a single-shot ∥-polarized pump beam as an example. The SEM images (figure 5.7a) and cross-sectional profiles obtained via AFM (lines 1 to 6 in figure 5.7b) show the effect of the increasing local fluence (F_{local}) on deformation, when moving towards the center of the illumination spots. On the SEM images in figure 5.7a, six lines are indicated by a number, which corresponds to the six cross sections of the lines as

shown in the AFM images in figure 5.7b. At relatively low fluences, the lines deform as they increase in height and become less rectangular (lines 1 and 2). As the fluence increases, the lines broaden and decrease in height, eventually forming a small double ridge (line 3). Hereafter, the line flattens completely (line 4), and *inversion* starts to occur (line 5), where lines transform into valleys (also called spaces) and vice versa. Interestingly, the lines that emerge post-inversion can exceed the original grating line amplitude (≈ 70 nm) while maintaining steep edges (line 6). Debris observed near the inversion onset (line 4) marks the ablation threshold (F_{abl}). As the local fluence approaches F_{crater}, the grating lines no longer have a fixed cross-section profile when taking cross sections of the same grating line in different locations along the line. This is due to irregular deformation along the grating line direction and is clearly visible in the irregular shape of the grating lines in the vertical direction in the lower right SEM image in figure 5.7a.

GRATING PARAMETERS AND POLARIZATION DEPENDENCY

The deformation sequence described above is relatively consistent across all examined gratings. This is demonstrated in figure H.4, where SEM line scans depict the evolution of deformations across the flat surface and for all six different gratings, each illuminated by $\perp$ or $\parallel$-polarized pump-pulses. While this general deformation pattern is observed across all samples, the specific progression depends on the grating parameters (pitch and duty cycle) and pump polarization. Optical near-field calculations, discussed in section 5.3.2 and shown in figure 5.6, reveal that the local absorbed power density is differently distributed within the considered unit cells, depending on grating parameters and pump polarization. This will effect how the grating lines will deform. For $\parallel$-polarized pump illumination, the power is more concentrated at the grating line slopes, while for $\perp$-polarization, this is around the center of the lines. Larger pitches exhibit a more diffuse power absorption, especially under $\perp$-polarized light, which possibly explains the less pronounced inversion. This difference is visible when comparing the deformed line shapes of the 950 nm and 980 nm pitch gratings, compared to that of smaller pitches, as can be seen from the SEM line scans in figure H.4. For the 430 nm/23.2%, 430 nm/34.8%, 950 nm/50% and 980 nm/50% samples, the shape of the deformed grating lines (for $F > F_{abl}$) differs substantially between $\parallel$ and $\perp$-polarization. These are the same samples that display the biggest change in local absorbed power density distribution (hot spots and distribution in figure 5.6) between the two considered polarizations as well.

REFLECTION CHANGE AFFECTED BY TOPOGRAPHY CHANGES

Previous studies on flat aluminum and ruthenium layers (see chapters 3 and 4) also show a reflectivity increase when exposed to single pump-pulse fluences below the ablation threshold. For the aluminum and ruthenium layers, this optical change is due to single-shot melting and resolidification, increasing the average grain size, leading to reflectivity increases between 0.1 and 5%. In silicon however, melting and resolidification changes the single crystal into a polycrystalline [147, 148] or amorphous structure [149, 150], which increases the reflectivity up to 30-40% around 800 nm [147]. By reaching this melting threshold, the resulting material flow can potentially cause the grating lines to deform. To further investigate the relationship between this topographical change and the optical reflection changes, RCWA far-field calculations were performed. Grating line deformation will directly change the diffraction efficiency, and thus changing the measured reflection
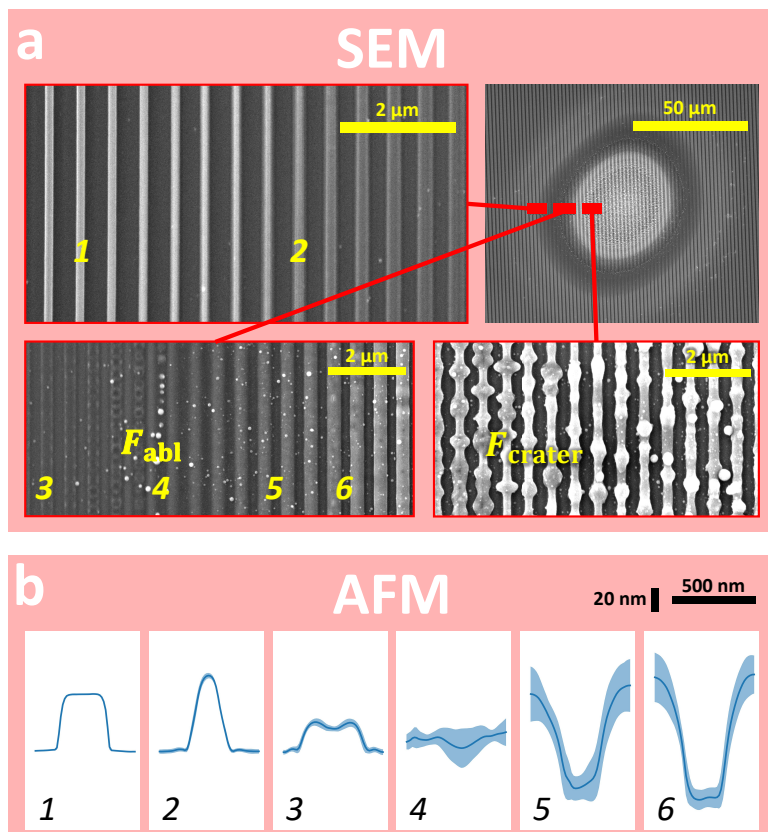
5

Figure 5.7: Overview of grating line deformation of a site on a 600 nm pitch, 50% duty-cycle grating illuminated with a single ‖-polarized pump shot. (a) SEM images and (b), cross sections measured by AFM. The local fluence F_{local} decreases when moving away from the illumination center. At the SEM images in (a), the red rectangles mark the sections of which zoomed-in versions are also shown. The numbers *1-6* mark the approximate locations of the cross sections as obtained by AFM shown in (b). The cross sections are derived from 2D height scans obtained by AFM, using the median and standard deviation along the direction of the grating lines, as the cross-section height (blue line) and uncertainty (light blue shading). The black rectangles indicate the vertical and horizontal scale of the AFM cross sections.

of the probe light. Therefore, we calculated the reflectivity of deformed grating lines that are exposed to a (local) fluence F_{local}, and compared this to the reflection of the unexposed geometry, resulting in a relative reflection change of the probe by only considering grating line deformation ΔR_{def} (equation (2.3/5.1)). In these calculations, it is thus assumed that the optical properties of the material itself have not changed. This is for sure incorrect but allows us to determine the effect of *only* a changing topography on the reflection. Each calculated ΔR_{def} value is obtained by making AFM scans of a few grating lines near the center of an illuminated site. From these, cross sections are obtained, and for each cross section the probe reflection is obtained by RCWA far-field calculations. This is then compared with the calculated reflection of pristine grating lines, which results in a relative reflection change for each grating line cross section. Since each AFM scan spans several unit cells, averaging over the cross sections of all unit cells results in an average value for ΔR_{def}. This is then repeated for each illuminated site. The results of these calculated values of ΔR_{def} are shown in figure 5.8, together with the measured ΔR_{meas} versus fluence for a 980 nm/50% grating illuminated by single ∥ (figure 5.8a) or ⊥-polarized (figure 5.8b) pump pulses. The 980 nm/50% grating is considered here because of the significant difference of the ΔR_{meas} curves between the two pump polarizations. As illustrated in figure 5.8b, when the grating is illuminated by a perpendicularly polarized pump beam, the measured ΔR_{meas} exhibits a characteristic double-peak behavior as the fluence increases. In contrast, this feature is absent when the grating is exposed to a parallel-polarized pump pulse, as shown in figure 5.8a.

At fluences near F_{crater}, the grating lines exhibit significant (quasirandom) deformations along their length, which compromises the reliability of the calculated ΔR_{def} values. These deformations result in an ill-defined cross section of the unit cell as used as input for the RCWA code [64], as it relies on the assumption of a constant, smooth topography along the grating lines. Therefore, our analysis focuses on ΔR_{def} for fluences below F_{crater}.

As shown in figure 5.8, The calculated ΔR_{def} begins to change around $F_\uparrow$, marking the onset of optical changes. This suggests that as optical changes occur, the grating lines start to deform, indicating that the material's melting temperature is reached at $F_\uparrow$. In the same figure where the measured ΔR_{meas} is shown, we have plotted the calculated ΔR_{def}, obtained by using the measured fluence dependent grating line cross sections in the RCWA calculations. It reproduces the same key features as ΔR_{meas}, with a single-peak curve for parallel pump-polarization and a double-peak curve for perpendicular pump-polarization. The calculated ΔR_{def} and measured ΔR_{meas} roughly follow the same fluence dependence ($\Delta R_{def} \propto \Delta R_{meas}$). However, the calculated ΔR_{def} tends to underestimate the measured relative reflection changes as measured at ΔR_{meas}. This is because ΔR_{meas} contains both the increase in reflectivity caused by grating line deformation, and those caused by refractive index changes, whereas the calculations ignore the latter. The impact of the reflectivity changes on ΔR is evident from the positive measured ΔR_{meas} observed on flat silicon surfaces (see figure 5.3a). Comparing the AFM cross sections depicted in figure 5.8c, the deformation sequence between ∥ and ⊥ pump polarization is indeed different. Especially around the double peak position (line 3 and 7), where, for ∥ polarization, the line and valley have the same shape, whereas for ⊥ polarization, only a small part of the line remains, and a steep slope at the inverted valleys is formed. When considering both probe polarizations, our calculations show that the double peak is
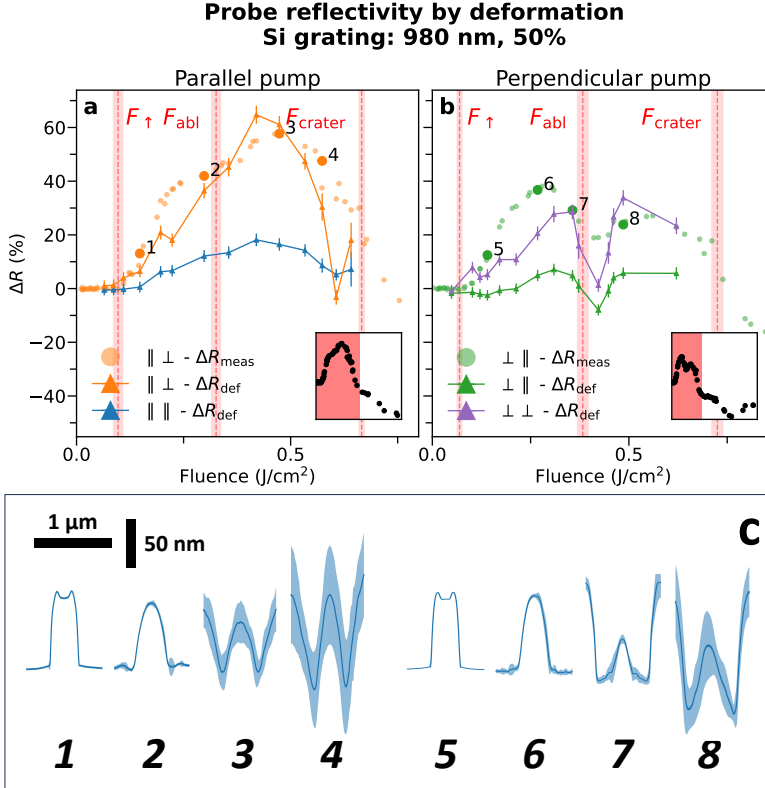
Figure 5.8: (a-b) the measured and calculated relative reflection change of the probe pulses ΔR_{meas} and ΔR_{def} versus pump (peak) fluence F, induced by pump-pulses polarized parallel (a) or perpendicular (b) to the lines of a 980 nm, 50% duty-cycle silicon grating. The round markers correspond to the measured values of ΔR_{meas}, and the triangular ones to the calculated ΔR_{meas}. ΔR_{def} is derived by obtaining the cross sections of the deformed and pristine grating lines by AFM and by calculating the reflection using far-field RCWA [64]. For ΔR_{def}, both parallel and perpendicular polarizations are considered, and for ΔR_{meas} only one is measured: perpendicular at (a) and parallel at (b). *1-8* mark the data points that correspond to the deformed unit cell cross sections shown in (c). The cross sections are derived from 2D height scans obtained by AFM, using the median and standard deviation along the direction of the grating lines, as the cross-section height (blue line) and uncertainty (light blue shading) respectively. The black rectangles indicate the vertical and horizontal scaling of the AFM cross sections.

absent for ∥ (figure 5.8a) but present for ⊥ (figure 5.8b) pump-polarization. Additionally, ⊥-polarized *probe* light enhances the sensitivity to the reflection change as induced by deformation. On top of this, the optical reflectivity shows reflection features, such as the double peak structure found in figure 5.8b, which can only be attributed to grating line shape changes only. So next to changes in the complex refractive index, the reflectivity of gratings is also strongly affected by modification in the shape of the grating, resulting in, for example, a double peak structure in the reflectivity change as function of pump pulse fluence.

5.4. CONCLUSIONS

We investigated light-induced optical and topographical changes on flat silicon and silicon gratings exposed to single ultrafast laser pulses, with pump polarization parallel or perpendicular to the grating lines. For the gratings, additional thresholds for structural changes such as deformation, ablation, and crater formation were identified. The damage threshold fluences were found to be 10 to 50% lower for gratings than for flat silicon. Calculations suggest that localized field enhancements resulting from the grating topography significantly influence damage thresholds, indicating that localized effects, rather than total power absorption, determine damage thresholds. Using near-field RCWA, we calculated power density profiles to predict fluence thresholds, showing moderate correlation with experimental values. Hence further model refinements are needed, such as the incorporation of heat diffusion, hydrodynamics, and nonlinear effects to make the model more quantitative. Our experiments show that the onset of optical changes coincides with the onset of grating line deformation, implying that the melting temperature is reached. On top of changes in the complex refractive index, we found that the enhanced relative reflection changes (ΔR) for gratings, with respect to those for flat silicon, were due to grating line deformation.

The onset of these deformations, resulting in optical changes, can serve as an early indicator of catastrophic failure. Our work provides the beginning of a framework for predicting and reducing light-induced damage in gratings by correlating grating pitch and duty cycle with optical damage.

Background for the General Reader

"I'm trying to elevate small talk into medium talk."

Larry David in *Curb Your Enthusiasm,* Season 8, Episode 6

Like the aluminum and ruthenium layers, the exposed silicon samples also initially exhibit a light-induced irreversible change. This occurs in both flat silicon samples and those with a ridged surface.

However, we found that in ridged samples, or **gratings**, this change occurs at lower light intensities compared to flat silicon. Since it is induced by melting, which deforms the ridges, this optical change is considered as catastrophic damage. This implies that similar structures may be affected during chip fabrication. Thus, the examined gratings are not only more susceptible to damage, but this damage is catastrophic too.

Furthermore, the exact **damage threshold** varies depending on the precise shape of the ridges. However, always testing all structures to obtain the thresholds beforehand is not feasible. Therefore, we estimated these damage thresholds by determining the damage threshold for flat silicon and incorporating it, along with the known grating shape, into a calculation model, and compared that to the values that we actually measured in the lab.

The goal of these calculations is to predict the damage threshold for structured samples relative to the, more easily obtainable, threshold for a flat version of the same material. However, while our calculations provide a better prediction of the damage thresholds, there is still room for improvement.

We tried to contribute to the understanding of damage, and at the same time lay the groundwork for future tools that can predict damage in practical applications.

6

VALORIZATION

This chapter features a description of an automated framework for determining damage thresholds directly from microscopy images, along with an overview of the experimentally obtained light-induced damage thresholds.

First, we introduce a Python-based algorithm developed for this purpose. The code uses a straightforward analysis to derive the fluence threshold from our experiments. It automatically extracts contours of damaged areas from images. Depending on the peak fluence, multiple damage contours may appear, which are analyzed using a RANSAC approach to automatically identify different damage *mechanisms* for each sample.

Hereafter, we provide a comprehensive overview of all identified damage thresholds. To illustrate the various damage mechanisms, additional optical microscopy, SEM, and AFM images are included. Besides gold, aluminum, ruthenium and gratings etched in silicon, materials described in previous chapters, this section also examines amorphous carbon, EUV resists, Si_3N_4 and SiO_2.

6.1. ANALYSIS

As is presented in section 1.3.1, a simple analysis can be used to obtain the fluence threshold F_{th} from our experiments. This uses the assumption that damage occurs where the local fluence $F(x, y)$ exceeds some threshold fluence F_{th} on the surface. This means that the boundary of that damaged area is where $F(x, y) = F_{th}$. Now, a simple analysis can be used to extract F_{th} from the experimentally obtained peak fluences F_0, the damaged areas A and the beam profile shape. For an (elliptical) Gaussian beam profile, the following relation applies:

$$A(F_0) = \frac{\pi d_x d_y}{4\ln(2)}(\ln F_0 - \ln F_{th}), \quad (1.54/6.1)$$

with d_x and d_y the full width at half maximum (FWHM) of the beam profile along the long and short axis respectively. During a measurement, several pristine sites of the inspected material are exposed with each a different peak fluence F_0. Since d_x, d_y and F_0 are directly measured, equation (1.54/6.1) can be solved for F_{th} once A is known. Therefore, microscopy images are obtained for each illuminated site from which the damaged area A is obtained.

To obtain the damaged area A from microscopy images, the images have to be properly processed and analyzed. This process is automated by a Python script [152]. This Python code extracts contours of the damaged area automatically from a set of images, each containing a single or a grid of illuminated sites. Depending on the (peak) fluence, multiple damage contours per illuminated site can be found. The Python code has been made available through `https://git.amolf.nl/Light-Matter_Interaction/contour.git`, and the developed algorithm is presented in this section.

6.1.1. IMAGE PROCESSING
The steps that are followed in computing the area from the microscopy image are shown in figure 6.1. As input, an image of an n by m grid containing multiple illuminated sites is used. From this, each site is isolated, and each isolated image is enhanced. The enhancement is done multiple times to be sensitive to both low and high-contrast damage edges. From each enhanced image, a set of contours are found using OpenCV, a computer vision library [146], and by using Canny edge detection [107]. Hereafter an algorithm is employed to select a proper subsection of all contours. This involves removing some contours based on their center offset with respect to the illumination center, imposing a maximum cutoff value for the contour area, making additional rules about overlap, and merging contours together.

6.1.2. ELLIPSE FITTING
To the obtained set of contours, multiple ellipses can be fitted. For a site illuminated by a peak fluence F_0, at least one ellipse is present for each damage mechanism with threshold fluence $F_{th} < F_0$, when visible in the processed image. This represents the corresponding border of the damaged area. However, sometimes one damage boundary creates two ellipses: one on the inside and one at the outside of the border as is depicted in figure 6.2.

To the set of selected contours, several ellipses are fitted. The fitting algorithm uses a random sample consensus (RANSAC) approach [139]. This is done by randomly selecting multiple points on a contour and fitting an ellipse through them. Points within a certain distance of the fitted curve are added to the selected points, and if not enough points are in proximity, the fit is omitted. The unfitted points are collected and are added to the points to consider for the next ellipse to fit. After multiple recursions, this results in a set of multiple ellipses, insensitive to, for example, droplets covering a damaged border as is depicted in figure 6.2. From each fitted ellipse, the area A is obtained from the ellipse parameters (see section 6.1.2).

An ellipse is fitted using the Halir and Flusser ellipse fitting algorithm [108]. This method is non-iterative, and therefore fast, and produces an ellipse-specific solution even for scattered data. Each fit returns the central coordinates (x_0, y_0), the semi-major and semi-minor axis a and b, and the angle of inclination ψ which is the angle between the
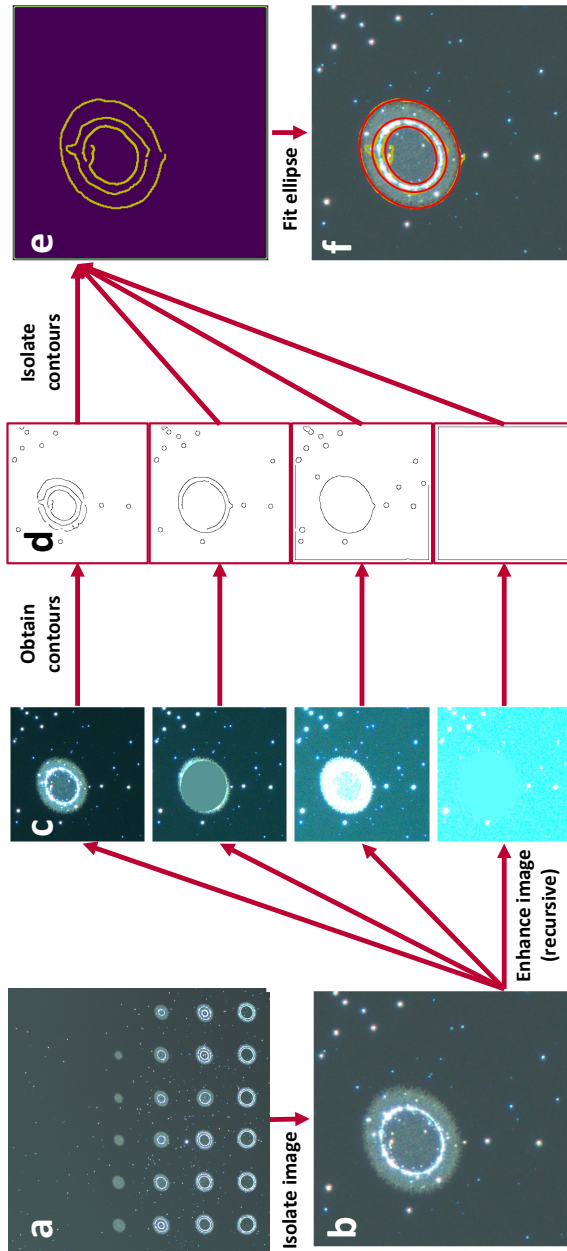
Figure 6.1: The steps that are followed in computing the area from the microscopy image. An optical dark-field image of 20 nm ruthenium on borosilicate glass is considered here. The input image (a) is a six-by-six grid containing illuminated sites with a varying peak fluence F_0. After isolation (b), multiple enhanced images are obtained (c). The enhancement is done multiple times to be sensitive to both low and high-contrast damage edges. From each enhanced image, a set of contours (d) is found using OpenCV, a computer vision library [146]. Hereafter a algorithm is employed to select a proper subsection of all contours (e). This is done by removing some contours based on their center offset with respect to the center, maximize the area of each contour and make additional rules about overlap, and merging contours together. To the resulting contours, several ellipses are fitted (f, section 6.1.2). The area A is obtained from the ellipse parameters.

Figure 6.2: A 10 nm thick gold layer on borosilicate glass illuminated above the ablation threshold. The delaminated ablation edge creates an inner and outer contour as is shown on the right side.

6

major axis and the horizontal axis. The area A equals πab.

6.1.3. RANSAC LINEAR FITTING

For all found ellipses of all illuminated sites exposed to a peak fluence F_0, the area A is obtained and plotted versus $\ln(F_0)$ in the so-called Liu-plot [74] as is shown in figure 6.3. This figure shows all fitted linear regression lines as obtained by our RANSAC-code. The values for F_{th} are extracted by the fitted lines, following equation (1.54/6.1), that intersect the x-axis with $\ln(F_{\text{th}})$. Additionally, the slopes of the lines scale with the spot size (see equation (1.54/6.1)), so the lines run (approximately) parallel to each other. This is clearly visible in, for instance, figure 6.3a. However, as can be seen in figure 6.3d, two nearby lines could have slightly different slopes, with the line on the left having a steeper, and the one on the right a less steep slope. This represents the area of the outer A_o, and the inner A_i contours as generated by a common edge created by the same damage mechanism, as is shown in figure 6.2. Here, both lines are described by:

$$A_o = a_o \ln(F_0) + b_0 \quad \text{and} \quad A_i = a_i \ln(F_0) + b_i, \tag{6.2}$$

with a_o, a_i and b_o, b_i the linear fit parameters. The averaged line from which the threshold fluence can be determined is approximately equal to:

$$A = \left(\frac{a_o + a_i}{2}\right)\ln(F_0) + \left(\frac{b_o + b_i}{2}\right). \tag{6.3}$$

To obtain the regression lines, some mis-fitted data points are omitted. This is done when the fitted inclination angle ψ, or $\frac{a}{b}$ (eccentricity) values deviate too much from that of the (measured) beam profile. While a beam profile follows a Gaussian function, in reality, it often tends to deviate more from this function at relative large distances from its center. In this case, a cutoff value for A has to be included. The same method that has been employed by fitting multiple ellipses (section 6.1.2), a recursive RANSAC approach is used to obtain multiple, almost parallel, linear fits. Here, the number of linear fits is not set beforehand, but each fit should contain at least a finite number of data points (input parameter) within a small distance from the fit and with a maximum area (A cutoff is taken to be 4000 μm^2 in figure 6.3). Most non-physical fits have been filtered

out automatically, and the few remaining ones have to be filtered out by visual inspection, such as the blue curve in figure 6.3e.
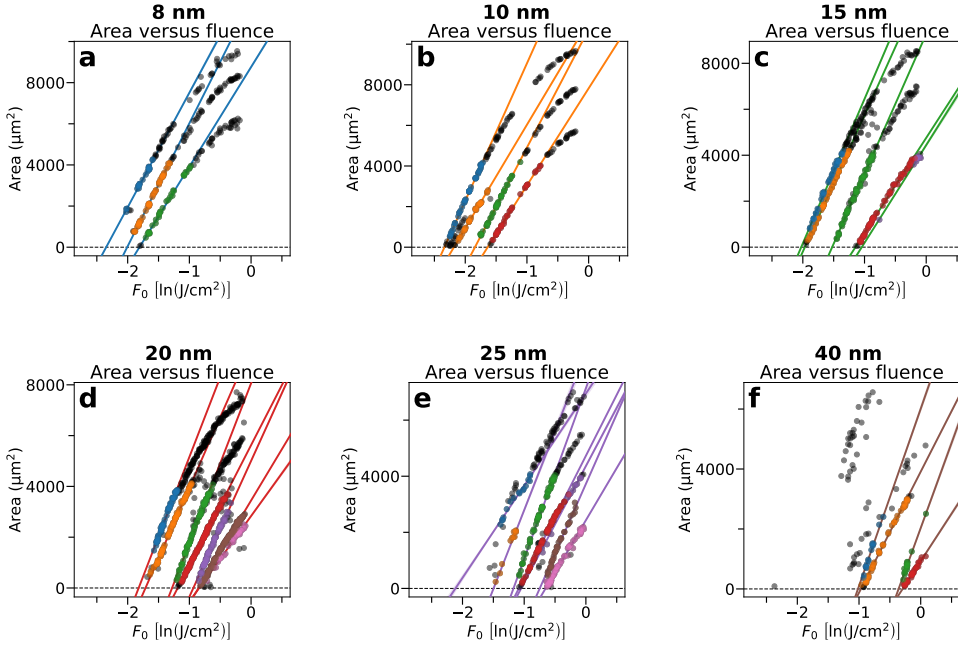

Figure 6.3: Liu-plots of single pulse laser damage experiments on 8, 10, 15, 20, 25 and 40 nm thick ruthenium layers on borosilicate glass substrates, obtained by inspecting dark-field images. The linear fits intersect the horizontal axis at $\ln(F_{th})$ where F_{th} is the fluence threshold of the corresponding damage mechanism. The fits are obtained by a recursive RANSAC approach [139]. Here, the amount of linear fits is not set beforehand, but each fit should contain at least ten data points within a small distance from the fit and with a maximum area (y cutoff) of 4000 μm^2. Most non-physical fits have been filtered out automatically, and the few remaining ones can be filtered out by visual inspection (blue line in e). The selected data points used for each fit are marked by a different color, which corresponds to the color of the fit.

6.2. THRESHOLDS AND DAMAGE MECHANISMS

As described in section 6.1, the areas of damaged sites are obtained by an automated inspection of microscopy images. From the automated Liu-analysis that follows, the fluence threshold value F_{th} for each damage mechanism is obtained. These fluence thresholds are presented here. To determine what type of damage belongs to each threshold, additional SEM and AFM images are often valuable.

Results of light-induced damage measurements on 8 to 80 nm thick gold, and on 10 to 30 nm thick aluminum layers have already been presented in chapter 3 and appendix F, and on 8 to 40 nm thick ruthenium layers in chapter 4 and appendix G, all deposited on borosilicate glass, sapphire, CaF$_2$ or Si substrates. Bulk flat silicon, and gratings etched in silicon are discussed in chapter 5 and appendix H. In the following, the damage mechanisms and thresholds of additional samples are presented. For each inspected material, a collection of in situ ΔR versus F_0, Liu-plots, SEM and/or optical microscopy

images are shown.

6.2.1. GOLD

Table 6.1: Threshold fluence and damage mechanism overview of gold (Au) layers

Material	Thickness (nm)	F_{th} (mJ/cm^2)	Mechanism	Figure
Au on BS	8	25.0 ± 0.20	Ablation	
	16	27.2 ± 0.7	Ablation	6.4
	24	40.1 ± 0.7	Ablation	(similar to
	32	50 ± 3	Ablation	20 nm)
	40	58 ± 1.7	Ablation	
	80	94 ± 5	Ablation	
Au with 5 nm adhesion layer on BS	20	57 ± 6	Recrystallization	6.5.3
		160 ± 4	Ablation	6.5.2
Au on sapphire	20	13.8 ± 0.4	Ablation	

BS = borosilicate glass

1. Just above the ablation threshold

2. Above the ablation threshold
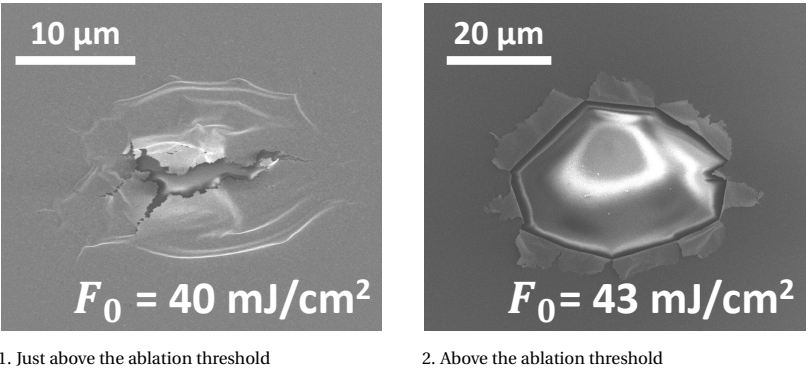
Figure 6.4: SEM images of two ablation sites of a 20 nm gold layer on 0.5 mm borosilicate glass for two different fluences

1. Whole damaged area 2. Ablated center 3. Recrystallization 4. Recrystallization zoom-in
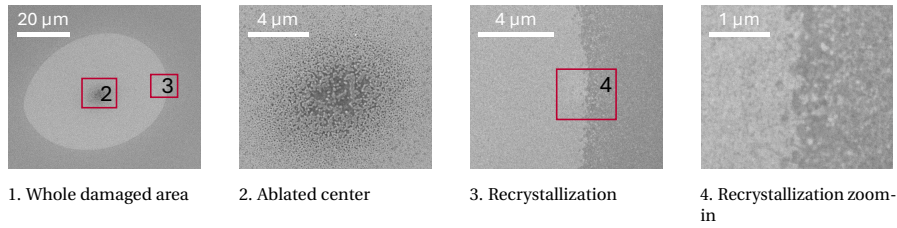
Figure 6.5: A single site at the 20 nm gold with a 5 nm adhesion layer on borosilicate glass (BS) sample, illuminated by a single laser-shot just above the ablation threshold

6.2.2. ALUMINUM

Table 6.2: Threshold fluence and damage mechanism overview of aluminum (Al) layers

Material	Thickness (nm)	F_{th} (mJ/cm^2)	Mechanism	Figure
Al on BS	14	24 ± 1.3	Spallation/ablation	
	18	47 ± 3	Spallation/ablation	
	20	50 ± 3	Spallation	
		177 ± 4	Ablation	
	22	60 ± 2.4	Spallation	
		189 ± 0.2	Ablation	
	26	70 ± 1.6	Spallation	
		194 ± 1.7	Ablation	
	30	83 ± 3	Spallation	
		205 ± 5	Ablation	
Al on sapphire	20	103 ± 9	Surface irregularities	6.6.2
		111 ± 23	Ablation	6.6.6
Al on CaF$_2$	20	$62 \pm 3^*$	Spallation	6.7.4 (outside rim)
		163 ± 16	Ablation	6.7.1-4 (center)
Al on Si	20	93 ± 8.5	Spallation	6.8.4 (outside rim)
		161 ± 6	Ablation	6.8.1-4 (outside bright rim)
		319 ± 22 and $398 \pm 20^*$	Substrate damage	6.8.1-4 (inner two bright rims)

BS = borosilicate glass.

∗ Indication that the threshold fluence is not obtained by an automated Liu-analysis, but by inspecting the optical microscopy images by eye to extract the contours for the Liu-analysis.
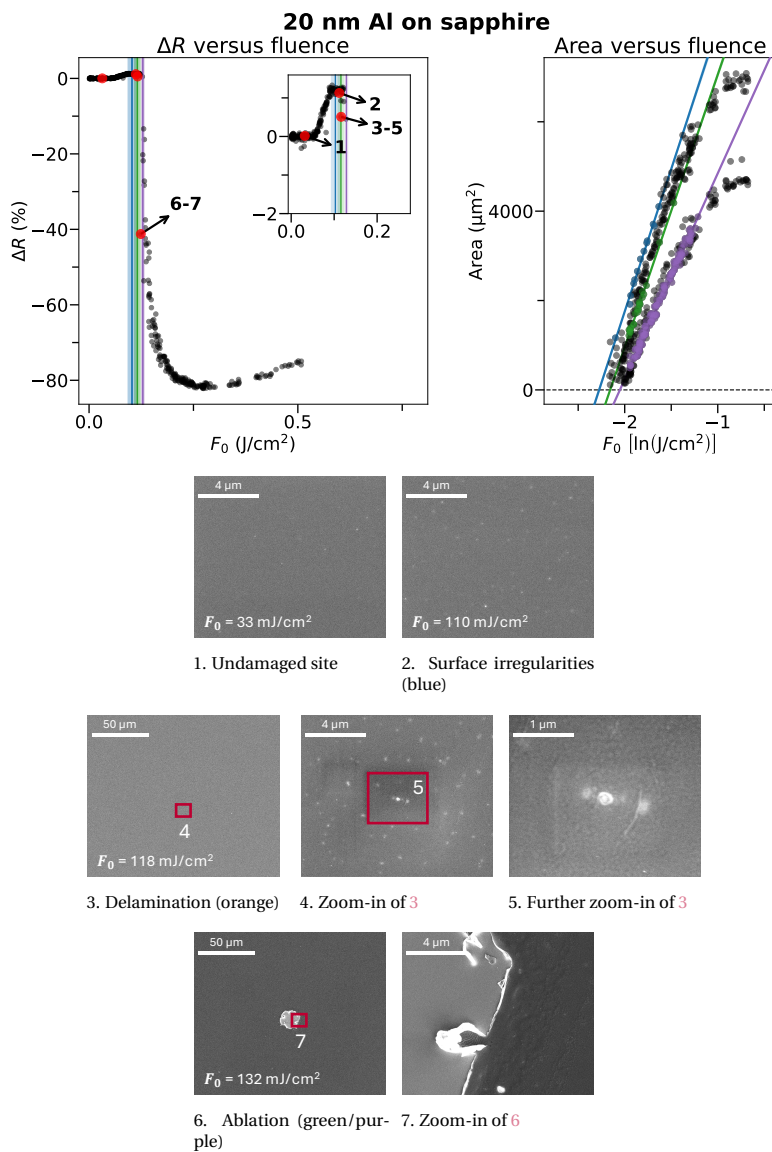
Figure 6.6: Result of single laser-shot measurements on 20 nm aluminum on a 1.1 mm thick sapphire substrate. ΔR versus the peak-fluence is plotted including the fluence thresholds (top left) obtained by Liu-analysis (top right), and shown by the colored lines and data points. The numbers indicate the data points corresponding to the SEM images.
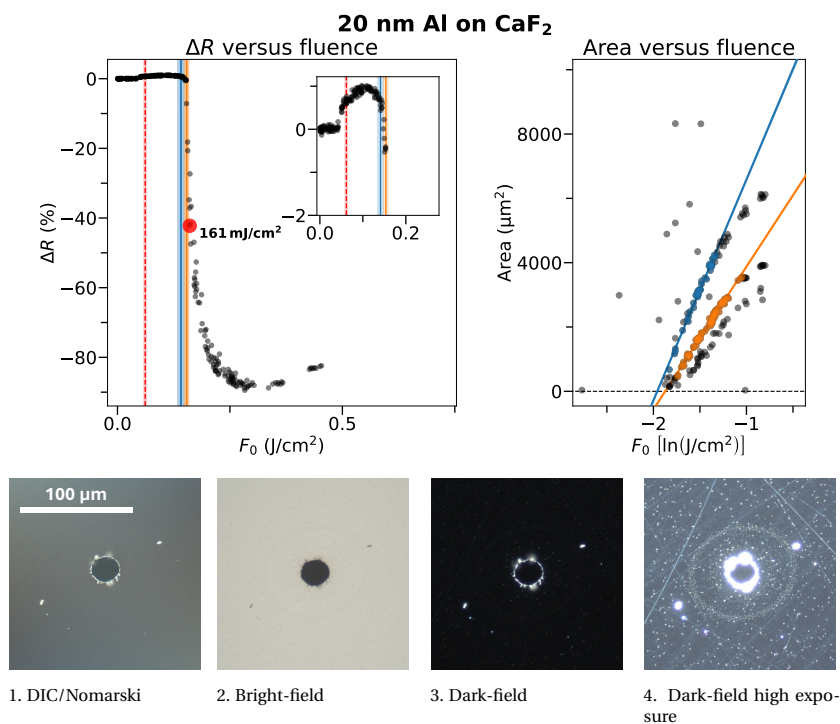
Figure 6.7: Result of single laser-shot measurements on 20 nm thick aluminum on a 0.5 mm thick CaF_2 substrate. ΔR versus the peak-fluence is plotted including the fluence thresholds (top left) obtained by Liu-analysis (top right), and shown by the colored lines and data points. Several optical microscopy images of the site indicated by the red dot are shown at the bottom. The colored lines correspond to the following damage mechanisms: spallation (red), and ablation (blue/orange).
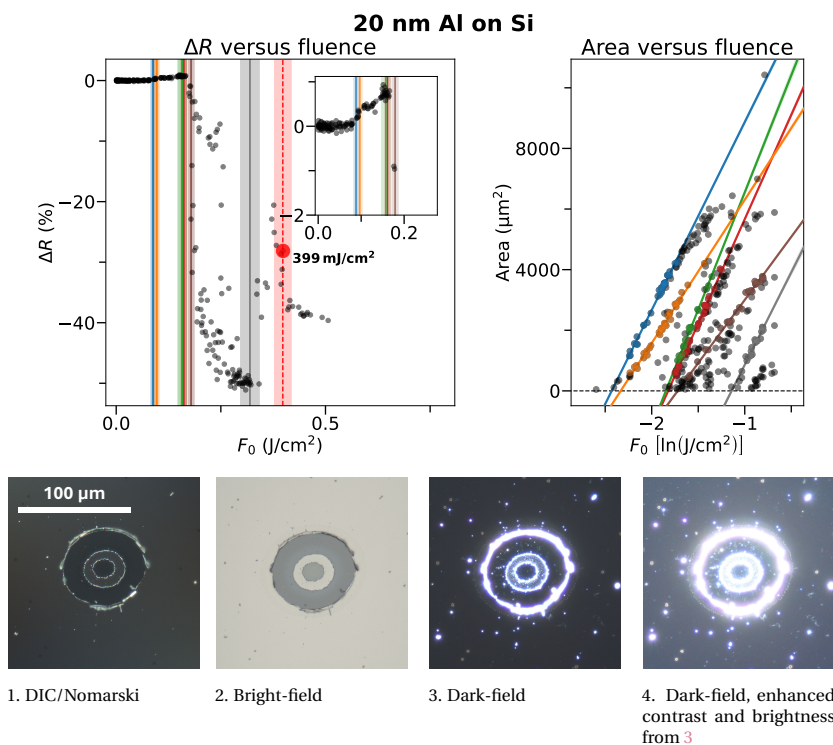
6

20 nm Al on Si

ΔR versus fluence

Area versus fluence

1. DIC/Nomarski   2. Bright-field   3. Dark-field   4. Dark-field, enhanced contrast and brightness from 3

Figure 6.8: Result of single laser-shot measurements on 20 nm thick aluminum on a 0.5 nm thick Si substrate. ΔR versus the peak-fluence is plotted including the fluence thresholds (top left) obtained by Liu-analysis (top right), and shown by the colored lines and data points. Several optical microscopy images of the site indicated by the red dot are shown at the bottom. The straight colored lines correspond to the following damage mechanisms: spallation (blue/orange), ablation (greed/solid red/brown), substrate damage (outside edge: gray, inside edge: dashed red).
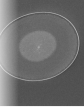
6.2.3. RUTHENIUM

Table 6.3: Threshold fluence and damage mechanism overview of ruthenium (Ru) layers

Material	Nominal thickness (nm)	F_{th} (mJ/cm^2)	Mechanism	Figure
Ru on BS	8	96 ± 6	Recrystallization edge	G.1b
		$104 \pm 7^*$	Buried cracks/nano-volcanoes	G.1g
		164 ± 5	Ablation	G.1h
	10	97 ± 3	Cracking edge	G.1f
		113 ± 4	Buried cracks	G.1f
		158 ± 4	Nanovolcanoes	G.1g-h
		195 ± 3	Ablation	G.1h
	15	132 ± 5	Big cracks	G.1j
		139.9 ± 1.9	Small cracks	G.1j
		218 ± 4	Nanovolcanoes/layer splitting	G.1k
		318 ± 3	Ablation	G.1k
	20	162 ± 5	Big cracks	G.1n
		181.6 ± 2.5	Small cracks	G.1n
		278 ± 4	Nanovolcanoes/layer splitting	G.1o
		305 ± 4	No nanovolcanoes	
		392 ± 5	Ablation	G.1p
		427.1 ± 2.0	Ablation	G.1p
	25	224 ± 18	Big cracks	G.1r
		$246 \pm 7^*$	Small cracks	G.1r
		309 ± 4	Nanovolcanoes/layer splitting	G.1r
		337 ± 3	No nanovolcanoes	G.1r
		473 ± 5	Ablation	G.1s
		520 ± 4	Ablation	G.1s
	40	$263 \pm 7^*$	Big cracks	G.1u-v
		379 ± 5	Small cracks/layer splitting	G.1v
		699 ± 4	Ablation	G.1w
		745.9 ± 2.4	Ablation	G.1w
Ru on sapphire	8	95 ± 4	Ablation	
Ru on CaF$_2$	8	57 ± 5	Nanovolcanoes	6.9.1
		82 ± 3	Ablation	6.9.3
Ru on Si	8	211 ± 31	Ablation	
Ru on sapphire	20	191 ± 9	Ablation	

Table 6.3: Threshold fluence and damage mechanism overview of ruthenium (Ru) layers

Material	Nominal thickness (nm)	F_{th} (mJ/cm^2)	Mechanism	Figure
Ru on CaF$_2$	20	114 ± 6	Spallation	
		147 ± 5	Ablation	
Ru on Si	20	121 ± 3	*Unknown*	
		181 ± 1.4	Cracking	6.10.1
		232 ± 4	No cracks	6.10.1
		295 ± 3	Top-level ablation	6.10.2
		473 ± 20	Full-ablation	6.10.4
Ru on sapphire	40	300 ± 10	'bubbling'	6.11.1
		365 ± 4	Top-level ablation	6.11.2
		676 ± 4	Full-ablation	6.11.5
Ru on CaF$_2$	40	284 ± 6	Ablation	
Ru on Si	40	$355 \pm 35^{*}$	Cracking	
		427 ± 5	Top-level ablation	
		994 ± 4	Ablation	

BS = borosilicate glass

∗ Indication that the threshold fluence is not obtained by Liu-analysis, but by estimating the local fluence from a SEM image.

| 1. Nanovolcanoes | 2. More nanovolcanoes | 3. Ablation | 4. Ablation edge |
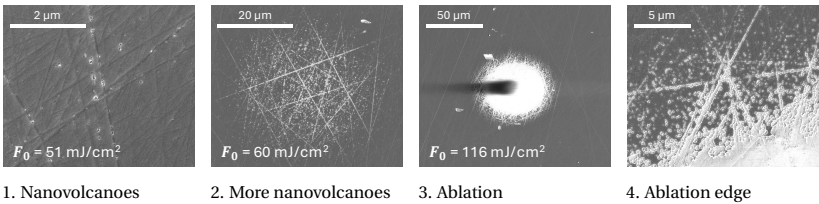
Figure 6.9: SEM images of various illuminated sites on 8 nm ruthenium on a 0.5 mm CaF$_2$ substrate. See also table 6.3.

| 1. Cracking | 2. Top-level ablation | 3. | 4. Full-ablation |
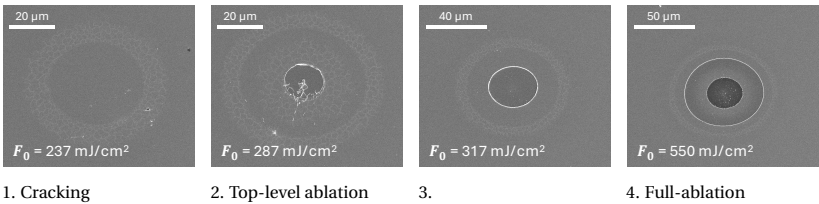
Figure 6.10: SEM images of various illuminated sites on 20 nm ruthenium on a Si substrate. See also table 6.3.

1. 'Bubbling' $F_0 = 312\,\mathrm{mJ/cm^2}$

2. Top-level ablation $F_0 = 387\,\mathrm{mJ/cm^2}$

3. Zoom-in of 2

4. $F_0 = 433\,\mathrm{mJ/cm^2}$

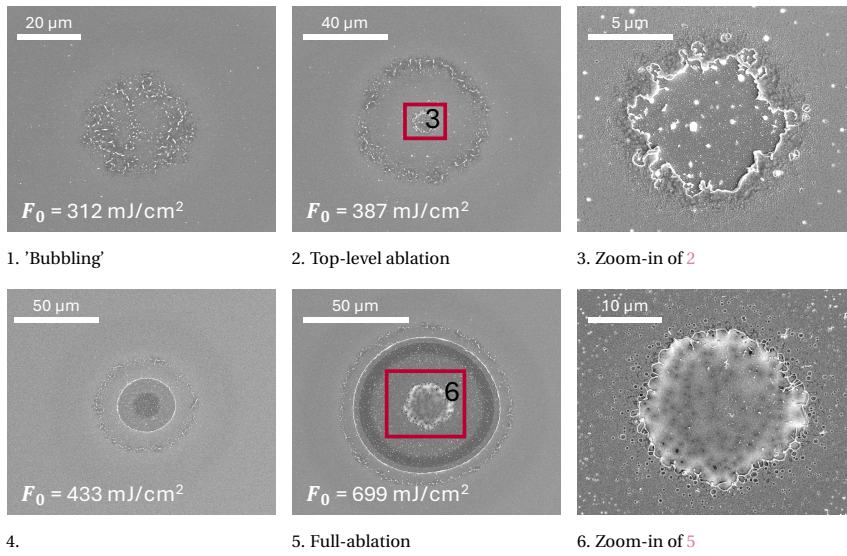5. Full-ablation $F_0 = 699\,\mathrm{mJ/cm^2}$

6. Zoom-in of 5

Figure 6.11: SEM images of various illuminated sites on 40 nm ruthenium on a 1.1 mm sapphire substrate. See also table 6.3.

6.2.4. AMORPHOUS CARBON

Table 6.4: Threshold fluence and damage mechanism overview of 100 nm amorphous carbon (aC) on Si

Material	Thickness (nm)	F_{th} (mJ/cm^2)	Mechanism	Figure
aC on Si	100	86 ± 4	Delamination	6.12.1
		114 ± 7	Substrate damage	6.12.2
		130 ± 5	Top-level ablation	6.12.3
		159 ± 8	Full-ablation	6.12.4
		226 ± 5	Crater formation	6.12.5

6
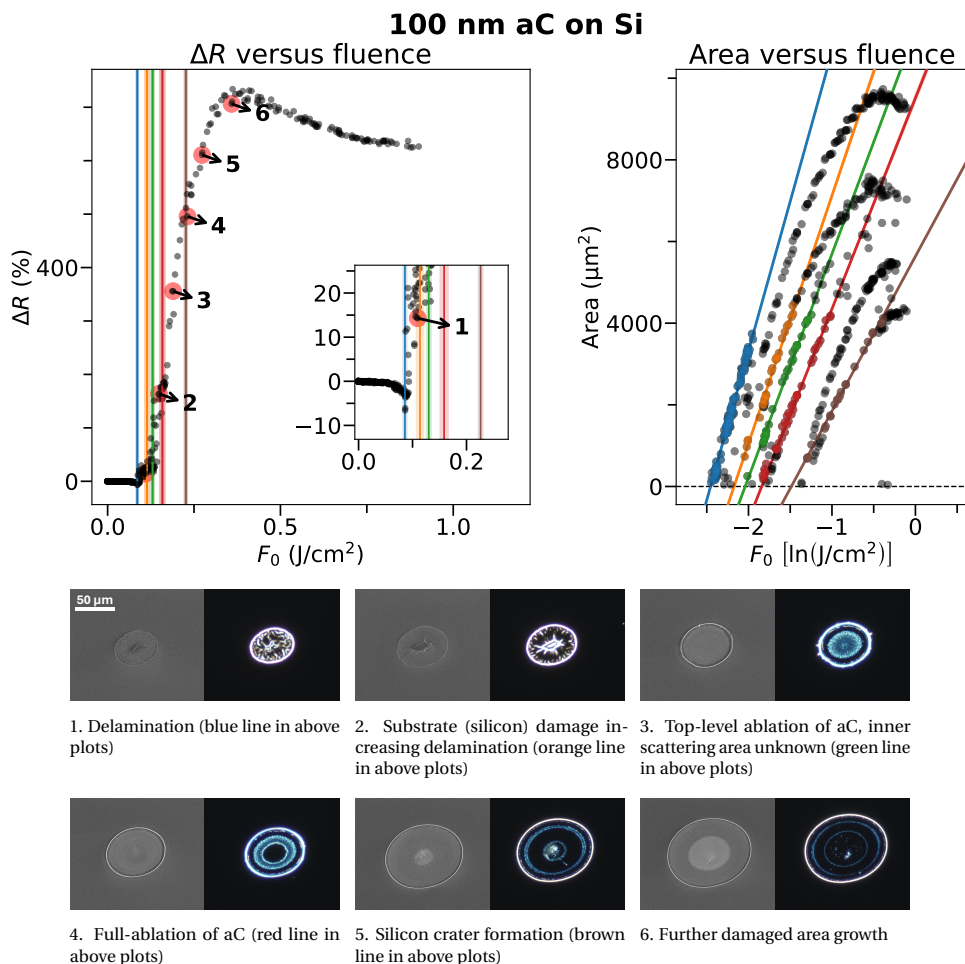
Figure 6.12: Result of single laser-shot measurements on 100 nm thick amorphous carbon (aC) on a silicon substrate. ΔR versus the peak-fluence is plotted including the fluence thresholds (top left) obtained by Liu-analysis (top right), and shown by the colored lines and data points. The numbers corresponds to the data points corresponding to the SEM (left) and optical dark-field image (right) shown at the bottom.

6.2.5. EUV RESISTS

Chemically amplified resists systems work by generating protons where the resist is exposed. The catalyzation of the chemical transformation, that is induced by the protons, has an amplification effect which makes these resists very sensitive compared to other common resists. Therefore, CARs are developed to use for nanolithography at small wavelengths such as EUV (EUV-CAR), X-ray and electron projection lithography (EPL) lithography [153]. However, going to higher-resolution lithography (high numerical aperture (NA)), a thinner resist is needed due to the reduced depth of focus. Therefore metal-oxide resist (MOR) is developed, which has a higher EUV absorption, generating more secondary electrons [154].

We therefore performed light-induced damage measurements on 40 nm thick EUV-CAR and 18 nm MOR on silicon substrates as is presented in table 6.5 and figures 6.13 and 6.14.

Table 6.5: Threshold fluence and damage mechanism overview of extreme ultraviolet (EUV) resists on Si

Material	Thickness (nm)	F_{th} (mJ/cm^2)	Mechanism	Figure
EUV-CAR on Si	40	60 ± 16	Delamination	6.13.1
		84 ± 5	Increased delamination	6.13.3
		123 ± 7	Substrate damage (uncertain)	6.13.4
		188 ± 6	Rupture	6.13.6
MOR on Si	18	48 ± 5	Optical change	6.13.1
		99 ± 7	*Uncertain*	
		113 ± 4	*Uncertain*	6.13.2
		126 ± 9	Buckling	6.13.3
		163 ± 8	Film rupture	6.13.4

6
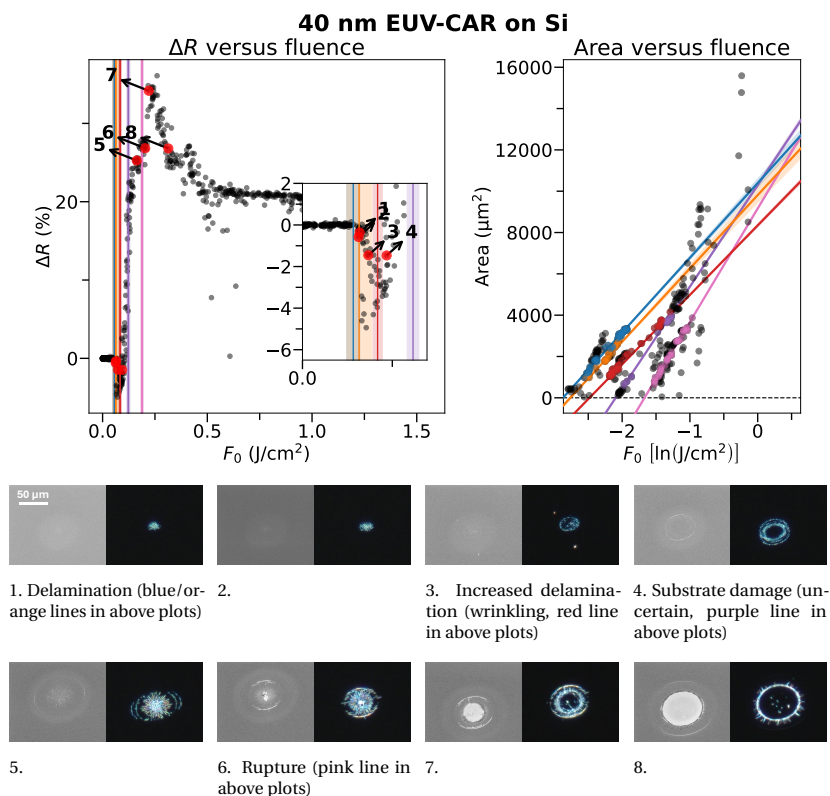

Figure 6.13: Result of single laser-shot measurements on 40 nm thick EUV-chemically amplified resist (CAR) resist on a silicon substrate. ΔR versus the peak-fluence is plotted including the fluence thresholds (top left) obtained by Liu-analysis (top right), and shown by the colored lines and data points. The numbers indicate the data points corresponding to the SEM (left) and optical dark-field image (right) shown at the bottom.
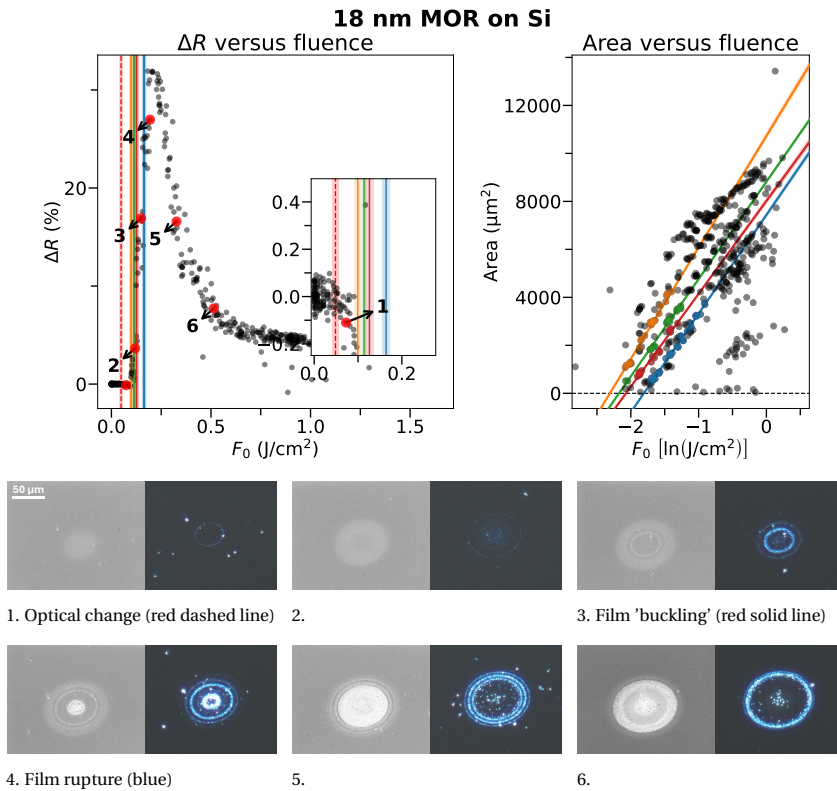
Figure 6.14: Result of single laser-shot measurements on 18 nm thick metal-oxide resist (MOR) resist on a silicon substrate. ΔR versus the peak-fluence is plotted including the fluence thresholds (top left) obtained by Liu-analysis (top right), and shown by the colored lines and data points. The numbers indicate the data points corresponding to the SEM (left) and optical dark-field images (right) shown at the bottom.

### 6.2.6. SiO_2 and Si_3N_4

Table 6.6: Threshold fluence and damage mechanism overview of silicon oxide (SiO_2) on Si

Material	Thickness (nm)	F_{th} (mJ/cm^2)	Mechanism	Figure
SiO_2 on Si	20	79 ± 1.7	Optical change	6.15.1
		113 ± 2	Ablation	6.15.5
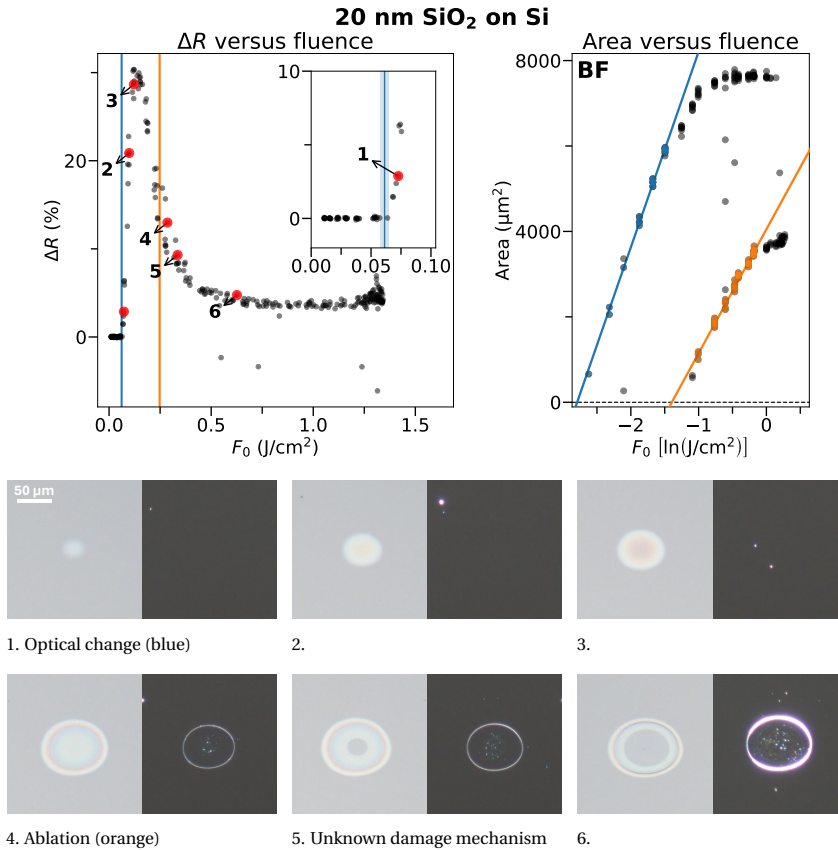
Figure 6.15: Result of single laser-shot measurements on 20 nm thick SiO$_2$ on a silicon substrate. ΔR versus the peak-fluence is plotted including the fluence thresholds (top left) obtained by Liu-analysis from bright-field microscopy images (top right), and shown by the colored lines and data points. The numbers indicate the data points corresponding to the optical bright-field (left) and dark-field images (right) shown at the bottom.
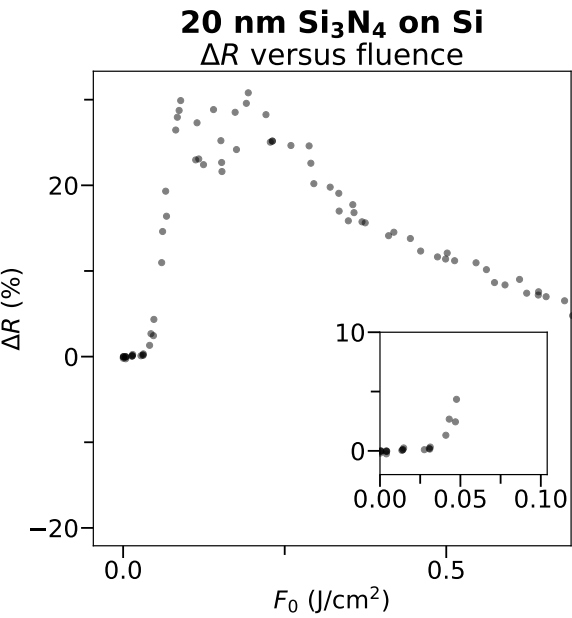
Figure 6.16: ΔR versus the peak-fluence for a single laser-shot measurement of 20 nm silicon nitride (Si$_3$N$_4$) on a silicon substrate

6.2.7. GRATINGS ETCHED IN SILICON

Table 6.7: Threshold fluence and damage mechanism overview for Si and gratings etched in silicon. This table is also presented as

Mechanism	Pump polarization	Pitch (nm)	Duty cycle (%)	F_{th} (mJ/cm^2)
$F_\uparrow$	$\parallel$	*Flat*		92 ± 22
		430	23.2	40 ± 24
		430	34.8	64 ± 14
		460	50.0	88 ± 16
		600	50.0	80 ± 14
		950	50.0	69 ± 35
		980	50.0	88 ± 15
$F_\uparrow$	$\perp$	*Flat*		90 ± 21
		430	23.2	37 ± 11
		430	34.8	58 ± 12
		460	50.0	78 ± 13
		600	50.0	71 ± 6
		950	50.0	59 ± 17
		980	50.0	59 ± 12
F_{dark}	$\parallel$	*Flat*		251 ± 21

Table 6.7: Threshold fluence and damage mechanism overview for Si and gratings etched in silicon. This table is also presented as table H.1

Mechanism	Pump polarization	Pitch (nm)	Duty cycle (%)	F_{th} (mJ/cm^2)
		430	23.2	195 ± 14
		430	34.8	162 ± 27
		460	50.0	198 ± 10
		600	50.0	158 ± 9
		950	50.0	170 ± 18
		980	50.0	178 ± 12
F_{dark}	$\perp$	*Flat*		295 ± 6
		430	23.2	201 ± 9
		430	34.8	186 ± 11
		460	50.0	216 ± 6
		600	50.0	149 ± 8
		950	50.0	205 ± 8
		980	50.0	240 ± 6
F_{abl}	$\parallel$	*Flat*		369 ± 24
		430	23.2	266 ± 9
		430	34.8	249 ± 11
		460	50.0	266 ± 10
		600	50.0	257 ± 12
		950	50.0	332 ± 16
		980	50.0	326 ± 12
F_{abl}	$\perp$	*Flat*		409 ± 8
		430	23.2	236 ± 10
		430	34.8	316 ± 6
		460	50.0	273 ± 12
		600	50.0	275 ± 11
		950	50.0	361 ± 11
		980	50.0	383 ± 15
F_{crater}	$\parallel$	*Flat*		816 ± 78
		430	23.2	410 ± 20
		430	34.8	448 ± 3
		460	50.0	435 ± 14
		600	50.0	434 ± 14
		950	50.0	653 ± 27
		980	50.0	666 ± 6

6

Table 6.7: Threshold fluence and damage mechanism overview for Si and gratings etched in silicon. This table is also presented as

Mechanism	Pump polarization	Pitch (nm)	Duty cycle (%)	F_{th} (mJ/cm^2)
F_{crater}	$\perp$	*Flat*		796 ± 44
		430	23.2	360 ± 12
		430	34.8	489 ± 26
		460	50.0	466 ± 11
		600	50.0	403 ± 23
		950	50.0	623 ± 26
		980	50.0	725 ± 14

Additional SEM images can be found in

LIST OF ACRONYMS & MATHEMATICAL SYMBOLS

LIST OF ACRONYMS

Al_2O_3	aluminum oxide.	*175*
Al	aluminum.	*47*, *54*, *125*, *175*
Au	gold.	*47*, *51*, *124*, *175*
CAR	chemically amplified resist.	*133*
CaF_2	calcium fluoride.	*31*, *61*, *62*
Cr	Chromium.	*61*
MOR	metal-oxide resist.	*133*
RuO_2	ruthenium oxide.	*77*, *176*
Ru	ruthenium.	*77*, *129*, *130*, *176*
SiO_2	silicon oxide.	*103*, *136*, *176*
Si_3N_4	silicon nitride.	*138*
Si	silicon.	*36*, *103*, *176*
Ti	titanium.	*61*
aC	amorphous carbon.	*131*

ADC	analogue-to-digital converter.	*36*
AFM	atomic force microscopy.	*40*, *41*, *49*, *51*, *58*, *79*
ARS	Angle Resolved Scattering.	*21*

BBO	Beta Barium Borate.	*34*–*36*, *179*
BF	bright-field.	*39*
BS	borosilicate glass.	*31*
BS	beamsplitter.	*35*, *48*
BSE	back-scattered electrons.	*39*

DF	dark-field.	*39*, *41*, *51*, *56*
DIC/Nomarski	differential interference contrast.	*39*, *41*, *51*
DM	dichroic mirror.	*35*, *36*

EBPVD	electron-beam physical vapor deposition.	*31*
EBSD	electron backscatter diffraction.	*40*, *67*, *68*, *70*
EDX	energy-dispersive X-ray spectroscopy.	*40*, *89*
EPL	electron projection lithography.	*133*

MATHEMATICAL SYMBOLS

BIBLIOGRAPHY

[1] I. B. H. Abram, *Jewish tradition as permanent education*, English translation from Dutch, trans. by C. E. Thirlway (Universiteit van Amsterdam, June 1986).

[2] M. Faraday, *Experimental researches in electricity*, 3 vols. Vols., Published in multiple volumes from 1839 to 1855 (R. & J. E. Taylor, London, 1839–1855).

[3] M. Faraday, "On the magnetization of light and the illumination of magnetic lines of force", Philosophical Transactions of the Royal Society of London **136**, 1–20 (1846).

[4] J. C. Maxwell, "XXV. on physical lines of force: Part I.–The theory of molecular vortices applied to magnetic phenomena", The London, Edinburgh, and Dublin Philosophical Magazine and Journal of Science **21**, 161–175 (1861).

[5] J. C. Maxwell, *A treatise on electricity and magnetism*, Vol. 1 (Clarendon press, 1873).

[6] H. Hertz, "Über sehr schnelle electrische schwingungen", Annalen der Physik **267**, 421–448 (1887).

[7] F. Remington, *The smoke signal*, https://en.wikipedia.org/wiki/Smoke_signal, Accessed 20-08-2024, 1905.

[8] P. A. Clock, *Brandaris*, https://nl.wikipedia.org/wiki/Brandaris_(vuurtoren), Accessed 20-08-2024, 1594.

[9] W. Cooke and C. Wheatstone, *Cooke and Wheatstone's five-needle, six-wire telegraph*, https://en.wikipedia.org/wiki/Cooke_and_Wheatstone_telegraph, Accessed 20-08-2024, 1837.

[10] Western Electric, *Push button telephone model 2500 dmg black*, https://en.wikipedia.org/wiki/Telephone, Accessed 20-08-2024, 1980.

[11] Springfield Massachusetts, *Multiwire broadcast t-antenna of early am station WBZ*, https://en.wikipedia.org/wiki/Radio_masts_and_towers, Accessed 20-08-2024, 1925.

[12] Soviet space program, *Spoetnik 1*, https://www.sciencephoto.com/media/338494/view/sputnik-1-satellite, Accessed 20-08-2024, 1957.

[13] CERN, *Tim Berners-Lee, world wide web inventor*, https://cds.cern.ch/images/CERN-GE-9407011-31, Accessed 20-08-2024, 1994.

[14] S. Moore, https://www.silicon.co.uk/mobility/10-apps-smartphone-data-save-191914, Accessed 20-08-2024, 2016.

[15] G. Zhang, M. Graef, and F. van Roosmalen, "The rationale and paradigm of "more than Moore"", in 56th electronic components and technology conference 2006 (2006), pp. 151–157.

[16] M. M. Waldrop, "The chips are down for Moore's law", Nature News **530**, 144 (2016).

[17] V. F. Pavlidis, I. Savidis, and E. G. Friedman, *Three-Dimensional integrated circuit design* (Elsevier, 2017), pp. 1–14.

[18] K. Krikhaar, *TSMC noemt 1,4nm en 1,0nm procedés voor het eerst op roadmaps*, https://tweakers.net/nieuws/216626/tsmc-noemt-1-komma-4nm-en-1-komma-0nm-procedes-voor-het-eerst-op-roadmaps.html, Accessed 14-08-2024, 2024.

[19] Institution of Electronics, *TSMC reaffirms path to 1-nm node by 2030 on track*, https://institutionofelectronics.ac.uk/2024/01/01/tsmc-reaffirms-path-to-1-nm-node-by-2030-on-track/, Accessed 14-08-2024, 2024.

[20] Applied Materials, Inc., *Applied materials panel discussion during iedm 2023*, https://ir.appliedmaterials.com/events/event-details/applied-materials-panel-discussion-during-iedm2023, Accessed 14-08-2024, 2023.

[21] R. Micheloni, L. Crippa, C. Zambelli, and P. Olivo, "Architectural and integration options for 3d nand flash memories", Computers **6**, 10.3390/computers6030027 (2017).

[22] A. J. den Boef, "Optical wafer metrology sensors for process-robust CD and overlay control in semiconductor device manufacturing", Surface Topography: Metrology and Properties **4**, 023001 (2016).

[23] N. Bloembergen, " Laser: The Inventor, the Nobel Laureate, and the Thirty-Year Patent War ", Physics Today **54**, 56–56 (2001).

[24] F. J. McClung and R. W. Hellwarth, "Giant Optical Pulsations from Ruby", Journal of Applied Physics **33**, 828–829 (1962).

[25] P. V. Avizonis and T. Farrington, "Internal self-damage of ruby and Nd-glass lasers", Applied Physics Letters **7**, 205–206 (1965).

[26] D. Ristau, *Laser-induced damage in optical materials* (CRC Press, Dec. 2014).

[27] W. Rudolph, L. Emmert, Z. Sun, D. Patel, and C. Menoni, "Laser damage in dielectric films: What we know and what we don't", in Laser-induced damage in optical materials: 2013, Vol. 8885, edited by G. J. Exarhos, V. E. Gruzdev, J. A. Menapace, D. Ristau, and M. Soileau (International Society for Optics and Photonics, 2013), p. 888516.

[28] J. R. Gulley, "Frequency dependence in the initiation of ultrafast laser-induced damage", in Laser-induced damage in optical materials: 2010, Vol. 7842, edited by G. J. Exarhos, V. E. Gruzdev, J. A. Menapace, D. Ristau, and M. J. Soileau (International Society for Optics and Photonics, 2010), 78420U.

[29] M. Jupé, L. Jensen, K. Starke, D. Ristau, A. Melninkaitis, and V. Sirutkaitis, "Analysis in wavelength dependence of electronic damage", in Laser-induced damage in optical materials: 2009, Vol. 7504, edited by G. J. Exarhos, V. E. Gruzdev, D. Ristau, M. J. Soileau, and C. J. Stolz (International Society for Optics and Photonics, 2009), 75040N.

[30] L. Gallais, D.-B. Douti, M. Commandré, G. Batavičiūtė, E. Pupka, M. Ščiuka, L. Smalakys, V. Sirutkaitis, and A. Melninkaitis, "Wavelength dependence of femtosecond laser-induced damage threshold of optical materials", Journal of Applied Physics **117**, 223103 (2015).

[31] B. Rethfeld, K. Sokolowski-Tinten, D. von der Linde, and S. Anisimov, "Timescales in the response of materials to femtosecond laser excitation", Applied Physics A **79**, 767–769 (2004).

[32] M. F. Koldunov, A. A. Manenkov, and I. L. Pokotilo, "Mechanical damage in transparent solids caused by laser pulses of different durations", Quantum Electronics **32**, 335 (2002).

[33] J.-Y. Natoli, L. Gallais, H. Akhouayri, and C. Amra, "Laser-induced damage of materials in bulk, thin-film, and liquid forms", Appl. Opt. **41**, 3156–3166 (2002).

[34] A. A. Manenkov and A. M. Prokhorov, "Laser-induced damage in solids", Soviet Physics Uspekhi **29**, 104 (1986).

[35] I. Milov, V. Zhakhovsky, D. Ilnitsky, K. Migdal, V. Khokhlov, Y. Petrov, N. Inogamov, V. Lipp, N. Medvedev, B. Ziaja, V. Medvedev, I. Makhotkin, E. Louis, and F. Bijkerk, "Two-level ablation and damage morphology of Ru films under femtosecond extreme uv irradiation", Applied Surface Science **528**, 146952 (2020).

[36] F. Akhmetov, I. Milov, S. Semin, F. Formisano, N. Medvedev, J. M. Sturm, V. V. Zhakhovsky, I. A. Makhotkin, A. Kimel, and M. Ackermann, "Laser-induced electron dynamics and surface modification in ruthenium thin films", Vacuum **212**, 112045 (2023).

[37] K. C. Phillips, H. H. Gandhi, E. Mazur, and S. K. Sundaram, "Ultrafast laser processing of materials: a review", Adv. Opt. Photon. **7**, 684–712 (2015).

[38] S. I. Anisimov, N. A. Inogamov, Y. V. Petrov, V. A. Khokhlov, V. V. Zhakhovskii, K. Nishihara, M. B. Agranat, S. I. Ashitkov, and P. S. Komarov, "Interaction of short laser pulses with metals at moderate intensities", Applied Physics A **92**, 939–943 (2008).

[39] J. D. Jackson, *Classical electrodynamics*, Third (John Wiley and Sons, New York, 1999), pp. 258–266.

[40] M. Born and E. Wolf, *Principles of optics, Electromagnetic theory of propagation interference and diffraction of light*, Sixth (Cambridge University Press, Cambridge, UK, 1980), pp. 51–70.

[41] D. J. Griffiths, *Introduction to electrodynamics*, Fourth (Cambridge University Press, Cambridge, UK, 2017), pp. 393–424.

[42] E. Abram, *Multilayers*, https://github.com/eabram/multilayers.git, version v3.0, 2025.

[43] M. Kaganov, "Relaxation between electrons and the crystalline lattice", Sov. Phys. JETP **4**, 173–178 (1957).

[44] S. I. Anisimov, "Effect of the powerful light fluxes on metals", Sov. Phys. Tech. Phys. **11**, 945 (1967).

[45]　S. Anisimov, B. Kapeliovich, T. Perelman, et al., "Electron emission from metal surfaces exposed to ultrashort laser pulses", Zh. Eksp. Teor. Fiz **66**, 375–377 (1974).

[46]　S. Zhvavyi and G. Ivlev, "Influence of the initial temperature of silicon on crystallization of a layer melted by nanosecond laser heating", Journal of engineering physics and thermophysics **69**, 608–611 (1996).

[47]　J. Hohlfeld, S.-S. Wellershoff, J. Güdde, U. Conrad, V. Jähnke, and E. Matthias, "Electron and lattice dynamics following optical excitation of metals", Chemical Physics **251**, 237–258 (2000).

[48]　R. Franz and G. Wiedemann, "Über die wärme-leitungsfähigkeit der metalle", Annalen der Physik **165**, 497–531 (1853).

[49]　L. Waldecker, R. Bertoni, R. Ernstorfer, and J. Vorberger, "Electron-phonon coupling and energy flow in a simple metal beyond the two-temperature approximation", Phys. Rev. X **6**, 021003 (2016).

[50]　F. Akhmetov, N. Medvedev, I. Makhotkin, M. Ackermann, and I. Milov, "Effect of atomic-temperature dependence of the electron–phonon coupling in two-temperature model", Materials **15**, 10.3390/ma15155193 (2022).

[51]　P. M. Norris, A. P. Caffrey, R. J. Stevens, J. M. Klopf, J. T. McLeskey Jr., and A. N. Smith, "Femtosecond pump–probe nondestructive examination of materials (invited)", Review of Scientific Instruments **74**, 400–406 (2003).

[52]　J. L. Hostetler, A. N. Smith, D. M. Czajkowsky, and P. M. Norris, "Measurement of the electron-phonon coupling factor dependence on film thickness and grain size in Au, Cr, and Al", Appl. Opt. **38**, 3614–3620 (1999).

[53]　G. Sciaini and R. J. D. Miller, "Femtosecond electron diffraction: heralding the era of atomically resolved dynamics", Reports on Progress in Physics **74**, 096101 (2011).

[54]　P. M. Kraus, M. Zürch, S. K. Cushing, D. M. Neumark, and S. R. Leone, "The ultrafast X-ray spectroscopic revolution in chemical dynamics", Nature Reviews Chemistry **2**, 82–94 (2018).

[55]　N. Medvedev and I. Milov, "Electron-phonon coupling in metals at high electronic temperatures", Phys. Rev. B **102**, 064302 (2020).

[56]　Y. V. Petrov, N. Inogamov, and K. P. Migdal, "Thermal conductivity and the electron-ion heat transfer coefficient in condensed media with a strongly excited electron subsystem", JETP letters **97**, 20–27 (2013).

[57]　Z. Lin, L. V. Zhigilei, and V. Celli, "Electron-phonon coupling and electron heat capacity of metals under conditions of strong electron-phonon nonequilibrium", Phys. Rev. B **77**, 075133 (2008).

[58]　A. M. Brown, R. Sundararaman, P. Narang, W. A. Goddard, and H. A. Atwater, "Ab initio phonon coupling and optical response of hot electrons in plasmonic metals", Phys. Rev. B **94**, 075120 (2016).

[59] M. Z. Mo, Z. Chen, R. K. Li, M. Dunning, B. B. L. Witte, J. K. Baldwin, L. B. Fletcher, J. B. Kim, A. Ng, R. Redmer, A. H. Reid, P. Shekhar, X. Z. Shen, M. Shen, K. Sokolowski-Tinten, Y. Y. Tsui, Y. Q. Wang, Q. Zheng, X. J. Wang, and S. H. Glenzer, "Heterogeneous to homogeneous melting transition visualized with ultrafast electron diffraction", Science **360**, 1451–1455 (2018).

[60] N. Subani, F. Jamaluddin, M. A. H. Mohamed, and A. D. H. Badrolhisam, "Analytical solution of homogeneous one-dimensional heat equation with Neumann boundary conditions", Journal of Physics: Conference Series **1551**, 012002 (2020).

[61] E. T. Swartz and R. O. Pohl, "Thermal boundary resistance", Rev. Mod. Phys. **61**, 605–668 (1989).

[62] H. J. Shin, J.-M. Lee, S. Bae, W.-H. Kim, and S. Sim, "Metal-insulator transition and interfacial thermal transport in atomic layer deposited Ru nanofilms characterized by ultrafast terahertz spectroscopy", Applied Surface Science **563**, 150184 (2021).

[63] C. Dias, "A method of recursive images to solve transient heat diffusion in multilayer materials", International Journal of Heat and Mass Transfer **85**, 1075–1083 (2015).

[64] van Kraaij, M.G.M.M., *Forward diffraction modelling: analysis and application to grating reconstruction*, 2011.

[65] S. Schröder, A. Duparré, L. Coriand, A. Tünnermann, D. H. Penalver, and J. E. Harvey, "Modeling of light scattering in different regimes of surface roughness", Opt. Express **19**, 9820–9835 (2011).

[66] *Optics and photonics — Test method for total scattering by optical components*, Standard (International Organization for Standardization, Geneva, CH, 2022).

[67] S. O. Rice, "Reflection of electromagnetic waves from slightly rough surfaces", Communications on Pure and Applied Mathematics **4**, 351–378 (1951).

[68] T. D. B. Jacobs, T. Junge, and L. Pastewka, "Quantitative characterization of surface topography using spectral analysis", Surface Topography: Metrology and Properties **5**, 013001 (2017).

[69] E. L. Church, H. A. Jenkinson, and J. M. Zavada, "Relationship between Surface Scattering and Microtopographic Features", Optical Engineering **18**, 182125 (1979).

[70] Y. Wang and W. L. Wolfe, "Scattering from microrough surfaces: comparison of theory and experiment", Journal of the Optical Society of America (1917-1983) **73**, 1596 (1983).

[71] S. Edward, H. Zhang, S. Witte, and P. C. M. Planken, "Laser-induced ultrasonics for detection of low-amplitude grating through metal layers with finite roughness", Opt. Express **28**, 23374–23387 (2020).

[72] J. C. Stover, *Optical scattering: Measurements and analysis, third edition* (Society of Photo-Optical Instrumentation Engineers, 2012).

[73] D. Jones, *The theory of electromagnetism*, International series of monographs in pure and applied mathematics (Pergamon Press, 1964).

[74] J. M. Liu, "Simple technique for measurements of pulsed Gaussian-beam spot sizes", Opt. Lett. **7**, 196–198 (1982).

[75] Siegert Wafer, *Silicon Wafer BW14008*, https://www.siegertwafer.com/datenbankaufruf_silicon.php?dia_100=on&ori_100=on&fin_ss=on&ttv=&bow=&warp=&thmin=&thmax=&remin=&remax=&s=&v=liste&l=en&p=1, Accessed 11-02-2025.

[76] Epredia Inc., *Microscope slides and coverslips* (2021).

[77] Ossila, *Sapphire substrates*, https://www.ossila.com/en-eu/products/sapphire-substrates, Visited 22-12-2022.

[78] Crystran Ltd, *CaF2 UV grade 25.4mm dia x 0.5mm polished window*, https://www.crystran.com/caf2-uv-grade-25-4mm-dia-x-0-5mm-polished-window, Accessed 11-02-2025.

[79] Complete EASE, *Software manual version 3.18, JA Woollam Co*, 2007.

[80] FEMTOLASERS Produktions GmbH, *Femtopower he user manual*, FEMTOLASERS Produktions GmbH (Fernkorngasse 10, 1100 Vienna, Austria, Dec. 2014).

[81] Swamp Optics, *GRENOUILLE*, https://www.swampoptics.com/grenouille.html, Visited 24-09-2024.

[82] H. Dachraoui and W. Husinsky, "Fast electronic and thermal processes in femtosecond laser ablation of Au", Applied physics letters **89**, 104102 (2006).

[83] J. Güdde, J. Hohlfeld, J. Müller, and E. Matthias, "Damage threshold dependence on electron–phonon coupling in Au and Ni films", Applied Surface Science **127-129**, 40–45 (1998).

[84] A. A. Ionin, S. I. Kudryashov, S. V. Makarov, A. O. Levchenko, A. A. Rudenko, I. N. Saraeva, D. A. Zayarny, C. R. Nathala, and W. Husinsky, "Nanoscale surface boiling in sub-threshold damage and above-threshold spallation of bulk aluminum and gold by single femtosecond laser pulses", Laser Physics Letters **13**, 025603 (2015).

[85] V. H. Whitley, S. D. McGrane, D. E. Eakins, C. A. Bolme, D. S. Moore, and J. F. Bingert, "The elastic-plastic response of aluminum films to ultrafast laser-generated shocks", Journal of Applied Physics **109**, 013505 (2011).

[86] J. Winter, S. Rapp, M. Spellauge, C. Eulenkamp, M. Schmidt, and H. P. Huber, "Ultrafast pump-probe ellipsometry and microscopy reveal the surface dynamics of femtosecond laser ablation of aluminium and stainless steel", Applied Surface Science **511**, 145514 (2020).

[87] X. Zhao and Y. C. Shin, "Femtosecond laser ablation of aluminum in vacuum and air at high laser intensity", Applied Surface Science **283**, 94–99 (2013).

[88] D. von der Linde and K. Sokolowski-Tinten, "The physical mechanisms of short-pulse laser ablation", Applied Surface Science **154-155**, 1–10 (2000).

[89] B. N. Chichkov, C. Momma, S. Nolte, F. Von Alvensleben, and A. Tünnermann, "Femtosecond, picosecond and nanosecond laser ablation of solids", Applied physics A **63**, 109–115 (1996).

[90] S. Sonntag, J. Roth, F. Gaehler, and H.-R. Trebin, "Femtosecond laser ablation of aluminium", Applied Surface Science **255**, Proceedings of the Sixth International Conference onPhoto-Excited Processes and Applications(6-ICPEPA), 9742–9744 (2009).

[91] S. Kudryashov and A. Ionin, "Multi-scale fluence-dependent dynamics of front-side femtosecond laser heating, melting and ablation of thin supported aluminum film", International Journal of Heat and Mass Transfer **99**, 383–390 (2016).

[92] M. Stafe, I. Vladoiu, and I. Popescu, "Impact of the lasr wavelength and fluence on the ablation rate of aluminium", Central European Journal of Physics **6**, 327–331 (2007).

[93] Y. Gan and J. K. Chen, "Nonequilibrium phase change in gold films induced by ultrafast laser heating", Opt. Lett. **37**, 2691–2693 (2012).

[94] A. Kuznetsov, J. Koch, and B. Chichkov, "Nanostructuring of thin gold films by femtosecond lasers", Applied Physics A **94**, 221–230 (2009).

[95] T. Pflug, J. Wang, M. Olbrich, M. Frank, and A. Horn, "Case study on the dynamics of ultrafast laser heating and ablation of gold thin films by ultrafast pump-probe reflectometry and ellipsometry", Applied Physics A **124**, 116 (2018).

[96] M. Olbrich, T. Pflug, C. Wüstefeld, M. Motylenko, S. Sandfeld, D. Rafaja, and A. Horn, "Hydrodynamic modeling and time-resolved imaging reflectometry of the ultrafast laser-induced ablation of a thin gold film", Optics and Lasers in Engineering **129**, 106067 (2020).

[97] E. Silaeva, L. Saddier, and J.-P. Colombier, "Drude-Lorentz model for optical properties of photoexcited transition metals under electron-phonon nonequilibrium", Applied Sciences **11**, 10.3390/app11219902 (2021).

[98] J. Chen, W.-K. Chen, J. Tang, and P. M. Rentzepis, "Time-resolved structural dynamics of thin metal films heated with femtosecond optical pulses", Proceedings of the National Academy of Sciences **108**, 18887–18892 (2011).

[99] S. J. Byrnes, *Multilayer optical calculations*, https://arxiv.org/abs/1603.02720, 2016.

[100] P. B. Johnson and R. W. Christy, "Optical constants of the noble metals", Phys. Rev. B **6**, 4370–4379 (1972).

[101] F. Cheng, P.-H. Su, J. Choi, S. Gwo, X. Li, and C.-K. Shih, "Epitaxial growth of atomically smooth aluminum on silicon and its intrinsic optical properties", ACS Nano **10**, PMID: 27656756, 9852–9860 (2016).

[102] W. M. Haynes, *CRC handbook of chemistry and physics*, 95th Edition (CRC press, 2014).

[103] A. Jain and A. J. H. McGaughey, "Thermal transport by phonons and electrons in aluminum, silver, and gold from first principles", Phys. Rev. B **93**, 081206 (2016).

[104] H. E. Elsayed-Ali, T. Juhasz, G. O. Smith, and W. E. Bron, "Femtosecond thermoreflectivity and thermotransmissivity of polycrystalline and single-crystalline gold films", Phys. Rev. B **43**, 4488–4491 (1991).

[105] L. Nguyen, T. Hashimoto, D. N. Zakharov, E. A. Stach, A. P. Rooney, B. Berkels, G. E. Thompson, S. J. Haigh, and T. L. Burnett, "Atomic-scale insights into the oxidation of aluminum", ACS Applied Materials & Interfaces 10, PMID: 29319290, 2230–2235 (2018).

[106] L. Jeurgens, W. Sloof, F. Tichelaar, and E. Mittemeijer, "Structure and morphology of aluminium-oxide films formed by thermal oxidation of aluminium", Thin Solid Films 418, 89–101 (2002).

[107] J. Canny, "A computational approach to edge detection", IEEE Transactions on Pattern Analysis and Machine Intelligence PAMI-8, 679–698 (1986).

[108] R. Halır and J. Flusser, "Numerically stable direct least squares fitting of ellipses", in Proceedings of the 6th international conference in central europe on computer graphics and visualization. wscg, Vol. 98 (1998), pp. 125–132.

[109] P. Gadenne, Y. Yagil, and G. Deutscher, "Transmittance and reflectance *in situ* measurements of semicontinuous gold films during deposition", Journal of Applied Physics 66, 3019–3025 (1989).

[110] K. H. Bennemann, *Non-linear optics in metals*, 98 (Oxford University Press, 1998), pp. 225–230.

[111] E. D. Palik, *Handbook of optical constants of solids*, Vol. 3 (Academic press, 1998).

[112] S. Zhang, Y. Pei, and L. Liu, "Dielectric function of polycrystalline gold films: Effects of grain boundary and temperature", Journal of Applied Physics 124, 165301 (2018).

[113] G. de Haan, J. Hernandez-Rueda, and P. C. M. Planken, "Femtosecond time-resolved pump-probe measurements on percolating gold in the ablation regime", Opt. Express 28, 12093–12107 (2020).

[114] M. Voncken and V. Faramarzi, Private Communication, ASML, De Run 6501, Veldhoven, The Netherlands, 2021.

[115] W. Xu, P. M. Wood-Adams, and C. G. Robertson, "Measuring local viscoelastic properties of complex materials with tapping mode atomic force microscopy", Polymer 47, 4798–4810 (2006).

[116] Precision Sapphire Technologies, *About Sapphire*, https://www.sapphire.lt/sapphire/, Visited 07-12-2023.

[117] Chemical BooK, *Silica glass(60676-86-0)*, https://www.chemicalbook.com/ProductMSDSDetailCB1199394_EN.htm, Visited 07-12-2023.

[118] Q. Jiang, B. Rogez, J.-B. Claude, A. Moreau, J. Lumeau, G. Baffou, and J. Wenger, "Adhesion layer influence on controlling the local temperature in plasmonic gold nanoholes", Nanoscale 12, 2524–2531 (2020).

[119] I. Hoogsteder, Private Communication, AMOLF NanoLab, Science Park 104, Amsterdam, The Netherlands, 2022.

[120] D. M. Mattox, "Chapter 12 - adhesion and deadhesion", in *Handbook of physical vapor deposition (pvd) processing (second edition)*, edited by D. M. Mattox, Second Edition (William Andrew Publishing, Boston, 2010), p. 464.

[121] L. Alber, *AbsorptionTMM*, https://github.com/udcm-su/AbsorptionTMM, 2019.

[122] M. B. Agranat, S. I. Anisimov, S. I. Ashitkov, V. V. Zhakhovskii, N. A. Inogamov, K. Nishihara, Y. V. Petrov, V. E. Fortov, and V. A. Khokhlov, "Dynamics of plume and crater formation after action of femtosecond laser pulse", Applied Surface Science 253, Proceedings of the Fifth International Conference on Photo-Excited Processes and Applications, 6276–6282 (2007).

[123] A. Lehmuskero, M. Kuittinen, and P. Vahimaa, "Refractive index and extinction coefficient dependence of thin al and ir films on deposition technique and thickness", Opt. Express 15, 10744–10752 (2007).

[124] P. Schmitt, S. Stempfhuber, N. Felde, A. V. Szeghalmi, N. Kaiser, A. Tünnermann, and S. Schwinde, "Influence of seed layers on the reflectance of sputtered aluminum thin films", Opt. Express 29, 19472–19485 (2021).

[125] T. T. Hu, J. H. Hsu, J. C. Huang, S. Y. Kuan, C. J. Lee, and T. G. Nieh, "Correlation between reflectivity and resistivity in multi-component metallic systems", Applied Physics Letters 101, 011902 (2012).

[126] W. Steinhögl, G. Schindler, G. Steinlesberger, M. Traving, and M. Engelhardt, "Comprehensive study of the resistivity of copper wires with lateral dimensions of 100 nm and smaller", Journal of Applied Physics 97, 023706 (2004).

[127] D. Josell, S. H. Brongersma, and Z. Tőkei, "Size-dependent resistivity in nanoscale interconnects", Annual Review of Materials Research 39, 231–254 (2009).

[128] D. Choi and K. Barmak, "On the potential of tungsten as next-generation semiconductor interconnects", Electronic Materials Letters 13, 449–456 (2017).

[129] T. M. Philip, N. A. Lanzillo, T. Gunst, T. Markussen, J. Cobb, S. Aboud, and R. R. Robison, "First-principles evaluation of fcc ruthenium for its use in advanced interconnects", Phys. Rev. Appl. 13, 044045 (2020).

[130] E. Milosevic, S. Kerdsongpanya, A. Zangiabadi, K. Barmak, K. R. Coffey, and D. Gall, "Resistivity size effect in epitaxial Ru(0001) layers", Journal of Applied Physics 124, 165105 (2018).

[131] C. Messinis, T. T. M. van Schaijk, N. Pandey, A. Koolen, I. Shlesinger, X. Liu, S. Witte, J. F. de Boer, and A. den Boef, "Aberration calibration and correction with nano-scatterers in digital holographic microscopy for semiconductor metrology", Opt. Express 29, 38237–38256 (2021).

[132] T. van Gardingen-Cromwijk, S. Konijnenberg, W. Coene, M. Adhikary, T. Tukker, S. Witte, J. F. de Boer, and A. den Boef, "Non-isoplanatic lens aberration correction in dark-field digital holographic microscopy for semiconductor metrology", Light: Advanced Manufacturing 4, 453 (2023).

[133] I. A. Makhotkin, I. Milov, J. Chalupský, K. Tiedtke, H. Enkisch, G. de Vries, F. Scholze, F. Siewert, J. M. Sturm, K. V. Nikolaev, R. W. E. van de Kruijs, M. A. Smithers, H. A. G. M. van Wolferen, E. G. Keim, E. Louis, I. Jacyna, M. Jurek, D. Klinger, J. B. Pelka, L. Juha, V. Hájková, V. Vozda, T. Burian, K. Saksl, B. Faatz, B. Keitel, E. Plönjes, S. Schreiber, S. Toleikis, R. Loch, M. Hermann, S. Strobel, R. Donker, T. Mey, and R. Sobierajski, "Damage accumulation in thin ruthenium films induced by repetitive exposure to femtosecond XUV pulses below the single-shot ablation threshold", J. Opt. Soc. Am. B **35**, 2799–2805 (2018).

[134] I. Milov, V. Lipp, D. Ilnitsky, N. Medvedev, K. Migdal, V. Zhakhovsky, V. Khokhlov, Y. Petrov, N. Inogamov, S. Semin, A. Kimel, B. Ziaja, I. Makhotkin, E. Louis, and F. Bijkerk, "Similarity in ruthenium damage induced by photons with different energies: From visible light to hard X-rays", Applied Surface Science **501**, 143973 (2020).

[135] S. Bucklow, "The description of craquelure patterns", Studies in Conservation **42**, 129–140 (1997).

[136] E. Abram, I. Milov, N. Orlov, K. van Druten, E. C. Garnett, and P. Planken, "Pre-ablation regime light-induced optical changes in nanometer thick metal films", Opt. Express **32**, 4564–4587 (2024).

[137] L. Ackermann, C. Roider, K. Cvecek, and M. Schmidt, "Methods for uniform beam shaping and their effect on material ablation", Applied Physics A **128**, 877 (2022).

[138] F. Brandi, N. Burdet, R. Carzino, and A. Diaspro, "Very large spot size effect in nanosecond laser drilling efficiency of silicon", Opt. Express **18**, 23488–23494 (2010).

[139] M. A. Fischler and R. C. Bolles, "Random sample consensus: a paradigm for model fitting with applications to image analysis and automated cartography", Commun. ACM **24**, 381–395 (1981).

[140] E. Abram and P. Planken, *Light-induced optical and nanostructural changes of Si gratings*, Submitted to Opt. Express, manuscript under review, 2025.

[141] S. Shead, *The Dutch firm that investors are going wild over is now creating a machine that could redefine electronics*, https://www.cnbc.com/2021/12/10/asmls-high-na-euv-lithography-machine-is-set-to-transform-chipmaking.html, Accessed 28-06-2024, Dec. 2021.

[142] M. Vreugdenhil and D. van Oosten, "Pulse duration dependence of single-shot pulsed laser ablation of gallium based III-V compound semiconductors", in Laser-induced damage in optical materials 2023, Vol. 12726, edited by C. W. Carr, D. Ristau, C. S. Menoni, and M. D. Thomas (International Society for Optics and Photonics, 2023), p. 1272609.

[143] Y. Li, Z. Yuan, J. Wang, and Q. Xu, "Laser-induced damage characteristics in fused silica surface due to mechanical and chemical defects during manufacturing processes", Optics & Laser Technology **91**, 149–158 (2017).

[144] E. Abram, N. Orlov, E. C. Garnett, and P. Planken, "Sub-ablation-threshold light-induced modification of thin ruthenium layers detected using optical reflectance", Journal of Applied Physics **136**, 245305 (2024).

[145] C. M. Herzinger, B. Johs, W. A. McGahan, J. A. Woollam, and W. Paulson, "Ellipsometric determination of optical constants for silicon and thermally grown silicon dioxide via a multi-sample, multi-wavelength, multi-angle investigation", Journal of Applied Physics **83**, 3323–3336 (1998).

[146] G. Bradski, "The OpenCV Library", Dr. Dobb's Journal of Software Tools (2000).

[147] F. Schwidefsky, "Increase of the refractive index of silicon films by dangling bonds", Thin Solid Films **18**, 45–52 (1973).

[148] S. Chandrasekhar, A. Vengurlekar, V. Karulkar, and S. Roy, "Temperature, light intensity and microstructure dependence of the refractive index of polycrystalline silicon films", Thin Solid Films **169**, 205–212 (1989).

[149] M. Janai, D. Allred, D. Booth, and B. Seraphin, "Optical properties and structure of amorphous silicon films prepared by CVD", Solar Energy Materials **1**, 11–27 (1979).

[150] D. Aspnes, "Optical properties of thin films", Thin Solid Films **89**, 249–262 (1982).

[151] L. Cruciani, M. Vreugdenhil, S. van Vliet, E. Abram, D. van Oosten, R. Bliem, K. van Druten, and P. Planken, "Direct laser patterning of ruthenium below the optical diffraction limit", Applied Physics Letters **124**, 171902 (2024).

[152] E. Abram, *Contours*, https://github.com/eabram/contour.git, version v1.0, 2025.

[153] R. L. Brainard, G. G. Barclay, E. H. Anderson, and L. E. Ocola, "Resists for next generation lithography", Microelectronic Engineering **61-62**, Micro- and Nano-Engineering 2001, 707–715 (2002).

[154] C. Luo, C. Xu, L. Lv, H. Li, X. Huang, and W. Liu, "Review of recent advances in inorganic photoresists", RSC Adv. **10**, 8385–8395 (2020).

[155] M. N. Polyanskiy, *Refractiveindex.info database of optical constants*, http://refractiveindex.info, Jan. 2024.

[156] I. H. Malitson and M. J. Dodge, "Refractive index and birefringence of synthetic sapphire", J. Opt. Soc. Am **62**, 1405 (1972).

[157] American Institute of Physics and D. E. Gray, *American institute of physics handbook: 3d ed* (McGraw-Hill, 1972).

[158] J. Hohlfeld, *Ultrafast electron, lattice and spin dynamics in metals: investigated by linear and nonlinear optical techniques*, Akademische Abhandlungen zur Physik (VWF, Verlag für Wiss. und Forschung, 1998).

[159] R. O. Duda, P. E. Hart, et al., *Pattern classification and scene analysis*, Vol. 3 (Wiley New York, 1973).

[160] G. Bradski and A. Kaehler, *Learning OpenCV: Computer vision with the OpenCV library* (" O'Reilly Media, Inc.", 2008), pp. 153–161.

[161]   W. Niblack, *An introduction to digital image processing* (Strandberg Publishing Company, 1985).

APPENDICES

A

A MATRIX APPROACH TO MULTILAYER OPTICS

In section 1.1.1, the transfer-matrix method (TMM) is introduced. This method describes the electromagnetic plane wave that propagates between two media (medium i and j). At the interface of the two, there is a *interface matrix M_{ij}* which *transfers* the waves in medium j that propagates away from and to medium i ($\widetilde{E}_{j\rightarrow}$ and $\widetilde{E}_{j\leftarrow}$) to the ones in medium i ($\widetilde{E}_{i\rightarrow}$ and $\widetilde{E}_{i\leftarrow}$). Next to this interface matrix, a propagation matrix M_j is also obtained that describes the waves traveling through the (absorbent) layer j.

By performing matrix multiplications for every transition and propagation in a layer of a multilayer stack, the reflection, transmission and absorption can be obtained, and even the locally absorbed power can be derived. This works for both s and p polarized (oblique) incident waves. Next to the polarization and incidence angle, only the refractive indices and thicknesses of each layer in the stack are needed as input parameters.

A.1. INTRODUCTION

The document provided with the python package Multilayers shows how to obtain a matrix approach to (thin) multilayer optics, with the aim of calculating reflection, transmission and absorption in full detail. Part of this document is incorporated in section 1.1.1. However, only normal incidence of the light onto the multilayer stack is presented there. This appendix, therefore, covers the TMM for oblique incidence as well, along with the

---

The computational method described in this chapter is based on notes provided by Klaasjan van Druten and included and implemented in the Python package Multilayers.

Note that we use κ for the imaginary part of the complex refractive index instead of k as used in all other chapters. This is mainly to distinguish it clearly from the various wave vectors k_0, k_i, $\tilde{k}$, $\boldsymbol{k}$, etc.

slight adjustments of the equations presented in section 1.1.1. The following is in essence a concise combination of the methods that can be found in the standard textbooks [39–41].

A.2. OBLIQUE INCIDENCE

We consider the situation where the incoming wave is not normal to the interface(s). We will still restrict ourselves to a planar situation, meaning that all interfaces are parallel.

When the incident light is at an angle, the situation becomes more complicated in several ways. For one, we now need to distinguish the two polarization directions, namely *in* the plane of incidence, and *perpendicular* to the plane of incidence. So instead of a 2×2 matrix, we will have at least two 2×2 matrices to deal with, and, if there is any coupling between in-plane and out-of-plane polarization, a 4×4 matrix per interface/propagation. Further, in the case of absorbing media, we need to distinguish propagation in the lateral direction (along the interfaces), from propagation normal to the interfaces. For incident plane waves (with a single wavevector $\vec{k}$), there is translational invariance of the waves along the lateral direction, so the amplitudes of the waves are independent of the lateral direction. Since for absorbing media the wave amplitudes *do* vary in the direction normal to the interfaces, this implies that the planes of constant amplitude will no longer be parallel to the planes of constant phase.

First, let's get started by defining the relevant quantities, see figure 1.1. The polarization with its electric field along the plane of incidence is indicated by p, while light with its electric field perpendicular to the plane of incidence is traditionally denoted by s (for *senkrecht*).

A.2.1. NONABSORBING MEDIA

For nonabsorbing media, we can just use the standard Fresnel coefficient expressions. in particular, for p polarization we have [41]:

$$r_p = \frac{\alpha - \beta}{\alpha + \beta}, \tag{A.1}$$

$$t_p = \frac{2}{\alpha + \beta}, \tag{A.2}$$

with $\beta = k_2/k_1 = n_2/n_1$, and

$$\alpha \equiv \frac{\cos\theta_T}{\cos\theta_I}, \tag{A.3}$$

with θ_I and θ_T the incident and transmitted angle, respectively. In terms of wavevectors, this is:

$$\alpha = \frac{k_{2\perp}}{k_2}\frac{k_1}{k_{1\perp}} = \frac{1}{\beta}\frac{k_{2\perp}}{k_{1\perp}}. \tag{A.4}$$

For s polarization (Prob. 9.17 of [41]) we have:

$$r_s = \frac{1 - \alpha\beta}{1 + \alpha\beta}, \tag{A.5}$$

$$t_s = \frac{2}{1 + \alpha\beta}. \tag{A.6}$$

A.3. Generalization

A.3.1. Macroscopic Maxwell equations

The macroscopic Maxwell equations [41] can be written as:

$$\vec{\nabla} \cdot \vec{D} = \rho_f, \tag{A.7}$$

$$\vec{\nabla} \times \vec{E} = -\frac{\partial \vec{B}}{\partial t}, \tag{A.8}$$

$$\vec{\nabla} \cdot \vec{B} = 0, \tag{A.9}$$

$$\vec{\nabla} \times \vec{H} = \vec{J}_f + \frac{\partial \vec{D}}{\partial t}. \tag{A.10}$$

A.3.2. Complexified version of Poynting's theorem

For determining the locally absorbed power, it is useful to consider (the derivation of) Poynting's theorem for harmonic fields. We follow Sections 6.9 (and 6.7) of Jackson [39], adopting the following notation (a mix of the above and of [39]). We write the harmonically oscillating fields as:

$$\vec{E}(\boldsymbol{r}, t) = \text{Re}(\boldsymbol{E}(\boldsymbol{r})e^{-i\omega t}) \equiv \frac{1}{2}\left[\boldsymbol{E}(\boldsymbol{r})e^{-i\omega t} + \boldsymbol{E}^*(\boldsymbol{r})e^{i\omega t}\right]. \tag{A.11}$$

Products such as $\vec{J} \cdot \vec{E}$ then can be rewritten as:

$$\vec{J}(\boldsymbol{r}, t) \cdot \vec{E}(\boldsymbol{r}, t) = \frac{1}{2}\text{Re}\left[\boldsymbol{J}^*(\boldsymbol{r}) \cdot \boldsymbol{E}(\boldsymbol{r}) + \boldsymbol{J}(\boldsymbol{r}) \cdot \boldsymbol{E}(\boldsymbol{r})e^{-2i\omega t}\right]. \tag{A.12}$$

When taking cycle-averages over time, the second term on the right-hand side then averages out. For the power dissipated, we are interested in the cycle-averaged value of $\vec{J} \cdot \vec{E}$, and hence in the first term on the right-hand side above. For harmonically oscillating fields, the macroscopic Maxwell equations then become:

$$\boldsymbol{\nabla} \cdot \boldsymbol{D} = \rho_f, \tag{A.13}$$

$$\boldsymbol{\nabla} \times \boldsymbol{E} = +i\omega\boldsymbol{B}, \tag{A.14}$$

$$\boldsymbol{\nabla} \cdot \boldsymbol{B} = 0, \tag{A.15}$$

$$\boldsymbol{\nabla} \times \boldsymbol{H} = \boldsymbol{J}_f - i\omega\boldsymbol{D}. \tag{A.16}$$

Using the vector identity

$$\boldsymbol{\nabla} \cdot (\boldsymbol{a} \times \boldsymbol{b}) = \boldsymbol{b} \cdot (\boldsymbol{\nabla} \times \boldsymbol{a}) - \boldsymbol{a} \cdot (\boldsymbol{\nabla} \times \boldsymbol{b}), \tag{A.17}$$

and using the two Maxwell's equations for the curl (of $\boldsymbol{H}$ and $\boldsymbol{E}$ respectively), yields (a complex-valued version of) Poynting's theorem:

$$\frac{1}{2}\boldsymbol{J}_f^* \cdot \boldsymbol{E} = -2i\omega(u_e - u_m) - \boldsymbol{\nabla} \cdot \boldsymbol{S}, \tag{A.18}$$

with (potentially complex-valued) defined quantities

$$u_e = \frac{1}{4}\boldsymbol{E} \cdot \boldsymbol{D}^*, \tag{A.19}$$

$$u_m = \frac{1}{4} \boldsymbol{B} \cdot \boldsymbol{H}^*, \tag{A.20}$$

and

$$\boldsymbol{S} = \frac{1}{2} \boldsymbol{E} \times \boldsymbol{H}^*. \tag{A.21}$$

The real part of equation (A.18) expresses conservation of energy for the cycle-averaged quantities. In particular, Re($\boldsymbol{S}$) is the Poynting vector, and the imaginary part Im($u_e - u_m$) accounts for dissipation in the material. The imaginary part of equation (A.18) relates to the reactive/stored energy and its alternating flow. In particular Re(u_e) is the instantaneous electric field energy density, and Re(u_m) the magnetic field energy density.

A.3.3. PLANE WAVES IN LINEAR MEDIA

We are interested in plane-wave solutions, but need to keep the vectorial form, i.e. we write:

$$\boldsymbol{E}(\boldsymbol{r}) = \boldsymbol{E}_0 e^{i\boldsymbol{k}\cdot\boldsymbol{r}}, \tag{A.22}$$

etcetera. Note that harmonic time-dependence is implied again here.

In a linear, isotropic and homogeneous medium, we may write constituent relations $\boldsymbol{D} = \tilde{\epsilon}(\omega)\boldsymbol{E}$, and $\boldsymbol{H} = \boldsymbol{B}/\tilde{\mu}(\omega)$. For simplicity we will limit ourselves to non-magnetic media ($\tilde{\mu} = \mu_0$). Furthermore, for a medium characterized by a conductivity $\sigma(\omega)$, we have $\boldsymbol{J}_f = \sigma(\omega)\boldsymbol{E}$. We will also take $\rho_f(\omega) = 0$ in the bulk of the medium. Note that below we will consider the boundary separately.

With this set of assumptions and simplifications, and inserting traveling-wave trial solutions of the form equation (A.22), the spatial and temporal derivatives lead to wave vector and angular frequency prefactors respectively:

$$\boldsymbol{k} \cdot \boldsymbol{E} = 0, \tag{A.23}$$

$$\boldsymbol{k} \times \boldsymbol{E} = \omega \boldsymbol{B}, \tag{A.24}$$

$$\boldsymbol{k} \cdot \boldsymbol{B} = 0, \tag{A.25}$$

$$i\boldsymbol{k} \times \boldsymbol{B} = \mu_0 \left[\sigma(\omega) - i\omega\tilde{\epsilon}(\omega) \right] \boldsymbol{E}. \tag{A.26}$$

Inserting equation (A.24) into equation (A.26) leads to:

$$\boldsymbol{k} \times (\boldsymbol{k} \times \boldsymbol{E}) = -\mu_0 \left[\omega^2 \tilde{\epsilon}(\omega) + i\omega\sigma(\omega) \right] \boldsymbol{E}. \tag{A.27}$$

Since $\boldsymbol{k}$ and $\boldsymbol{E}$ are orthogonal ($\boldsymbol{k} \cdot \boldsymbol{E} = 0$), the cross products on the left-hand side of the above simplify to $-(\boldsymbol{k} \cdot \boldsymbol{k})\boldsymbol{E}$, and equation (A.26) simplifies to:

$$\boldsymbol{k} \cdot \boldsymbol{k} \equiv \tilde{k}^2 = \mu_0 \left[\omega^2 \tilde{\epsilon}(\omega) + i\omega\sigma(\omega) \right]. \tag{A.28}$$

Writing $\boldsymbol{k} = \vec{k}_0[n(\omega) + i\kappa(\omega)]$, with $|\vec{k}_0| \equiv k_0 \equiv \omega/c$ as before, and $\mu_0\epsilon_0 = 1/c^2$ results in:

$$\tilde{n}^2 = (n + i\kappa)^2 = \frac{1}{\epsilon_0} \left(\tilde{\epsilon} + \frac{i\sigma}{\omega} \right). \tag{A.29}$$

Thus, specifying n and κ of a (linear, isotropic, and homogeneous) material at a certain frequency, is sufficient to capture the behavior of electromagnetic waves in the material at that frequency. In particular, from the imaginary part of equation (A.29), we have:

$$2\epsilon_0 n\kappa = \text{Im}\tilde{\epsilon} + \frac{\sigma}{\omega}. \tag{A.30}$$

A.3.4. PLANE WAVES WITH A FIXED INCIDENT ANGLE

For a plane wave incident from a lossless medium, the incident field will have a constant amplitude at the interface, and the boundary conditions enforce that the transmitted wave will have the same spatial dependence along the interface. Thus, we can write:

$$\boldsymbol{k} = k_0(\vec{n} + i\vec{\kappa}), \tag{A.31}$$

with $\vec{\kappa}$ perpendicular to the interface, and the parallel part of $\vec{n}$ determined by the incoming wave. Note that $\boldsymbol{k}$, $\vec{n}$, and $\vec{\kappa}$ are all within the plane of incidence.

Starting from equation (A.31), we have

$$\tilde{k}^2 = \boldsymbol{k} \cdot \boldsymbol{k} = k_0^2(\vec{n} \cdot \vec{n} + 2i\vec{n} \cdot \vec{\kappa} - \vec{\kappa} \cdot \vec{\kappa}). \tag{A.32}$$

Thus, for a material with given n and κ, we need for the wavevector

$$\vec{n} \cdot \vec{n} - \vec{\kappa} \cdot \vec{\kappa} = n^2 - \kappa^2, \tag{A.33}$$

$$\vec{n} \cdot \vec{\kappa} = n\kappa. \tag{A.34}$$

For a plane-wave boundary condition at a planar interface, the parallel part of $\vec{n}$ is fixed, $n_\parallel = k_\parallel / k_0$, and $\vec{\kappa}$ is strictly normal to the interface. Thus the above simplifies to:

$$n_\parallel^2 + n_\perp^2 - \kappa_\perp^2 = n^2 - \kappa^2, \tag{A.35}$$

$$n_\perp \kappa_\perp = n\kappa, \tag{A.36}$$

and we have two equations with two unknowns ($n_\perp$ and $\kappa_\perp$), which can be solved directly. Namely with shorthand:

$$b = n^2 - \kappa^2 - n_\parallel^2, \tag{A.37}$$

$$n_\perp = \sqrt{\frac{b + \sqrt{b^2 + 4n^2\kappa^2}}{2}}, \tag{A.38}$$

$$\kappa_\perp = \frac{n\kappa}{n_\perp}. \tag{A.39}$$

Note that for $n_\parallel = 0$ we recover $n_\perp = n$ and $\kappa_\perp = \kappa$, as should be. For what follows below, it is useful to define

$$\tilde{n}_\perp \equiv n_\perp + i\kappa_\perp. \tag{A.40}$$

In summary, then, with the coordinate system of figure 1.1, we have

$$\boldsymbol{k} = k_0 \left[n_\parallel \hat{x} + (n_\perp + i\kappa_\perp)\hat{z} \right] = k_0 \left(n_\parallel \hat{x} + \tilde{n}_\perp \hat{z} \right). \tag{A.41}$$

OUT-OF-PLANE POLARIZATION

For s polarization, the above can be worked out relatively easily, since $\boldsymbol{E}$ is perpendicular to the plane of incidence, while $\boldsymbol{k}$, $\vec{n}$, $\vec{\kappa}$, are within this plane.

As a consequence, the first Maxwell equation is satisfied, the second Maxwell equation ensures that $\boldsymbol{k}$ and $\boldsymbol{B}$ are orthogonal so that the third is automatically satisfied, and what remains is to satisfy equation (A.27). Thus we can write:

$$\boldsymbol{E}(\boldsymbol{r}) = \tilde{E}_0 \hat{y} e^{i\boldsymbol{k} \cdot \boldsymbol{r}}, \tag{A.42}$$

$$\boldsymbol{B}(\boldsymbol{r}) = \frac{1}{c} \tilde{E}_0 \left(n_\parallel \hat{z} - \tilde{n}_\perp \hat{x} \right) e^{i\boldsymbol{k} \cdot \boldsymbol{r}}. \tag{A.43}$$

IN-PLANE POLARIZATION

For p polarization, the situation is similar, with the roles of $\tilde{\vec{B}}$ (which is now perpendicular to the plane of incidence) and $\tilde{\vec{E}}$ exchanged. For later convenience, we would like to keep the same phase definition of the $\hat{x}$ component of $\tilde{\vec{E}}$ leading to slightly more complicated expressions here. Namely,

$$\boldsymbol{E}(\boldsymbol{r}) \;=\; \frac{\tilde{E}_0}{N}\left(\hat{x}-\frac{n_\parallel}{\tilde{n}_\perp}\hat{z}\right)e^{i\boldsymbol{k}\cdot\boldsymbol{r}}, \tag{A.44}$$

$$\boldsymbol{B}(\boldsymbol{r}) \;=\; \frac{\tilde{E}_0\hat{y}}{Nc}\left(\frac{n_\parallel^2}{\tilde{n}_\perp}+\tilde{n}_\perp\right)e^{i\boldsymbol{k}\cdot\boldsymbol{r}}, \tag{A.45}$$

with normalization

$$N=\sqrt{1+\frac{n_\parallel^2}{n_\perp^2+\kappa_\perp^2}}. \tag{A.46}$$

A.3.5. REFLECTION AND TRANSMISSION FROM BOUNDARY CONDITIONS

To get to the boundary conditions, for the interface between two linear, isotropic and homogeneous media, we return to the macroscopic Maxwell equations. The medium with index j can then be characterized with dielectric function $\tilde{\epsilon}_j(\omega)$ and conductivity $\sigma_j(\omega)$. For media with nonzero conductivity, we can have (free) surface charge density σ_f built up at the interface. At charge conservation,

$$\boldsymbol{\nabla}\cdot\vec{J}_f=-\frac{\partial\rho_f}{\partial t}, \tag{A.47}$$

applied to the interface between media 1 and 2 then yields at frequency ω,

$$i\omega\sigma_f=-J_{f\perp 1}+J_{f\perp 2}, \tag{A.48}$$

and the boundary condition from the first Maxwell equation reads:

$$\left(\tilde{\epsilon}_1+\frac{i\sigma_1}{\omega}\right)\tilde{E}_{\perp 1}=\left(\tilde{\epsilon}_2+\frac{i\sigma_2}{\omega}\right)\tilde{E}_{\perp 2}. \tag{A.49}$$

Note that the same combination of $\tilde{\epsilon}$ and σ appears here as in the previous equations, so this can again be rephrased in terms of n_i and κ_i of the materials involved. Also, note that the above σ_1 and σ_2 are conductivities, not to be confused with the free surface charge density σ_f.

Again taking $\mu=\mu_0$ for all materials, for simplicity, and assuming there is no surface current density, the other boundary conditions are more common:

$$\vec{E}_{\parallel 1} \;=\; \vec{E}_{\parallel 2}, \tag{A.50}$$

$$B_{\perp 1} \;=\; B_{\perp 2}, \tag{A.51}$$

$$\vec{B}_{\parallel 1} \;=\; \vec{B}_{\parallel 2}. \tag{A.52}$$

For the discussion below, it is useful to state explicitly that for the wave vector in the direction of reflection, and the choice of coordinates of figure 1.1, we have

$$\boldsymbol{k}_R = k_0 \left(n_\parallel \hat{x} - \tilde{n}_\perp \hat{z} \right), \tag{A.53}$$

while for the incident (and transmitted) direction we have

$$\boldsymbol{k}_I \equiv \boldsymbol{k} = k_0 \left(n_\parallel \hat{x} + \tilde{n}_\perp \hat{z} \right), \tag{A.54}$$

as defined before.

OUT-OF-PLANE POLARIZATION

For s polarization, we write the electric and magnetic field of the reflected wave as:

$$\begin{align}
\boldsymbol{E}_R(\vec{r}) &= \tilde{E}_{R0} \hat{y} e^{i \boldsymbol{k}_R \cdot \boldsymbol{r}}, \tag{A.55}\\
\boldsymbol{B}_R(\vec{r}) &= \frac{1}{c} \tilde{E}_{R0} \left(n_\parallel \hat{z} + \tilde{n}_\perp \hat{x} \right) e^{i \boldsymbol{k}_R \cdot \boldsymbol{r}}. \tag{A.56}
\end{align}$$

The first boundary condition is now automatically satisfied (since the perpendicular component of $\boldsymbol{E}$ is zero), while the rest yields the same expressions for the amplitude reflection and transmission coefficients:

$$\begin{align}
r_s &= \frac{1 - \beta_s}{1 + \beta_s}, \tag{A.57}\\
t_s &= \frac{2}{1 + \beta_s}, \tag{A.58}
\end{align}$$

with a modified β,

$$\beta_s = \frac{\tilde{n}_{\perp 2}}{\tilde{n}_{\perp 1}}. \tag{A.59}$$

These are readily shown to be consistent with the usual Fresnel expressions (without absorption) and the expressions for normal incidence (with absorption).

IN-PLANE POLARIZATION

For p polarization, we write the electric and magnetic field of the reflected wave as:

$$\begin{align}
\boldsymbol{E}_R(\boldsymbol{r}) &= \frac{\tilde{E}_{R0}}{N} \left(\hat{x} + \frac{n_\parallel}{\tilde{n}_\perp} \hat{z} \right) e^{i \boldsymbol{k}_R \cdot \boldsymbol{r}}, \tag{A.60}\\
\boldsymbol{B}_R(\boldsymbol{r}) &= -\frac{\tilde{E}_{R0} \hat{y}}{Nc} \left(\frac{n_\parallel^2}{\tilde{n}_\perp} + \tilde{n}_\perp \right) e^{i \boldsymbol{k}_R \cdot \boldsymbol{r}}, \tag{A.61}
\end{align}$$

and the boundary conditions lead to the expressions for the reflection and transmission coefficients:

$$\begin{align}
r_p &= \frac{\alpha_p - \beta_p}{\alpha_p + \beta_p}, \tag{A.62}\\
t_p &= \frac{2}{\alpha_p + \beta_p}, \tag{A.63}
\end{align}$$

with α and β,

$$\alpha_p = \frac{N_1}{N_2}, \tag{A.64}$$

$$\beta_p = \frac{\tilde{n}_2^2}{\tilde{n}_1^2} \frac{\tilde{n}_{\perp 1}}{\tilde{n}_{\perp 2}} \frac{N_1}{N_2}. \tag{A.65}$$

These are indeed consistent with the normal-incidence expressions (with absorption), and with the usual Fresnel (no absorption) expressions.

A.3.6. TRANSMITTED AND REFLECTED INTENSITY

To get to the transmitted and reflected intensity (per area of the interface), we need to take into account the angle between the interface and the wavefronts; this leads to an extra cosine term, i.e.

$$I = \frac{1}{2}\epsilon_0 n c E^2 \cos\theta, \tag{A.66}$$

for the incident, reflected and transmitted part of the waves. Thus, the intensity reflection and transmission coefficients are:

$$R = \frac{I_R}{I_I} = |r|^2, \tag{A.67}$$

and

$$T = \frac{I_T}{I_I} = |t|^2 \frac{n_T \cos\theta_T}{n_I \cos\theta_I}. \tag{A.68}$$

Note that $\theta_R = \theta_I$, and with θ_T given by Snell's law:

$$\frac{\sin\theta_T}{\sin\theta_I} = \frac{n_I}{n_T}. \tag{A.69}$$

A.3.7. LOCALLY ABSORBED POWER

Returning now to the issue of a useful expression for the locally absorbed (cycle-averaged) power, we now use the complex-valued version of Poynting's theorem, equation (A.18). For the linear, isotropic, homogeneous and non-magnetic ($\mu = \mu_0$) materials under consideration here, the real part of equation (A.18) yields

$$p \equiv -\text{Re}\langle \boldsymbol{\nabla} \cdot \boldsymbol{S} \rangle = \frac{1}{2}\left[\sigma(\omega) + \omega\text{Im}(\tilde{\epsilon}(\omega))\right]\langle \boldsymbol{E}^* \cdot \boldsymbol{E} \rangle. \tag{A.70}$$

Here, we encounter the same combination of σ and $\text{Im}(\tilde{\epsilon})$ again, so that the result can be simplified in terms of $n\kappa$, as:

$$p = \epsilon_0 \omega n\kappa \langle \boldsymbol{E}^* \cdot \boldsymbol{E} \rangle. \tag{A.71}$$

Writing the field $\boldsymbol{E}(\boldsymbol{r})$ as a superposition of incoming and reflected wave amplitudes as $\tilde{E}_{I0}(\boldsymbol{r}) = \tilde{c}_I E_0$ and $\tilde{E}_{R0}(\boldsymbol{r}) = \tilde{c}_R E_0$, p can now be further worked out for both polarizations.

For s polarization the electric field points along $\hat{x}$ for both the transmitted and reflected direction, and the above simplifies to:

$$p = \epsilon_0 \omega n\kappa E_0^2 f_s, \tag{A.72}$$

with

$$f_s = (\tilde{c}_I + \tilde{c}_R)(\tilde{c}_I^* + \tilde{c}_R^*). \tag{A.73}$$

For p polarization, the amplitudes of transmitted and reflected electric fields add along x, but subtract along z, and the result is

$$p = \epsilon_0 \omega n\kappa E_0^2 f_p, \tag{A.74}$$

with

$$f_p = \tilde{c}_I\tilde{c}_I^* + \tilde{c}_R\tilde{c}_R^* + \frac{1}{N^2}(\tilde{c}_I\tilde{c}_R^* + \tilde{c}_R\tilde{c}_I^*)\left(1 - \frac{n_\parallel^2}{n_\perp^2 + \kappa_\perp^2}\right), \tag{A.75}$$

or, equivalently,

$$f_p = (\tilde{c}_I + \tilde{c}_R)(\tilde{c}_I^* + \tilde{c}_R^*) - 2(\tilde{c}_I\tilde{c}_R^* + \tilde{c}_R\tilde{c}_I^*)\frac{n_\parallel^2}{n_\perp^2 + \kappa_\perp^2}. \tag{A.76}$$

So the absorbed power density relative to the incident intensity is

$$\frac{p}{I_I} = \frac{2k_0 n\kappa f}{n_I \cos\theta_I}, \tag{A.77}$$

with f set to f_s or to f_p depending on the polarization.

A.3.8. IMPLEMENTATION

In summary, to implement the above we can treat the combination of oblique incidence and multiple lossy layers as follows. First, from the incident angle and incident (lossless) medium with refractive index n_i calculate the parallel wavevector $k_\parallel = n_\parallel k_0$ and parallel index $n_\parallel$ from:

$$n_\parallel = n_i \sin(\theta_i), \tag{A.78}$$

and $k_0 = 2\pi/\lambda_0 = \omega_0/c$, with λ_0 the wavelength in vacuum. Next, for each layer, calculate $\tilde{n}_\perp$ from:

$$b = n^2 - \kappa^2 - n_\parallel^2, \tag{A.79}$$

$$n_\perp = \sqrt{\frac{b + \sqrt{b^2 + 4n^2\kappa^2}}{2}}, \tag{A.80}$$

$$\kappa_\perp = \frac{n\kappa}{n_\perp}, \tag{A.81}$$

and

$$\tilde{n}_\perp \equiv n_\perp + i\kappa_\perp. \tag{A.82}$$

Combine these to obtain

$$\boldsymbol{k} = k_0\left[n_\parallel \hat{x} + (n_\perp + i\kappa_\perp)\hat{z}\right] = k_0\left(n_\parallel \hat{x} + \tilde{n}_\perp \hat{z}\right), \tag{A.83}$$

and normalization factor

$$N = \sqrt{1 + \frac{n_\parallel^2}{n_\perp^2 + \kappa_\perp^2}}. \tag{A.84}$$

For each interface between (possibly lossy) media we then have complex-valued reflection and transmission coefficients:

$$r \quad = \quad \frac{\alpha - \beta}{\alpha + \beta}, \tag{A.85}$$

$$t \quad = \quad \frac{2}{\alpha + \beta}, \tag{A.86}$$

with $\alpha_s = 1$ and $\beta_s = \tilde{n}_{\perp 2}/\tilde{n}_{\perp 1}$ for out-of-plane polarization, and $\alpha_p = N_1/N_2$ and $\beta_p = \tilde{n}_2^2 \tilde{n}_{\perp 1} N_1 / \tilde{n}_1^2 \tilde{n}_{\perp 2} N_2$ for in-plane polarization. The matrix relating in- and outgoing waves then can be written as:

$$\begin{pmatrix} t & -r \\ r & \alpha\beta t \end{pmatrix}, \tag{A.87}$$

and the matrix relating the fields in the two media as:

$$\begin{pmatrix} \frac{1}{t} & \frac{r}{t} \\ \frac{r}{t} & \frac{r^2}{t} + \alpha\beta t \end{pmatrix}, \tag{A.88}$$

which actually simplifies to:

$$\frac{1}{2}\begin{pmatrix} \alpha + \beta & \alpha - \beta \\ \alpha - \beta & \alpha + \beta \end{pmatrix}, \tag{A.89}$$

inserting the proper α and β for either s or p polarization.

The propagation matrix within a layer (with thickness d) becomes

$$\begin{pmatrix} e^{-ik_0 \tilde{n}_\perp d} & 0 \\ 0 & e^{+ik_0 \tilde{n}_\perp d} \end{pmatrix}. \tag{A.90}$$

B

SAMPLES

An overview of the samples used in the experiments described in chapters 3 and 4 is given in tables B.1 and B.2.

Table B.1: Samples

Material	Thickness (nm)	Substrate material	Substrate thickness (mm)	Fabrication method
Au	8[*]	BS	0.5	EBPVD
Au	16[*]	BS	0.5	EBPVD
Au	20	BS	0.5	EBPVD
Au	20	BS	0.5	EBPVD
Au	20	UVFS with a 20 arcmin wedge	12.0	Resistance heating evaporation
Au	20 +5 nm Cr adhesion layer	BS	0.5	EBPVD
Au	24[*]	BS	0.5	EBPVD
Au	32[*]	BS	0.5	EBPVD
Au	40[*]	BS	0.5	EBPVD
Au	80[*]	BS	0.5	EBPVD
Al	10[†]	BS	0.5	EBPVD
Al	14[†]	BS	0.5	EBPVD
Al	18[†]	BS	0.5	EBPVD
Al	20	BS	0.5	EBPVD
Al	20	Sapphire	1.1	EBPVD
Al	20	CaF_2	0.5	EBPVD
Al	20	Si	0.5	EBPVD
Al	22[†]	BS	0.5	EBPVD
Al	26[†]	BS	0.5	EBPVD
Al	30[†]	BS	0.5	EBPVD

BS = Borosilicate glass, EBPVD = Electron Beam Physical Vapor Deposition. ∗ or † mark that these samples were fabricated in the same run and therefore were deposited under comparable vacuum conditions, evaporation pressures and deposition rates.

Table B.2: Samples

Material	Thickness (nm)		Substrate material	Substrate thickness (mm)	Note
	Nominal	Measured			
Ru	8	9.2	BS	0.5	These samples were not fabricated at once. However they were fabricated immediately after each other, under comparable vacuum conditions.
Ru	10	11.6	BS	0.5	
Ru	15	17.2	BS	0.5	
Ru	20	23.0	BS	0.5	
Ru	25	28.8	BS	0.5	
Ru	40	45.9	BS	0.5	
Ru	8[*]	≈ 9.2	BS	0.5	
Ru	8[*]	≈ 9.2	Sapphire	1.1	
Ru	8[*]	≈ 9.2	CaF_2	0.5	
Ru	8[*]	≈ 9.2	Si	0.5	
Ru	20[†]	≈ 23.0	BS	0.5	
Ru	20[†]	≈ 23.0	Sapphire	1.1	
Ru	20[†]	≈ 23.0	CaF_2	0.5	
Ru	20[†]	≈ 23.0	Si	0.5	
Ru	40[‡]	≈ 45.9	BS	0.5	
Ru	40[‡]	≈ 45.9	Sapphire	1,1	
Ru	40[‡]	≈ 45.9	CaF_2	0.5	
Ru	40[‡]	≈ 45.9	Si	0.5	
Ru	8[§]	≈ 9.2	BS	0.5	
Ru	8[§]	≈ 9.2	BS - S‖	0.5	
Ru	8[§]	≈ 9.2	BS - S⊥	0.5	
Ru	15[‖]	≈ 17.2	BS	0.5	
Ru	15[‖]	≈ 17.2	BS - S‖	0.5	
Ru	15[‖]	≈ 17.2	BS - S⊥	0.5	

BS = Borosilicate glass. All samples are fabricated by Magnetron Sputter Physical Vapor Deposition (MSPVD). ∗, †, ‡, § or ‖ mark that these samples were fabricated in the same run. Therefore, the deposition took place under the same vacuum conditions, evaporation pressures and deposition rates. S‖ and S⊥ indicate that scratches have been made in the substrate respectively parallel and perpendicular to the pump beam polarization direction. The nominal thickness is used to report throughout this paper. The measured (inferred) thickness is obtained from ellipsometry measurements where a native oxide of 0.5 nm is assumed, and used for further calculations.

C

MATERIAL PROPERTIES

Table C.1: Optical and thermal mechanical properties of gold (Au), aluminum (Al) and aluminum oxide (Al_2O_3).

	Au	Al	Al_2O_3
$n + ik$ @ 400 nm	$1.4684 + 1.9530i$[a]	$0.31448 + 3.8005i$[b]	1.7865[c]
$n + ik$ @ 400 nm ellipsometry	$1.57 + 1.89i$	$0.68 + 4.34i$	
$n + ik$ @ 800 nm	$0.15352 + 4.9077i$[a]	$1.8385 + 6.9757i$[b]	1.7601[c]
$n + ik$ @ 800 nm ellipsometry	$0.23 + 4.74i$	$2.25 + 7.30i$	
T_m (K)	1337.33[b]	933.47[b]	2327[d]
Native oxide thickness (nm)	None	4	n/a
κ_l ($Wm^{-1}K^{-1}$)	318[e]	246[f]	35–26[d]
C_l ($10^6\,Jm^{-3}K^{-1}$)	2.4[g]	2.42[f]	13–30[d]

[a]Ref. [100], [b]Ref. [101], [c]Ref. [155, 156], [e]Ref. [47], [f]Ref. [103], [g]Ref. [104], [d]Ref. [102, p.6-146, p.6-148, p.12-223 and p.12-225]

Table C.2: Optical and thermal mechanical properties of ruthenium (Ru) and ruthenium oxide (RuO$_2$).

	Ru	RuO$_2$
$n + ik$ @ 400 nm	$2.40 + 4.64i$[a]	
$n + ik$ @ 400 nm ellipsometry	$2.60 + 5.04i$	$3.30 + 0.16i$
$n + ik$ @ 800 nm	$5.04 + 3.94i$[a]	
$n + ik$ @ 800 nm ellipsometry	$5.51 + 5.10i$	$2.64 + 0.028i$
Melting point T_m (K)	2606[b]	
Boiling point T_b (K)	4420[b]	
Thickness (nm)	$8 - 40$	0.5 (native oxide)
Thermal conductivity κ_l (Wm^{-1}K^{-1})	117[b]	
Specific heat C_l (10^6 Jm^{-3}K^{-1})	2.88[b]	

[a]Ref. [111, pp.256-261], [b]Ref. [102, p.12-218]

Table C.3: Optical and thermal mechanical properties of silicon (Si) and silicon oxide (SiO$_2$)

	Si	SiO$_2$
$n + ik$ @ 400 nm	$5.631716 + 0.285821i$[a]	1.744466[b]
$n + ik$ @ 800 nm	$3.679123 + 0.004060i$[a]	1.730794[b]
T_m (K)	1687[c]	
Thickness (nm)	Bulk	2.1[d] (native oxide)
κ_l @ 300 K (Wm^{-1}K^{-1})	124.0[c]	
C_l @ 300 K (10^6 Jm^{-3}K^{-1})	1.63[c]	

[a]Ref. [111, pp.555-569], [b]Ref. [145], [c]Ref. [102, p.12-80], [d]Obtained by ellipsometry

D

BEAM PROFILE AND ALIGNMENT

D.1. BEAM PROFILE

As an example for a typical pump beam profile used throughout chapters 3 to 5, we present one of these measured beam profile here.

On the left side of figure D.1, the beam profile of the pump beam as measured with a Gentec-EO Beamage-4M beam-profiler is shown. This beam profile is measured at the position of the sample before sample placement. On the right side of figure D.1, the horizontal, vertical, long axis and short axis cross sections are shown, along with their Gaussian fits. The eccentricity of the beam is 0.70 and the cross sections follow the Gaussian fit reasonably well. Therefore, the assumption that the beam is an elliptical Gaussian is assumed to hold.

D.2. PUMP-PROBE ALIGNMENT

Figure D.2 shows two ΔR versus peak fluence (F_0) measurements of 20 nm Ru on borosilicate glass. One with a bad and one with a good pump-probe alignment. For the bad alignment, the spread in measured ΔR values is greater. Furthermore, the steep decrease in $\Delta R(F_0)$ is 'weaker' for the misaligned measurement, with more data points to the left of the good aligned measurements. This indicates that the probe does not probe the center of the illuminated site, but any area slightly next to it.

Measured beam profile and cross sections
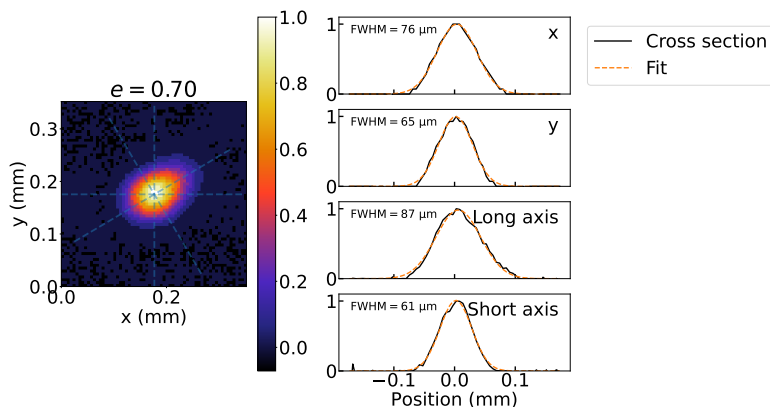
Figure D.1: Left the beam profile as measured by a Gentec-EO Beamage-4M beam-profiler. Here the four blue dashed lines indicate the positions of the horizontal, vertical, long axis and short axis cross sections as shown in the four figures on the right side in black. Here the orange lines are the Gaussian fits. Since the cross sections follow the Gaussian fit reasonably well, the assumption that the beam can be considered an elliptical Gaussian is assumed to hold. The eccentricity e of the beam is 0.70.

20 nm Ru on Borosilicate glass

Figure D.2: ΔR versus peak fluence F_0 of 20 nm Ru on borosilicate glass for one bad and one good pump-probe alignment measurement shown in blue and orange respectively.

E

PULSE STRETCHING

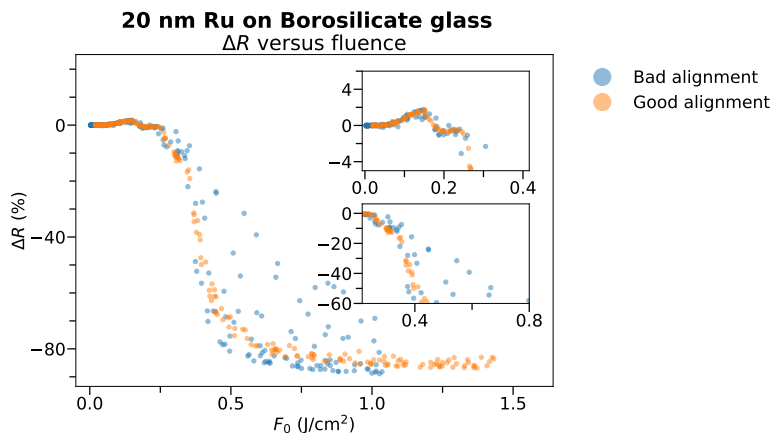To measure the pulse duration of the 400 nm pulse and 800 nm probe pulses, a cross-correlate between the two is measured. The cross-correlate is measured by replacing the sample from the setup by a Beta Barium Borate (BBO) crystal. The 267 nm sum-frequency signal that is generated by the 400 nm pump and 800 nm probe pulses in the BBO crystal, is measured by a UV-photodiode. By changing the time separation between the two pulses using a mechanical delay line, the cross-correlate is obtained. From this, the pulse length of both the pump and probe is extracted.

The cross-correlate signal has a FWHM width, τ_{cc}, of:

$$\tau_{cc} = \sqrt{\tau_{pump}^2 + \tau_{probe}^2},$$ (E.1)

with τ_{pump} and τ_{probe} the FWHM pulse durations of the pump and probe pulses respectively. It is assumed that the probe pulse dispersion by the setup, so between the laser output and the position where the cross-correlate is measured, can be neglected. This is a valid assumption since the 800 nm pulses have a low group velocity dispersion, and only one transmissive optic is used in its beam path (the focusing lens, see figure 2.3).

Furthermore, the pump pulses can be stretched from $\approx 40\,\text{fs}$ into longer pulses, by transmitting through a dispersive medium. In this case, the following relations apply:

$$\tau_{probe} = \tau_0 \sqrt{1 + \left(\frac{4\log(2) \cdot k_2 \cdot g}{\tau_1^2}\right)^2},$$ (E.2)

and

$$\tau_{pump}(d) = \tau_0 \sqrt{1 + \left(\frac{4\log(2) \cdot k_2 \cdot (d + z + g)}{\tau_0^2}\right)^2},$$ (E.3)

with k_2 the group velocity dispersion (GVD), g the initial chirp of the light immediately after the laser output ($\approx 0\,\text{m}$, figure 2.2), d the total thickness of the dispersive medium

179

the pump pulses travel through, and z the dispersion of the pump pulses due to other optical components in the setup ($\approx 0\,\mathrm{m}$). z and g are expressed in meter because of the multiplication of k_2. Now the full expression for τ_{cc} becomes:

$$\tau_{\mathrm{cc}} = \tau_0 \sqrt{2 + \left(\frac{4\log(2) \cdot k_2 \cdot (d + z + g)}{\tau_0^2}\right)^2 + \left(\frac{4\log(2) \cdot k_2 \cdot g}{\tau_0^2}\right)^2}. \tag{E.4}$$

E

F

SUPPLEMENTAL MATERIAL: GOLD AND ALUMINUM

F.1. SPALLATION, ABLATION AND ESTIMATED ENERGY DENSITIES

An overview of all spallation and ablation fluence thresholds obtained by Liu-analysis is shown in figure F.1. At the threshold fluences, the reached energy density E (J/cm^3) in the layers caused by the absorbed pump light is obtained using:

$$E(F_{\text{th}}, l) = \frac{F_{\text{th}}}{l} \cdot \left(\sqrt{\frac{4\ln(2)}{\pi}} \cdot \frac{1}{\Delta\lambda} \int\limits_{-\infty}^{\infty} a(\lambda, l, F_{\text{th}}) e^{-4\ln(2)(\frac{\lambda-\lambda_0}{\Delta\lambda})^2} d\lambda \right), \tag{F.1}$$

where a is the absorbed fraction and l the thickness of the layer. $\Delta\lambda$ is the spectral FWHM (50 nm) and λ_0 the central wavelength (800 nm). a is integrated over λ so a normalization factor is included ($\sqrt{\frac{4\ln(2)}{\pi}}\Delta\lambda$). Since we only consider thin layers, E is taken constant in the direction of l. Unfortunately, the absorption a is not directly measured in our setup. Therefore we calculate a with the transfer-matrix method (section 1.1.1 and appendix A) and use the optical parameters either from literature or obtained by ellipsometry (see appendix C). Here, we ignore any nonlinear dependence of a on the pump fluence ($a(\lambda, l, F_{\text{th}}) = Abs(\lambda, l) \cdot F_{\text{th}}$) and thus neglect any self-induced absorption changes of the pump pulse during excitation. For example, the fast heating of the electron gas causes subsequent changes in the optical absorption within the duration of the pump pulse. Therefore, our simplification holds for low fluences only. The higher the fluence, the more our calculations will deviate from reality. The ablation and spallation fluences are shown in figure F.1a and c and the calculated values of E are shown in figure F.1b and d. For gold, the absorbed energy density versus layer thickness is apparently constant at $E \approx 1 \times 10^5$ J/cm^3 for all thicknesses except for the 8 nm. This layer is around the percolation threshold of gold [113], which makes it significantly different from the others. For the other thicknesses, the weak dependence on layer thickness of the energy density

at the ablation threshold suggests that ablation is a thermally driven process. The same is true for the thickness dependence of the energy density at the spallation threshold in aluminum. At ablation, the energy density in the aluminum does not show a thickness-independent behavior.
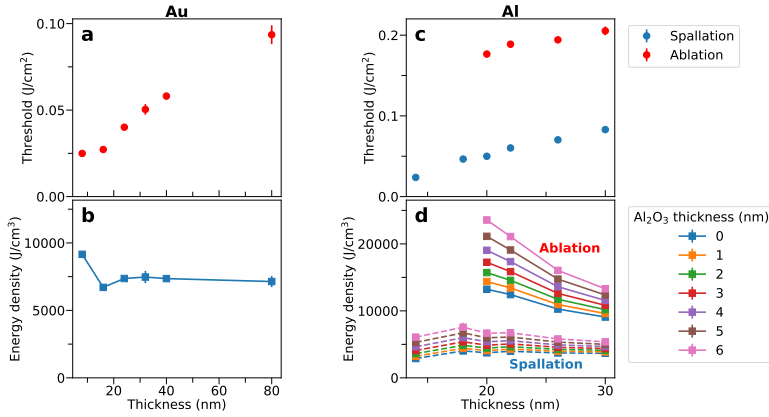
Figure F.1: The fluence thresholds obtained by Liu-analysis and corresponding energy densities obtained by transfer-matrix method calculations versus layer thickness for (a and b) ablation of gold, and (c and d) spallation and ablation of aluminum. The different lines in (d) each represents a different oxide thickness by which the total thickness of the aluminum and the oxide is indicated on the horizontal axis. The dashed lines represent the energy density at the spallation and the solid lines at the ablation fluence. Note that for the gold layer, there is no native oxide.

F.2. Spallation grid example

Figure F.2a shows a dark-field microscopy image of a six-by-six grid of single pump-shot illuminated areas on a 20 nm thick aluminum layer on 0.5 mm borosilicate glass substrate. A picture of a pristine, unilluminated site is also shown. For each illuminated area, the pump shot fluence is given. From this image, it is clear that there are also bright spots apparent in the pristine layer. Some of these bright spots represent the absence of grains too. However, one can see that at pump fluences of $F_0 = 52\,\mathrm{mJ/cm^2}$ and higher (figure F.2c-e), significantly more bright dots start to appear in the center of the area. This is where the center of the pump spot is located and shows the formation of pump-induced spallation sites. For $41\,\mathrm{mJ/cm^2}$ and lower (figure F.2b), no pump-induced spallation is present. However, there are still bright dots apparent, similar to the ones on the pristine material.

F.3. Electron backscatter diffraction

Figure F.3b-f shows the five obtained EBSD maps from the illuminated site shown in figure F.3a. Figure F.3g-k are the corresponding grain size distributions.

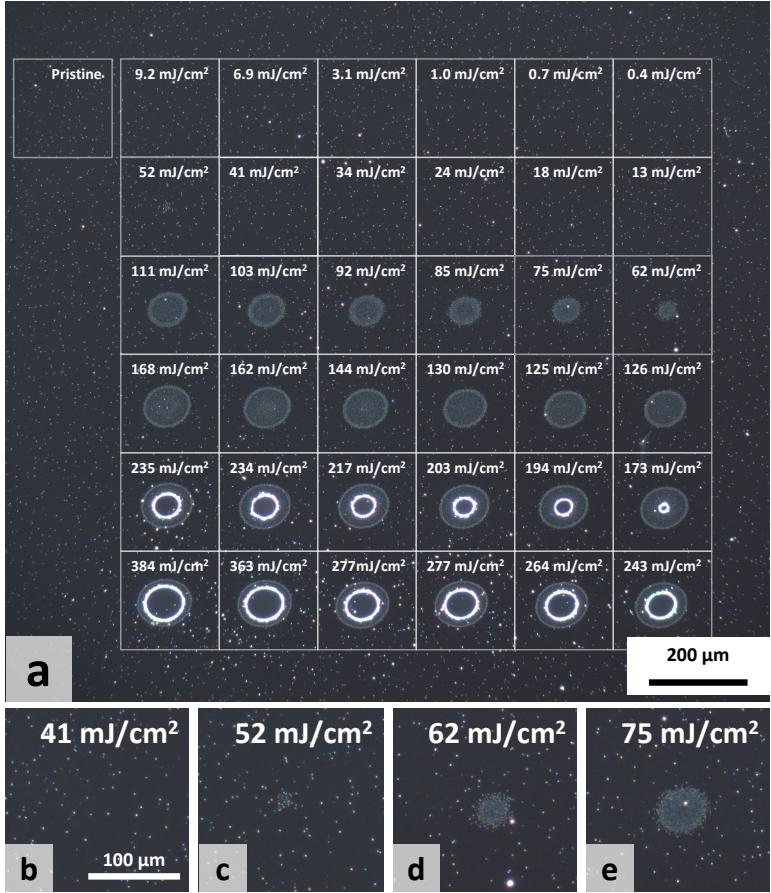Figure F.2: Dark-field microscopy images of 20 nm thick aluminum on 0.5 mm borosilicate glass and their peak fluence values. (a) is a six-by-six grid. Each area on the grid is illuminated by a single pump-shot with different fluences. The area around the grid is in pristine condition. However, for clarification an extra area is marked as 'pristine'. (a-e) are the close-ups of four illuminated sites around the spallation threshold.
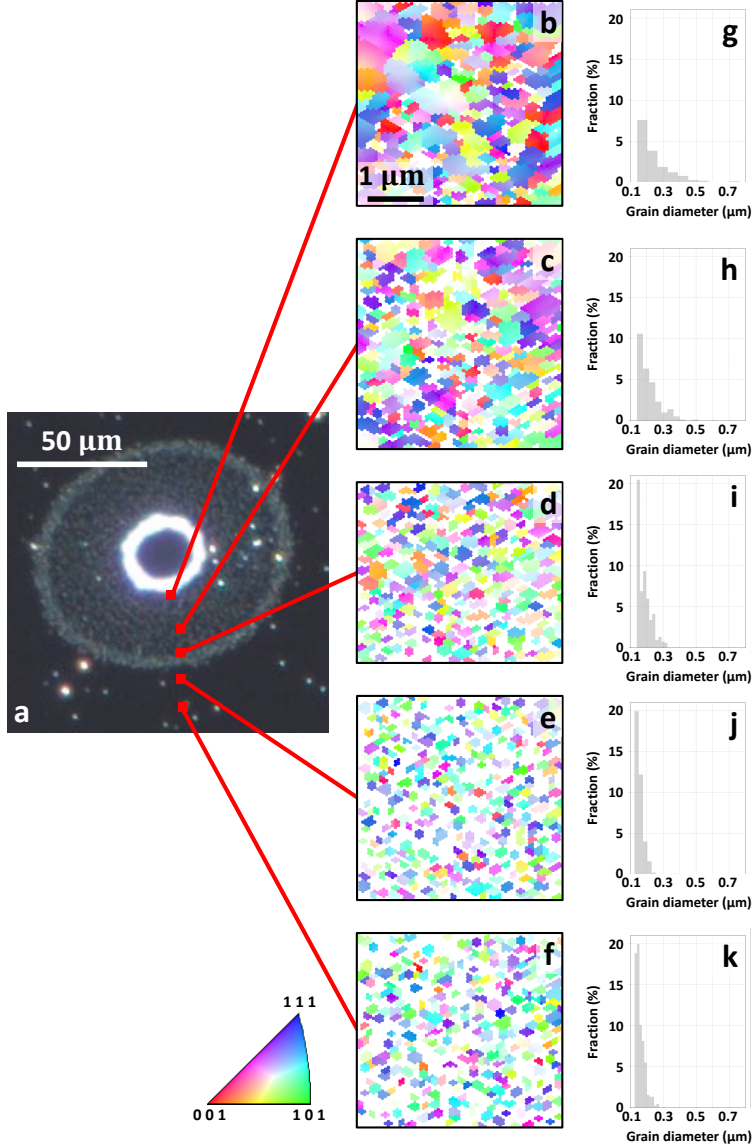
Figure F.3: The dark-field microscopy image (a) of an ablated site on a 20 nm aluminum on borosilicate glass sample. The red rectangles indicate the positions of the corresponding EBSD maps (b-f). The different colors show the different crystal orientations, while similar neighboring pixel colors indicate that they belong to the same aluminum grain. The scans are obtained at different distances from the center of the illuminated site. Therefore, each spot samples a different local fluence F_{local} for which $F_{local} < F_{spal}$ (b-c), and $F_{local} > F_{spal}$ (d-f). From (d-f) it is clearly visible that the average grain size has increased. (g-k) show the corresponding grain-size distributions. Here the grain size is expressed in the equivalent circular diameter of the grain area (see equations (3.5) to (3.6)).

G

SUPPLEMENTAL MATERIAL: RUTHENIUM

G.1. RUTHENIUM THRESHOLD OVERVIEW

8, 10, 15, 20, 25 and 40 nm thick (nominal) ruthenium layers on borosilicate glass substrates all display a variety of damage mechanisms. All obtained threshold values are given in table G.1. Accompanying labeled SEM images are shown in figure G.1, and associated Liu-plots are shown in figure G.5a-f. A more graphical overview of all damage thresholds is shown in figure G.3, along with their $\Delta R(F_0)$ trend.

The ΔR versus fluence plots and additional Liu-plots of 8, 20 and 40 nm thick (nominal) ruthenium layers on borosilicate glass, sapphire, CaF_2 and Si substrates are shown in figure G.5g-r. Their corresponding damage thresholds for all observed damage mechanisms are graphically shown in figure G.3b-d.

Table G.1: Threshold fluence and damage mechanism overview

Nominal thickness (nm)	F_{th} (mJ/cm^2)	d (μm)	Mechanism	Figure reference
8	96 ± 6	74.6	Recrystallization edge	G.1b
	$104 \pm 7^*$		Buried cracks/nanovolcanoes	G.1c
	164 ± 5	69.6	Full-ablation	G.1d
10	97 ± 3	82.3	Cracking edge	G.1f
	113 ± 4	71.4	Buried cracks	G.1f
	158 ± 4	76.3	Nanovolcanoes	G.1g-h
	195 ± 3	69.1	Full-ablation	G.1h
15	132 ± 5	79.3	Big cracks	G.1j
	139.9 ± 1.9	77.0	Small cracks	G.1j
	218 ± 4	78.0	Nanovolcanoes/height increase	G.1k
	318 ± 3	64.4	Full-ablation	G.1l
20	162 ± 5	79.2	Big cracks	G.1n
	181.6 ± 2.5	74.5	Small cracks	G.1n
	278 ± 4	79.3	Nanovolcanoes/top-level ablation	G.1o
	305 ± 4	68.8	No nanovolcanoes	
	407 ± 5	64.4	Full-ablation	G.1p
25	224 ± 18	75.0	Big cracks	G.1r
	$246 \pm 7^*$		Small cracks	G.1r
	309 ± 4	78.0	Nanovolcanoes/top-level ablation	G.1r
	337 ± 3	66.0	No nanovolcanoes	G.1r
	413 ± 6	62.0	Full-ablation	G.1s
40	$263 \pm 7^*$		Big cracks	G.1u-v
	379 ± 5	63.3	Small cracks/top-level ablation	G.1v
	715 ± 10	62.4	Full-ablation	G.1w

∗ Indication that the threshold fluence is not obtained by Liu-analysis, but by estimating the local fluence from a SEM image.

G
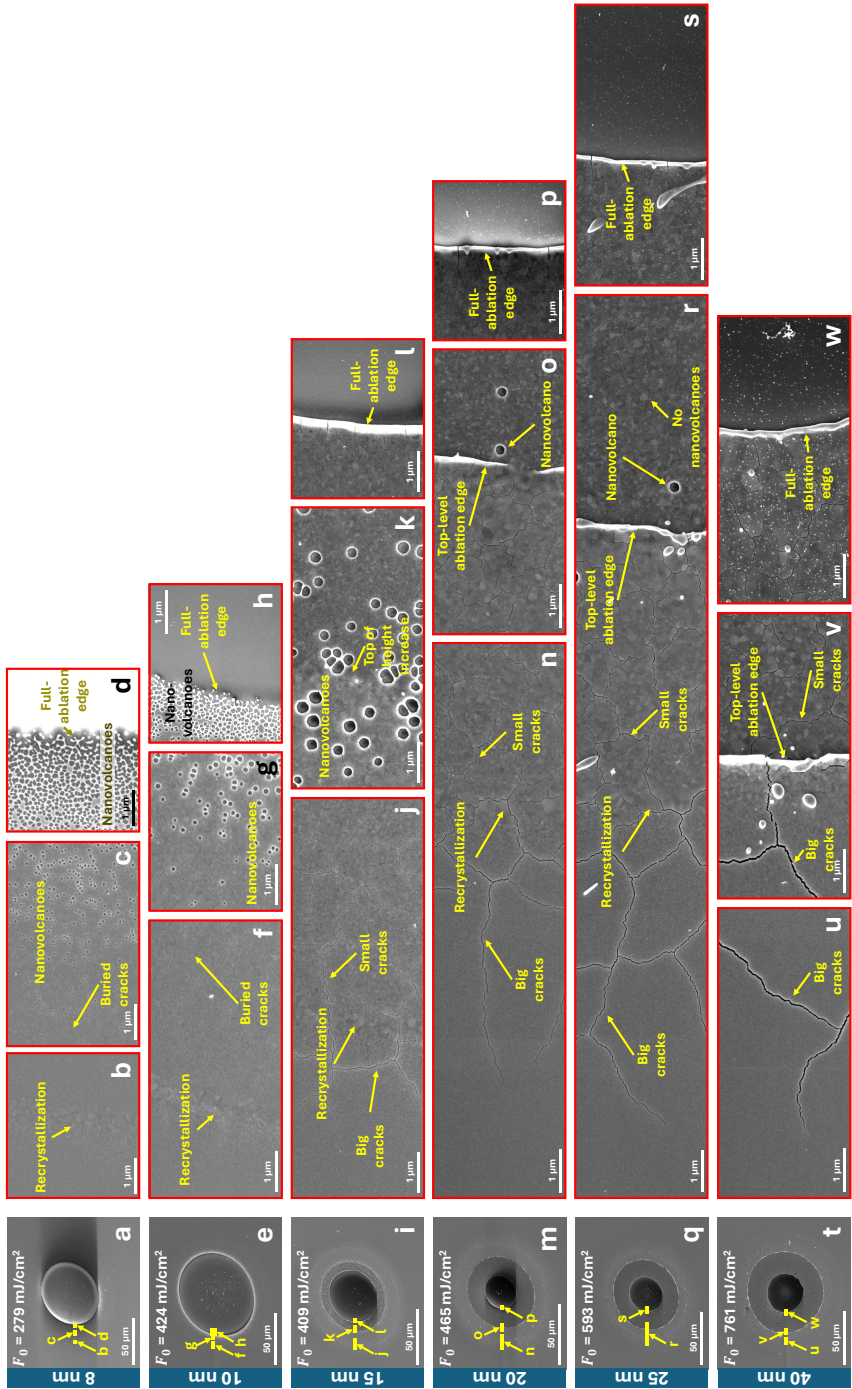
Figure G.1: SEM images of 8, 10, 15, 20, 25 and 40 nm thick (nominal) ruthenium layers illuminated above the full-ablation damage threshold. The yellow rectangles and arrows in (a, e, i, m, q, t) indicate the location of the zoomed-in images shown on the right.

G

Figure G.2: SEM images of nanovolcanoes in 8 nm (a) and 20 nm (b) ruthenium on borosilicate glass. In both images cracks are visible that run through every nanovolcano.

Forms of damage

Figure G.3: *Continued on next page.*

Forms of damage
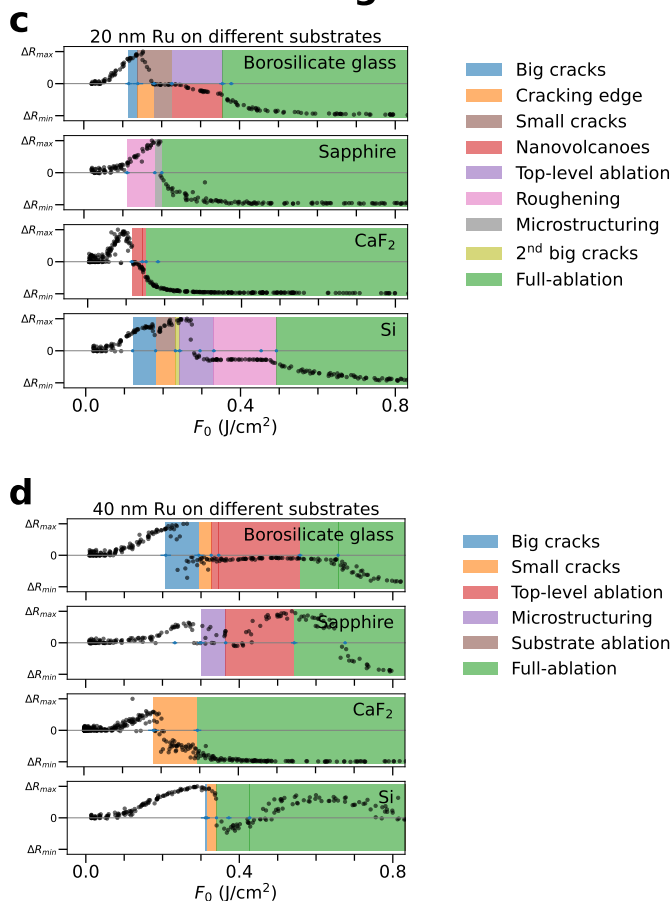
Figure G.3: *Continued from previous page.* Schematic overview of the obtained damage thresholds, plotted versus the $\Delta R(F_0)$ trend and shown for 8, 10,15, 20, 25, an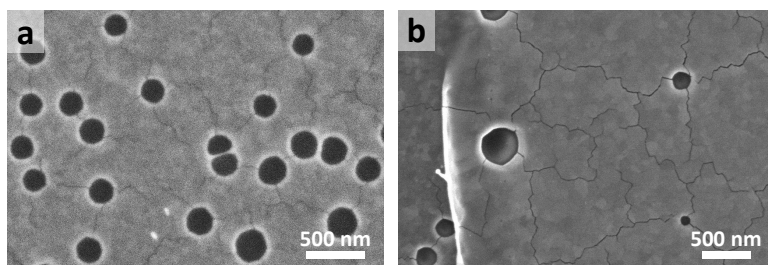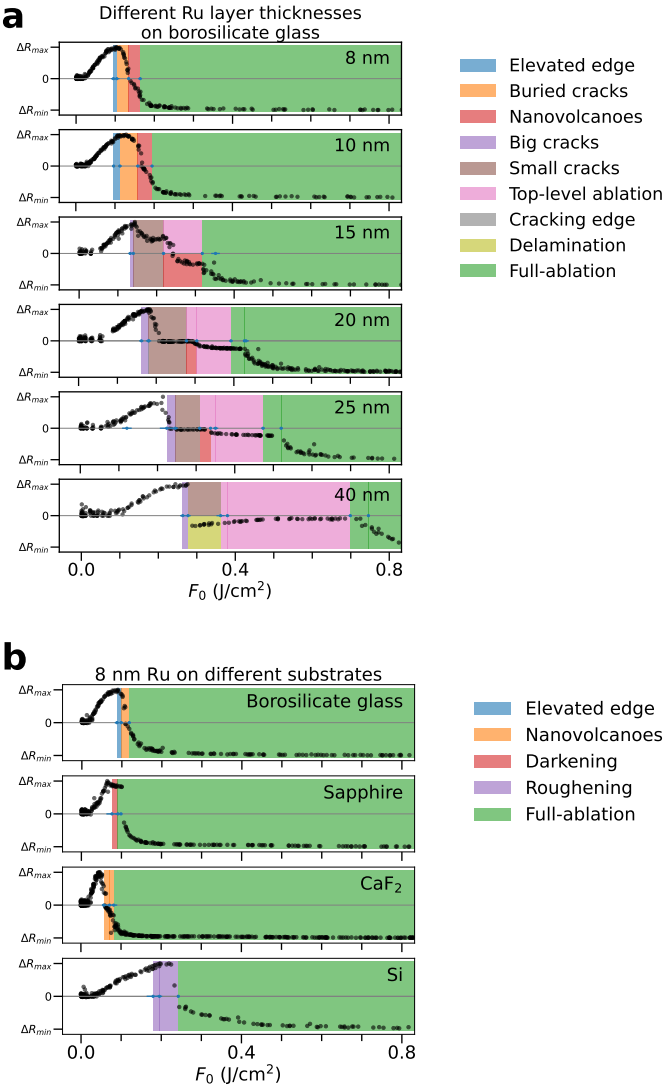d 40 nm thick (nominal) ruthenium layers on borosilicate glass (a). In (b-d), the same figure is shown for 8, 20 and 40 nm thick (nominal) ruthenium deposited on different substrates. Here, the used substrates are 0.5 mm borosilicate glass, 1.1 mm sapphire, 0.5 mm CaF$_2$ and 0.5 mm Si. All positive ΔR values are scaled by their maximum value $|\Delta R_{\max}|$ and the negative values are scaled by $|\Delta R_{\min}|$ to make the ΔR versus F_0 trend better visible. All colored areas indicate the fluence region where a certain damage mechanism or morphological change is visible as indicated in the legends. Additional SEM images of the damage mechanisms of the samples with borosilicate glass substrates can be found in figure G.1.

The (effective) energy density in the material u will affect the ruthenium layers directly. For this reason, we calculated u by using the threshold fluences F_{th} and multiplying this with $\frac{f_{abs}}{d}$. Here f_{abs} is the absorbed fraction of the incident light, obtained by transfer-matrix method calculations [40, 99] (see section 1.1.1 and appendix A). u is averaged over the layer thickness because we divide by the measured thickness d of the ruthenium layer. In figure G.4, the measured incident threshold fluence and calculated effective energy density are plotted versus the nominal ruthenium layer thickness for the 8, 10, 15, 20, 25, and 40 nm thick (nominal) ruthenium layers on borosilicate glass substrates. Note that in this figure, the measured thicknesses obtained by ellipsometry are $\approx 15\%$ thicker than the nominal thicknesses (see table B.2). Throughout this paper, the nominal thicknesses are reported, which is done for the purpose of readability. The calculated effective energy density ($[u] = \mathrm{W\,m}^{-3}$) is not the same for all layer thicknesses (figure G.4b) when reaching the nanovolcano formation, top-level ablation or full-ablation fluence threshold. Therefore, it can be concluded that the threshold values are not directly determined by a single, common absorbed fluence threshold value in all ruthenium layers. Additional two-temperature model (TTM) calculations are performed. Here F_m, the incident fluence for which the lattice just reaches the melting temperature ($T_m = 2606\,\mathrm{K}$) is obtained and indicated by the black dashed line in figure G.4a. The obtained values for F_m are less than the experimentally obtained nanovolcano, top-level ablation and full-ablation threshold fluences. This indicates that at those damage mechanisms, melting already takes place. Regarding the TTM equations, more information can be found in [136]. The thermal properties of Ru and RuO_2 are listed in table G.2.
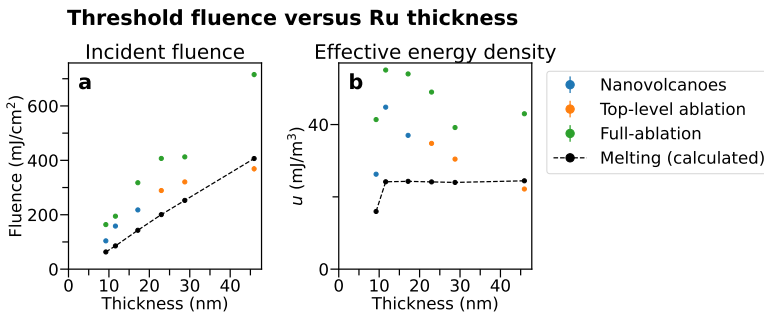
Figure G.4: (a) The incident threshold fluence and (b) the effective energy density u versus the measured ruthenium layer thickness. Note that the measured thicknesses are obtained by ellipsometry and are $\approx 15\%$ thicker than the reported nominal thicknesses throughout this paper (see table B.2). Two-temperature model (TTM) calculations are used to obtain the fluences for which T_m is reached. They are plotted in (a) and (b) as the black dashed line.

Figure G.5 shows plots of ΔR versus the peak fluence and Liu-plots of single-pulse laser-damage experiments on 8, 20 and 40 nm thick (nominal) ruthenium layers on borosilicate glass, sapphire, CaF_2 and Si substrates, obtained by inspecting dark-field images. The Liu-fits are obtained by a recursive RANSAC approach [139]. Here, the number of linear fits is not set beforehand, but each fit should contain at least ten data points within a small distance from the fit and with a maximum area (y cutoff) of $4000\,\mu\mathrm{m}^2$. Most non-physical fits have already been filtered out automatically, and a few remaining

Table G.2: Properties of ruthenium and ruthenium oxide used for two-temperature model calculations.

	Ru	RuO$_2$
$n + ik$ @ 400 nm by ellipsometry	$2.60 + 5.04i$	$3.30 + 0.16i$
Melting point T_m (K)	2606[a]	
Thickness (nm)	9.2-45.9 (measured)	0.5 (native oxide)
Thermal conductivity electrons κ_e (Wm^{-1}K^{-1})	117[a]	
Thermal conductivity lattice κ_i (Wm^{-1}K^{-1})	0 (neglect on small timescale)	
Specific heat electrons C_e (10^6 Jm^{-3}K^{-1})	$400 \cdot T_e$[b]	
Specific heat lattice C_l (10^6 Jm^{-3}K^{-1})	2.88[a]	
Electron-phonon coupling g (10^{16} Wm^{-3}K^{-1})	110[c]	

[a]Ref. [102, p.12-218], [b]Ref. [47] using [157],[c]Ref. [158]

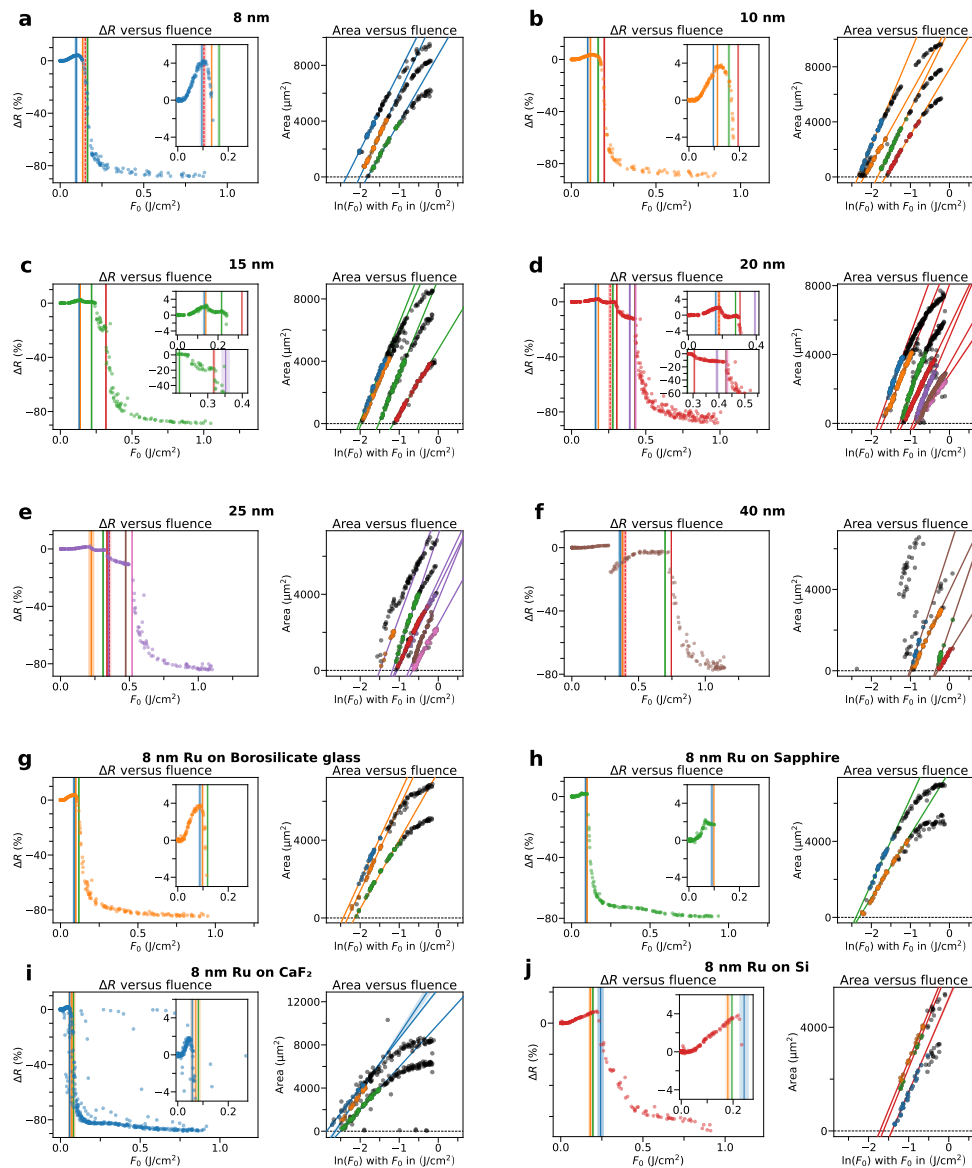ones are filtered out by visual inspection.

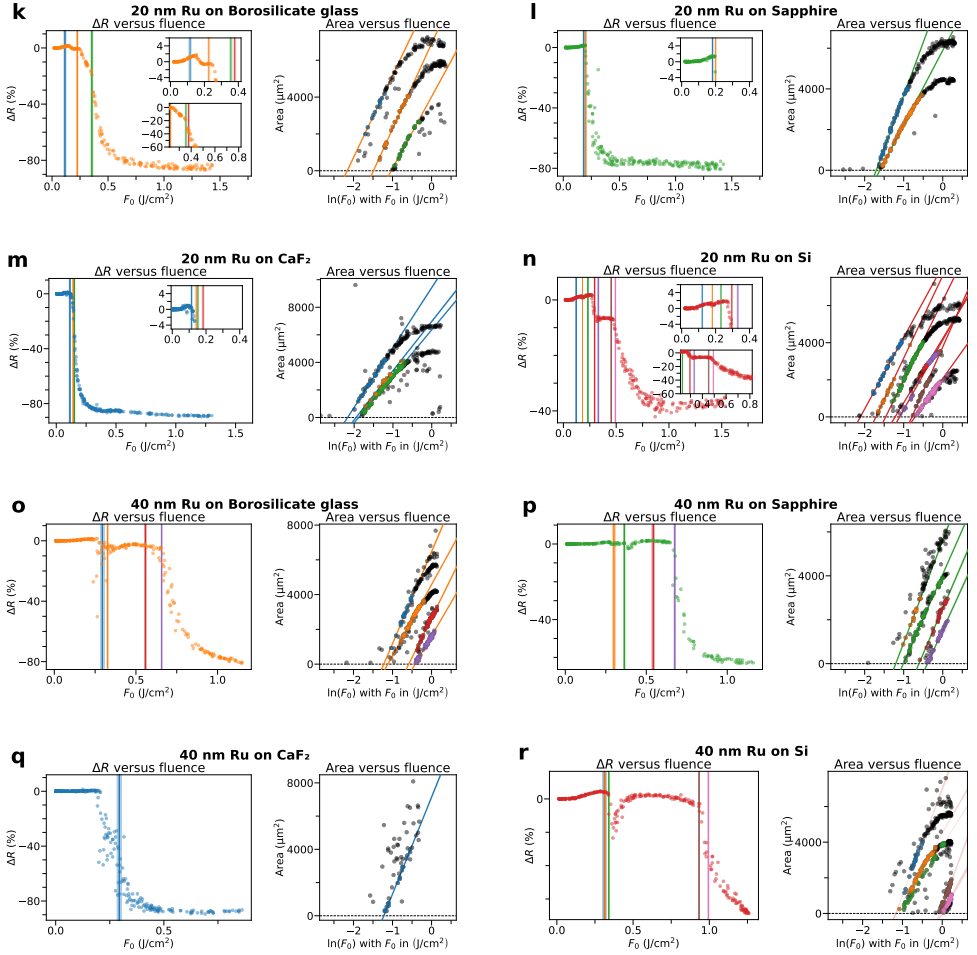Figure G.5: *Continued on next page.*

Figure G.5: *Continued from previous page.* ΔR versus peak fluence (left) and Liu-plots (right) of single pulse laser damage experiments on 8, 20 and 40 nm thick (nominal) ruthenium layers on borosilicate glass, sapphire, CaF$_2$ and Si substrates, obtained by inspecting dark-field images. The linear fits, seen in the Liu-plots, intersect the horizontal axis at $\ln(F_{\text{th}})$ where F_{th} is the corresponding fluence threshold of the corresponding damage mechanism. The fits are obtained by a recursive RANSAC approach [139]. Here, the amount of linear fits is not set beforehand, but each fit should contain at least ten data points within a small distance from the fit and with a maximum area (y cutoff) of 4000 μm^2. Most non-physical fits have been filtered out automatically, and the few remaining ones are filtered out by visual inspection. The selected data points used for each fit are marked by a different color, which corresponds to the color of the fit. The same color is used for the vertical lines in the left figures, which shows the obtained F_{th} values extracted from the linear fits of the right figures.

G.2. Reflectivity versus ruthenium thickness

Figure G.6 shows the calculated relative reflection change (ΔR) caused by partially ablation of the ruthenium film, as obtained by the transfer-matrix method [99]. These

calculations show that, in almost all cases, ΔR will decrease for smaller ruthenium thicknesses. Only for the 40 nm thick layer, there is a small regime (final thickness $\gtrsim 27$ nm), where $\Delta R > 0$. However, in the measured ΔR versus fluence plots, in the $\Delta R > 0$ regime, no partial ablation was observed here (by SEM/AFM).
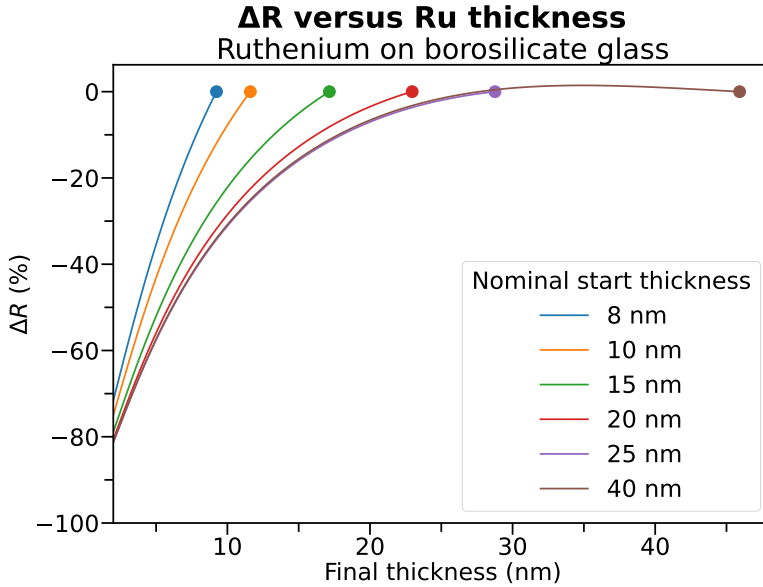

Figure G.6: Calculated ΔR for 8, 10, 15, 20, 25 and 40 nm (nominal) thick ruthenium with 0.5 nm RuO_2 on a 0.5 nm borosilicate glass substrate versus layer thickness decrease, as a result of top-level ablation. The transfer-matrix method [99] is used to calculate the percentage of reflection change with respect to the original thickness (indicated by the colored dots). Note that the dots are positioned at the original thickness which is the *measured* thickness, whereas the legend indicates the nominal thickness (see table B.2).

G.3. STATISTICAL ANALYSIS

For different ruthenium layers, the nanovolcano size, spatial distribution and coverage ratio varies. Since many nanovolcanoes are present in the 8, 10 and 15 nm Ru layers, these thicknesses can be used to perform a statistical analysis. On these three ruthenium layers, several high-resolution AFM scans are obtained and stitched together. Each AFM scan is located between FIB markers. This allows us to match every location on an AFM scan with the corresponding location on a SEM image. This SEM image, along with the known beam profile, is used to calculate the local fluence F_{local} at each nanovolcano center. Additionally, the vent and rim contours are identified. This is done by combining the height and gradient signals into a thresholding algorithm. For the thicker 20, 25 and 40 nm Ru layers, this AFM analysis is omitted. Here, a more qualitative analysis is performed since fewer nanovolcanoes are present.

For each nanovolcano, ellipses are fitted to the vent and rim contours. These contours are used to identify each pixel of the AFM scan as belonging to either a *vent*, a *rim* or the *surrounding surface*. Hereafter, the AFM scan is divided into small regions where each

region covers one nanovolcano and some surrounding area. The borders of these regions are equidistant to two neighboring nanovolcano centers. Here, the nanovolcano centers are defined at the center of each vent contour. For every such piece, the average height $\bar{h}_t$ and area A_t of the vent, rim and surrounding area are determined using:

$$\bar{h}_t = \frac{\sum_{i=1}^{I} h_{t,i}}{\sum_{i=1}^{I} 1}, \tag{G.1a}$$

$$A_t = \sum_{i=1}^{I} dA, \tag{G.1b}$$

where $h_{t,n}$ is the height of the ith number of a total of I pixels of type t, and t can either be *vent*, *rim* or *surrounding area*, and dA is the pixel size. From this, $\bar{h}_{\text{surrounding area}}$ is considered to be equal to the reference height and the vent and rim volume, V_{vent} and V_{rim} are obtained as follows:

$$V_{\text{vent}} = (\bar{h}_{\text{vent}} - \bar{h}_{\text{surrounding area}}) \cdot A_{\text{vent}}, \tag{G.2a}$$

$$V_{\text{rim}} = (\bar{h}_{\text{rim}} - \bar{h}_{\text{surrounding area}}) \cdot A_{\text{rim}}. \tag{G.2b}$$

Since V_{vent}, V_{rim}, A_{vent} and A_{rim} are obtained for each nanovolcano on the AFM scan, boxplots of the distribution versus their local fluence F_{local} are obtained. For the vents, this is shown in figure G.7. In these boxplots, each box extends from the first quartile to the third quartile, with a line at the median and a marker indicating the mean value. The whiskers extend from one side of the box to the outer data point. For the 8 and 10 nm layers, the median nanovolcano volume and area increase with local F_{local} quite linearly. However, for 15 nm Ru, the largest nanovolcanoes are positioned around F_{NV}, where the layer has increased in height, but no top-level ablation occurred yet as is the case for thicker layers. There are also fewer volcanoes present, making the layer under-sampled. Additionally, larger vent areas are able to form for thicker ruthenium layers.

Besides AFM scans, the vents of the nanovolcano are clearly visible by SEM too. Here, the vents appear as high contrast dark circles/ellipses. Therefore, number density (n) and vent area coverage fraction (the percentage of surface area occupied by vents) versus local fluence F_{local} of the nanovolcanoes have been obtained from high resolution SEM images. These images cover the entire illuminated site, and therefore provide data with a higher statistical significance. However, unlike the AFM images, only the spatial distribution of the vents can be obtained and no volume information is present. Also, identifying the vents by contrast is less reliable than using AFM data. Figure G.8a-e and G.8f-j show respectively the nanovolcano number density n and the area coverage fraction A versus local fluence F_{local} for 8, 10, 15, 20 and 25 nm thick (nominal) ruthenium films. The onset of nanovolcano formation is in agreement with the obtained threshold values. For the thinnest layers, n and the area coverage fraction scale approximately linearly with F_{local} until ablation is reached. However, for 15 nm and thicker layers, it first increases with F_{local} but rapidly decreases hereafter. These are the samples where the Ru layer is thick enough for layer elevation[a] or top-level ablation to occur. Top-level ablation is associated

---

[a]The 15 nm thick ruthenium layer is considered to be a *transition* thickness between the thin layers where top-level ablation does not occur, and thick layers where it does occur. There is no clear top-level ablation edge for 15 nm Ru. However, the top-layer is slightly elevated but not ablated.

Volume and area distributions of vents
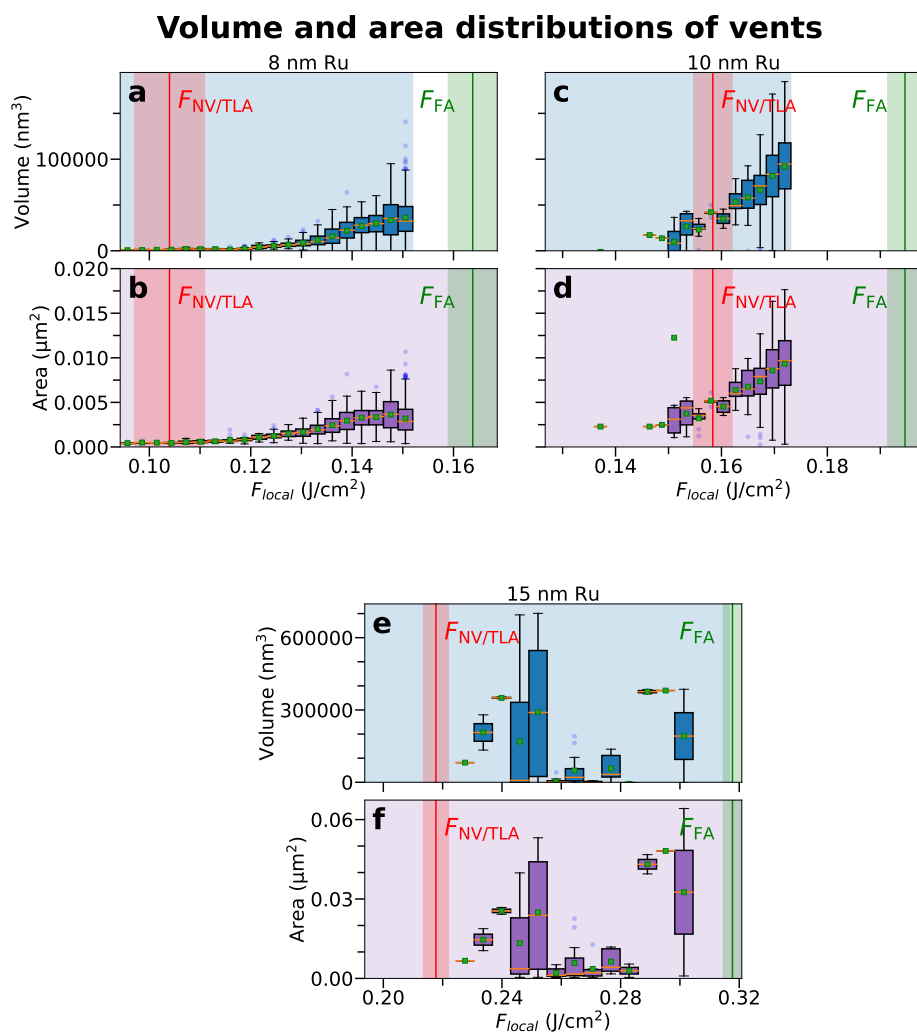
Figure G.7: Boxplots containing the volume (blue, a, c, e) and area (purple, b, d, f) versus the local fluence (F_{local}) of the nanovolcanoes obtained by several stitched-together AFM scans of 8, 10 and 15 nm thick ruthenium layers on borosilicate glass. Each box extends from the first quartile to the third quartile. Inside each box, the median is indicated by the horizontal orange line segment, and the mean by the green marker. The whiskers extend from one side of the box to the outer data point. If a data point lies outside a 1.5× inter-quartile range, it is considered an outlier (blue dots). The blue and purple background indicates the probed fluence ranges. The red and green vertical lines indicate the nanovolcano and full-ablation fluence thresholds respectively. Note that the higher F_{local}, the fewer AFM pixels have these values, thus increasing statistical uncertainty. The obtained distributions are normalized to/divided by the obtained F_{local} distribution.

with a decrease in the number density and vent area coverage fraction in the layer still left on the surface.
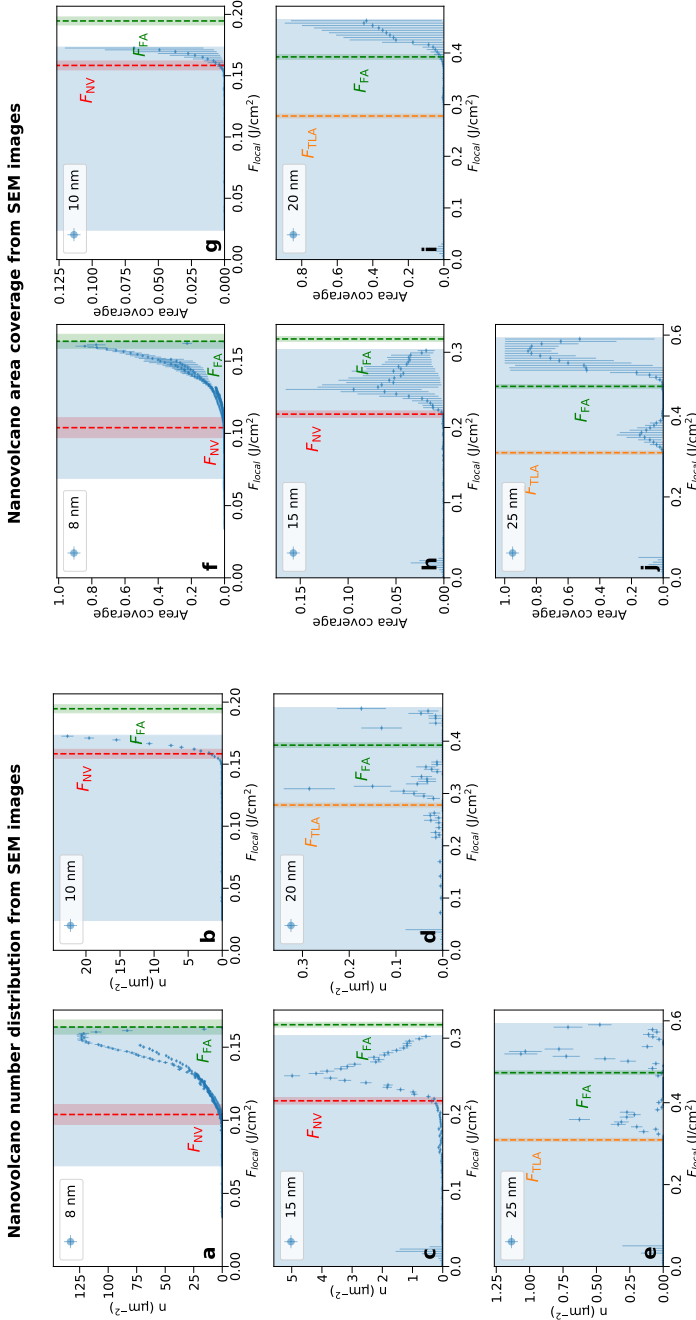
Figure G.8: Nanovolcano number density n (a-e) and vent area coverage (f-j) obtained from high-resolution SEM images. The inspected F_{local} range is indicated by the light-blue background. The red, orange and green vertical lines indicate the nanovolcano, top-level ablation and full-ablation thresholds respectively, which are obtained by Liu-analysis. The blue markers and its error bars indicate the calculated nanovolcano number density n or area coverage. The vents are identified by taking the Hough transform [159, 160] which results in a number density. However, when closely packed, this Hough transform is less reliable, which makes n less reliable near the ablation threshold. The nanovolcano number density is obtained by assigning each pixel of the SEM image to either be in a vent or not. This is accomplished by three different methods: by using a constant threshold value, Niblack thresholding [161] and by finding the vents using the Hough transform [159, 160]. Since all three methods are sensitive to a different vent-packing range, taking a weighted average of the three to the vent-packing range sensitivity, resulted in the values and error margins shown in the figure.

H

SUPPLEMENTAL MATERIAL: SILICON GRATINGS

H.1. OPTICAL MICROSCOPY AND SEM

Figure H.1 shows optical bright-field, dark-field and SEM images for three damaged sites: a flat silicon surface (figure H.1a-c), and a 950 nm pitch, 50% duty-cycle grating, illuminated with $\perp$-polarized (figure H.1d-f), and $\parallel$-polarized (figure H.1g-i) pump-light. Because the local pump fluence exceeded the ablation threshold in the center of all illuminated sites, all (lower fluence) damage mechanisms are present when moving away from the illumination center, to lower local fluences.

In figure H.1b, the dark-field image of the flat surface displays a single bright ring which represents the ablation edge. Outside this edge and inside the ablation crater, the surface is still relatively flat, and therefore appears dark in the image. Unlike the flat surface, the gratings scatter strongly, making the dark-field image bright (figures H.1e and H.1h). Extracting the ablation edge is therefore less straightforward. Because of this, a set of edges is acquired by obtaining contours and fitting ellipses to the bright and dimmer rings visible in both the bright and dark-field images. From the areas spanned by these ellipses, Liu-analysis (see section 1.3) is performed to obtain the corresponding fluence thresholds. For each fluence threshold, the corresponding damage mechanism is obtained by inspection of additional SEM images. The ellipse fitting procedure (see section 6.1) is executed three times, with slight differences in the algorithm used: once using dark-field images (DF), and twice using the bright-field images with two different contrast settings (BF1 and BF2) indicated by the blue, orange and green ellipses respectively as shown in figure H.1. Figure H.2a, c and e show the area of the fitted ellipses A versus $\ln F_0$, the so-called Liu-plots, per sample for all three contour finding procedures (DF, BF1 and BF2). Since the pump beam profile is an (elliptical) Gaussian, A and $\ln F_0$ follow a linear relation [74]. Linear fits are obtained by a recursive RANSAC procedure [139] for every damage mechanism. In figure H.2, only the linear fits are shown which correspond to the contours as indicated in figure H.1, Note that this is only a selection of all linear fits.
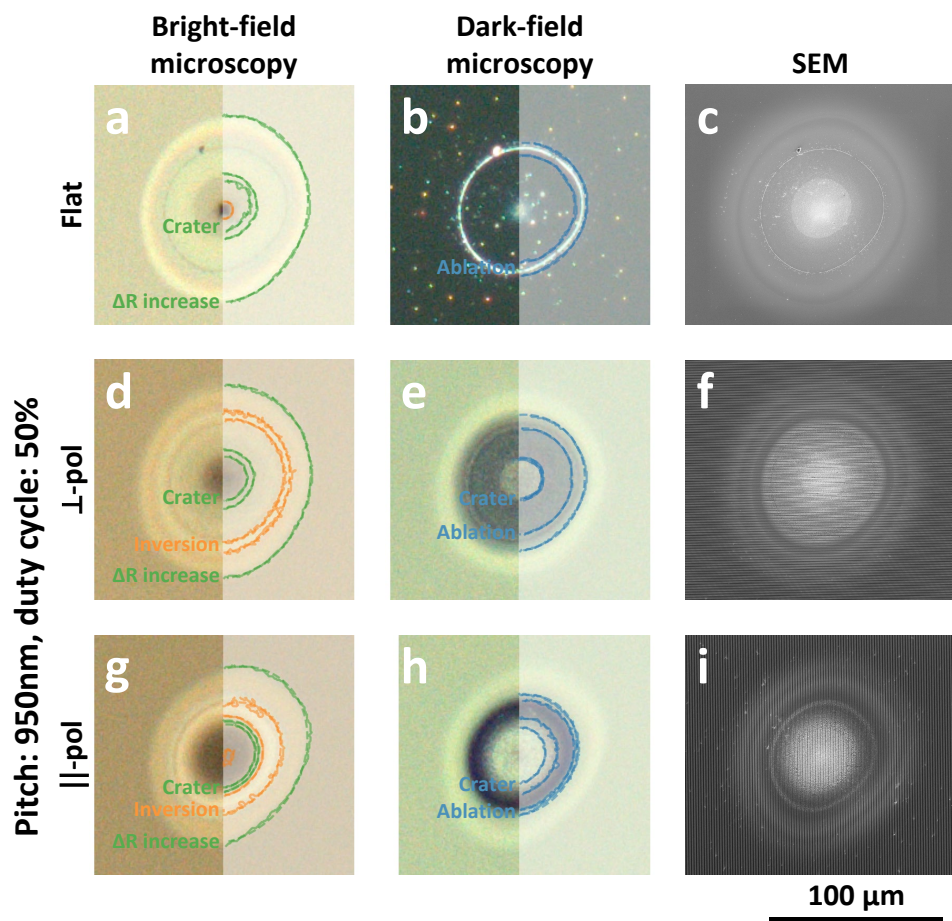
Figure H.1: Optical bright-field, dark-field and SEM images for three damaged sites: a flat silicon surface (a-c), and a 950 nm pitch, 50% duty-cycle grating illuminated with ⊥-polarization (d-f), and ∥-polarization (g-i). Because the local pump fluence exceeded the crater formation threshold in the center of all illuminated sites, all (lower fluence) damage mechanisms are observed when moving away from the illumination center, to lower local fluences. An ellipse fitting procedure (see section 6.1) applied to the damaged contours is compiled using an algorithm three times: once using dark-field images, and twice using the bright-field images with two different contrast settings indicated by the blue, orange and green ellipses respectively. The corresponding damage mechanism is obtained by inspection of additional SEM images. The corresponding Liu-plots [74] are shown in figure H.2. This picture is presented as figure 5.4 in chapter 5 as well.

The linear fits intersect the horizontal axis at the corresponding threshold fluence. These threshold fluences are indicated by the vertical lines drawn in figure H.2b, d, and f, where the in situ optical change, ΔR, versus peak fluence F_0 is shown. Here the various reflection 'jumps' in $\Delta R(F_0)$ are clearly visible around the thresholds found by the Liu-analysis [74]. After this, the fluence threshold values are compared with SEM images to assign each threshold to a damage mechanism.
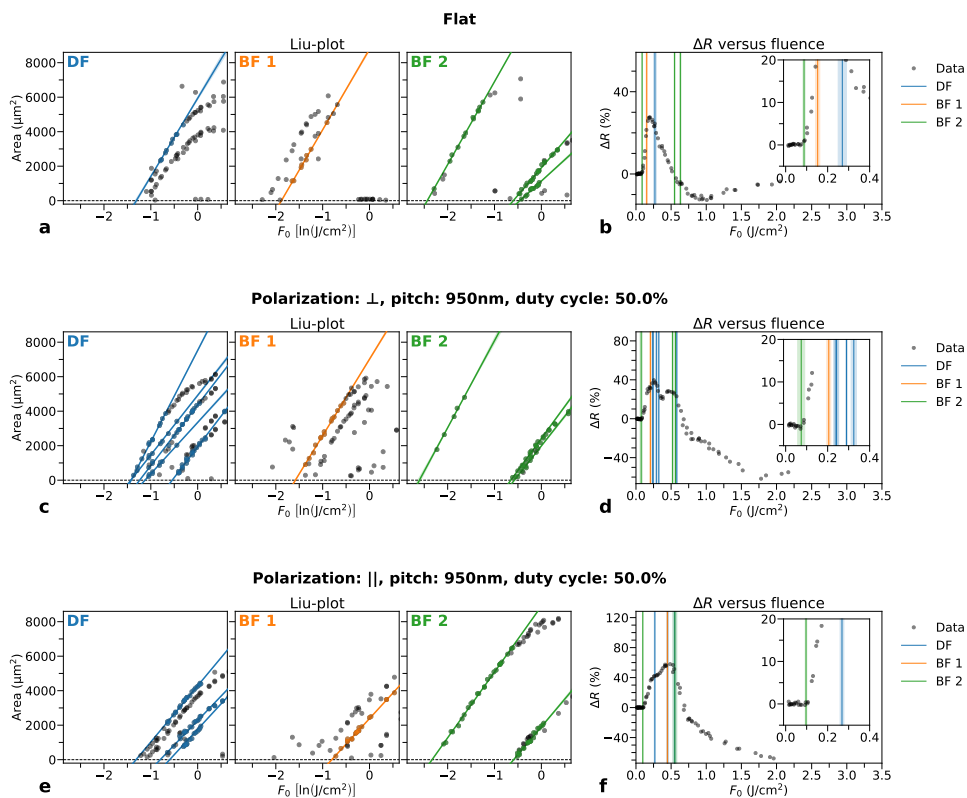
Figure H.2: Liu-plots of a flat surface (a), and of a 950 nm pitch, 50% duty-cycle grating illuminated with single $\perp$-polarized (c), and $\parallel$-polarized (e) pump-pulses. The area of the fitted ellipses A spanned by the contours of the damaged area is plotted versus $\ln F_0$. Here. the ellipse fitting procedure (see section 6.1) is compiled using an algorithm three times: once using dark-field images, and twice using the bright-field images with two different contrast settings indicated by the blue (left), orange (middle) and green (right) linear fits respectively (see figure H.1) The linear fits intersect the horizontal axis at $\ln(F_{\text{th}})$ where F_{th} is the fluence threshold of the corresponding damage mechanism. The fits are obtained by a recursive RANSAC approach [139]. Only fluence thresholds of a subset of all found damage mechanisms are shown here. More can be found in table H.1. The obtained threshold fluences are drawn by vertical lines in the corresponding ΔR versus peak fluence F_0 plots (b, d, and f).

This Liu-analysis has been performed for all samples and a list of fluence thresholds and corresponding damage mechanisms is obtained and listed in table H.1.

H

H.2. Threshold overview

At F_{dark}, a dark shade arises in the SEM images, as can be seen in figure H.1. This is used to select the proper F_{dark} for the flat surface, since this dark shade is also visible on the flat surface but no grating line deformation can be present. Finally, the high-fluence damage thresholds F_{abl} and F_{crater} are determined. Here, material is ablated, where at F_{abl} material is removed superficially, and at F_{crater} a crater starts to form. F_{abl} and F_{crater} are distinguished by comparing the optical microscopy images with SEM images (see figure H.1). Table H.1 lists the found fluence threshold values for $F_{\uparrow}$, F_{dark}, F_{abl} and F_{crater} for all gratings and for the flat silicon surface illuminated by a pump-pulse polarized either parallel or perpendicular to the grating lines. Figure H.4 are additional SEM images, showing the morphological changes.

H.3. Near-field calculations

We calculated the local electric **E** and magnetic field **H** inside the silicon when exposed to the pump-pulse. Here we assume an infinite periodic structure along the x-direction. Hereafter, the rigorous coupled-wave analysis (RCWA) discretization strategy is used to solve the Maxwell equations by forward diffraction modelling [64, pp.53-68].

For all samples, a 2D AFM scan of a pristine site on all samples is obtained. After preprocessing of the heightmap, the cross sections are obtained by taking the median in the direction of the grating lines. From this, one single grating line is isolated, representing a unit cell of the periodic surface structure. It is used as the input geometry for our near-field calculations[a]. From this, the local $\mathbf{E}(x,z)$ and $\mathbf{H}(x,z)$ fields are obtained for a wavelength $\lambda = 400\,\text{nm}$, equal to the central wavelength of the pump pulse. This is done for both $\parallel$ and $\perp$ pump-polarizations, and at normal incidence. From $\mathbf{E}(x,z)$ and $\mathbf{H}(x,z)$, the time-averaged Poynting vector, $\langle \mathbf{S} \rangle$, is derived:

$$\langle \mathbf{S} \rangle (x,z) = \frac{1}{2} \operatorname{Re}(\mathbf{E}(x,z) \times \mathbf{H}^*(x,z)), \qquad (1.46a/5.2a)$$

from which the local absorbed power density $\frac{du}{dt}$ equals

$$\frac{du}{dt}(x,z) = -\nabla \cdot \langle \mathbf{S} \rangle . \qquad (1.46b/\text{H.1a})$$

In figure H.3, the $|\mathbf{E}(x,z)|$, $|\mathbf{H}(x,z)|$ and $\frac{du}{dt}(x,z)$ profiles are shown for all samples.

---

[a]Since the calculations assume periodic structures, the unit cell is mirrored and placed next to the original during calculations. Because of this use of a double unit cell, artifacts due to the height jumps at the boundaries of the cross section are avoided.
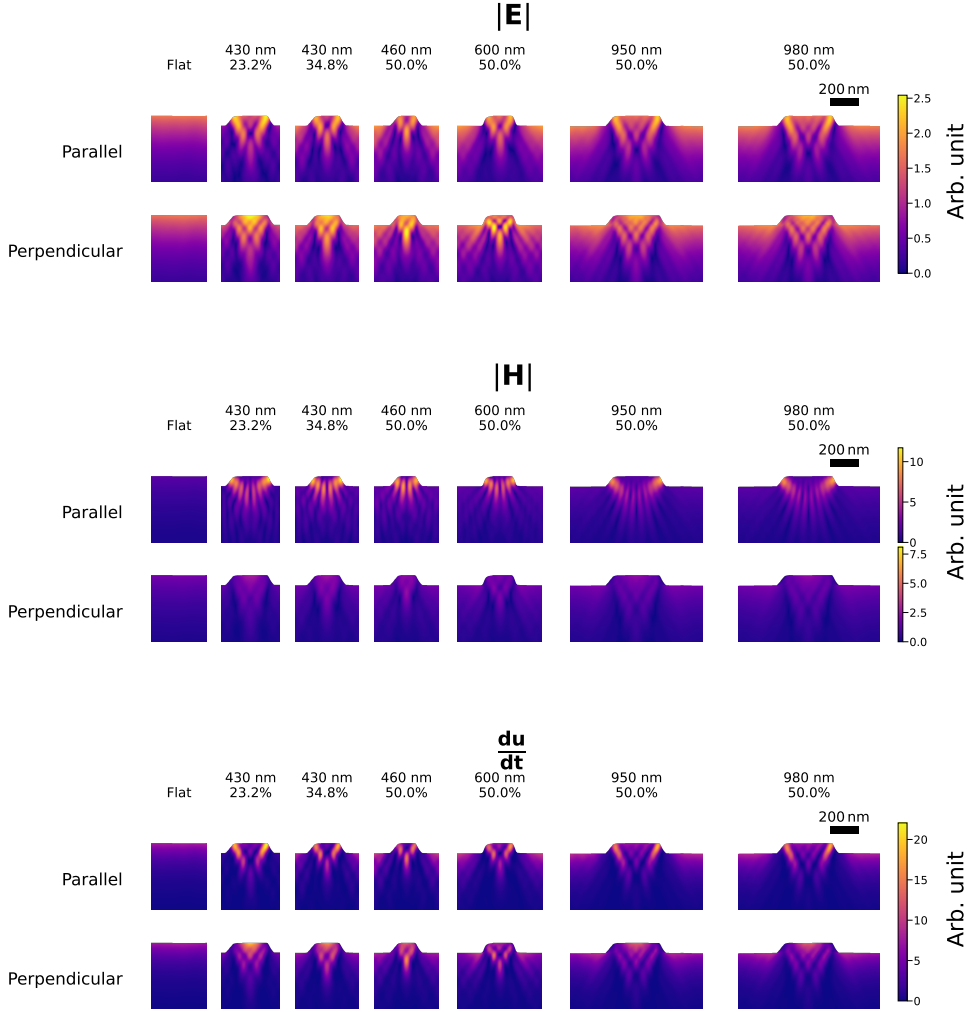
Figure H.3: The calculated $|\mathbf{E}(x,z)|$, $|\mathbf{H}(x,z)|$ and absorbed local power density $\frac{du}{dt}(x,z)$ for all samples illuminated by the same incident fluence with a polarization parallel (top) and perpendicular (bottom) to the grating lines. These profiles are derived using forward diffraction modelling using rigorous coupled-wave analysis (RCWA) [64], for a 400 nm wavelength and linear absorption is assumed.

Table H.1: Threshold fluence and damage mechanism overview for Si and gratings etched in Si

Mechanism	Pump polarization	Pitch (nm)	Duty cycle (%)	F_{th} (mJ/cm^2)
$F_\uparrow$	$\parallel$	*Flat*		92 ± 22
		430	23.2	40 ± 24
		430	34.8	64 ± 14
		460	50.0	88 ± 16
		600	50.0	80 ± 14
		950	50.0	69 ± 35
		980	50.0	88 ± 15
$F_\uparrow$	$\perp$	*Flat*		90 ± 21
		430	23.2	37 ± 11
		430	34.8	58 ± 12
		460	50.0	78 ± 13
		600	50.0	71 ± 6
		950	50.0	59 ± 17
		980	50.0	59 ± 12
F_{dark}	$\parallel$	*Flat*		251 ± 21
		430	23.2	195 ± 14
		430	34.8	162 ± 27
		460	50.0	198 ± 10
		600	50.0	158 ± 9
		950	50.0	170 ± 18
		980	50.0	178 ± 12
F_{dark}	$\perp$	*Flat*		295 ± 6
		430	23.2	201 ± 9
		430	34.8	186 ± 11
		460	50.0	216 ± 6
		600	50.0	149 ± 8
		950	50.0	205 ± 8
		980	50.0	240 ± 6
F_{abl}	$\parallel$	*Flat*		369 ± 24
		430	23.2	266 ± 9
		430	34.8	249 ± 11
		460	50.0	266 ± 10
		600	50.0	257 ± 12
		950	50.0	332 ± 16
		980	50.0	326 ± 12
F_{abl}	$\perp$	*Flat*		409 ± 8
		430	23.2	236 ± 10
		430	34.8	316 ± 6
		460	50.0	273 ± 12
		600	50.0	275 ± 11
		950	50.0	361 ± 11

Table H.1: Threshold fluence and damage mechanism overview for Si and gratings etched in Si

Mechanism	Pump polarization	Pitch (nm)	Duty cycle (%)	F_{th} (mJ/cm^2)
F_{crater}	$\parallel$	980	50.0	383 ± 15
		Flat		816 ± 78
		430	23.2	410 ± 20
		430	34.8	448 ± 3
		460	50.0	435 ± 14
		600	50.0	434 ± 14
		950	50.0	653 ± 27
		980	50.0	666 ± 6
F_{crater}	$\perp$	Flat		796 ± 44
		430	23.2	360 ± 12
		430	34.8	489 ± 26
		460	50.0	466 ± 11
		600	50.0	403 ± 23
		950	50.0	623 ± 26
		980	50.0	725 ± 14

Additional SEM images can be found in figure H.4

H

H.4. THRESHOLD PREDICTIONS

First, the incident electric and magnetic field amplitudes are set equal for all samples to compute $(\frac{du}{dt})_{calc}$. Since linear absorption is assumed, the absorbed local power density scales with the incident fluence F:

$$\frac{du}{dt} \propto F \cdot \left(\frac{du}{dt}\right)_{calc}. \tag{H.2}$$

We can use the derived $\frac{du}{dt}$ profiles to estimate how the fluence thresholds of the gratings will scale with respect to the flat silicon surface. One can simply state that damage occurs when a certain threshold power density P is exceeded ($\frac{du}{dt} \geq P$), which is where $(\frac{du}{dt})_{calc}(x, z)$ is at its maximum. This implies that if the power density starts to reach P in an infinitesimally small area in the sample, the damage threshold has been reached. However, this method is sensitive to numerical errors. Therefore we need to come up with a rule *when* damage will occur given some $(\frac{du}{dt})_{calc}$ profile. We do this by introducing $(\frac{du}{dt})_{eff}$, which is an effective threshold value for the energy density. The threshold fluence should scale with the inverse of $(\frac{du}{dt})_{eff}$. Therefore, P has been taken equal to the mean value of a closed area of size A_{eff} where everywhere inside A_{eff}, $\frac{du}{dt} \geq P$. This means that at least an area A_{eff} has to exceed a certain power density for damage to occur. This simple assumption is more physical, and requires less computation time. However, this does not include time and position-dependent thermal effects. From this defined P, the ratios of the damage threshold fluences of a grating n and the flat surface should be:
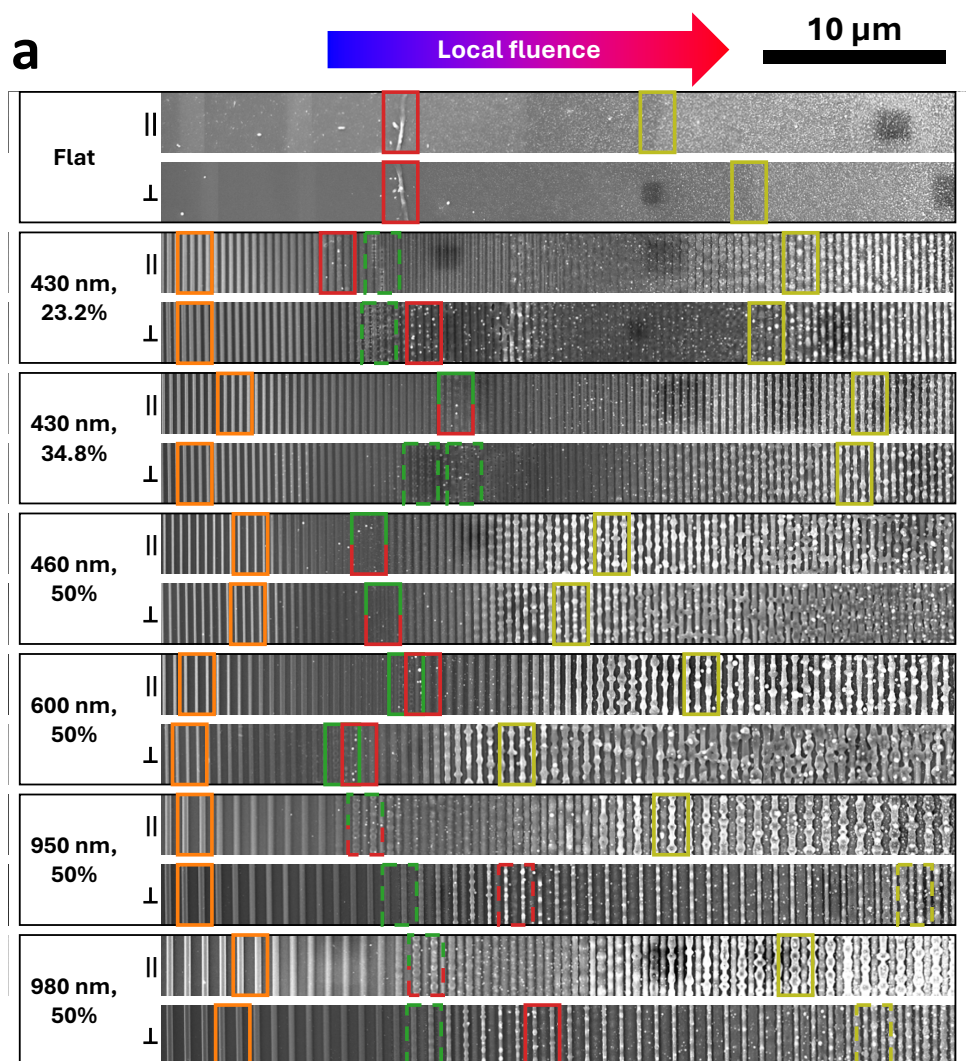
Figure H.4: (a) SEM line scans of segments of illuminated sites by either a ⊥ or ∥ polarized pump pulse above F_{crater} of the flat silicon and six gratings. Since the line scans cover a broad part of the illuminated sites, the local fluence increases from below $F_↑$ to above F_{crater} when moving from the left to the right side. The rectangles indicate the onset of deformation (orange), flattening and/or inversion of the lines (green), ablation onset/droplet formation (red), and the crater edge (olive, not as strongly visible by SEM) respectively. A dashed rectangle indicates a slightly different topography. In (b), individual images are shown at the location of the rectangles. *Figure continues on next page.*
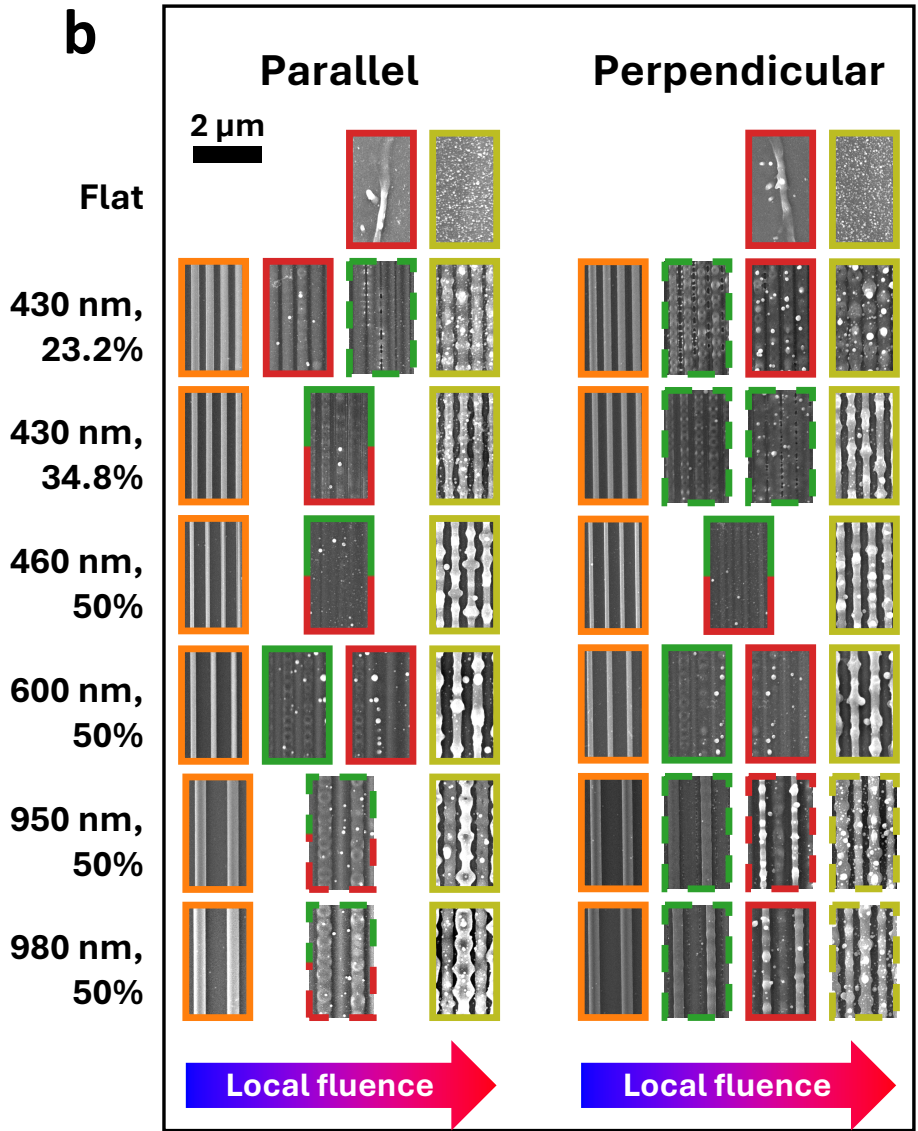
Figure H.4: *Figure continued from previous page.* (b) individual images at the location of the rectangles on the line scans as shown in (a). The colored rectangles indicate the onset of deformation (orange), flattening and/or inversion of the lines (green), ablation onset/droplet formation (red), and the crater edge (olive, not as strongly visible by SEM) respectively. A dashed rectangle indicates a slightly different topography.

$$\frac{F_{\text{th},n}}{F_{\text{th,flat}}} = \frac{P_{\text{flat}}}{P_n}. \tag{H.3}$$

To use as example here, figure H.5 shows the cross section of the 430 nm/23.2% duty-cycle grating multiple times. Here, the area marked in yellow represents A_{eff}, which is obtained by employing two different methods. A_{eff} is set equal to a relatively large size of 2000 nm^2 for clarity. The shapes of the yellow areas are defined such that the mean value $\frac{du}{dt}(x,z)$ under the area is maximized.
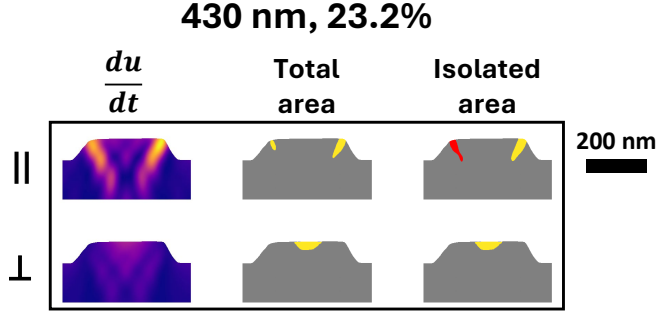

Figure H.5: Calculated $\frac{du}{dt}$ profiles (left) and obtained locations of $A_{\text{eff}} = 2000$ nm^2 (middle and right) for a parallel (top) and perpendicular (bottom) polarized pump pulse illuminating the 430 nm, 23.2% duty-cycle silicon grating. The yellow areas mark the 2000 nm^2 area within which the average $\frac{du}{dt}$ is maximized. The middle and left figures show two methods that can be employed. In the middle, the 2000 nm area is spread out over multiple regions (yellow), and at the right, an extra condition for the position of A_{eff} is applied, where the area has to be one contiguous area. The red area marks the omitted part which contains $\frac{du}{dt}$ values equal and higher than the lowest $\frac{du}{dt}$ value in the yellow area.

In figure H.6, the colored solid and dashed lines are the calculated values for $\frac{P_{\text{flat}}}{P_n}$ at parallel (∥) and perpendicular (⊥) pump beam polarization respectively. Here, different values for A_{eff} between 10 and 2000 nm^2 are used as indicated by the different colors. The data points are the obtained $\frac{F_{\text{th},n}}{F_{\text{th,flat}}}$ values for the four selected damage mechanisms. Here $F_{\text{th},n}$ are experimentally obtained fluence thresholds as presented in table H.1. A correlation between the data points and the calculated values is present, however not as strong as stated in equation (H.3). Additionally, figure H.6 shows that for the experimentally obtained values of $F_\uparrow$, F_{def}, F_{abl} and F_{crater}, the polarization does not influence the threshold significantly, whereas for the calculated values, a perpendicular polarization of the pump beam with respect to the grating lines will result in a higher threshold for the longer pitched gratings.

This analysis however, is very sensitive to the obtained thresholds $F_{\text{th,flat}}$ and calculated values P_{flat} for the flat surface. So despite the correlation, between the calculations and experimentally obtained values, a better, more phenomenological relation between the fluence thresholds and calculated energy density is required.
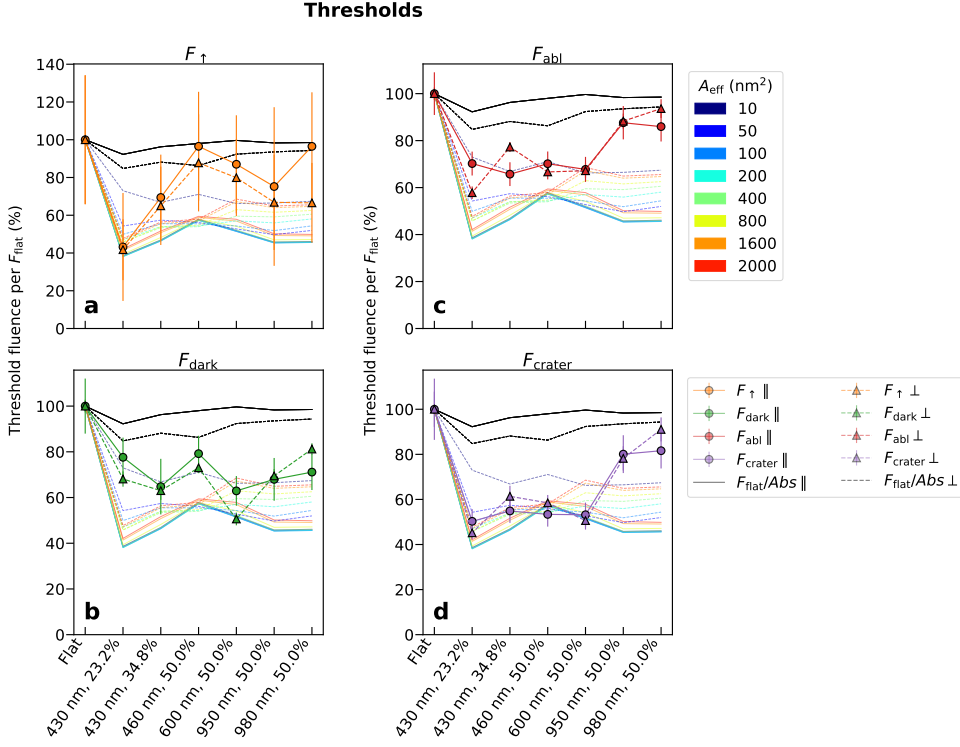
Figure H.6: Experimentally obtained and calculated fluence thresholds $F_\uparrow$ (a), F_{dark} (b), F_{abl} (c) and F_{crater} (d) and total absorption, shown for the flat silicon surface and gratings etched in silicon. All solid and dashed lines indicate parallel ($\parallel$) and perpendicular ($\perp$) pump polarization respectively, and all lines are included as a guide to the eye only. The lines containing markers indicate the experimentally obtained threshold values. The solid and dashed black lines indicate $\frac{Abs_{flat}}{Abs}$, which show the inverse of the calculated absorbed fraction (Abs) scaled to the absorbed fraction of the flat surface. If the amount of total absorbed light defines the values of the damage threshold, the black lines should follow the $F_\uparrow$, F_{dark}, F_{abl} and F_{crater} data points (orange, green, red and purple), which they do not. Closed areas A_{eff} of size 10 to 2000 nm^2 are obtained using the *isolated area* condition (see figure H.5). For each A_{eff}, P, the mean value of $\frac{du}{dt}(x, z)$ within A_{eff}, is calculated. From this, the calculated fluence thresholds using near-field calculations ($\frac{P_{flat}}{P_n}$) are obtained and shown by the colored solid and dashed lines at $\parallel$ and $\perp$ pump beam polarizations respectively.

ACKNOWLEDGMENTS

Now the part that will be read the most: the Acknowledgements. Since everybody will immediately look for their own name, I made it easier for you by **highlighting** every name.

Most outsiders — and perhaps even some insiders — see a four-year PhD program as something really tough: years of struggling, uncertainty about the work, and worrying about submitting the thesis on time. However, for me, it was completely different. Working at ARCNL, in such a great environment with so many wonderful colleagues, was truly a huge pleasure. I'm still a bit surprised by the fact that this was actually a job — and not just a (very serious) hobby.

The one mostly to thank for this is **Paul**. I still remember one of our first conversations about the PhD position. It was mid-Covid, so we met online. Time just flew by as we chatted about just anything. It didn't feel like an interview at all. And then, at the end of the call, you asked me to become a new PhD student in your group. Without any background check or a more in-depth discussion of the position, you expressed your trust in me. So after both skipping some 'minor' details, like presenting to the group, I suggested you should probably check my references. After meeting the rest of the group members, you became my supervisor. From you, I learned to simply have fun in the lab and to feel free to explore anything that sparked my curiosity — although I may have taken that a bit too far at times. You helped me countless times with writing papers, especially when I lost overview again. To me, you were a fantastic promotor, supervisor, sparring partner, and so on. You've truly inspired me, and I'm sure we'll stay in touch. So don't hesitate to send me a message — you'll never be a bother.

Klaasjan, you are such a friendly and sympathetic person. After we started collaborating, I felt truly honored when you suggested becoming my supervisor — though neither of us could have foreseen my later urge to 'give my own twist' to my thesis. Thank you for the needed support through all of this.

At the start of my PhD, **Stephen** was there to teach me everything about what would become 'my baby': the laser setup. Thank you so much for your patience and for showing me how to move around in the lab. At the same time, you were also training Lorenzo.

Lorenzo, we grew to be friends, but more than anything, I see you as my Italian brother. You're always genuinely interested in others and a one-of-a-kind person. I still feel sorry for kind of neglecting you in my last two years (as I slowly turned into a computer-staring zombie). I'm really glad we're still in touch, and hopefully we will be in the future.

Together with **Thomas**, we formed the new batch of PhD students in the group. Thomas, you made the office such fun to be in. Countless chats about anything and laughing quite a bit. Not only discussing football, but so many other (less important) matters as well. You are a stand-up-guy with a lot of cultural interests, and always up for a beer (after marathon training season of course).

By now, it might sound a bit fake or unreal, but alongside Lorenzo and Thomas, there is a third unique person I can call my friend: **Vina**. Before meeting you, I saw you as this big-shot ASML researcher (which, of course, you are). But you turned out to be someone with a remarkably broad perspective. You know so much about so many research-related topics, yet you can always put things into perspective. I often joke about it, but if you ever start your own company or research group, I want to work for you! Especially because you know that there is more than just this sciency world. And maybe because of the creative side we both have (you in your artwork, and me in playing music), we have this nice match. Next to a friend, I also see you as the face of somebody who can be humane within a corporate environment.

I want to thank all the other members of the *Light–Matter Interaction group*, especially **Guido**, who first introduced me to PhD life, as well as **Reynolds**, **Christoph**, **Komal**, **Soonia**, **Jordi**, and of course, **Thomas Meijvogel**. Thomas, as our group technician, you were always there to fix something or fabricate whatever I needed. Fortunately, you often stepped in with great solutions, and great conversations too.

Of course, many more people helped me along the way. **Bob**, **Igor**, **Dylan**, **Cyrian**, and **Tunç**, thank you for training me to work in the cleanroom and with the AFM, and for always being there to help out. **Dries** and **Marnix**, I really appreciated our collaboration. The many visits in Utrecht always impressed me and I always enjoyed the engaging discussions we had. **Nikolai**, you not only gave our research more depth, but I also really appreciated the time we spent side by side in front of the 'big microscope'. **Adinda**, thank you so much for the design of the amazing cover of this booklet.

As I mentioned earlier, it never really felt like work. This might be because of the nice ambiance in ARCNL, due to people described above and my many (former) colleagues. Always had fun with my office mates **Stefan van Vliet**, **Matthias**, **Augustas**, **Fengling**, **Antonios**, and **Parikshit**. And of course **Yahia**, **Lucas**, **Matthijs**, **Maksym**, **Kevin**, **Natalïa** my conference roommate, **Barsha**, **Kian**, **Jorge**, **Maisie**, **Randy** — whether it was during lunch, the **ARCNL band**, or the **ARCeNaL** futsal team, let's still keep in touch, having fun and discussing weird academic intrigues.

I would also like to thank **Joost**, **Wim**, and **Marjan** for fostering such a friendly, open environment: a flat organization where you could always raise concerns or have a casual conversation with just anybody. That said, I sometimes feel that management tends to get most of the credit for this culture, when it's really built by the people doing the real work. **Jusra**, **Jet**, **Celine**, **Marja** and **Ellen**. Bij jullie kon ik altijd zo veel lachen; want binnenpretjes en roddels werken toch nét iets beter in het Nederlands.

Furthermore, I would like to thank the committee members **prof. dr. ir. H.B. van Linden van den Heuvell**, **prof. dr. A.F. Koenderink**, **prof. dr. I.D. Setija**, **dr. K.I.E. Olsson**, and **dr. D. van Oosten** (mentioned before), all **user committee members** and **NWO**, **ASML** and **ALSI** for their financial support.

Eigenlijk is zo'n dankwoord een beetje raar. want iedereen heeft zo zijn dagelijkse werk of bezigheden. Dat PhD-werk van mij genereert alleen misschien wat aanzien omdat er een onnodige titel aan verbonden is. Moet ik daarom zeggen door wie dit allemaal mogelijk is in mijn omgeving? Ik gebruik dit stuk liever als een algemeen dankwoord voor de vele familieleden en vrienden, waardoor ik zo geniet van mijn leven. En natuurlijk om op te scheppen dat ik er zo veel heb.

Je omgeving is erg belangrijk in je ontwikkeling en de kansen die je krijgt. Voor iemand die houdt van nerdy dingen, had ik geen betere ouders kunnen wensen. Mijn vader **Ido** zag altijd de meerwaarde van leren in [1]. Ik heb daarbij nooit enige druk gevoeld om mijn interesses te *moeten* verkennen. Door hun steun doe ik dit altijd vanuit plezier. En mijn moeder **Debby**, die af en toe checkte of het wel een beetje ergens op sloeg, schept altijd enorm op vanuit trots. En nu heb ik dat beta-achtige voor een groot deel van papa; het niet-onhandige, sociale en de liefde om over mijn onderzoek te vertellen komt helemaal van jou mam.

Samen met mijn moeder, is er nog één persoon die mij goed in de gaten heeft gehouden en zo nodig (en dat was vaak) ervoor zorgde dat ik wat at. **Lea**, zus/huisgenoot/kok, ik ben zo blij met onze bijzondere band. Hier profiteer ik niet alleen van, maar ook de vele anderen die bij ons over de vloer komen. Altijd een super uitgebreide maaltijd in een handomdraai, maar vooral ook iemand om altijd mee babbelen, filosoferen en vooral (uit) te lachen, te dollen en te analyseren, en om jezelf te citeren: "Wat ben jij toch geweldig" (oorspronkelijk: "Wat ben ik toch geweldig").

Het flexibele werken is iets dat ik geweldig vond: experimenten die draaien tussen voetbaltraining door, en af en toe laat nog werken na een bandrepetitie. **Lotje** en **Tim**, ik heb zo veel plezier om samen met jullie, **Casper** en **Metehan** in onze band **MatraK** (#AD) te spelen. Ik heb echt geleerd dat creativiteit geen grenzen kent, en lol ook niet. Naast de band zijn de pubquizzen, schaatsritjes en andere dingen mij ook erg dierbaar. **Lenneke**, **Hanneke**, **Laetita**, **Julia**, **Annabel**, **Dorisha**, **Heleen**, **Liora**, **Maaike**, **Marlinde**, **Maud**, **Soraya**, **Tesse**, **Tessel**, **Titia**, **Zsa Zsa** en nog veel meer mensen van o.a. voormalig **De Meer Vr2** en nu **DVVA Vr3**; het is zo lekker altijd weer te huppelen in de wei en even uit mijn natuurkundebubbel te treden, op voetbalvakantie te gaan of bij al onze andere activiteiten. Ik wil toch ook **Clau** nog noemen; in het begin was je een enorme steun voor me en diegene die het meest geïnteresseerd was in wat ik deed. Verder wil ik ook nog mijn oom **Max**, **Els**, de CERN-buddy's **Anastasija**, **Anna-Monica**, **Elena**, **Lia**, **Sivi** en **Susanna**, en (roei)vrienden **Maaike**, **David**, **Sarah** en **Pascalle** 'acknowledgen'. Ook aan **Ajax**, **TeamNL** en de stad **Amsterdam**; bedankt voor de steun én struggles de afgelopen jaren!

Dat ik vrienden voor het leven heb, zie je aan hoe lang ze al meegaan. **Jonne**, jij spant natuurlijk de kroon! Altijd zijn we erg betrokken geweest in elkaars leven, en dat gaan we lekker zo houden. Jij bent, samen met **Sandra** en **Lily**, familie voor me! Lily, het is zo fijn jou dicht bij in de buurt te hebben. Viool, kletsen, zwemmen, het maakt niet uit, het is altijd chill (wat mij betreft dan). **Michelle**, **Sindy**, **Carlos**, **Awital**, **Carly** (Lotje en Tim zijn al eerder genoemd); ik wil hierbij een compliment aan mezelf maken over mijn perfecte gevoel voor goede, oprechte en niet-saaie vrienden.

Er missen nog twee erg belangrijke namen, mijn (aangenomen) zus en broer: **Binkie** en **Maarten** aka de "Para's". Natuurlijk bedank ik jullie voor het officiële gedeelte: het organiseren van dit alles als mijn paranymfen. Maar dat is peanuts vergeleken met de steun en plezier die ik altijd bij jullie kan vinden. Binkie, onze humor heeft geen grenzen. Acht uur wandelen gaat zelfs zo voorbij als je non-stop naar 'Radio Binkie' kan luisteren. En Maarten, dat ondanks mijn schaamteloosheid, je mij kan handelen, toont onze diepe band.

LIST OF PUBLICATIONS

This thesis is based on the following publications:

Chapter 3: E. Abram[1,2,3,4,5,6,7], I. Milov[4,6], N. Orlov[2,3,6], K. van Druten[4], E. C. Garnett[8], and P. Planken[1,7,8], "Pre-ablation regime light-induced optical changes in nanometer thick metal films", Opt. Express **32**, 4564–4587 (2024).

Chapter 4: E. Abram[1,2,3,4,5,6,7], N. Orlov[2,3,6], E. C. Garnett[8], and P. Planken[1,4,7,8], "Sub-ablation-threshold light-induced modification of thin ruthenium layers detected using optical reflectance", Journal of Applied Physics **136**, 245305 (2024).

Chapter 5: E. Abram[1,2,3,4,5,6,7] and P. Planken[1,7,8], Light-induced optical and nanostructural changes of Si gratings, Manuscript submitted, 2025.

The author contributed to the following published works:

E. Abram, V. Faramarzi, R. Dziobek-Garrett, R. Bliem, and P. Planken, "Light-induced damage in semiconductor device manufacturing: present and future challenges", Manuscript in preparation, not presented in this thesis.

G. de Haan[1,2,3,4,5,6,7], E. Abram[4,7], T. J. van den Hooven[2,7], and P. C. M. Planken[1,7,8], "Plasmonic enhancement of photoacoustic strain-waves on gold gratings", AIP Advances **12**, 025227 (2022).

L. Cruciani[1,2,3,4,5,6,7], M. Vreugdenhil[2,7], S. van Vliet[2,3,7], E. Abram[2,7], D. van Oosten[7,8], R. Bliem[7,8], K. van Druten[1,7,8], and P. Planken[1,2,4,7,8], "Direct laser patterning of ruthenium below the optical diffraction limit", Applied Physics Letters **124**, 171902 (2024).

The author wrote the following Python packages, which are made publicly available:

E. Abram, *Multilayers*, `https://github.com/eabram/multilayers.git`, version v3.0, 2025.

E. Abram, *Contours*, `https://github.com/eabram/contour.git`, version v1.0, 2025.

---

[1]Conceptualization, [2]Data acquisition (experiments), [3]Data analysis, [4]Simulations/calculations, [5]Manuscript preparation, [6]Writing (original draft), [7]Writing (review), [8]Supervision